

The University of Nottingham

UNITED KINGDOM · CHINA · MALAYSIA

Polymer Particle Formation for Bacterial Cell Attachment Control

Amanda Hüsler, BSc. MSc.

Thesis submitted to the University of Nottingham for the degree of

Doctor of Philosophy

September 2017

ABSTRACT

Bacterial attachment and subsequent biofilm formation are the cause for most healthcare-associated infections, leading to both morbidity and mortality. As the post-antibiotic era dawns on us, there is an urgent need to fully understand material-performance relationships for specific biological applications. This facilitates to move towards rational design of improved biomaterials.

In this thesis, a step change in formation and screening from planar 2D to particulate 3D surfaces was achieved. A library of microparticles composed of (meth)acrylates was generated using photopolymerisation with either piezoelectric inkjet printing or microfluidics. The surface chemistry and topography of the generated particles was fully characterised prior to bacterial biofilm formation testing with *Pseudomonas aeruginosa.* Microfluidics has been shown to be the superior particle fabrication methodology, yielding significantly more microparticles with enhanced properties and uniformity. Microparticles formed using microfluidics were perfectly spherical in shape, exhibited narrow size distributions and low average surface roughness alongside a mostly defect-free surface. By comparing inkjet printing with microfluidics in terms of particle properties and yields, the differences in performance were related to the disruptions caused by crossing a phase boundary in the inkjet printing system; from gaseous to liquid. For both techniques, adding a surfactant was necessary to obtain stable droplet formation. Assessing the effect of particle surface chemistry, architecture and size on *P. aeruginosa* attachment was complicated by the presence of surfactant on both microfluidic and inkjet printed particles. Poly(vinyl alcohol-co-vinyl acetate) (PVA) demonstrated biofilm resistant properties both as bulk and surfactant but with varied efficacy depending on the PVA content.

The novel contribution of this work is the generation of a microparticle library of 20 (meth)acrylates made from photocrosslinkable monomers with inkjet printing and microfluidics. For the first time, this study presents a comparison between the two particle fabrication methodologies with respect to microparticle production and characteristics. The work presented in this thesis has provided insights towards the identification of material-property relationships for *P. aeruginosa* attachment to particles. In prospect for the future, the vision is to progress this effort for applications that require particle delivery into the body such as medical devices with low-fouling coatings, drug delivery and cell carriers in regenerative medicine strategies.

PUBLICATIONS

Journals - Included in this Thesis

Under Review:

- Hüsler Amanda, Haas Simon, Parry Luke, Romero Manuel, Nisisako Takasi, Williams Paul, Wildman Ricky and Alexander Morgan, 2017. Effect of surfactant on *Pseudomonas aeruginosa* colonization of polymer microparticles and flat films.

Journals - Not included in this Thesis

Published:

- Michl Thomas D., Coad Bryan R., Hüsler Amanda, Valentin Jules D. P., Vasilev Krasimir and Griesser Hans J., 2016. Effects of Precursor and Deposition Conditions on Prevention of Bacterial Biofilm Growth on Chlorinated Plasma Polymers. *Plasma Processes and Polymers*. 13(6), 654-662.
- Michl Thomas D., Coad Bryan R., Hüsler Amanda, Vasilev Krasimir and Griesser Hans J., 2015. Laboratory Scale Systems for the Plasma Treatment and Coating of Particles. *Plasma Processes and Polymers*. 12(4), 305-313.
- Michl Thomas D., Coad Bryan R., Doran Michael, Osiecki Michael, Kafshgari Morteza H., Voelcker Nicolas H., Hüsler Amanda, Vasilev Krasimir and Griesser Hans J., 2015. Nitric oxide releasing plasma polymer coating with bacteriostatic properties and no cytotoxic side effects. *Chemical Communications*. 51(32), 7058-7060.
- Michl Thomas D., Coad Bryan R., Doran Michael, Hüsler Amanda, Valentin Jules D. P., Vasilev Krasimir and Griesser Hans J., 2014. Plasma polymerization of 1,1,1-trichloroethane yields a coating with robust antibacterial surface properties. *RSC Advances*. 4(52), 27604-27606

In Progress:

- Taresco Vincenzo, Styliari Ioanna D., Conte Claudia, Hüsler Amanda, Nieto-Orellana Alejandro, Hook Andrew, Alexander Morgan, Garnett Martin, Alexander Cameron and Louzao Iria, 2017. High throughput miniaturized screening of nanoparticles formation via inkjet printing.

Conference Presentations

Oral Presentation:

- Hüsler Amanda, Wildman Ricky D. and Alexander Morgan R., 2015. Polymer particle formation using inkjet printing. *26th Annual International Solid Freeform Fabrication (SFF) Symposium, Austin, USA.*
    - Peer-reviewed manuscript:
      Hüsler A, Wildman RD and Alexander MR, 2015. Polymer particle formation using inkjet printing. *SFF Symposium Proceedings*. 1679-1687.
- Hüsler Amanda, Wildman Ricky D. and Alexander Morgan R., 2016. Polymer particle formation using inkjet printing and microfluidics. *Laboratory of Biophysics and Surface Analysis (LBSA) Conference, Nottingham, UK.*

Poster Presentation:

- Hüsler Amanda, Wildman Ricky D. and Alexander Morgan R., 2015. Polymer particle formation using inkjet printing. *Postgraduate Research Poster Presentation Session 2015/16. Nottingham, UK.* (Best Academic Assessor Feedback)
- Hüsler Amanda, Wildman Ricky D. and Alexander Morgan R., 2016. Polymer particle formation using inkjet printing. *10th World Biomaterials Congress, Montreal, Canada.*
    - Published abstract:
      Hüsler A, Wildman RD and Alexander MR, 2016. Polymer particle formation using inkjet printing. Front. Bioeng. Biotechnol. Conference Abstract: 10th World Biomaterials Congress. doi: 10.3389/conf.FBIOE.2016.01.01612

ACKNOWLEDGEMENTS

I would like to thank my supervisors, Professor Morgan Alexander and Professor Ricky Wildman for their guidance, expertise and supervision throughout my whole PhD. Working with Morgan and Ricky allowed me to develop my research skills, work independently but also receive great support from both research groups.

I am also deeply grateful to the Japan Society for the Promotion of Science (JSPS) which generously funded my pre-doctoral fellowship at the Tokyo Institute of Technology. This three-month experience would not have been possible without the support, trust and patience of Associate Professor Takasi Nisisako and Professor Takeshi Hatsuzawa.

I would also like to express my gratitude and thank the technicians Mark Hardy, Mark East and Joe White for helping me with the inkjet printer, Paul Cooling for providing me various trainings, Christine Grainger-Boultby and Professor Xinyong Chen for their expertise and technical support in SEM microscopy and AFM imaging, respectively.

Furthermore, I am very thankful to Dr Andrew Hook, Dr David Scurr, Dr Vincenzo Taresco, Dr Yinfeng He, Dr Manuel Romero, Craig Sturgess and Luke Parry for their wealth of advice and assistance. I also deeply appreciate the support I received from my colleagues in Advanced Materials and Healthcare Technologies (AMHT) and Centre for Additive Manufacturing (CfAM).

I have been greatly supported and would like to thank my parents, Robert and Irene, my sister, Jenny, and my brothers, Steven and Kenny, for their fullest support and their appreciation of my limited number of visits. I would also like to give a special thanks to Dr Matthias Hirsch who always lent me an ear when I needed it most and for supporting me both personally and professionally.

“Success is no accident.

It is hard work, perseverance, learning,

studying, sacrifice and most of all,

love of what you are doing or learning to do.”

– Pelé –

TABLE OF CONTENTS

Abstract i

Publications ii

Acknowledgements iv

Table of Contents vi

List of Figures xi

List of Tables xxv

List of Equations xxviii

Nomenclature xxix

1. Introduction 1

1.1. Background 1

1.2. Scope of Thesis 2

2. Literature Review 3

2.1. Polymeric Micro- and Nanoparticles 3

2.1.1. Particle Fabrication Methodologies 3

2.2. Inkjet Printing 7

2.2.1. Inkjet Printing - An Overview 7

2.2.2. Piezoelectric Inkjet Printing 9

2.3. Microfluidics 12

2.3.1. Microfluidics - An Overview 12

2.3.2. Microchips 13

2.3.3. Droplet-based Microfluidics 14

2.4. Free Radical Based UV Curing Reaction 17

2.4.1. Basic Concept 18

2.4.2. Photoinitiator - Type I and Type II 19

2.4.3. Oxygen Inhibition 21

2.5. (Meth)acrylates 24

2.6. Problems Associated with Bacteria 27

2.6.1. Bacterial Cell Wall and Surface Structures 27

2.6.2. Biofilm Formation 30
2.6.3. Prevention of Bacterial Attachment 32
2.6.4. Mechanism of Action of Non-fouling Materials 33
2.7. Summary of Research Gaps 36
3. Materials and Methods 38
3.1. Introduction 38
3.2. Microsphere Formation 38
3.2.1. Piezoelectric Inkjet Printing 38
3.2.2. Microfluidics 40
3.3. Materials 42
3.4. Material Characterisation Techniques 45
3.4.1. Viscosity Measurement 45
3.4.2. Surface Tension Measurement 46
3.4.3. Photo-Differential Scanning Calorimetry (Photo-DSC) 47
3.4.4. Fourier Transform Infrared Spectroscopy 48
3.5. Particle Characterisation Techniques 49
3.5.1. Optical Microscopy 49
3.5.2. Scanning Electron Microscopy 49
3.5.3. Particle Sizing 50
3.5.3.1. Measuring the Size Distribution of Microfluidic Particles 50
3.5.3.2. Measuring the Size Distribution of Printed Particles 51
3.5.4. Time-of-Flight Secondary Ion Mass Spectrometry 52
3.5.5. Atomic Force Microscopy 53
3.6. Bacterial Attachment Assays 53
3.6.1. Bacteria and Growth Conditions 53
3.6.2. Confocal Microscope Image Acquisition 54
3.6.3. Biofilm Quantification 55
3.7. Summary 58
4. Results - Generation of a Particle Library 59

4.1. Introduction 59
4.2. Experimental 60
4.2.1. Preliminary Experiments 60
4.2.1.1. Optimal Solution Ratio of Isopropanol in Deionised Water 60
4.2.1.2. Manuel Pipetting Experiments 60
4.2.1.3. High Speed Imaging of Pipetting 62
4.2.2. Interfacial Tension Measurement 63
4.2.3. Preparation of Fluids for Particle Formation 64
4.2.3.1. Preparation of Fluids for Inkjet Printing 64
4.2.3.2. Freeze-pump-thaw Cycling 65
4.2.3.3. Preparation of Fluids for Microfluidics 66
4.2.4. Printing in Air 66
4.2.5. Focused Ion Beam Measurement 67
4.3. Results and Discussion 68
4.3.1. Preliminary Experiments 68
4.3.1.1. Optimal Solution Ratio of Isopropanol in Deionised Water 68
4.3.1.2. Manual Pipetting Experiments 69
4.3.2. Characterisation of Photopolymerisation Kinetics 70
4.3.2.1. Monitoring of Radiation Curing by Photo-DSC 71
4.3.3. Generation of Particles using Inkjet Printing 77
4.3.3.1. Comparison with the Manual Pipetting Experiment 77
4.3.3.2. Interdependency Analysis of Monomers and Collecting Fluids 80
4.3.3.3. Effect of Different Parameters on Particle Formation 81
4.3.3.4. Printing in Air 89
4.3.4. Generation of Particles using Microfluidics 91
4.3.4.1. Formation of Homopolymeric Droplets in a T-junction 91
4.3.4.2. Formation of Pre-blended Co-polymerised Particles in a T-junction 95
4.3.4.3. Formation of On-chip Co-polymerised Particles in a Y-shaped Channel Leading to a T-junction 98

4.3.5. Comparison between Inkjet Printing and Microfluidics 102
4.4. Summary 105
5. Results - Microparticle Characterisation 108
5.1. Introduction 108
5.2. Experimental 109
5.2.1. Particle Defect Assessment Method 109
5.2.2. Post-treatment of Microparticles 109
5.2.2.1. Washing of Particles for Removal of Silicon-based Contamination 109
5.2.2.2. Washing of Particles for PVA Coverage Removal 110
5.3. Results and Discussion 110
5.3.1. Characterisation of Inkjet Printed and Microfluidic Produced Particles 110
5.3.1.1. Particle Size and Size Distribution 110
5.3.1.2. Particle Shape 114
5.3.1.3. Surface Roughness 120
5.3.2. Assessment of Microparticle Surface Chemistries 125
5.3.2.1. Removal of Silicon-based Contamination 125
5.3.2.2. PVA Coverage on Particles 130
5.3.3. Comparison between Inkjet Printing and Microfluidics 133
5.4. Summary 135
6. Results - Bacteria Biofilm Assays on Inkjet Printed and Microfluidic Produced Particles 137
6.1. Introduction 137
6.2. Experimental 138
6.2.1. Preparation of Pipetted Thin Films 138
6.2.1.1. Preparation of Control Films 138
6.2.1.2. Preparation of PVA ‘Embedded’ Films 139
6.2.1.3. Preparation of pHEMA Films 139
6.2.1.4. Preparation of Pipetted Films with Different Thicknesses 140

6.2.2. Microbial Cell Viability Assays 140
6.3. Results and Discussion 141
6.3.1. Bacterial Attachment Assays - Effect of PVA Surfactant 141
6.3.1.1. Bacterial Attachment on Washed Microparticles 141
6.3.1.2. Bacterial Attachment on Pipetted Films 145
6.3.2. Bacterial Attachment Assays - Comparison from 2D to 3D 147
6.3.2.1. Bacterial Attachment on Microparticles and Pipetted Thin Films 147
6.3.2.2. Effect of Shape on Bacterial Attachment 149
6.3.2.3. Other Parameters affecting the Bacteria Attachment 151
6.4. Summary 156
7. Conclusions 159
7.1. General Conclusions 159
7.2. Recommendations for Future Work 162
8. References 164
Appendix A - Dynamic Light Scattering 195
Appendix B - Time-of-Flight Secondary Ion Mass Spectromerty 196
Appendix C - Atomic Force Microscopy 201
Appendix D - Confocal Laser Scanning Microscopy 203
Appendix E - Preliminary Experiments 204
E.1. Optimal Solution Ratio of Isopropanol in Deionised Water 204
E.2. High Speed Imaging of Pipetting 206
Appendix F - Results of Monomers Performed in Manual Pipetting Experiments ... 208
Appendix G - Surface Chemical Analysis of Inkjet Printed Particles 210
Appendix H - On-chip Co-polymerised Microspheres with Applied Flow Rates and Measured Particle Sizes 211
Appendix I - Physiochemical Properties of the Monomers in the Generated Library 212
Appendix J - Molecular Physiochemical Properties of Selected Monomers 214

LIST OF FIGURES

Figure 2.1: Schematic of polymeric particle preparation using double emulsion polymerisation (W/O/W). Image adapted from Fonseca et al. [35]. 4

Figure 2.2: Schematic illustration of forming drug-encapsulated particles using phase separation: a) dispersion of drug compounds in a polymer solution, b) formation of colloidal polymer droplets as a result of adding a contrasting agent, c) adsorption of the colloidal polymer aggregates around the drug particles, d) solidification of the microspheres. Image adapted from Augustin et al. [47]. 5

Figure 2.3: Schematic representation of an electrostatic spraying system used for producing alginate microparticles. Image adapted from Zhang et al. [24]. 6

Figure 2.4: Schematic representation portraying the functionality of a continuous inkjet (CIJ) printer (a) and drop-on-demand (DOD) inkjet printing devices (b). DOD inkjet printers are classified into thermal (i) and piezoelectric (ii) DOD inkjet printers. Images adapted from B. Derby [86]. 8

Figure 2.5: Schematic representation of two out of three jetting arrangements: a) straight co-flow nozzle, b) curved co-flow nozzle. The generated particles are carried by a stream of deionised water into a rotating beaker filled with water. The third configuration, which involves a print head directly submerged in a collection beaker, is not shown. Images adapted from Fletcher et al. [95]. 10

Figure 2.6: Schematic depiction of the experimental setup to print submerged into an aqueous PVA solution. The nozzle is kept in the adjustment compartment for frequency and pressure adjustments. After reaching a stable printing behaviour, the nozzle is moved to the production compartment to start the production. Image adapted from Böhmer et al. [32]. 10

Figure 2.7: Schematic illustration of fabricating uniform microparticles using a piezoelectric inkjet printer coupled with a drying process: a) monodisperse particles were obtained by evaporating moisture during their fall within an air-drying device prior to gelification, b) various sizes of dried microparticles could be easily manufactured by changing the materials concentration. Images adapted from Iwanaga et al. [98]. 11

Figure 2.8: Particle fabrication using piezoelectric inkjet printing onto hydrophobic surfaces: a) optical microscope image shows a droplet, prepared from several thousand individual drops, on a treated silicon substrate after ejection from the

print head, b) high tilt SEM image exhibits several inorganic spherical cap-shaped salt particles from a printed array. Images adapted from Gillen et al. [71]. 12

Figure 2.9: Summary of the materials used to fabricate microfluidic devices. The materials are presented in dependence of their fabrication costs and usage in research or industry. Image adapted from Ren et al. [113]. 14

Figure 2.10: Droplet-based particle synthesis: a) schematic illustration of the experimental setup, b) optical micrograph showing monodisperse multi-compartment capsules with cores, containing a water-based ferrofluid, surrounded by poly(isobornyl acrylate) shells. Images adapted from Nurumbetov et al. [123]. 16

Figure 2.11: Droplet-based microfluidic particle synthesis: a) schematic representation of a microfluidic cross-flowing system for fabricating biphasic droplets, b) optical micrograph showing Janus droplets made from silicone oil (white) and polymerisable hexanediol diacrylate phase (blue). Images adapted from Nisisako et al. [124]. 16

Figure 2.12: Basic concept of the UV curing free radical polymerisation process. Adapted from W. A. Green [127]. 18

Figure 2.13: Chemical structure of the aryl ketone group. 20

Figure 2.14: Type I alpha-scission process showing the formation of free radicals from the photoinitiator 2,2-dimethoxy-2-phenylacetophenone (DMPA). 20

Figure 2.15: Type II bimolecular hydrogen abstraction process showing the formation of free radicals from the photoinitiator benzophenone and the synergist hydrogen donor 21

Figure 2.16: Oxygen inhibition at different stages of a radical-induced photopolymerisation. Adapted from Studer et al. [149]. 22

Figure 2.17: Reactions showing the oxygen scavenging by tertiary amines. Adapted from W. A. Green [127]. 23

Figure 2.18: Basic chemical structures of an acrylate (a) and a methacrylate (b). ... 24

Figure 2.19: The chemical structures of the 22 selected monomers, which were classified into major (1-16) and minor (A-F) components, are presented. Image adapted from Hook et al. [163]. 25

Figure 2.20: Schematic of the microarray printing using a pin. Initially, the pin is loaded with a monomer solution in a substrate well (left) followed by depositing the

monomer solution onto a pHEMA-coated glass slide (middle). The inset (right) shows a microarray after incubation with fluorescent bacteria. Image adapted from Hook et al. [164]. 25

Figure 2.21: General polymerisation reaction and chemical structures of the monomers are shown: a) diacrylated macromers were synthesised by the condensation reaction of an amine with a diacrylate, b) a library of 120 photocrosslinkable macromers was produced using 12 amines (1-12) and 10 diacrylates (A-J). Figure adapted from Anderson et al. [161]. 26

Figure 2.22: Representation of the cell wall structure of Gram-positive bacteria. Image adapted from Brown et al. [186]. 28

Figure 2.23: Illustration of the cell wall of Gram-negative bacteria. The zoomed-in image shows a lipopolysaccharide with its three components. Image adapted from Brown et al. [186]. 29

Figure 2.24: The five stages of biofilm development: 1) initial attachment, 2) irreversible attachment, 3) growth and division of bacteria, 4) mature biofilm formation, 5) partial dispersion of bacterial cells from the biofilm. Image adapted from Van Houdt et al. [196]. 30

Figure 2.25: Schematic of the bacterial adhesion process according to the DLVO theory: a), reversible adhesion at the secondary energy minimum b) irreversible adhesion at the primary energy minimum by protruding, for example, pili and flagella through the energy barrier. Images adapted from Hori et al. [202]. 32

Figure 2.26: SEM images of statically cultured S. aureus on smooth (left) and Sharklet AF™ (right) PDMS elastomer surfaces were taken on day 0 (a), day 7 (b) and day 21 (c). Areas of bacteria were highlighted with colour to enhance contrast. Figures adapted from Chung et al. [211]. 33

Figure 2.27: Schematic representation of surface hydration and chain flexibility of hydrophilic polymers (a) and zwitterionic polymers carrying positive (red dots) and negative (purple dots) charges (b) to resist protein adsorption. Images adapted from Chen et al. [206]. 35

Figure 2.28: Schematic representation of the entropic protein adsorption model: a) proteins adsorb easily on non-swellable polymer networks, b) protein adsorption on highly swellable polymer networks prevented due to entropic shielding. Images adapted from Wörz et al. [221]. 36

Figure 3.1: Schematic diagram of a piezoelectric inkjet printhead with an orifice of 21 µm. 38

Figure 3.2: The Dimatix DMP-2800 printer with its user-refillable cartridge which is able to print 10 pl drops with a 10-µm drop-placement accuracy. 39

Figure 3.3: Schematic of the experimental setup which was used for ejecting ink droplets into collecting fluids while polymerising them simultaneously by exposure to UV light. 39

Figure 3.4: Schematic of the planar microfluidic geometries: a) simple T-junction applied for homopolymeric and pre-blended copolymerised particles, b) Y-shaped channel leading to a T-junction used for the production of copolymerised on-chip particles. 41

Figure 3.5: Schematic of the experimental microfluidic setup. 41

Figure 3.6: Basics of a photopolymerisation reaction are shown: a) chemical structure of an acrylate, b) chemical structure of a methacrylate, c) initiation of the reaction by absorbing UV energy by the photoinitiator (PI), forming radicals and attacking monomers (M) to generate reactive monomer radicals (PIM•), d) chemical structure of the photoinitiator DMPA. 42

Figure 3.7: Chemical structures of all monomers tested with the inkjet printer. 44

Figure 3.8: Cone and plate measuring system used for rheological measurements on materials with small sample volumes (<1 ml) and/or viscosities of 10 cP and higher: a) schematically drawn, b) photograph. 45

Figure 3.9: Coaxial cylinder in the cup and bob measuring system used to study the rheological behaviour of low viscosity fluids: a) schematically sketched, b) photograph. 46

Figure 3.10: Measuring surface tension on a pendant drop. Red region defines the analysis zone, whereas the first two blue lines are used for the magnification calibration. The third blue line, which is below the needle tip, defines the border below which the shape of the drop will be determined. The green line represents the Young-Laplace fit. 47

Figure 3.11: (Meth)acrylates analysed for their curing kinetics using Photo-DSC. ... 48

Figure 3.12: Multiple internal reflection of a beam of infrared light at the interface between the ATR crystal and sample. 49

Figure 3.13: Schematic of the laser diffraction: laser beam passes through a sample cell where particles scatter the light onto Fourier lenses. The Fourier lenses focus the diffracted light and the scattered light is accurately recorded by detectors. . 51

Figure 3.14: Schematic of the spinning disc: a) front view, b) cross section view. Images adapted from CPS Instruments Europe [239]. 52

Figure 3.15: Schematic description of the developed algorithm to quantify biofilm on 3D surfaces. 56

Figure 3.16: Images highlighting the effect of applying both a volumetric filter and a threshold on confocal data. A cross-section through confocal volumes of inkjet printed particles is shown for: a) before applying a filter, b) after applying the Matlab in-built 3D median filter, c) after applying a threshold on unfiltered data, d) after applying a threshold on noise-filtered data. 57

Figure 3.17: Biomass quantification on microparticles: a) successful circle detection (red) of microparticles present in the optical brightfield image, b) biomass captured on particles after applying the cylindrical mask to the volumetric images. 57

Figure 4.1: Schematic drawing of the experimental setup to visualise the ink droplet (5 µl) behaviour in the collecting fluid after being pipetted from 10 mm above the collecting fluid. 60

Figure 4.2: Schematic representation of the macroscopic pipetting experiment. 61

Figure 4.3: Schematic of the testing array in a 24-well plate. 62

Figure 4.4: Schematic representation of the two different jetting arrangements: a) pipetting from above the collecting fluid, b) pipetting with the tip submerged in the fluid. 63

Figure 4.5: Schematic of the Wilhelmy plate method for measuring the interfacial tension at the monomer-PVA solution interface. 64

Figure 4.6: Abbreviation and chemical structure of each monomer tested using the Dimatix printer. 65

Figure 4.7: Simple waveform with a period of 15 µs was applied for printing in air... 67

Figure 4.8: Schematic illustration of the experimental setup employed for ejecting a monomer solution into an empty petri dish in air while being exposed simultaneously to UV light. 67

Figure 4.9: (Meth)acrylates capable of forming particles when pipetting a small volume (5 µl) into 17 wt% IPA/DIW under argon atmosphere. 69

Figure 4.10: Image showing spherical particles on a glass slide. These particles were obtained by manually pipetting 5 µl of the monomer solutions, HMDA and EG3DMA with 1 wt% DMPA each, from above and below 17 wt% IPA/DIW under argon atmosphere. 70

Figure 4.11: Normalised heat flow is plotted against time for seven chemically similar monomers (chemical structures shown right). The samples were exposed to UV light for 180 s starting at 90 s (dash-dot line). 72

Figure 4.12: Photopolymerisation rates are displayed against time for seven chemically similar inks. The exposure to UV light occurred for 180 s starting at 90 s (dash-dot line). 73

Figure 4.13: The effect of chain length and number of C=C double bonds on polymerisation rates are shown. The chemical structures of the monomers are shown at the bottom. The dash-dot line at 90 s represents the starting point of UV exposure. 74

Figure 4.14: Conversion of monomer (%) was calculated for 23 monomers at the gel-point as a function of time between onset and peak of maximal curing rate. The inks capable of forming particles are illustrated with solid symbols (e.g. ■) and the ones that did not succeed with hollow symbols (e.g. □). 75

Figure 4.15: Total conversion in percentage was computed for 23 monomers as a function of time to reach maximal curing rate. The inks succeeding in particulate formulation are displayed with solid symbols (e.g. ■) and the ones that did not form spheres with hollow symbols (e.g. □)..... 76

Figure 4.16: Brightfield micrographs acquired after printing PEGDA250-DMPA into a) 17 wt% IPA/DIW, b) deionised water and c) hexane. Scale bars are 20 µm. 77

Figure 4.17: SEM pictures taken after jetting PEGDA250-DMPA into 17 wt% IPA/DIW under reduced oxygen atmosphere: a) particles exhibiting few surface pores, b) polymeric network entrapping microspheres. 78

Figure 4.18: Schematic representing the proposed process of multiple particle coalescence due to incomplete cured outer layers of particles. 78

Figure 4.19: FIB images showing an inkjet printed polyPEGDA250 particle: a) before sectioning, b) after sectioning top view, c) after sectioning side view. Scale bars are 2 µm..... 79

Figure 4.20: Monomers capable of forming microspheres, independent on the actual yield, using the Dimatix printer. 79

Figure 4.21: SEM images of polyPEGDA250 particles containing rhodamine B: a) polymer network capturing particles, b) free-flowing particle showing increased surface porosity, c) fractured particle revealing a hollow structure. 82

Figure 4.22: Microparticles with dimpled surfaces were observed when printing pEGPhEA-DMPA into 0.1 wt% SDS dissolved in 17 wt% IPA/DIW. 84

Figure 4.23: The updated library of (meth)acrylates capable of producing microparticles using the Dimatix printer. 86

Figure 4.24: SEM images of particle shapes observed at a printing velocity of 10 m/s: a) flattened particles, b) hemispheres, c) disc-like shapes. 87

Figure 4.25: SEM images presenting particles obtained from printing PEGDA250-DETX-EDB into an empty petri dish under ambient air. Zoomed image reveals the impacted spherical shape of particles. 90

Figure 4.26: Collimating the UV light by inserting a specific lens: a) sketch illustrating how the light will propagate after passing the collimated lens, b) front view showing the collimated lens incorporated into the printing setup, c) side view of the experimental setup. 90

Figure 4.27: Images taken at a glass T-junction: a) stable monomer droplets observed using 2 wt% PVA, b) constant monomer stream seen in the microfluidic chip without adding PVA as a surfactant. 92

Figure 4.28: Images showing the inability of the monomer DMPAm to form droplets: a) in a hydrophobically coated cross-junction glass chip, b) in a glass T-junction using SDS as the surfactant in the continuous phase. 92

Figure 4.29: Flow pattern diagrams of three monomers with different viscosities indicating the regions where monodisperse particles were formed: a) HMDA with 6 cP, b) EGdPEA with 20 cP, c) TCDMDA with 140 cP. Qd is the flow rate of the dispersed phase whereas Qc is the flow rate of the continuous phase. The upper horizontal axis represents the capillary number Ca. The crosses (x) indicate the conditions under which monodisperse droplets were not formed reproducibly. All other symbols (●, ∆, ○) represent the conditions under which monodisperse particles were reproducibly generated. The hollow circles (○, Qd = 0.1 ml/h) and the hollow triangles (∆, Qd = 0.3 ml/h) show the conditions where the particle size

was measured. The boundary between the two regimes, represented as a line, was estimated empirically. 94

Figure 4.30: Effect of the continuous phase (Qc) and monomer stream (Qd) flow rate on particle size is presented for three monomers with different viscosities: a) HMDA with 6 cP, b) EGdPEA with 20 cP, c) TCDMDA with 140 cP. The particle diameters were measured at two fixed Qd. The hollow circles (○) and the hollow triangles (∆) indicate the dispersed flow rate of 0.1 and 0.3 ml/h, respectively. The error bars represent the standard deviation of the measured particle sizes. 95

Figure 4.31: Uniform microparticles were generated from the monomer combination 70 wt% EGdPEA - 30 wt% HMDA: a) brightfield image with a scale bar of 100 µm, b) SEM image with a scale bar of 300 µm. 96

Figure 4.32: Formation of droplets from pre-blended photocurable monomers: a) schematic of a simple T-junction, b) five sequential images illustrating the one-step process of generating droplets at a T-junction. The flow rates of the dispersed and continuous phase are 0.1 and 5.0 ml/h, respectively. 96

Figure 4.33: Examples of unsuccessful droplet formation: a) break-up into droplets did not occur within the channel length when using TMPTA-HFiPA at Q_d= 0.07 ml/h and Q_c= 10.0 ml/h, b) instable flow happened when testing HMDA-DMPAm at Q_d= 0.1 ml/h and Q_c= 5.0 ml/h. 98

Figure 4.34: Schematic of the on-chip copolymerisation method. 98

Figure 4.35: Formation of on-chip co-polymerised droplets from two different photocurable monomers. All the monomers were injected at the same flow rate of 0.05 ml/h into the stream of aqueous PVA solution at 3.0 ml/h: a) sequence of images showing the generation of droplets from two similar monomers (EGdPEA-EGPEA) - good miscibility, b) five sequential images illustrating the one-step process of two dissimilar monomers (EGPEA-TMPTA) - to a lesser extent miscible. 99

Figure 4.36: Instability of HMDA-DMPAm flow resulting in polydisperse droplets using on-chip copolymerisation. Zoomed image shows the phase separation of the monomers. 101

Figure 4.37: Polydisperse microparticles were generated by blending the monomers HMDA and DMPAm in the glass chip. Phase-separation of the monomers resulted in circular features on the particles. 101

Figure 4.38: Formation of co-polymerised droplets from the monomer combination EGPEA-TMPTA using two different copolymerisation approaches: a) blended-before copolymerisation, b) on-chip copolymerisation. The specific properties of the monomers affect the results in on-chip copolymerisation more compared to the mixed properties in blended-before copolymerisation – phase separation might have occurred in on-chip copolymerisation..... 102

Figure 4.39: Schematic representation of the workflow, aspiring and dispensing material, enabled by the sciFLEXARRAYER printer. 105

Figure 5.1: Particle size distribution of inkjet printed microparticles measured using centrifugal sedimentation stabilised by a sucrose density gradient. Particle diameter plotted against normalised relative weight are shown for inkjet printed polyTCDMDA (a) and polyTMPTA (b) microparticles. 111

Figure 5.2: Particle size distribution shown for microfluidic produced particles measured utilising the Coulter LS230. The particle diameter versus normalised differential volume is plotted for microfluidic produced polyTCDMDA (a) and polyTMPTA (b) particles. 112

Figure 5.3: The size distribution of co-polymerised microparticles was determined using the Coulter LS230. The particle diameter is plotted against the normalised differential volume for the microfluidic produced blended-before (a) and on-chip (b) co-polymerised EGPEA-TMPTA particles. 113

Figure 5.4: SEM images of inkjet printed microparticles revealing smooth surfaces with mostly spherical shapes: a) printed polyHMDA particles exhibited some line-like features on the surface, b) sample charge build-up caused some difficulties during SEM analysis. Microparticles were gold sputter-coated prior to the analysis. .. 115

Figure 5.5: SEM micrographs of observations frequently made using inkjet printing: a) polymeric agglomerations with microparticles exhibiting rough features on the surface, b) particles coalesced prior to curing and shrinkage caused a wrinkled appearance, c) particle agglomeration of partially cured microparticles, d) presence of smaller particles emerged from break-up of droplets at the gas-liquid interface. 116

Figure 5.6: SEM images of microfluidic produced particles. The majority of the homopolymeric particles were perfectly spherical in shape and exhibited smooth surfaces as shown for polyEGdPEA (a) and polyTMPTA (b) microspheres. 116

Figure 5.7: SEM micrographs of different defects observed mostly on co-polymerised particles fabricated utilising glass microfluidic chips: a) some degree of asphericity and surface cracking, b) particle agglomeration with few smaller particles revealing surface holes, c) polydispersity and some detachment marks visible on particle surfaces, d) broken microspheres and particles with polymeric residues attached. 117

Figure 5.8: The relation between incidence of defects and monomer identity is plotted for homopolymeric microparticles fabricated using microfluidics. The scale is based on 0 indicating no defects and 1 containing a defect on every particle.. 119

Figure 5.9: The relations between incidence of defects and monomer identity are plotted for blended-before (a) and on-chip (b) co-polymerised microparticles fabricated using microfluidic glass chips. The scale is based on 0 indicating no defects and 1 containing a defect on every particle. 120

Figure 5.10: Arithmetic average roughness derived from AFM measurements is presented for inkjet printed (black) and microfluidic produced (red) microparticles. Roughness values were calculated from 5 randomly selected particles within a sample aliquot, whereas areas of 3 × 3 µm were analysed on top of the particles. 3D topographical images (z-axis range: 160 nm) are shown for the highlighted letters. 121

Figure 5.11: AFM derived arithmetic average roughness is illustrated for blended-before (black) and on-chip (red) co-polymerised microfluidic microparticles. Roughness values were calculated from 5 randomly selected particles within a sample aliquot, whereas areas of 3 × 3 µm were analysed on top of the particles. 3D topographical images (z-axis range: 220 nm) are shown for the highlighted letters. 123

Figure 5.12: Graph revealing a trend that pre-blended co-monomers with large differences in the molecular descriptor parameter $\boldsymbol{\alpha}$ exhibited continuous and discontinuous phase separated morphologies. 124

Figure 5.13: Positive ToF-SIMS spectra of the surface of on-chip co-polymerised EGPEA-TMPTA microparticles from a mass of: a) 0-100 u, b) 101-200 u. Peaks used in the subsequent analysis are labelled. 126

Figure 5.14: FTIR-ATR spectra of crosslinked PDMS (reference, black), evaporated acetone after being shaken in plastic syringe (red) and unwashed on-chip co-polymerised EGPEA-TMPTA particles (blue) are shown for wavenumbers ranging

from 4000-500 cm^{-1}. Zoomed-in image displays a section of the spectra ranging from 2000-500 cm^{-1}. 127

Figure 5.15: Microfluidic on-chip co-polymerised EGPEA-TMPTA particles were washed with four different solvents (hexane, methylated spirit, Dow Corning, Silstrip Liquid) and assessed for their surface chemistry in the positive polarity: a) proportion of total counts [%] with its standard deviation and b) proportion of total counts in relation to the unwashed sample (control) are shown for three representative ions: $C_2H_3O^+$ (PVA), $Si(CH_3)_3^+$ (contamination), $C_6H_5^+$ (monomer). 129

Figure 5.16: ToF-SIMS images displaying an overlay of the characteristic cations ($C_2H_3O^+$ (red, PVA), $Si(CH_3)_3^+$ (green, contamination), $C_6H_5^+$ (blue, monomer)) identified within the ToF-SIMS spectra for: a) unwashed on-chip co-polymerised EGPEA-TMPTA particles, b) on-chip co-polymerised EGPEA-TMPTA microparticles washed with Silstrip Liquid. 130

Figure 5.17: SEM micrographs presenting on-chip co-copolymerised EGPEA-TMPTA particles: a) unwashed as a control, b) after extensive washing applying Silstrip Liquid. 130

Figure 5.18: ToF-SIMS data acquired in the negative ion polarity are showing: a) the fragmentation of the poly(vinyl alcohol-co-vinyl acetate) (PVA) compound into the acetate anion (CH_3COO^-, m/z = 59), b) the proportion of total counts [%] of the acetate anion with its standard deviation for the polyEGdPEA particles varying in wash cycles and its corresponding pipetted thin film. PVA (Mw 25,000) with a hydrolysis degree of 88% was used as control and particle surfactant. 131

Figure 5.19: ToF-SIMS data acquired in the negative ion polarity are showing: a) the fragmentation of the monomer EGdPEA into the cyclopentadienyl anion ($C_5H_5^-$), b) the ratio of the cyclopentadienyl anion to the acetate anion (m/z = 59) for the polyEGdPEA particles varying in wash cycles and its corresponding pipetted thin film. 132

Figure 5.20: Negative ToF-SIMS imaging showing the overlay of CH_3COO^- (red, PVA) and $C_5H_5^-$ (blue, EGdPEA) for: a) pipetted thin film, b) untreated microspheres, c) particles after performing 10 wash cycles. 133

Figure 5.21: Negative ToF-SIMS imaging revealing the inhomogeneous distribution of PVA surfactant on microparticles after the first wash. An overlay of CH_3COO^- (red, PVA) and $C_5H_5^-$ (blue, EGdPEA) is shown. 133

Figure 6.1: Monomers, used to prepare the pipetted control films, are shown with their abbreviations and chemical structures. 138

Figure 6.2: Monomers, used to prepare the PVA embedded films, are shown with their abbreviations and chemical structures. 139

Figure 6.3: Schematic illustration of the preparation of pipetted control and PVA embedded films. 139

Figure 6.4: Chemical structure of poly(2-hydroxyethyl methacrylate) (pHEMA). 140

Figure 6.5: Quantification of biomass on polyEGdPEA microparticles varying in repeats of wash cycles and pipetted polyEGdPEA films: a) biomass volume divided by surface area ($\mu m^3/\mu m^2$) and its standard deviation is plotted against the tested samples, whereas non-tissue culture polystyrene and pieces of silicone catheter served as references of high bacterial attachment surfaces, b) correlation between the biomass captured on surfaces and the percentage of total counts of the acetate anion $[CH_3COO]^-$ detected by ToF-SIMS. 142

Figure 6.6: Biofilm assessment on polyEGdPEA microparticles showing the successful circle detection on acquired brightfield images (left) and the determined biomass (right) for: a) particles as produced (no washing), b) particles washed 10 times prior to bacterial incubation. 143

Figure 6.7: SEM micrographs showing two different defects detected on the surfaces of microfluidic produced polyEGdPEA microparticles: a) detachment marks, b) surface porosity. 144

Figure 6.8: Microbial cell viability assays performed on microfluidic produced polyEGdPEA particles, PVA and polystyrene (reference). The average number of viable P. aeruginosa cells with its standard deviation, which was determined based on quantification of the ATP present, is shown. 144

Figure 6.9: The biofilm of PAO1-N mCherry was quantified on pipetted thin films from the volumetric images acquired using confocal microscopy. The effect of PVA surfactant on bacterial attachment was assessed by comparing polymer films with PVA embedded films applying four different acrylates. Polystyrene and pieces of a silicone catheter were included as references of high bacterial attachment surfaces. 146

Figure 6.10: The biomass of PAO1-N mCherry was quantified on pipetted thin films, inkjet printed and microfluidic produced particles prepared from six different acrylates. By comparing 2D to 3D surfaces, the effect of surface chemistry, shape

and size on bacterial attachment was assessed. Polystyrene and pieces of a silicone catheter were included as references of high bacterial attachment surfaces. 148

Figure 6.11: Biofilm quantified on inkjet printed particles after 24 h incubation in polystyrene wells of 48-well plates. Brightfield (top row) and fluorescence images are shown in orthogonal (middle row) and 3D (bottom row) view for: a) polyHMDA particles, b) polyHPhOPA microparticles. 149

Figure 6.12: The biomass of PAO1-N mCherry was captured on PVA embedded thin films and microfluidic particles. The biofilm quantification involved the custom Matlab algorithm. The effect of particle shape on bacterial attachment was assessed by comparing PVA embedded films with microfluidic particles applying four different acrylates. 150

Figure 6.13: The biomass of PAO1-N mCherry was quantified on pipetted thin films from the volumetric images acquired using confocal microscopy. The effect of pHEMA on bacterial attachment was assessed by comparing polymer films prepared from six different acrylates with and without having a thin, homogeneous pHEMA film underneath. Polystyrene was included as a reference of a high bacterial attachment surface. 152

Figure 6.14: The biovolume of PAO1-N mCherry was assessed at the particle surfaces of three different particle chemistries. The effect of pHEMA on bacterial attachment at particle surfaces was studied by comparing microfluidic polymer particles in untreated and oxygen plasma-activated pHEMA coated wells in 48-well plates. 153

Figure 6.15: The biofilm was quantified on pipetted thin films and microfluidic produced particles composed of polyEGdPEA after 24 h incubation in PAO1-N mCherry suspension under agitation (shaking at 60 rpm). The influence of flow conditions on biofilm-associated bacteria was analysed by washing the samples three times in two different ways, manual pipetting (‘Pipetting’) and applying linear shake movements for five minutes prior to removal of the fluids using a pipette (‘Shaking’). 154

Figure 6.16: The biovolume per surface area was quantified on pipetted polyEGdPEA films which were prepared by pipetting different quantities of monomer solution (25, 40, 55 and 100 µl) onto the well bottoms of 48-well plates. The effect of film thickness on anti-adhesive efficacy was analysed by testing the polyEGdPEA films

varying in thickness with PAO1-N mCherry for 24 h under agitation (shaking at 60 rpm). 156

Figure B.1: A schematic drawing of a collision cascade initiated by the impact of primary ions (red). 196

Figure B.2: Schematic illustration of the operating principle of a ToF-SIMS instrument with its main components. Image adapted from Hofmann et al. [309]. 197

Figure B.3: Comparison of the CN^- peak derived from the negative ion spectrum and the corresponding total ion image. ToF-SIMS data was obtained from a microsphere system: a) in 'high current bunched' mode, b) in 'burst alignment' mode of operation. Images adapted from A. Rafati [313]. 198

Figure B.4: Illustration of a microsphere that becomes distorted in the SIMS imaging process caused by the angle of incidence of the primary ion beam to the particle surface. The secondary ions are extracted in the z-direction. Image adapted from Rangarajan et al. [317]. 199

Figure B.5: Shadowed region formed around a pluronic-coated latex particle (25 µm in diameter) on a glass substrate. The direction of the primary ion beam is shown by an arrow in the top right corner. Image adapted from Vickerman et al. [318]. .. 199

Figure C.1: Schematic representation of the main components of a typical AFM setup. 201

Figure D.1: Schematic representation of a confocal laser scanning microscopy. ... 203

Figure E.1: Sequences of images are shown after pipetting 5 µl of PEGDA250-DETX-EDB: a) into air (reference), b) from above 17 wt% IPA/DIW, c) below 17 wt% IPA/DIW, d) from above 1-octanol, e) from above deionised water. 206

LIST OF TABLES

Table 2.1: Cross-flow, co-flow and flow-focusing geometries for single and multiple structured polymeric particles. Images adapted from Gokmen et al. [120]. 15

Table 2.2: Typical formulation and function of an UV curable ink. Adjusted from R. Schwalm [99]. 19

Table 2.3: Physical and chemical methods to mitigate oxygen inhibition. 22

Table 3.1: All monomers with their corresponding abbreviations tested using the inkjet printer. 43

Table 4.1: Collecting fluids with their physiochemical properties. 61

Table 4.2: Additives dissolved in monomers depending on the test environment. 62

Table 4.3: Monomers employed for microparticle production using microfluidics. 66

Table 4.4: Amount of heat released during photopolymerisation and time at which the peak maximum occurred are listed for seven chemically similar monomers. 72

Table 4.5: Summary of the four different surfactants, which were dissolved into the collecting fluid (17 wt% IPA/DIW), with their chemical structure and HLB value. 83

Table 4.6: Brightfield images showing the results of printing BDDA- and pEGPhEA-DMPA into 17 wt% IPA/DIW supplemented with 0.1 wt% surfactant (PVA, SDS, Triton X-100 and Tween 20). Scale bars are 20 µm. 83

Table 4.7: Brightfield images were taken after printing three different inks (EG4DMA-, EG3DMA- and DEGDMA-DMPA) into 0.1 wt% Triton X-100 dissolved in 17 wt% IPA/DIW. Prior to printing, the monomer solutions were degassed by either bubbling with nitrogen gas or by freeze-pump-thaw cycling. 85

Table 4.8: SEM images showing polyTCDMDA particles ejected at a velocity of 2, 4, 6, 8 and 10 m/s. The images were taken at a magnification of 500x (left, scale bar: 50 µm) and 1500x (right, scale bar: 10 µm), respectively. 87

Table 4.9: Comparison of microparticles printed with three different inks (TCDMDA, EGdPEA and TMPTA) containing standard (1 wt%) and increased DMPA concentration (3-5 wt%), respectively, into Triton X-100 (0.1 wt%) dissolved in 17 wt% IPA/DIW. Scale bars are 20 µm. 88

Table 4.10: Comparison of the monomers employed in microfluidics and piezoelectric inkjet printing with respect to microparticle fabrication. Successful particle formation is highlighted in green whereas the inability to form particles is

highlighted in red. Monomers, which failed to produce homopolymeric particles but were retained for trying to fabricate co-polymerised particles, are highlighted in purple. 93

Table 4.11: Summary of the produced pre-blended co-polymerised microspheres with the applied flow rates and the measured particle sizes. 97

Table 4.12: Summary of the monomer combinations tested for their ability to fabricate microparticles using blended-before and on-chip copolymerisation: successful particle formation (green) and inability to generate particles (red). 100

Table 4.13: Summary showing a comparison between inkjet printing and microfluidics with respect to materials, production rates, sizes, shapes, costs and scalability. 103

Table 5.1: Trade products, Dow Corning and Silstrip Liquid, are listed with their chemical components and their appropriate concentrations. 110

Table 5.2: Summary of the particle sizing data obtained for polyTCDMDA and polyTMPTA microparticles produced by piezoelectric inkjet printing (inkjet) and microfluidics (mf). Disc centrifuge and laser light diffraction were used to measure the particle size distribution of inkjet printed and microfluidic produced particles, respectively. 113

Table 5.3: Summary of the particle sizing data obtained for blended-before (bb) and on-chip (on) co-polymerised EGPEA-TMPTA microparticles. 114

Table 5.4: Summary of possible defects observed on microfluidic produced microparticles and their origin 118

Table 5.5: List of the monomer combinations and their occurrence of continuous and discontinuous phase separated morphologies using blended-before and on-chip copolymerisation: no phase separation (green), phase separation (red) and partial phase separation (purple). 125

Table 5.6: Structure of the monomers (EGPEA, TMPTA), stabiliser PVA, silicone contamination and their representative ions emerged during ToF-SIMS analysis. 128

Table 5.7: Comparison between piezoelectric inkjet printing and microfluidics in terms of the methods and particle characteristics (particle size, size distribution, shape, surface topography and chemistry). Advantages and disadvantages are highlighted in green and red, respectively. 134

Table 6.1: Different volumes of the EGdPEA-DMPA solution, which were pipetted into 48-well plates, and their resultant computed polymer thicknesses. 140

Table E.1: Effect of changing the ratio of isopropanol in deionised water on droplet formation was analysed by pipetting two different inks (Solsys EMD6415, PEGDA250-DMPA) from 10 mm above the collecting fluid into a glass beaker. The inks were tested with and without rhodamine B (rho B). The images were acquired utilising an USB2-Micro-200x USB microscope. 205

LIST OF EQUATIONS

Eq. 2.1: Gibbs free energy 35
Eq. 2.2: Entropic component of the Gibbs free energy 35
Eq. 3.1: Reynolds number 40
Eq. 3.2: Young-Laplace equation - Pressure difference 46
Eq. 3.3: Simplified Stokes equation - Particle diameter 52
Eq. 3.4: Colony forming units per mililitre 54
Eq. 4.1: Interfacial tension 63
Eq. 4.2: Photopolymerisation rate 73
Eq. 4.3: Monomer conversion in percentage 75
Eq. 4.4: Capillary number 93
Eq. 5.1: Relative span 113
Eq. 5.2: Molecular descriptor parameter 123
Eq. A.1: Stokes-Einstein equation - Hydrodynamic particle diameter 195
Eq. A.2: Rayleigh scattering - Intensity of scattered light 195
Eq. B.1: Mass-to-charge ratio 196

NOMENCLATURE

2D	Two-dimensional
3D	Three-dimensional
Abbr.	Abbreviation
AFM	Atomic Force Microscopy
AMHT	Advanced Materials and Healthcare Technologies
ATP	Adenosine triphosphate
ATR	Attenuated Total Reflectance
AU	Airy Unit
Ca	Capillary number
Calu3	Cultured human airway epithelial cells
CfAM	Centre for Additive Manufacturing
CFU	Colony Forming Units
CFU/ml	Colony Forming Units per millilitre
CIJ	Continuous Inkjet
CLSM	Confocal Laser Scanning Microscopy
Coeff.	Coefficient
DCM	Dichloromethane
DETX	2,4-Diethyl-9H-thioxanthen-9-one
DIW	Deionised water
DLS	Dynamic Light Scattering
DLVO	Derjaguin-Landau-Verwey-Overbeek
DMPA	2,2-Dimethoxy-2-phenylacetophenone
DMSO	Dimethyl sulfoxide
DOD	Drop-on-demand
DSC	Differential Scanning Calorimetry

EDB	Ethyl 4-(dimethylamino)benzoate
EPS	Exopolysaccharides
FDA	Food and Drug Administration
FDTS	Perfluorodecyltrichlorosilane
FIB	Focused Ion Beam
FTIR	Fourier Transform Infrared Spectroscopy
HEMA	2-Hydroxyethyl methacrylate
hESC-CM	Cardiomyoctes derived from human embryonic stem cells
HLB	Hydrophile-Lipophile Balance
IPA	Isopropanol
IPA/DIW	Isopropanol in deionised water
IR	Infrared
JSPS	Japan Society for the Promotion of Science
LB	Luria-Bertani
LED	Light-Emitting Diode
LPS	Lipopolysaccharides
Mf	Microfluidics
M_n	Number average molecular weight
MPC	2-Methacryloyloxylethyl phosphorylcholine
MRC5	Cultured human fetal lung fibroblasts
m/z	Mass-to-charge ratio
OCT4	Octamer-binding transcription factor 4
OD	Optical Density
OTS	Objective Threshold Selection
O/W	Oil-in-water emulsion
PA	Pseudomonas aeruginosa

PAO1-N	Specific lab strain representative of *P. aeruginosa* (Nottingham strain)
PBS	Phosphate Buffer Saline
PDMS	Poly(dimethyl siloxane)
PEG	Poly(ethylene glycol)
PGA	Polyglycolic acid
pHEMA	Poly(2-hydroxyethyl methacrylate)
PI	Photoinitiator
PLA	Polylactic acid
PLGA	Poly(D,L-lactide-co-glycolide)
PMT	Photomultiplier
ppb	parts per billion (10^{-9})
ppm	parts per million (10^{-6})
PTFE	Polytetrafluoroethylene
PVA	Poly(vinyl alcohol-co-vinyl acetate)
PVC	Polyvinyl chloride
PZT	Lead zirconate titanate
QNM	Quantitative Nanoscale Mechanical
Re	Reynolds number
rho B	rhodamine B
RPMI	Roswell Park Memorial Institute
RT	Room Temperature
SBMA	Sulfobetaine methacrylate
SDS	Sodium dodecyl sulfate
SE	Secondary Electron imaging
SEM	Scanning Electron Microscopy

Si	Silicon
T_g	Glass transition temperature
ToF-SIMS	Time-of-Flight Secondary Ion Mass Spectrometry
T-PMT	Transmission-Photomultiplier
UHV	Ultra High Vacuum
UV	Ultraviolet
W/O/W	Water-in-oil-in-water emulsion
XPS	X-ray Photoelectron Spectroscopy

1. INTRODUCTION

1.1. BACKGROUND

Micro- and nanoparticles are of great interest because of their potential for trafficking into the body for applications such as low-fouling coatings on medical devices, drug delivery in pharmaceutics [1] and cell carriers in regenerative medicine strategies [2,3]. In the past, polymeric microparticles have been fabricated by a number of techniques including emulsion polymerisation [4], phase separation [5] and spray drying [6]. In order to allow for industrial uptake in a high throughput manner, the current low production rates, lack of control over particle characteristics and the inability to readily access a library of available materials with tailored and designed properties need to be overcome.

A recent versatile manufacturing technique called inkjet printing has attracted attention in the research community due to its capability to precisely deposit picolitre volumes of fluid in well-defined patterns without the need for masks [7,8]. In this thesis, inkjet printing, specifically piezoelectric drop-on-demand inkjet printing, is compared against microfluidics, an alternative, well-established particle fabrication methodology. Both techniques show potential to overcome the low production rates whilst increasing the control over particle characteristics.

This research is focused on the extension of materials discovery through the use of novel fabrication techniques, particularly from planar 2D sample formats (e.g. microarrays) to 3D microparticles, for specific biological applications. To fully exploit the benefits of materials discovery, a combinatorial particle library was generated. Photopolymerisation, which allows in-situ polymerisation while ensuring a close spatiotemporal control, is employed as a method for crosslinking microparticles with a wide range of chemistries. In order to identify new and to optimise existing materials, a full understanding of material-performance relationships is required for a desired application. In this work, microparticles formed using piezoelectric inkjet printing and microfluidics were comprehensively analysed with regards to their surface chemical and structural properties before being tested for their bacterial attachment using *Pseudomonas aeruginosa*. *P. aeruginosa* is a pathogen that is frequently found in medical device-associated infections [9] and, hence, steps to reduce its biofilm formation have been investigated.

1.2. SCOPE OF THESIS

The aims of this thesis are to enable the formation and screening from 2D to 3D surfaces. This demonstrates the potential to identify material-performance relationships for a desired biological response, such as bacterial biofilm formation in this case. This knowledge enables the move towards a rational design of biomaterials which is required to identify materials for specific applications involving interfacial contact between the material and its surrounding environment. To achieve these aims, the following objectives will be explored within this project:

1. Generate a combinatorial library of microparticles based on (meth)acrylates using photopolymerisation in combination with either piezoelectric inkjet printing or microfluidics; both methods show potential for high throughput fabrication.
2. Compare piezoelectric inkjet printing and microfluidics in terms of microparticle production and characteristics including size, size distribution, shape and surface properties.
3. Examine the effect of particle surface chemistry, architecture and size on bacterial attachment of *P. aeruginosa* PAO1-N mCherry.

2. LITERATURE REVIEW

This chapter provides a brief overview of the most common methodologies to fabricate micro- and nanoparticles with a special focus on inkjet printing and microfluidics. Previous studies of forming particles using these two techniques are presented. An introduction to the free radical based UV curing reaction is then given including a description of the two types of photoinitiators, oxygen inhibition and practical measures to circumvent the oxygen inhibition. Furthermore, (meth)acrylates are introduced and presented as a class of materials promising for biomedical applications. Problems and preventive strategies are elucidated, thereafter, in terms of biofilm-associated bacteria. Eventually, a summary of the identified research gaps is given as support for this body of work.

2.1. POLYMERIC MICRO- AND NANOPARTICLES

In the past decades, polymer micro- and nanoparticles have aroused great interest because of their wide range of applications in industry and modern technology [10]. For example, monodisperse micro- and nanoparticles have been used as cell carriers for cardiac regeneration [11] and for oral delivery of insulin to treat diabetes [12,13]. Moreover, particles have also attracted attention in optical, opto-electrical and electrical applications, for use as light diffuser/scatterer, micro-lenses but also for use in handwriting-enabled displays [10,14–16]. Due to their unique properties, such as being able to alter the elasticity and viscosity, polymeric particles are also useful in suspension rheology [17,18].

2.1.1. PARTICLE FABRICATION METHODOLOGIES

Conventionally, polymeric particles have been produced by a number of techniques including emulsion polymerisation [19–21], phase separation [5,22,23], spraying [6,24–26], microfluidics [27–30] and inkjet printing [31–34]. These methodologies are described and an overview of the state of the art will be given in the following sections with focus on particle fabrication in the micrometre range.

EMULSION POLYMERISATION

Emulsion polymerisation followed by solvent evaporation is the most commonly used approach for fabricating particles [2,3,35]. This technique has been employed both on bench and industrial scale [36,37]. The basic principle involves the dissolution of a

monomer in a water immiscible, volatile organic solvent. For this manufacturing technique, dichloromethane (DCM) is the most commonly used solvent [2,23]. The resulting organic phase is then emulsified in a large volume of water in presence of an initiator and emulsifier to form an oil-in-water (O/W) emulsion. Emulsifiers (surfactants), such as poly(vinyl alcohol), are required to prevent particle coalescence. After homogenisation of the O/W emulsion, the organic solvent is evaporated and the particles are isolated from the aqueous phase by filtration, sieving or centrifugation followed by lyophilisation [3,35]. This single emulsion process is predominantly applied for preparing pure polymeric microparticles [38] and for encapsulating hydrophobic drugs and biomolecules [4,35,39]. The O/W emulsification process is not suitable, however, for the encapsulation of water-soluble drugs due to their poor encapsulation efficiency [40,41].

Water-in-oil-in-water (W/O/W) double (or multiple) emulsions provide the possibility to encapsulate hydrophilic compounds. A schematic representation of this method is illustrated in Figure 2.1.

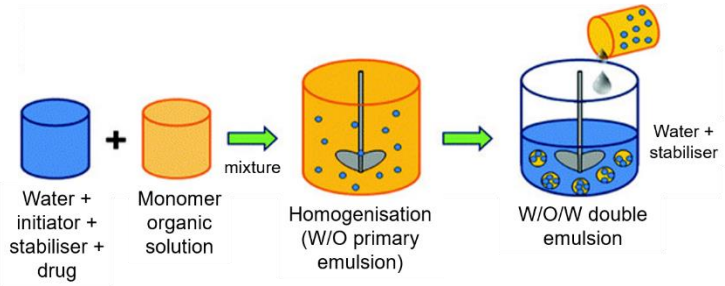


Figure 2.1: Schematic of polymeric particle preparation using double emulsion polymerisation (W/O/W). Image adapted from Fonseca et al. [35].

Initially, the hydrophilic drug is solubilised in water and additives such as an initiator and stabiliser are combined with the aqueous phase (W). This solution is then added to the organic phase (O) containing the monomer and the organic solvent to yield the primary emulsion (W/O). By adding the primary emulsion to another aqueous phase containing a stabiliser, the double emulsion (W/O/W) is prepared. The microparticles are collected in the same way as described using a single emulsification [35].

The lack of controlling the size, size distribution and shape limit the further application of microparticles produced by emulsion polymerisation [42]. In addition, the complete removal of surfactants has been shown as a problem [37].

Phase Separation

Phase separation is a process that is based on decreasing the solubility of the polymeric solution by adding a contrasting component [40]. At some point, this process yields two distinct liquid phases: a polymer containing phase and a supernatant phase

depleted in polymer [2]. When applying this method in the context of drug delivery applications, both hydrophilic and hydrophobic drugs can be encapsulated [23]. In this case, the polymer is initially dissolved in an organic solvent followed by dispersion of drug compounds in the polymeric solution. Subsequently, the contrasting component is added to the polymer-drug-solvent system under stirring, which interacts with the organic solvent resulting in its extraction [43]. As a consequence, phase separation occurs which leads to the formation of colloidal polymer droplets aggregating around the drug particles. To harden the microspheres, the system is transferred to a large quantity of a solvent in which it is not soluble [44–46]. This simple and fast process, which is depicted in Figure 2.2, can be summarised into four steps: a) dispersion of active agents such as drug particles in a polymer solution, b) phase separation leading to initial colloidal polymer droplets after adding a contrasting component, c) surface adsorption of the colloidal polymer aggregates and d) solidification of the microspheres.

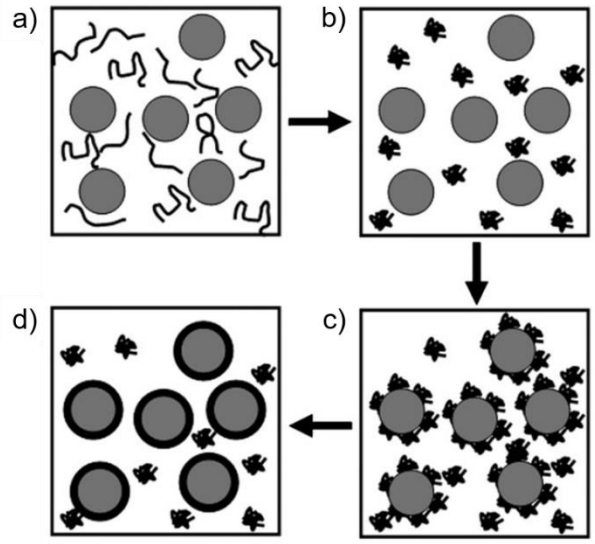


Figure 2.2: Schematic illustration of forming drug-encapsulated particles using phase separation: a) dispersion of drug compounds in a polymer solution, b) formation of colloidal polymer droplets as a result of adding a contrasting agent, c) adsorption of the colloidal polymer aggregates around the drug particles, d) solidification of the microspheres. Image adapted from Augustin et al. [47].

This technique, however, reveals several limitations including the use of strong solvents, batch to batch variability and the tendency of particles to agglomerate [23,48,49]. Moreover, the stirring speed and pH value of the system affect the particle size, whereas the particle shape is influenced by the polymer concentration [3,50].

Spray Drying

Spraying processes have been commonly employed both at the bench and on industrial scales [26]. This technique has found widespread use due to its ease in operation, high efficiency and possibility to generate microparticles in a sterile

environment [24,51–53]. This particle fabrication approach involves spraying a polymer based solution through an atomisation nozzle into compressed air, carbon dioxide or nitrogen. A drug-carrier solution is injected through a heated nozzle followed by its evaporation via a hot stream of flowing gas [54,55]. In this process, the particle size is affected by several parameters such as the spraying rate, polymer-drug solution loading rate and drying temperature [56]. The high temperatures reached in the system can induce denaturation of thermally labile drugs and hence, limit the application for drug encapsulation. The main drawback of spray drying involves the adhesion of microparticles to the inner walls of the nozzle [57]. Furthermore, polymer solutions with high viscosities will result in fibres instead of microspheres due to the inability to break the polymeric stream into small droplets.

Electrospraying is a similar method to spray drying. In this modified technique, however, a polymeric solution is extruded from a syringe by applying an electric field between the collection beaker and the needle [24,53]. A schematic of electrospraying a sodium alginate solution into a calcium chloride gelling bath is depicted in Figure 2.3.

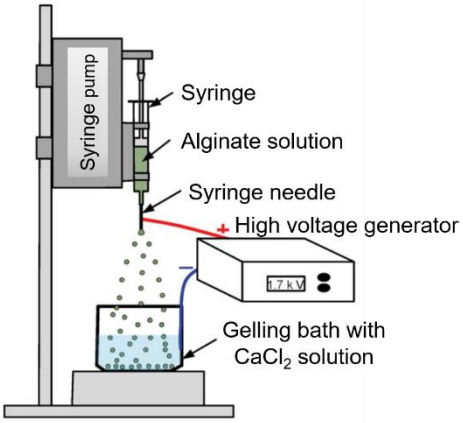


Figure 2.3: Schematic representation of an electrostatic spraying system used for producing alginate microparticles. Image adapted from Zhang et al. [24].

Electrospraying can only be applied to polymer solutions that have a low viscosity and are sufficiently conductive. Moreover, degradation of macromolecules may be induced by stress arising in the drying process or in the nozzle [58].

Summary of Conventional Fabrication Techniques

Most of these conventional particle fabrication methodologies have mainly been used for materials approved by the Food and Drug Administration (FDA). For example, particles consisting of alginates and polyesters, including poly(lactide) (PLA), poly(glycolide) (PGA) and poly(lactide-co-glycolide) (PLGA), have been fabricated in a variety of sizes ranging from micro-to nanometre. Although each of these techniques revealed its own advantages, disadvantages are predominantly caused by the

imprecise control of the process conditions which results in polydispersed and irregular particle sizes and shapes [59–62]. The particle size, size distribution and shape, however, determine the bulk properties, performance and stability of the free-flowing particulate powder [63]. Therefore, they can critically impact, for instance, the drug-release rates, passive targeting to specific cellular types and available routes of administration in case of drug delivery [64–67]. In addition, the ability to control the shape enables to understand and identify the role of geometric parameters for particles functioning in a wide field of applications [68]. Consequently, because of the importance to control these parameters, researchers have introduced filters/sieves, among others, to narrow the particle size distribution.

Several reports have recently been published that allowed the production of monodisperse microparticles in a reproducible manner [1,59,69–71]. The proposed methodologies are inkjet printing and microfluidic based techniques. These techniques appear to be promising in overcoming the issues related to the particle size and shape in controlled drug delivery applications. Additionally, inkjet printing and microfluidics show potential to readily access a library of materials and to fabricate particles in a high throughput manner. This is required for practical and large-scale application in industry. Both particle fabrication methodologies are described in more detail in Sections 2.2 and 2.3, respectively.

2.2. Inkjet Printing

2.2.1. Inkjet Printing - An Overview

A versatile manufacturing technique called inkjet printing has recently gained attention because of its novel and unique manufacturing capabilities. This technique has been widely accepted in the graphical industries for converting digitized information into printed copies; it has lately become an important non-contact patterning technology suitable for a wide range of applications [7,72–75]. For example, inkjet printing has been employed for fabricating multicolour polymer light-emitting diodes (LED) [75,76], polymer electronics [72,73,77] but also devices for inductor and antenna applications [78–80]. In addition, it has also shown potential for biomedical applications including drug delivery [33,81,82] and tissue engineering [83–85]. The features that distinguish inkjet printing from conventional particle fabrication techniques, are the ability to precisely deposit picolitre droplets of solutions or suspensions in well-defined patterns onto substrates with high speed [8,86,87]. Moreover, inkjet printing is capable of

forming structures without the need for masks which in turn has beneficial effects on the number of processing steps, time, space and waste consumption [7,75].

There are two main technologies in use by which contemporary inkjet printers form droplets, namely continuous inkjet (CIJ) printing and drop-on-demand (DOD) inkjet printing [77,86]. Schematic illustrations that present the functionality of a CIJ (a) and DOD (b) printing device are shown in Figure 2.4. The DOD printing mechanism is categorised into thermal DOD (i) and piezoelectric DOD (ii) inkjet printing.

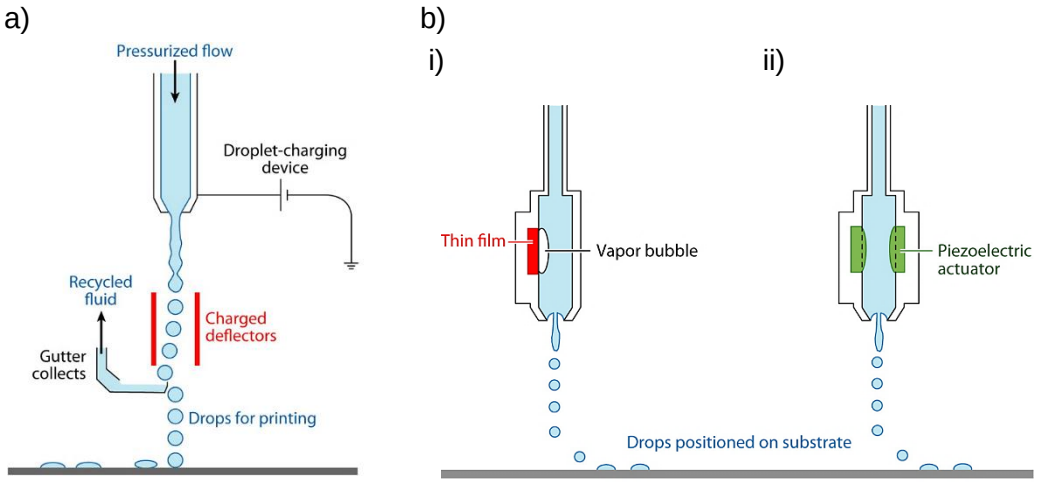


Figure 2.4: Schematic representation portraying the functionality of a continuous inkjet (CIJ) printer (a) and drop-on-demand (DOD) inkjet printing devices (b). DOD inkjet printers are classified into thermal (i) and piezoelectric (ii) DOD inkjet printers. Images adapted from B. Derby [86].

In CIJ printing, a fluid is ejected through a small orifice under pressure which results in a stream of small droplets. These droplets are formed by the Rayleigh instability causing the fluid stream to break up [34,86]. A small charge is imparted to the droplets upon formation due to the nozzle being kept at a potential relative to ground. By applying an electrostatic or magnetic field, the individual drops can, thus, be steered in flight. CIJ printing, as its name implies, produces a continuous stream of drops. The unwanted droplets are deflected to a gutter accordingly and recycled [88,89].

The second mode of generating droplets is DOD inkjet printing which is shown in Figure 2.4 b). In contrast to CIJ printing, droplets are only formed when required and therefore, this way of delivering an ink is more economical. Drops are ejected if the pressure pulse, which propagates through a fluid filled chamber towards the nozzle, exceeds a certain threshold. Otherwise, the liquid is retained in the nozzle due to surface tension acting at the orifice [8]. Within this mechanism two principal methods, thermal and piezoelectric DOD inkjet printing, exist [90,91]. In thermal DOD jetting, a small vapour bubble is produced by applying a current to a thin-film heater which is placed in direct vicinity of the fluid as depicted in Figure 2.4 b) i). After removal of the current, the bubble collapses. This rapid forming and collapsing of the vapour bubble

generates pressure waves which are required to eject droplets [86,88]. In piezoelectric DOD printing, however, the pulse arises from a sudden volumetric change caused by direct mechanical actuation of a piezoelectric transducer (shown in Figure 2.4 b) ii)) [90,92]. By comparing the two mentioned DOD printing systems, piezoelectric DOD printing is the method of choice because it offers more benefits over thermal DOD printing. Piezoelectric inkjet printers allow to deposit a wider variety of materials including a broader spectrum of applicable viscosities. This is due to thermal printers mostly being confined to water-based inks exhibiting a high vapour pressure under ambient conditions [91,93,94]. Moreover, the ease of adjusting the actuation pulse in piezoelectric devices allows for greater control of the droplet dimensions [86].

With regard to commercial applications, CIJ printers are restricted to marking applications and low resolution printing whereas DOD printing systems are prevalent in materials science applications [86,88]. Although CIJ printers operate at much higher droplet generation rates, DOD printing devices are preferred due to their higher spatial resolution, greater placement accuracy and wider range of fluids available for deposition [34,86,92]. Consequently, DOD printing, specifically piezoelectric DOD inkjet printing, is the method of choice for further discussion in this thesis.

2.2.2. Piezoelectric Inkjet Printing

In this subchapter, three different ways to produce particles are described using piezoelectric inkjet printing: i) co-flow and submerged printing, ii) inkjet printing coupled with a drying process and iii) inkjet printing onto hydrophobic substrates.

Co-flow versus Submerged Printing

Within piezoelectric inkjet printing, two different nozzle arrangements were used to fabricate uniform poly(D,L-lactide-co-glycolide) (PLGA) microspheres [32,67,95]. These thermoplastic aliphatic polyesters have been extensively used in veterinary and medical applications, for instance as suture materials, due to their mechanical strength, biocompatibility and biodegradability into non-toxic lactic and glycolic acids [20,40,96,97]. Fletcher et al. examined three different jetting configurations as a way to minimise the particle size distribution [95]. Microspheres were prepared from PLGA (85:15 PLA to PGA) containing either explosives or explosive simulant by applying the following three jetting configurations: nozzle directly submerged in a rotating beaker of water, straight and curved co-flow nozzle arrangements. The straight and curved co-flow nozzle configuration are schematically depicted in Figure 2.5.

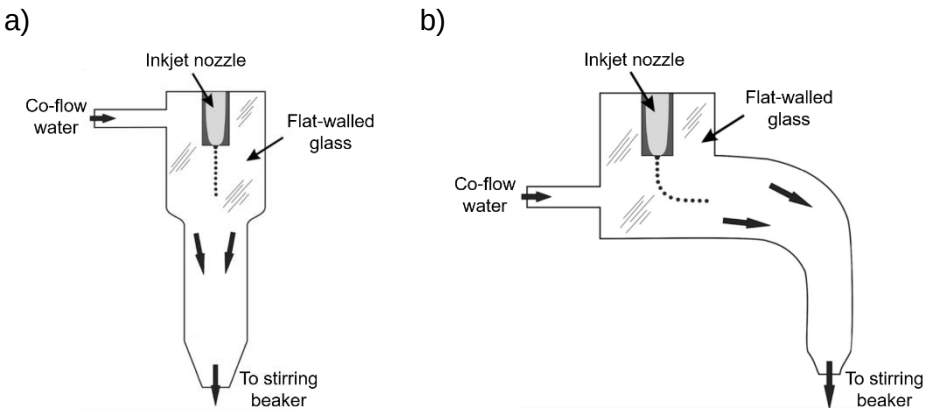


Figure 2.5: Schematic representation of two out of three jetting arrangements: a) straight co-flow nozzle, b) curved co-flow nozzle. The generated particles are carried by a stream of deionised water into a rotating beaker filled with water. The third configuration, which involves a print head directly submerged in a collection beaker, is not shown. Images adapted from Fletcher et al. [95].

In the work by Fletcher et al., it was shown that the size distribution analysis revealed particle coalescence in case of utilising the co-flow nozzle arrangements. The flow rate of the co-flow fluid, which transported the polymer droplets through the tube, was not sufficiently high to allow particle separation. Therefore, fractions of droplets could coalesce prior to solidification of the particles. This issue was prevented by printing submerged [95].

Böhmer et al. have demonstrated the formation of well-defined polymer particles with narrow size distribution using submerged piezoelectric inkjet printing [32]. Droplets composed of a solution of PLGA in dichloroethane were immediately sheared from the nozzle by the rotating 0.3 wt% aqueous PVA solution. As illustrated in Figure 2.6, the experimental print setup consisted of two compartments and a collection reservoir. The nozzle was submerged in the adjustment compartment until a stable jetting behaviour was obtained by adjusting the frequency and pressure accordingly. Afterwards, the nozzle was switched to the other compartment to start the production. The droplets were collected and converted into particles by removing the solvent with stirring [32].

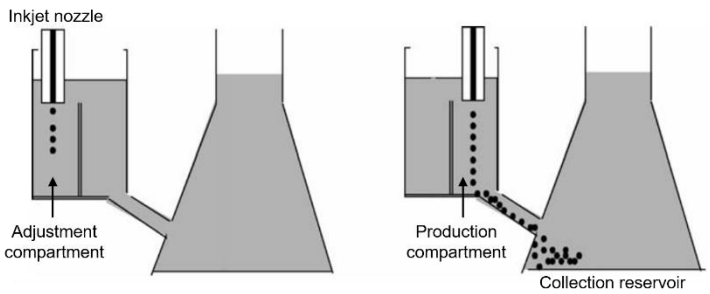


Figure 2.6: Schematic depiction of the experimental setup to print submerged into an aqueous PVA solution. The nozzle is kept in the adjustment compartment for frequency and pressure adjustments. After reaching a stable printing behaviour, the nozzle is moved to the production compartment to start the production. Image adapted from Böhmer et al. [32].

Inkjet Printing coupled with a Drying Process

Another method that has enabled the fabrication of uniform microparticles consists of piezoelectric inkjet printing combined with a drying process. Iwanaga et al. have presented this rapid and facile method for producing sodium alginate microparticles in a variety of sizes by simply altering the concentration of the alginate solution [98]. The concept of generating monodisperse microparticles by using an inkjet printing system via a drying process prior to gelification is shown in Figure 2.7.

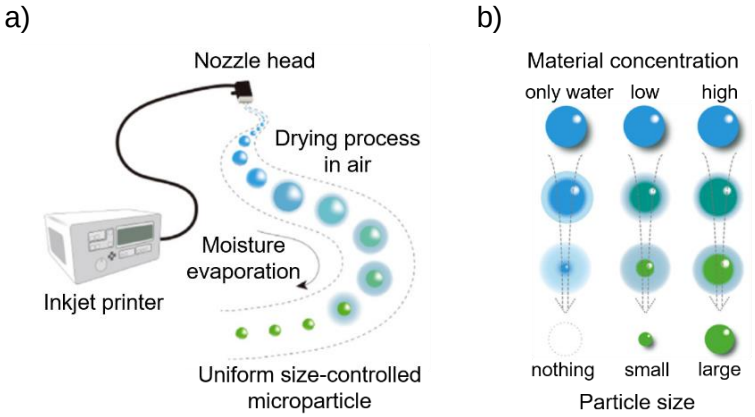


Figure 2.7: Schematic illustration of fabricating uniform microparticles using a piezoelectric inkjet printer coupled with a drying process: a) monodisperse particles were obtained by evaporating moisture during their fall within an air-drying device prior to gelification, b) various sizes of dried microparticles could be easily manufactured by changing the materials concentration. Images adapted from Iwanaga et al. [98].

A linear relationship was found between the initial concentration of the alginate solution and the volume of dried microparticles. The size of the microparticles remained almost unchanged after soaking them into a calcium chloride gelling solution. Loading alginate solutions with nanoparticle-supported drugs enables tandem drug delivery systems, which releases the drug molecules from both the nano- and microparticles with different release rates [98].

Inkjet Printing onto Hydrophobic Substrates

Gillen et al. have introduced another method based on piezoelectric DOD inkjet printing that allows the fabrication of patterned arrays of monodisperse solid spherical cap-shaped microparticles [71]. Microdroplets of concentrated aqueous ammonium nitrate solutions were dispensed onto a silicon wafer, which has been previously rendered hydrophobic by treating it with perfluorodecyltrichlorosilane (FDTS). By depositing hydrophilic fluid droplets onto hydrophobic substrates, the liquid drops tend to minimise its contact with the surface forming spherical shaped caps as shown in Figure 2.8. The deposited liquid droplets maintain this geometry even during solvent evaporation resulting in micrometre-sized inorganic salt particles (depicted in Figure 2.8 b)).

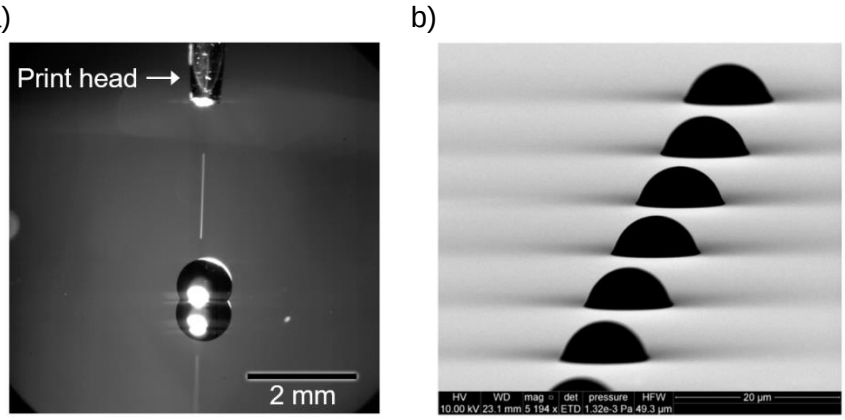


Figure 2.8: Particle fabrication using piezoelectric inkjet printing onto hydrophobic surfaces: a) optical microscope image shows a droplet, prepared from several thousand individual drops, on a treated silicon substrate after ejection from the print head, b) high tilt SEM image exhibits several inorganic spherical cap-shaped salt particles from a printed array. Images adapted from Gillen et al. [71].

This recently developed procedure ensures precise control of particle concentration, size and shape within particle arrays. Furthermore, the number of particles and their spatial distribution on the substrate can easily be modified by employing piezoelectric inkjet printing. Printing discrete particle arrays contributes to the development of trace detection test materials which can be used to screen for particle residues of contraband materials, such as explosives or narcotics [71].

All techniques, which have been reviewed thus far, utilise solvent-based methods. This limits the range of polymers that can be printed since they must be either polymerised in advance or gelled afterwards. In addition, solvent removal is required to obtain hardened particles. This processing step, however, is time-consuming and excessive quantities of volatile chemicals are consumed which might adversely impact the environment. The use of monomers and hence, the adoption of photoinitiated polymerisation technology is extremely desirable to protect the environment [99,100].

2.3. MICROFLUIDICS

2.3.1. MICROFLUIDICS - AN OVERVIEW

Factors such as the drive to fabricate structures and patterns in micro- and nanometre length scales and downscaling efforts in laboratory-based analysis systems has increased the research drive of microfluidic based technologies over the last decades [101,102]. Microfluidics is referred to as the science and technology that uses channels with dimensions of tens to several hundreds of micrometres to process and manipulate small quantities of fluids (10^{-9}-10^{-18} litres) [103,104]. Benefiting from the new capabilities to precisely control molecules in space and time, this technology offers

advantages including reduced sample and reagent volumes, improved portability and relatively fast sample processing. In addition, microfluidic-based analysis platforms allow separations and detections with high resolution and sensitivity at reduced costs and shorter times [102,105,106]. The potential to integrate and automate microfluidic systems and thereby, simultaneously reduce human intervention, has been shown to be beneficial for a variety of application fields [107]. For example, microfluidics has been utilised in diagnostics for point-of-care analysis, in pharmaceutical industries for drug design, testing and delivery and in biotechnology for DNA and cell chips [101,104,108]. Moreover, its applications also include environmental quality measurements, consumer electronics and automotive [101,103,104]. The ease to synthesise monodisperse micro-and nanoparticles with controlled morphologies has particularly increased interest in this technology [27,29,109,110]. However, forming particles on a drop-by-drop basis generally limits high throughput production [59,111,112]. This shortcoming can be overcome by parallelisation of the microfluidic synthesis, as for instance shown by Lim et al. [30].

2.3.2. MICROCHIPS

A microchip is the device used in microfluidics in which a set of microchannels has been etched or moulded [113]. These microchannels form a network that is connected to the outside by input and output ports pierced through the chip. These holes allow fluids to be injected and removed from the microfluidic chip by using, for instance, tubing, syringes and pressure controllers. In this way, fluids can be directed, mixed or separated. The microchannel network is specifically designed for a desired application such as particle fabrication, cell sorting or DNA analysis [114]. The microchip material is selected based on a compromise of ease of prototyping, performance of the device, cost of production and reliability in use [113]. Initially, microfluidic devices consisted of silicon and glass and later on, as the field advanced more, other materials were introduced [115,116]. These materials can be divided into three broad classes [115,116]:

i) inorganic materials with silicon, glass and ceramics,
ii) polymers with elastomers, thermosets and thermoplastics,
iii) paper, biodegradable and hydrogel materials.

Figure 2.9 outlines the materials used to fabricate microchips in association with their fabrication costs and usage at bench or commercial scales. Recently, trends have emerged, which reveal the common use of glass, silicon and poly(dimethyl siloxane)

(PDMS) (example for thermosets) in research laboratories while paper and plastics appear more promising for commercial fabrication [113].

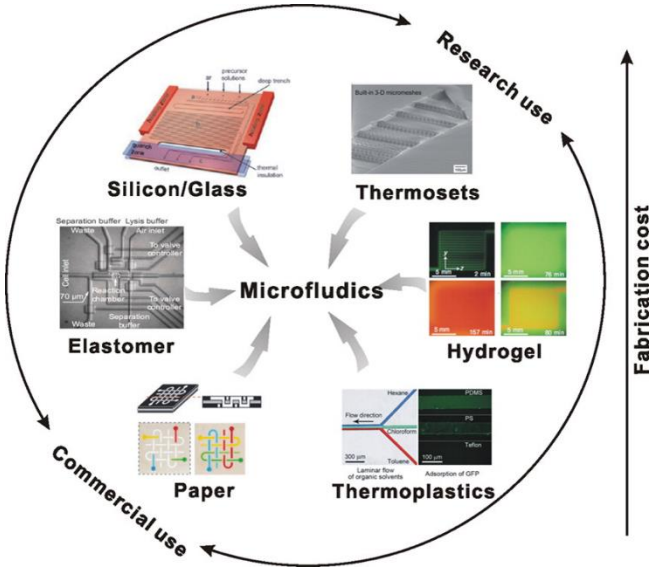


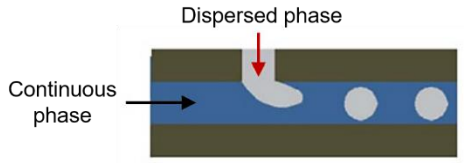
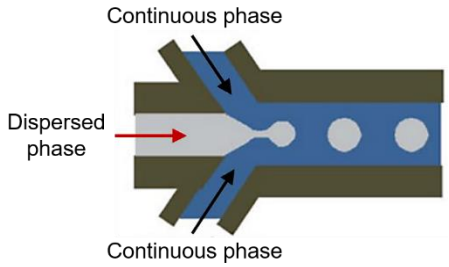
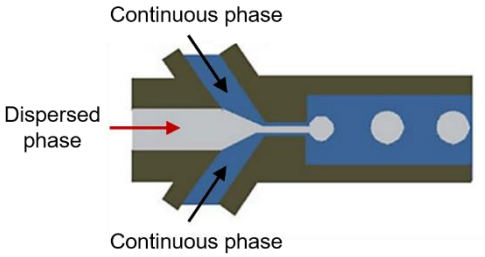
Figure 2.9: Summary of the materials used to fabricate microfluidic devices. The materials are presented in dependence of their fabrication costs and usage in research or industry. Image adapted from Ren et al. [113].

For the fabrication of microfluidic chips, several techniques are employed, such as photolithography, soft lithography, hot embossing, laser photoablation and etching techniques [117–119]. The fabrication method should be selected with respect of the substrate material, the cost and time of manufacturing but also regarding the desired functions required for a specific application [114].

2.3.3. Droplet-based Microfluidics

Single and multiple structured polymeric particles have been produced through droplet-based microfluidic approaches using a combination of cross-flow, co-flow and flow-focusing configurations [18]. These microfluidic device configurations are illustrated in Table 2.1.

Table 2.1: Cross-flow, co-flow and flow-focusing geometries for single and multiple structured polymeric particles. Images adapted from Gokmen et al. [120].

Geometry	Microfluidic device
Cross-flow	
Co-flow	
Flow-focusing	

In cross-flowing geometries, which includes X-, Y- and T-junctions, droplets of the dispersed phase are generated by a combination of shear forces and squeezing caused by the continuous phase [121]. In co-flowing microfluidic configurations, the dispersed phase enters through a capillary and is segmented into droplets by the shear force of the surrounding continuous phase acting on the dispersed phase. Very similar to the co-flowing geometry, the dispersed phase is squeezed by the coaxially flowing continuous phase streams in the flow-focusing configuration. All the fluids are extruded through a narrow orifice, where high local shear stresses are created, causing the dispersed phase to break up into droplets [122].

Kim et al. demonstrated the fabrication of functional microparticles by applying droplet-based microfluidics [27]. The particles can be functionalised through shaping, compartmentalising and microstructuring. In the following paragraphs, cross-flowing microfluidic devices, especially T-junctions and Y-shaped channels leading to T-junctions, are looked at in more details.

T-JUNCTION

Nurumbetov et al. have reported the fabrication of a simplified microfluidic device by gluing a syringe needle, plastic tubes and two glass capillaries together [123]. The experimental setup, which consist of a serial combination of a co-flow configuration and a T-junction, is illustrated in Figure 2.10 a).

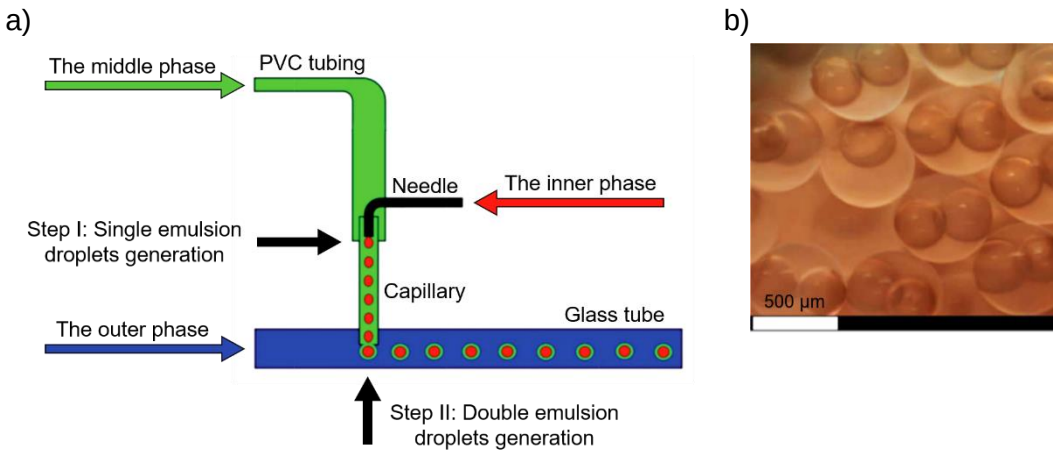


Figure 2.10: Droplet-based particle synthesis: a) schematic illustration of the experimental setup, b) optical micrograph showing monodisperse multi-compartment capsules with cores, containing a water-based ferrofluid, surrounded by poly(isobornyl acrylate) shells. Images adapted from Nurumbetov et al. [123].

By using this simplified microfluidic device, a range of droplets-in-droplets, in this case polymeric microcapsules, were produced as shown in Figure 2.10 b). The generated capsules were comprised of photopolymerised poly(isobornyl acrylate) shells which entrapped compartments containing waterborne ferrofluid or dispersion of heat-sensitive colour changing pigments. Such functionalised microcapsules are potentially applicable as sensors and mobile magnetically attractive capsules by exerting an external field [123].

Y-shaped Channel leading to a T-junction

Nisisako et al. have demonstrated the production of Janus droplets and shape-controlled polymer microparticles using two immiscible fluids and a microfluidic device consisting of Y-shaped channel leading to a T-junction [124]. The asymmetric cross-flowing microfluidic system is depicted in Figure 2.11 a).

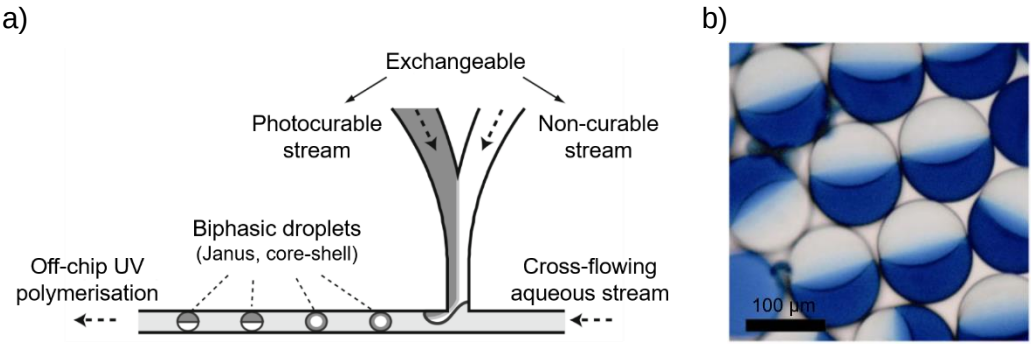


Figure 2.11: Droplet-based microfluidic particle synthesis: a) schematic representation of a microfluidic cross-flowing system for fabricating biphasic droplets, b) optical micrograph showing Janus droplets made from silicone oil (white) and polymerisable hexanediol diacrylate phase (blue). Images adapted from Nisisako et al. [124].

Depending on the combination of the non-curable fluid with the photocurable hexanediol diacrylate phase, monodisperse biphasic droplets formed either a Janus or

a core-shell configuration. Janus droplets, as presented in Figure 2.11 b), were reproducibly generated in a one-step process when using silicone oil as the non-curable phase. The use of perfluorocarbon led to uniform core-shell droplets which were formed in a two-step regime. By modifying the ratio of the two dispersed phases, particles with controlled convex and concave surfaces were engineered. This microfluidic method enables the synthesis of Janus particles by employing two photocrosslinkable immiscible fluids. Janus particles are potentially applicable for handwriting-enabled electronic papers [16] or for directional self-propulsion in targeted cancer therapy [125]. Moreover, extending and optimising the method can result in the fabrication of more functional microparticles, such as multi-faceted or multi-pore particles [124].

2.4. Free Radical Based UV Curing Reaction

Two types of polymerisation reactions, free radical and ionic, can be induced by the excitation of a photoinitiating system under lights. Photoinitiated ionic polymerisation is divided into anionic and cationic reactions due to their ability to generate electron-donating (cationic) or electron-withdrawing (anionic) compounds [126]. Free radical photopolymerisation is by far the most popular reaction system for applications, where (meth)acrylate based monomers are involved [127]. Consequently, this type of photo-induced reaction was selected for this work and is described in more detail.

Photo-induced polymerisation requires photons to initiate free radical polymerisation reactions. Free radical polymerisation offers several advantages compared to thermal and redox polymerisations including spatiotemporal control across the sample, high rates of polymerisation, environmental benefits and reduced material costs due to solvent-free systems [128]. Due to the spatial and temporal control afforded during photoinitiated polymerisation, photocrosslinkable materials have widely emerged in the general field of biomaterials [126,129]. The controlled nature of this type of reaction has allowed for a variety of applications, for example, as injectable biomaterials for critical bone defects and cartilage repair [130,131]. Additionally, crosslinked photopolymers are also used in dentistry [132,133] as well as for the encapsulation and controlled delivery of bioactive molecules [134–136].

In this section, the basic concept of free radical photopolymerisation is presented. The mechanism of generating free radicals upon UV light absorption is described for photoinitiator Type I and II. Furthermore, the problem of oxygen inhibition is illustrated, and practical measures that can be used to overcome the issue, are outlined.

2.4.1. BASIC CONCEPT

Free radical based UV curing reactions can be divided into four stages: initiation, propagation, chain transfer and termination. The basic principles of the polymerisation process are presented in Figure 2.12 and are described using acrylates as the monomer containing functional groups.

Initiation:
$$PI \xrightarrow{h\nu} PI^{\bullet}$$
$$PI^{\bullet} + M \longrightarrow PIM^{\bullet}$$

Propagation:
$$PIM^{\bullet} + M \longrightarrow PIMM^{\bullet}$$

Chain transfer:
$$PIM^{\bullet} + DH \longrightarrow PIMH + D^{\bullet}$$
$$D^{\bullet} + M \longrightarrow DM^{\bullet}$$

Termination:
$$PIMM^{\bullet} + PIMM^{\bullet} \longrightarrow PIMM - MMPI$$
$$PI^{\bullet} + PI^{\bullet} \longrightarrow PI - PI$$

Figure 2.12: Basic concept of the UV curing free radical polymerisation process. Adapted from W. A. Green [127].

The initiation of the curing reaction is the only step which is photosensitive, all other stages are thermally driven [127]. The photochemical process starts with activation of the photoinitiator (PI) by absorbing photons from the UV source. This leads to the generation of reactive initiating species ($PI^{\bullet}$) which attack unsaturated C=C double bonds of an acrylate monomer (M). A reactive alkyl monomer radical ($PIM^{\bullet}$) is formed. The initiating compound formed by the photoinitiator molecule is locked into the propagating polymer chain [127]. Propagation occurs when the reactive monomer radical ($PIM^{\bullet}$) reacts with additional acrylate monomers within the formulation inducing a chain reaction ($PIMM^{\bullet}$). Consequently, the molecular weight of a polymer is built in this stage and networks can be formed through crosslinkage of multifunctional monomers [99,137]. As the polymerisation continues, the amount of acrylate functional groups decreases and also the mobility of the growing polymer chain is confined because of the viscosity built up in the system. This restriction in chain mobility makes it more difficult to find unsaturated double bonds, therefore stopping the propagation. Chain transfer reactions can occur which involve abstraction of hydrogen radicals from hydrogen donors (DH). This hydrogen transfer stops the growth of the polymer chain and the remaining donor radical ($D^{\bullet}$) can start a new polymer chain by reacting with more monomers. Hydrogen donors, which are included as essential compounds in the photoinitiation Type II mechanism, can be applied to modify the molecular weight of polymers [127]. Termination of the curing reaction can occur by interaction of two

growing polymer chains. However, recombination of photoinitiating species can also result in termination.

Typical Composition of an UV Curable Formulation

A typical formulation of an UV ink is listed in Table 2.2. Monomers and oligomers, which contain unsaturated chemical bonds, make up the largest part of an ink composition (25-90 wt%) [99]. Therefore, they are the key determinants responsible for film formation and define the properties of the final product. Reactive diluents are preferred to solvents for adjusting the ink viscosity in order to comply with the requirements of selected application equipment. Low molecular weight compounds, for example acrylate monomers or acrylate oligomers, are incorporated into the polymer network affecting the material performance [137]. Another component, the photoinitiator, is essential for UV curable inks to initiate the crosslinking reaction. Photoinitiators are chemicals that can generate free radicals from the absorption of UV light. There are mainly two types of free radical photoinitiators, Type I and Type II, which are discussed in Section 2.4.2. The required concentration of a photoinitiator varies between 1-8 wt% depending on factors such as initiation mechanism, UV light source or specific performance requirements [99,137]. According to the manufacturing process or product requirements, some additives such as surfactants, pigments, accelerators are also required. These additives tailor the processability of the ink and also the properties of the final product [99].

Table 2.2: Typical formulation and function of an UV curable ink. Adjusted from R. Schwalm [99].

Component	Concentration [wt%]	Function
Monomer or oligomer	25-90	Main part of ink responsible for film formation and, thus, defines basic properties
Reactive diluents	15-60	Adjust viscosity and crosslink density
Photoinitiator	1-8	Absorbs UV light and initiate photopolymerisation
Additives	1-50	Additives such as surfactants, pigments, fillers modify ink properties

2.4.2. Photoinitiator - Type I and Type II

A photoinitiator is specifically added to an UV curable ink formulation due to its ability to convert absorbed UV light energy into chemical energy by forming free radicals

[138,139]. Most photoinitiators, which are available commercially, absorb UV light in the wavelength range of 250 to 550 nm [140]. Aryl ketone groups, shown in Figure 2.13, are chromophores that absorb light most efficiently [127].

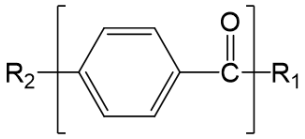


Figure 2.13: Chemical structure of the aryl ketone group.

Photoinitiators are designated into two distinct classes, Type I and Type II, based on their mechanism of free initiating radical formation [141,142]. Substitutions on the ketone at R_1 influence the radical forming mechanism, whereas substitutions at R_2 affect the wavelength at which photons are absorbed by the photoinitiator. Substituting R_1 with an alkyl group leads to a Type I scission process (mostly alpha-scission, also called Norrish Type I reaction), where a direct photofragmentation occurs upon absorption of UV light [127]. In this case, the absorbed UV energy (~70-80 kcal/mol) overcomes the CO-alkyl bond energy (~65-70 kcal/mol) resulting in homolytic bond cleavage generating two free radicals [140,143]. These formed radicals are capable of inducing polymerisation. An example of a Type I photoinitiator is the substituted acetophenone photoinitiator, 2,2-dimethoxy-2-phenylacetophenone (DMPA), whose cleavage process is illustrated in Figure 2.14.

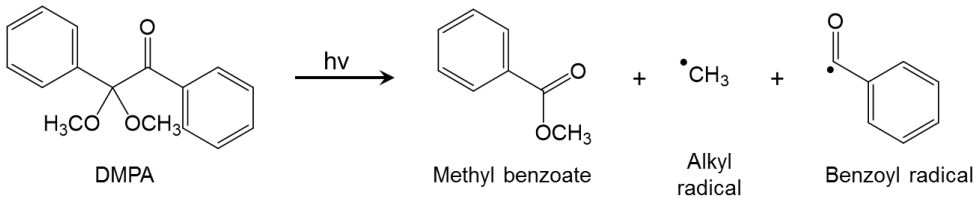


Figure 2.14: Type I alpha-scission process showing the formation of free radicals from the photoinitiator 2,2-dimethoxy-2-phenylacetophenone (DMPA).

Type II photoinitiator reactions occur when aryl groups are substituted at R_1. In this case, the absorbed UV energy is insufficient to break the CO-aryl bond (~80-90 kcal/mol) [127]. Therefore, a co-initiator (synergist, also called accelerator) is required which is usually a tertiary amine that can readily have hydrogens abstracted [138,144]. Upon irradiating with UV light, the photoinitiator remains in an excited state until reacting with the donor molecule [137,145]. By abstracting a hydrogen atom, two radicals are produced: a ketyl radical with low reactivity and a donor radical which is highly reactive [127]. A Type II hydrogen abstraction process is presented for the photoinitiator benzophenone and co-initiator hydrogen donor in Figure 2.15.

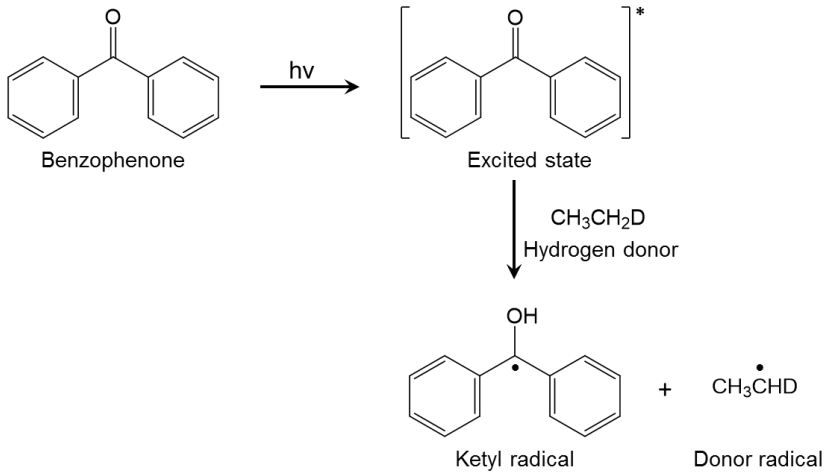


Figure 2.15: Type II bimolecular hydrogen abstraction process showing the formation of free radicals from the photoinitiator benzophenone and the synergist hydrogen donor.

Tertiary amines are usually employed as hydrogen donors for enhanced efficiency in combination with photoinitiators containing aromatic ketones [141]. In addition, the use of tertiary amines retards the inhibition of polymerisation by oxygen. This is explained by the ability of alkylamino radicals to scavenge peroxy radicals [138,141].

2.4.3. OXYGEN INHIBITION

Oxygen is known to be an effective inhibitor of free radical polymerisation. It is present in ambient air as molecular oxygen but can also be in raw materials as dissolved oxygen. Oxygen, especially molecular oxygen, can react with free radicals generated in all stages of polymerisation. The curing reaction is effectively impaired in two ways which is outlined in Figure 2.16. First, oxygen can quench the excited state of a photoinitiator, transforming back to its non-reactive state [141,146]. As a result, fewer radicals are generated by the photoinitiator, which leads to fewer initiated polymer chains and, hence, less polymer formation. This is more likely to affect Type II photoinitiators due to their relatively long triplet lifetimes [127]. Second, oxygen can also react with radicals and, thus, scavenge free propagating radicals. In this way, the carbon-based growing polymer chain is converted to an oxygen-based polymer chain (peroxy radicals), which is less reactive, reducing the rate of polymerisation. Lower molecular weight chains are obtained because of scavenging radicals [127]. Oxygen inhibition, which impairs crosslinking, manifests itself mostly as tackiness at photopolymer surfaces or air interfaces [100,147,148].

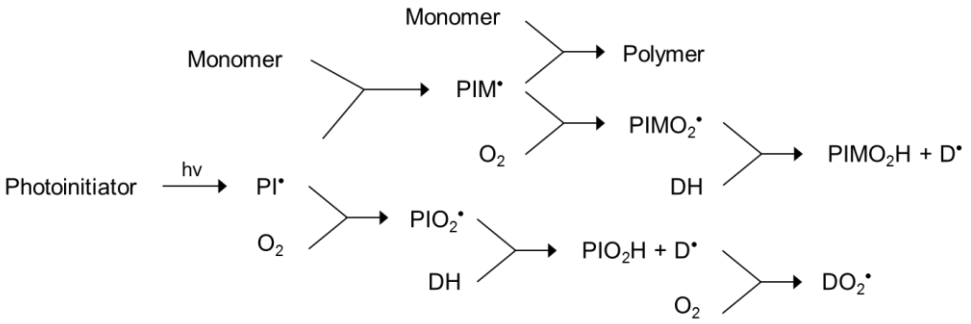


Figure 2.16: Oxygen inhibition at different stages of a radical-induced photopolymerisation. Adapted from Studer et al. [149].

Several methods have been developed over the last decades which help to mitigate oxygen inhibition and improve surface cure, respectively. Physical and chemical measures, some of which are listed in Table 2.3, can be applied to circumvent this oxygen problem [99,127,137,148,150].

Table 2.3: Physical and chemical methods to mitigate oxygen inhibition.

Physical Methods	Chemical Methods
Curing in an inert atmosphere	Increase photoinitiator concentration
Use of high intensity light source	Use of Type II photoinitiators
Use shorter wavelengths	Addition of excess tertiary amines
Use of physical barriers like wax, shielding films	Addition of oxygen scavengers

The most common methods are curing in an inert atmosphere, use of Type II photoinitiators and increase of the free radical concentration. These methods are described in more detail in the following paragraphs.

USE OF INERT GAS

The most efficient way to exclude oxygen is by using an inert gas atmosphere [149]. This is done by blanketing with nitrogen, carbon dioxide and argon. It has been shown that carbon dioxide (CO_2) exhibits some advantages over nitrogen. It is easily available and cheaper than nitrogen [99]. Moreover, CO_2 is heavier than air and can therefore be kept in a container without much loss [149]. This technique enables faster and more complete curing which results in improved surface properties. However, applying inert gas reveals some drawbacks that include higher process costs and increased complexity in the system design.

USE OF TYPE II PHOTOINITIATORS

Type II photoinitiators, which require a co-initiator to generate initiating radicals (described in Section 2.4.2), have frequently been reported as a measure for impaired oxygen inhibition [150]. This is attributed to the presence of tertiary amines (hydrogen

donors) [151,152]. As shown in Figure 2.17, the carbon-based radical, which is formed by hydrogen abstraction, can scavenge molecular oxygen to produce an inactive peroxy radical. The peroxy radical can further abstract a hydrogen atom from another tertiary amine producing an active alkylamino radical and a neutral hydroperoxide. The reactive alkylamino radical can reinitiate polymerisation [99,153–155]. The overall effect is explained by scavenging oxygen from the system by transforming them into an unreactive peroxide form. In this way, the free radical polymerisation reaction can proceed more efficiently.

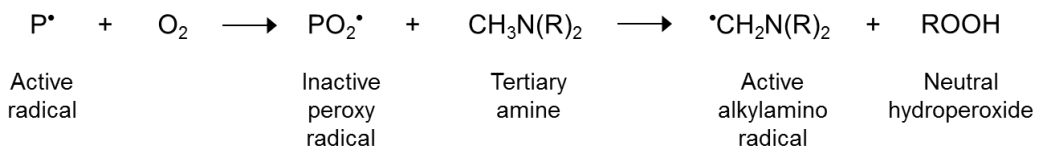


Figure 2.17: Reactions showing the oxygen scavenging by tertiary amines. Adapted from W. A. Green [127].

Despite the great ability to mitigate oxygen inhibition, amines present in an ink formulation have some adverse effects such as yellowing of the film, odour, plasticising effect and deteriorated weathering resistance [99,149].

INCREASING THE FREE RADICAL CONCENTRATION

Increased concentration of free radicals reduces the oxygen inhibition by quenching more oxygen in the system due to their ease to react [149]. Thereby, diffusion of oxygen into deeper layers is prevented. Moreover, increasing the amount of free radicals results in higher formulation reactivity which positively influences the curing speed [99,149]. Consequently, the reaction time, during which atmospheric oxygen diffuses into the specimen, is shortened. High concentrations of free radicals are achieved by increasing the photoinitiator concentration or by irradiating with a high intensity UV source. However, a high photoinitiator concentration may result in reduction of the final product molecular weight which in turn could affect the photopolymer properties. Furthermore, increased amounts of undesired by-products could arise from increased photoinitiator concentrations [146].

An optimum manufacturing environment can be ensured given all the interconnected parameters. Organic polymers enable readily the formation of a large numbers of diverse chemistries and physical properties by applying synthesis approaches.

2.5. (METH)ACRYLATES

To accelerate materials discovery, combinatorial material libraries, which can rapidly be evaluated for their performance in the desired application, have shown to be promising [156–158]. Such libraries should contain materials with diverse chemistries and physical properties to explore the most combinatorial space. Broadening of the combinatorial chemical space can be achieved through synthesis approaches that are readily performed using organic polymers. (Meth)acrylates have been identified as a relevant class of biomaterials applied in surgical glues, drug delivery, tissue engineering and health care products such as intraocular lenses [126,159,160]. Moreover, a large diversity of (meth)acrylates are commercially available and can readily be polymerised in conjunction with a photoinitiator by exposure to UV light. UV initiation ensures spatiotemporal control during polymerisation since the generated radicals are uniformly released with time and across the specimen upon demand [161,162]. The basic chemical structures of an acrylate and methacrylate are presented in Figure 2.18.

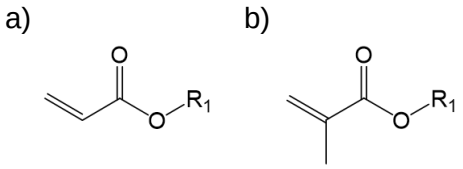


Figure 2.18: Basic chemical structures of an acrylate (a) and a methacrylate (b).

Hook et al. applied high throughput techniques to discover polymers based on (meth)acrylates by screening their performance in biofilm resistance [156]. To conduct screening assays, 22 commercially available (meth)acrylates, providing chemical diversity, were selected to form a library. To broaden the combinatorial space, monomers defined as major components (1-16) were blended with minor monomers (A-F) at various ratios to create 496 unique monomer mixtures. The chemical structures of the 22 selected monomers are depicted in Figure 2.19.

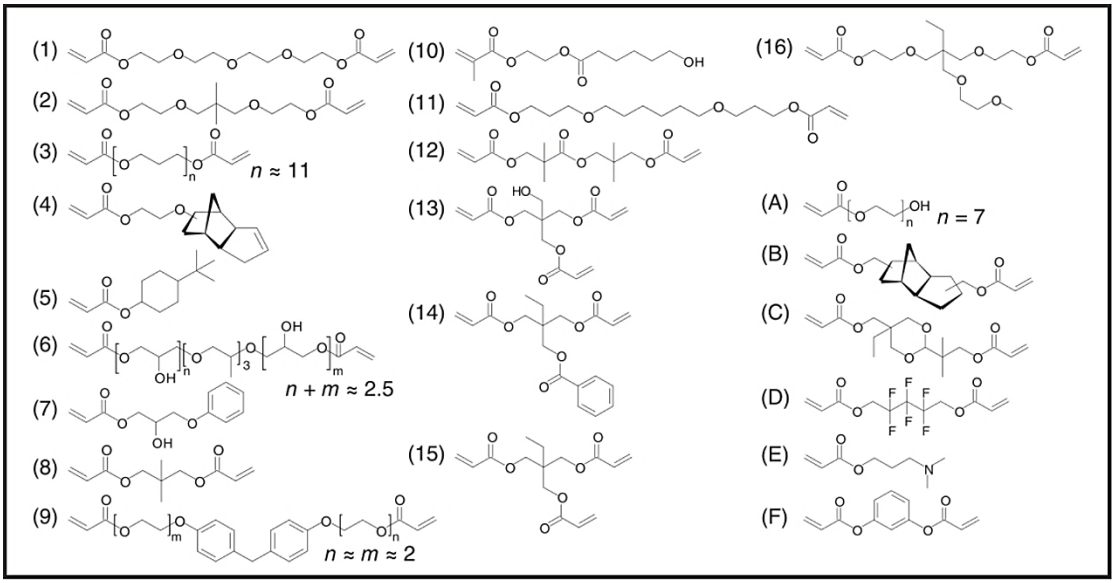


Figure 2.19: The chemical structures of the 22 selected monomers, which were classified into major (1-16) and minor (A-F) components, are presented. Image adapted from Hook et al. [163].

These monomer solutions were printed in a microarray format onto poly(hydroxyl ethylmethacrylate) (pHEMA)-coated glass slides where they were crosslinked by a photoinitiated free radical polymerisation (Figure 2.20). Afterwards, the microarrays were incubated with fluorescent bacteria for 72 hours and assessed for their resistance to bacteria by quantifying the fluorescence intensity on each polymer spot. By applying high throughput techniques, a new class of polymers resistant to bacterial attachment was discovered.

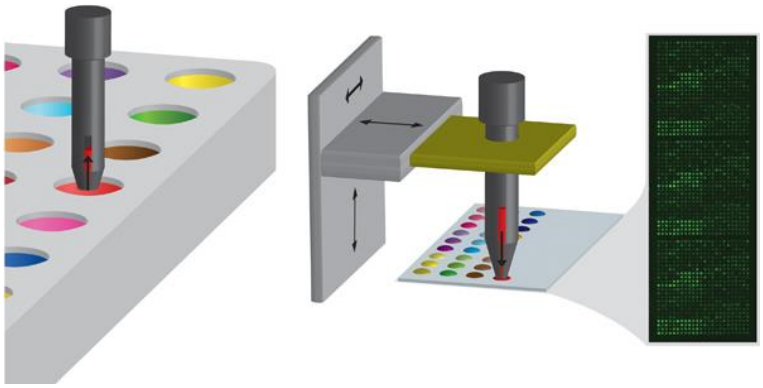


Figure 2.20: Schematic of the microarray printing using a pin. Initially, the pin is loaded with a monomer solution in a substrate well (left) followed by depositing the monomer solution onto a pHEMA-coated glass slide (middle). The inset (right) shows a microarray after incubation with fluorescent bacteria. Image adapted from Hook et al. [164].

(Meth)acrylates have been shown to be promising for biomedical applications. Acrylates enable to be turned into degradable polymers when synthesised with amines via the Michael addition to form hydrolysable amino ester groups. The first combinatorial library of degradable and photocrosslinkable materials, which was composed of 120 macromers, has been reported by Anderson et al. [161]. Macromers were synthesised through the conjugate addition of primary or secondary amines with

diacrylates. These diacrylated macromers were then polymerised by a step-growth mechanism to form functionalised poly(β-amino ester)s. The general polymerisation reaction (a) and the chemical structures of the monomers (b), including 12 amines and 10 diacrylates, are outlined in Figure 2.21.

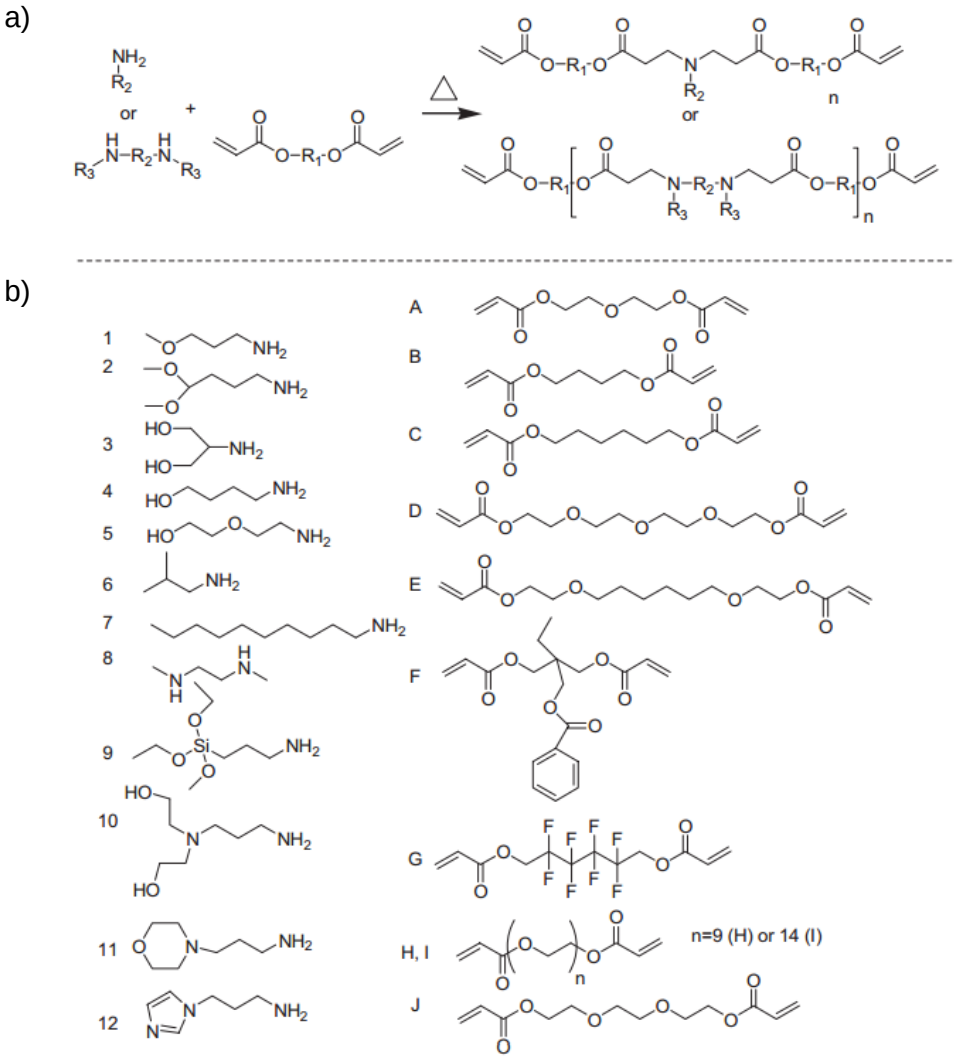


Figure 2.21: General polymerisation reaction and chemical structures of the monomers are shown: a) diacrylated macromers were synthesised by the condensation reaction of an amine with a diacrylate, b) a library of 120 photocrosslinkable macromers was produced using 12 amines (1-12) and 10 diacrylates (A-J). Figure adapted from Anderson et al. [161].

Functionalised poly(β-amino ester)s, which vary in their hydrolytic degradation behaviour and hardness, demonstrate potential for a wide range of biomedical applications. For example, hard polymers can be applied in hard tissue regeneration (e.g. orthopaedics, dentistry) whereas soft materials are preferred in soft tissue regeneration, for instance, as scaffolds for skin or vascular tissue reconstruction. Besides this, these macromers can be useful for applications where slow degradation is desired over an extended time of period to applications where fast degradation is required [161].

2.6. Problems Associated with Bacteria

Biofouling, which refers to the undesirable adhesion and colonisation of proteins, cells and other biological materials, pose severe challenges in numerous applications. Applications include but are not limited to biomedical implants and devices [165,166], biosensors [167], food packaging [168] and marine equipment [169,170]. In this subchapter, the focus is on healthcare-associated infections which are acknowledged to be the cause of severe complications leading to increased morbidity and mortality [171,172]. It has been reported that approximately 65% of all microbial infections and 80% of all chronic infections are associated with microbial biofilms [173]. These are bacterial communities that accumulate on surfaces and are entrapped within a self-produced matrix of extracellular polymeric substances [174]. Cells embedded in biofilms acquire 10 to 1000 times higher resistance to antibiotics and human immune system than their planktonic counterparts [175,176]. This phenomenon is also called recalcitrance of biofilm bacteria [177]. Therefore, treating infectious diseases, where biofilms are commonly involved in, has proven to be particularly challenging [178]. In addition, established biofilm matrices act like diffusion barriers capable of limiting the penetration of antimicrobials. This, as well as the repeated and prolonged use of antibiotics, resulted in increased antimicrobial resistance. This is now a major global threat [179].

Attachment of bacterial cells to solid surfaces is a complex process that is affected by several factors [180]. The main factors involved are the physiochemical properties of the bacteria, surface properties of the substrate and the properties of the suspending liquid medium [181]. Some properties of the bacterial cell are discussed in the following sections.

2.6.1. Bacterial Cell Wall and Surface Structures

In order to understand the interactions between the bacteria and substrate surfaces, it is necessary to know the chemical functionalities present at the surface of bacterial cells.

Historically, bacteria have been classified into two groups based upon their ability to retain the colour of the stains, crystal violet and iodine, used during the Gram staining [182]. The bacteria which remained purple after staining were denoted as Gram-positive whereas those bacteria which decolourised by alcohol, hence losing the colour of the primary stain were classed as Gram-negative. Gram-negative bacteria received a pink colour from the counterstain applied. The differences in staining correlate to

structural differences in the bacterial cell wall, specifically to differences in the peptidoglycan layer present in the cell wall [183].

Gram-positive Bacteria

Gram-positive bacteria such as *Staphylococcus aureus* posse a thick, multilayered cell wall which is predominantly composed of peptidoglycan (Figure 2.22). Peptidoglycan is a polysaccharide made of two alternating glucose derivatives, N-acetylglucosamine and N-acetylmuramic acid, which can account for 30-70% of the total cell wall [184]. As adjacent layers of peptidoglycan are formed, they are crosslinked by short peptide units creating a strong and rigid cell wall. The composition and structure of the peptidoglycan varies greatly between species of Gram-positive bacteria whereas it remains rather constant for Gram-negatives [184].

Another major constituent of the cell wall of Gram-positive bacteria is teichoic acid, a glycopolymer, that is embedded within the peptidoglycan layers. Teichoic acids is believed to play numerous, fundamental roles in the bacterial physiology [185].

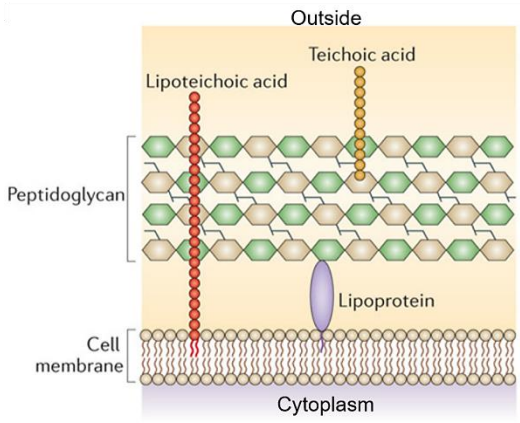


Figure 2.22: Representation of the cell wall structure of Gram-positive bacteria. Image adapted from Brown et al. [186].

Gram-negative Bacteria

The cell wall of Gram-negative bacteria such as *Pseudomonas aeruginosa* are more complex than that of Gram-positive bacteria. Moreover, the composition of the cell wall is quite different in these two groups of bacteria [184]. One of the most notable differences is the presence of a plasma membrane in Gram-negative bacteria that is located outside of the thin peptidoglycan layers [185], as depicted in Figure 2.23. This plasma membrane, also known as outer membrane, consists of a lipid bilayer of lipopolysaccharides (LPS) and lipoprotein. LPS is composed of three constituents: 1) the O-antigen (or O-polysaccharide) representing the outermost part of the structure, 2) the core polysaccharide and 3) the lipid A (or endotoxin) which anchors the LPS into the outer membrane [187]. LPS is known to play a crucial role in many different

functions for the cell for example it is responsible for the activation of the innate immunity cascade [188].

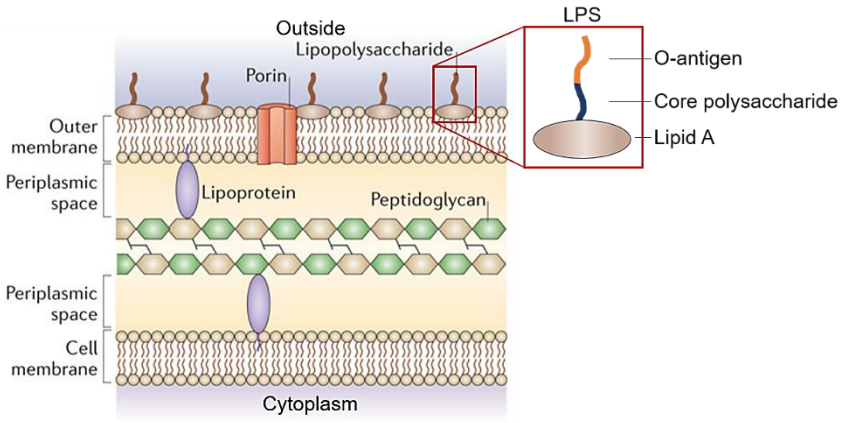


Figure 2.23: Illustration of the cell wall of Gram-negative bacteria. The zoomed-in image shows a lipopolysaccharide with its three components. Image adapted from Brown et al. [186].

Bacterial Surface Charge

It is well known that most of the microorganism possess an overall electronegative charge whose magnitude varies from strain to strain [189]. Furthermore, it is very likely that distinct regional charge disparities exist due to different chemical components at the surface [183]. As discussed, the cell wall of Gram-positive bacteria consists mainly of teichoic acid, whereas the Gram-negative bacteria contain lipopolysaccharides. Both constituents have been reported to impart a negative charge at the bacterial surfaces [187]. Bacterial cells also exhibit phospholipid stabilised membranes which induce a net negative charge at the surface due to the negatively charged phosphate groups [190].

Bacterial Motility

It has been shown that *Pseudomonas aeruginosa*, selected as the bacterial strain within this thesis, are capable of swimming in liquids by means of flagella [191]. Once the initial surface contact occurs and bacterial cells form a monolayer, bacteria continue to move on the surface via a twitching motility [192]. *P. aeruginosa* can move across surfaces by actively extending and retracting the type IV pili [193] which is approximately 100-fold slower than the flagellar-dependent swimming [192]. A generally accepted model proposes that the flagella mediate transport of the bacteria to the surface by overcoming repulsive forces at the surface-water interface. Moreover, microcolonies and subsequent biofilm formation are formed by the type IV pili-driven cell aggregation [175,192]. Klausen et al. reported, however, that the cellular attachment on surfaces occurs independently of flagella and type IV pili.

Due to the fact that protein adsorption is a prerequisite for the control of biological cells, a brief insight into protein adsorption is provided here. Protein adsorption to solid surfaces is typically divided into two kinetic phases, an initial rapid phase and a slower phase upon approaching a steady-state value. In the initial phase, proteins adsorb immediately as they come into contact with a largely empty surface. In the later phase, the adsorption slows down due to the limited adsorption sites making it more difficult for the arriving proteins to find and fit into an empty spot on the already partially coated surface [194]. The initial phase is a diffusion-controlled process, hence, the surface concentration of proteins is proportional to the diffusion coefficient which in turn is inversely proportional to the molecular size [195].

2.6.2. BIOFILM FORMATION

Biofilm formation and development is a highly complex process in which bacterial cells convert from a planktonic (suspended) to a sessile state [173]. The process of forming a differentiated and mature bacterial biofilm is commonly described via five developmental stages, which are visualised in Figure 2.24:

i) initial attachment,
ii) irreversible attachment,
iii) growth and division of bacteria (maturation I),
iv) mature biofilm formation (maturation II),
v) partial dispersion of bacterial cells from the biofilm.

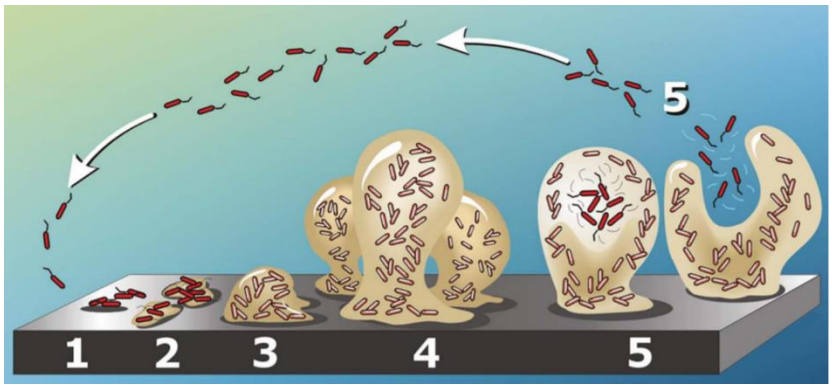


Figure 2.24: The five stages of biofilm development: 1) initial attachment, 2) irreversible attachment, 3) growth and division of bacteria, 4) mature biofilm formation, 5) partial dispersion of bacterial cells from the biofilm. Image adapted from Van Houdt et al. [196].

Initially, planktonic cells are transported from the bulk liquid to a generally pre-conditioned surface. A pre-conditioned surface is a surface which is coated with a conditioning film through adsorption of biological macromolecules, consequently, altering the surface properties [196]. This conditioning layer provides anchorage and

nutrients for bacterial cells. Bacterial cells are able to initially attach (reversible) to the surface when the attractive van der Waals forces are greater than the repulsive electrostatic (double layer) interactions [197]. These interaction energies are generally described in the Derjaguin-Landau-Verwey-Overbeek (DLVO) theory [180]. After initial adhesion of bacteria, the surface binding becomes more stable promoting adhesion sites to other planktonic cells. As the matrix builds up and bacteria undergo cell divisions, exopolysaccharides (EPS) are secreted after reaching a certain threshold size [175]. Bacterial proliferation within the EPS matrix results eventually in microcolony formation [198]. As the bacterial colonisation progresses, an initial biofilm architecture is formed [196]. The three-dimensional biofilm grows and matures further. In this stage, extracellular polymeric substances, capable of trapping nutrients from the surroundings, continue to be produced. In addition, water channels and pores are generated which serve to transport nutrients within the multi-layered clusters [173,196]. Once a critical biomass is reached, biofilm cells are dispersed into the surrounding environment to prevent density-mediated starvation and hence, to enhance microbial survival. The detached cells return quickly to their planktonic state and are ready to colonise other surfaces [199].

Classical DLVO Theory to Describe Reversible Attachment

Bacterial adsorption has been described by the DLVO theory which originally outlines the interaction of a colloidal particle with a surface. Due to the bacterial size being nearly in the range of colloidal particles, this theory has been shown remarkably useful in understanding the correlation between material properties and cell adhesion [200]. According to this theory, the net interaction between a cell and a flat surface is the summation of their van der Waals and Coulomb (electrostatic) interactions [201]. Attractive van der Waals forces are dominant in the vicinity of a surface whereas repulsive electrostatic interactions become more dominant away from the surface since the van der Waals forces strongly decrease with distance [202]. When a bacterial cell approaches a surface, in most cases it cannot irreversibly adhere directly on the surface as there is an energy barrier which needs to be overcome first [203]. However, there is a secondary energy minimum several nanometres outside of the energy barrier where reversible attachment of the bacterial cells to the surface takes place (Figure 2.25 a)).

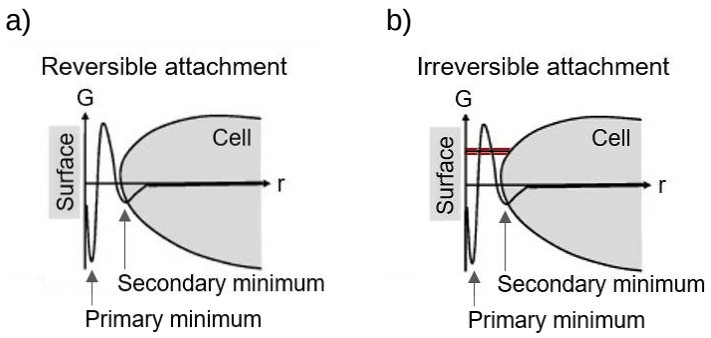


Figure 2.25: Schematic of the bacterial adhesion process according to the DLVO theory: a), reversible adhesion at the secondary energy minimum b) irreversible adhesion at the primary energy minimum by protruding, for example, pili and flagella through the energy barrier. Images adapted from Hori et al. [202].

In the course of time, bacteria, which are weakly bound at the position of the secondary minimum, may reach the primary minimum by piercing, for instance, flagella and pili through the energy barrier. In this way, a bridge between the surface and the bacterial cell will be formed resulting in an irreversible attachment, as shown in Figure 2.25 b) [202,203].

2.6.3. Prevention of Bacterial Attachment

Due to the known biofilm recalcitrance, most strategies designed to reduce biofilm-associated infections aim to prevent bacterial attachment at the earliest possible stage. Two distinct approaches have been employed to resist biofilm formation: i) modification of existing materials used to manufacture indwelling medical devices which kill bacteria upon contact [204,205], ii) development of new materials which are inherently resistant to bacterial attachment and subsequent biofilm formation. It is believed that greater efficacy in preventing biofilm formation is achieved by applying anti-adhesive materials which do not induce an increase of bacterial resistance. Polymeric materials have shown to be well suited for biofilm prevention due to their ease of tailoring the properties by simply altering their chemistry [206]. Three types of synthetic polymers, able to resist bacterial attachment, have been reported on: poly(ethylene glycol) (PEG)-based polymers [207], zwitterionic polymers [208] and weakly amphiphilic poly(meth)acrylates [172].

Besides material-based approaches, surface topographical approaches have recently been demonstrated as a measure to control biofilm formation of diverse biofilm-associated bacteria. Hochbaum et al. have reported controlled bacterial patterning on single-cell level induced by periodic arrays of high-aspect ratio polymeric nanostructures [209]. Depending on the periodicity of the features, different patterns

were spontaneously observed for several bacterial strains, both gram positive and negative. This bacterial ordering presents a way to control natural biofilm organisation on a cellular level. Furthermore, other studies have revealed that periodically structured surface features govern the initial bacterial cell attachment during biofilm formation [210]. Chung et al. have demonstrated an effective solution for disrupting biofilm formation of statically cultured *Staphylococcus aureus* by engineering PDMS elastomer surfaces with a shark skin inspired micropattern, Sharklet AF™ [211]. By comparing *S. aureus* colonisation and biofilm formation on smooth and Sharklet AF™ PDMS elastomer surfaces, engineered topographical surfaces were promising in blocking biofilm development until day 21, as depicted in Figure 2.26.

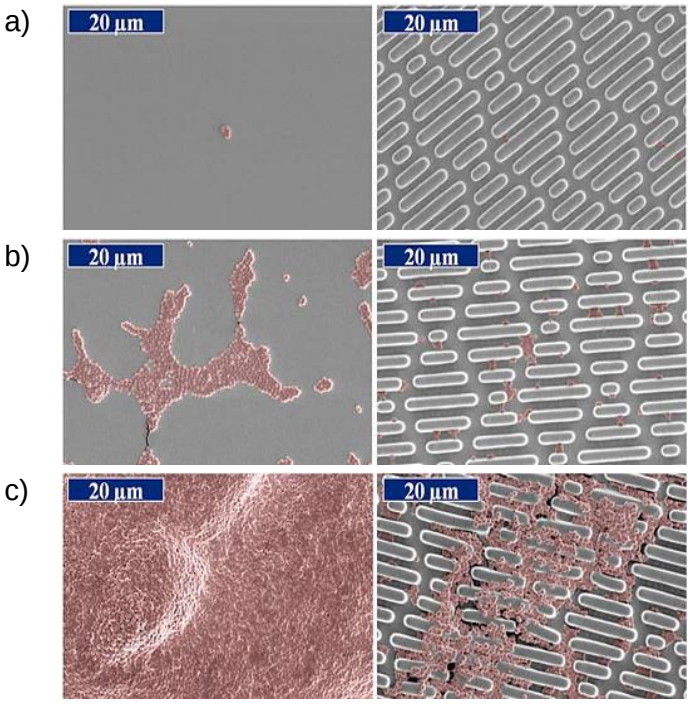


Figure 2.26: SEM images of statically cultured *S. aureus* on smooth (left) and Sharklet AF™ (right) PDMS elastomer surfaces were taken on day 0 (a), day 7 (b) and day 21 (c). Areas of bacteria were highlighted with colour to enhance contrast. Figures adapted from Chung et al. [211].

2.6.4. Mechanism of Action of Non-fouling Materials

There are two major classes of non-fouling materials that have been widely studied, namely polyhydrophilic materials and zwitterionic polymers [206,212]. Among the hydrophilic polymers, poly(ethylene glycol) (PEG), has been recognised for its antifouling properties for decades and has been used in biomedical applications [213]. Other hydrophilic low-fouling materials that have been reported include polysaccharides [214], poly(2-hydroxyethyl methacrylate) (pHEMA) [215,216] and poly(vinyl alcohol) (PVA) [217]. Many of these non-fouling polymers share some

common characteristics such as their hydrophilic nature, electrical neutrality, hydrogen-bond acceptors or lone-pair donors [218,219].

Zwitterionic polymers can be differentiated into polybetaines and polyampholytes. Polybetaines, such as 2-methacryloyloxylethyl phosphoryl-choline (MPC), sulfobetaine methacrylate (SBMA), carry a positive and a negative charge on the same monomer unit whereas polyampholytes carry a 1:1 positive and negative charge on two different monomer units [206].

The mechanism of resistance of both polymer classes to protein and cell adsorption is not yet fully understood and continues to be under debate [219,220]. Several different models of repelling proteins have been reported in the literature and some popular modes of action have been discussed by Wörz et al. [221].

SURFACE HYDRATION AND CHAIN FLEXIBILITY

Recently, it has been increasingly hypothesised that the non-fouling ability of both hydrophilic and zwitterionic polymers result from a hydration layer near the surface [222,223]. Water molecules residing on the surface can form a tightly surface-bound water layer through hydrogen-bonding and ionic solvation in the case of hydrophilic and zwitterionic materials, respectively [206]. This hydration layer is thought to act as a physical and energetic barrier preventing stable adsorption of proteins and cells [212]. The strength of this formed barrier is mainly dependent on the physiochemical properties of the materials and their surface packing [206]. Moreover, chain flexibility also plays a significant role in the reduction of protein and cell adsorption due to steric repulsion caused by the compression of polymer chains [224,225]. Consequently, the best anti-fouling activity can only be achieved by materials that function via a combination of surface hydration and steric repulsion [206]. A schematic representation of surface hydration and chain flexibility is shown for hydrophilic (a) and zwitterionic (b) polymers in Figure 2.27.

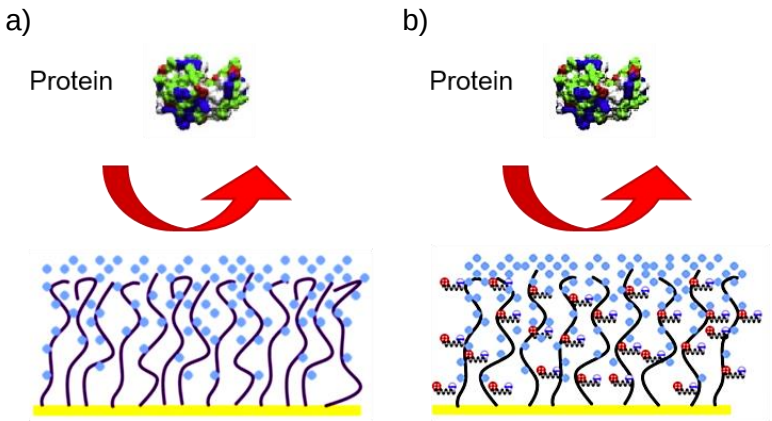


Figure 2.27: Schematic representation of surface hydration and chain flexibility of hydrophilic polymers (a) and zwitterionic polymers carrying positive (red dots) and negative (purple dots) charges (b) to resist protein adsorption. Images adapted from Chen et al. [206].

ENTROPIC SHIELDING

Another highly discussed protein adsorption model is called the entropy model. This model considers only the interaction of the proteins with the polymer network unless the protein is able to penetrate deep down to the substrate material. In this case, the free energy of the adsorption process (ΔG) comprises both an enthalpic component (ΔH), describing the strength of interaction between the protein and the polymer, and an entropic component (ΔS) (Eq. 2.1):

$$\Delta G = \Delta H - T\Delta S \qquad \text{Eq. 2.1}$$

where T is the temperature [221]. In cases where the interactions between the protein and the polymer network is strong, protein adsorption occurs due to the strong enthalpic contribution. However, if the interaction between the protein and polymer is weak, the contribution of the adsorption enthalpy is negligible, hence the entropic term will determine whether proteins adsorb or not provided that the size of the protein is smaller than the mesh size of the polymer network. The entropic component of the Gibbs free energy consists of the entropy of mixing (ΔS_{mix}) and the entropy of conformation of the surface-attached polymer chains (ΔS_{conf}) (Eq. 2.2):

$$\Delta S = \Delta S_{conf} - \Delta S_{mix} \qquad \text{Eq. 2.2}$$

The entropy of mixing favours an even distribution of molecules in its surrounding whereas the entropy of conformation of the surface-bound polymer chains can result in extended polymer molecule stretching due to enhanced segment-segment interactions and osmotic pressure caused by the addition of more material to the polymer layers. This extended stretching away from the surface leads to a strong reduction of the entropy of conformation. If the loss of the entropy due to conformational changes is larger than the gain of entropy of mixing, the diffusion of the protein molecules into the layer is energetically unfavourable and hence, no protein

adsorption occurs. A schematic depiction of protein adsorption on non-swellable polymer networks (a) and prevention of protein adsorption on swellable polymer chains due to entropic shielding is shown in Figure 2.28.

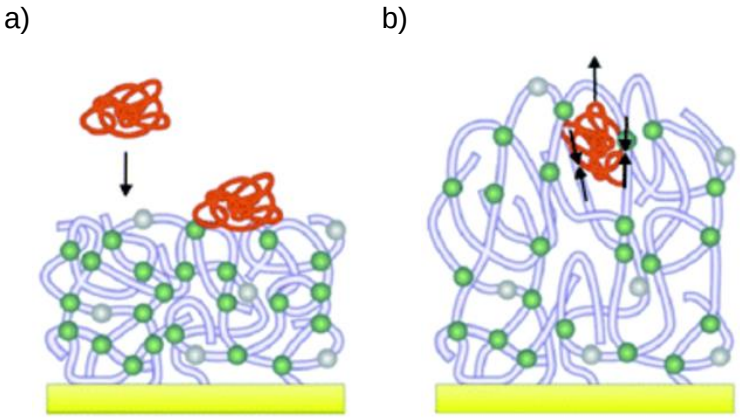


Figure 2.28: Schematic representation of the entropic protein adsorption model: a) proteins adsorb easily on non-swellable polymer networks, b) protein adsorption on highly swellable polymer networks prevented due to entropic shielding. Images adapted from Wörz et al. [221].

2.7. Summary of Research Gaps

This chapter has introduced the most common methodologies to fabricate micro- and nanoparticles with a specific focus on inkjet printing and microfluidics. The fundamentals, materials, application areas and previous studies relating to these two techniques have been explored. Photo-induced polymerisation is presented as a type of polymerisation that offers several advantages compared to thermal and redox polymerisations, including spatiotemporal control, high rates of polymerisation, environmental benefits and reduced material costs due to solvent-free systems [128]. (Meth)acrylate based monomers, which are polymerised by exposure to UV light, have been shown to be a promising class of materials for biomedical applications such as low-fouling coatings. Finally, the current state-of-the-art in preventive strategies are outlined in terms of biofilm-associated bacteria.

This overview allows for the identification of knowledge gaps and opportunities of original research. In order to address the gaps in the literature, the following research problems have been identified and summarised into three main areas, as listed below:

- Previous research has reported on the synthesis of a combinatorial library of photocrosslinkable and degradable materials [161]. Furthermore, microparticle formation using piezoelectric inkjet printing [98] and microfluidics [124] have been researched. However, the combination of producing microparticles from a combinatorial library of UV curable monomers using piezoelectric inkjet

printing has not been investigated. In terms of microfluidics, microparticles were fabricated using photocurable monomers but a diverse particulate library has never been generated.

1. Chapter 4 focuses on the generation of a combinatorial library of microparticles based on (meth)acrylates using photopolymerisation in combination with either piezoelectric inkjet printing or microfluidics.

- A number of particle fabrication technologies have been developed, reported and compared amongst each other [3,23]. A direct comparison between piezoelectric inkjet printing and microfluidics has not yet been made so far.

2. For the first time, presented in Chapter 5, a comparison between piezoelectric inkjet printing and microfluidics is conducted in terms of microparticle production and characteristics including size, size distribution, shape and surface properties.

- The majority of research has focused on microparticle fabrication for drug delivery applications. Recently, polymeric microparticles have also been generated and optimised for use in tissue engineering and regenerative medicine. However, screening from 2D to 3D surfaces has not been conducted for a desired biological response.

3. Chapter 6 assesses the effect of particle surface chemistry, architecture and size on bacterial attachment of *P. aeruginosa* PAO1-N mCherry.

3. Materials and Methods

3.1. Introduction

In this chapter, the methods for microsphere production that have been employed throughout this thesis are described. A complete list of materials used in this thesis is presented. In order to understand how these materials will behave in microsphere production, material characterisation methods are presented; these provide means to understand the fluid behaviour within the particle forming processes. Following, information is given for different particle characterisation techniques for the purpose of optimising the particle fabrication. There is a need for deepening the understanding of both the material and microparticle properties for interpreting biological responses. For this, methods for bacterial attachment testing are presented.

3.2. Microsphere Formation

3.2.1. Piezoelectric Inkjet Printing

A piezoelectric drop-on-demand (DOD) printhead is illustrated schematically in Figure 3.1. This printhead consists of a pumping chamber including a fluid inlet which terminates in an orifice. A piezoelectric diaphragm is attached to one side of the chamber.

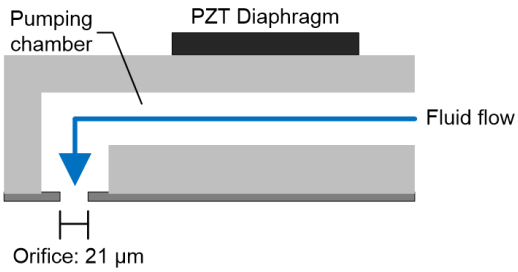


Figure 3.1: Schematic diagram of a piezoelectric inkjet printhead with an orifice of 21 µm.

Applying a voltage to the piezoelectric actuator causes the diaphragm to bend inwards to the pumping chamber [226]. This motion generates pressure waves, which push the fluid to the outlet. A droplet is expelled from the orifice when the kinetic energy transferred outwards exceeds the surface tension of the fluid [8]. The size of the droplets is controlled by the voltage applied, the pulse duration and the orifice diameter [227].

PREPARATION OF PRINTED POLYMERIC MICROSPHERES

Polymeric microspheres were prepared by using a piezoelectric inkjet printer (Dimatix DMP-2800, Fujifilm Dimatix Inc.) employing a disposable cartridge (Model DMC-11610), as shown in Figure 3.2. This cartridge is composed of two parts that clip together. The top part of the cartridge contains a fluid bag and a fill port whereas the bottom part includes connectors, heater and a nozzle plate with 16 nozzles. The nozzles exhibit typical drop sizes of 10 picoliters (resulting in diameters of 26.7 µm).

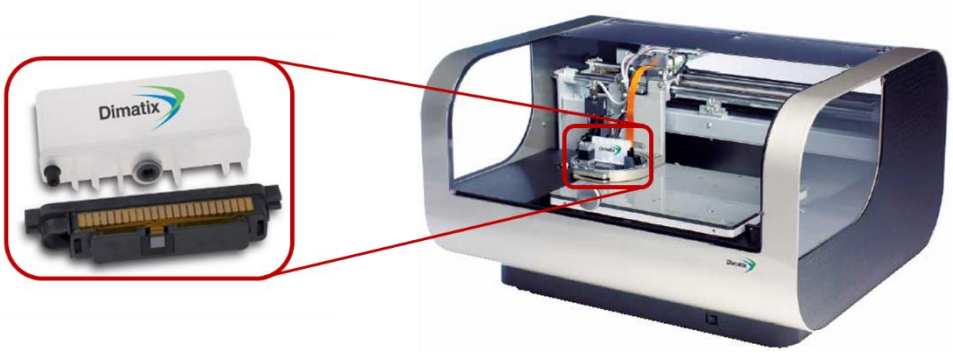


Figure 3.2: The Dimatix DMP-2800 printer with its user-refillable cartridge which is able to print 10 pl drops with a 10-µm drop-placement accuracy.

For printing, the photocrosslinkable monomer solution was loaded into the cartridge. The ink was repeatedly printed in patterns of 30 × 30 drops into a 24-well plate filled with aqueous collecting fluids. The droplets were polymerised simultaneously by exposure to UV light (wavelength of 365 nm, PEL UV Control Unit 365) in a reduced oxygen atmosphere (nitrogen, O_2 concentration: <1%). The experimental printing setup is schematically illustrated in Figure 3.3. The droplets were ejected at printing velocity and frequency of 6 m/s and 3 kHz, respectively. The actual jetting behaviour of the fluid was viewed by using the Dimatix Drop Watcher camera. At the end, the inkjet printed particles were washed five times with deionised water to remove any unpolymerised monomers.

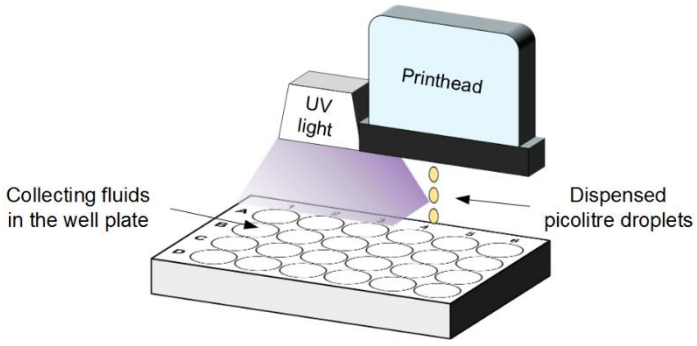


Figure 3.3: Schematic of the experimental setup which was used for ejecting ink droplets into collecting fluids while polymerising them simultaneously by exposure to UV light.

The Dimatix Drop Manager (DMP 2800, version 2.0.0.1) was used to control the printing setup which includes the print pattern, substrate and cartridge settings. In the cartridge settings, the stability of ejecting an ink was fine-tuned by modifying the waveform, printing frequency, cartridge temperature and voltage. The voltage can be adjusted individually for each nozzle.

3.2.2. MICROFLUIDICS

Microfluidics is the technology of systems that uses channels with dimensions of tens to hundreds of micrometres in order to process or manipulate small (10^{-9} to 10^{-18} litres) amounts of fluids normally under laminar flow conditions [103]. Fluids are usually characterised by the three important parameters; density (ρ), viscosity (η) and surface tension (σ). In microsystems, the flow characteristics can be described as the ratio of inertial forces to viscous forces [104]. This expression, given in Eq. 3.1, is called the dimensionless Reynolds number (Re):

$$Re = \frac{F_{inertial}}{F_{viscous}} = \frac{\rho L \nu}{\eta}, \qquad \text{Eq. 3.1}$$

where ρ is the fluid density, L is the typical length scale (e.g. diameter or channel length), ν is the average velocity of the moving liquid and η is the viscosity. Due to the small dimensions of microchannels, it is obvious that that a low Reynolds number is attained that is usually much less than 100, often even less than 1. Reynolds number lower than about 2000 is referred to as the laminar flow regime [102]. In this region, flow is completely laminar and no onset of turbulences occurs which results in a predictable manner of fluid transport through microchannels. However, in the region in which Reynolds number are larger than about 2300, inertial forces are dominant leading to a turbulent flow [102].

PREPARATION OF MICROFLUIDIC PRODUCED MICROSPHERES

The microparticles were produced using a planar microfluidic geometry, comprising of only a T-junction (Figure 3.4 a)) for the homopolymeric and pre-blended copolymerised particles and a Y-shaped channel leading to a T-junction (Figure 3.4 b)) in case of the on-chip copolymerised particles. Both devices have a uniform channel width and depth of 100 µm. The particles were continuously exposed to UV light (wavelength of 365 nm, HAYASHI LA-410UV) at the end of the outlet tube from the microfluidic device. After collection in a beaker containing 2 wt% aqueous PVA solution, the output was then filtered through a nylon mesh (grid size 20 × 20 µm) to remove satellite droplets.

Any particles smaller than 20 µm fitted through the mesh, whereas larger particles remained on the mesh. Subsequently, the larger particles were rinsed with ethanol and distilled water to remove PVA residues from the continuous phase. The particles were air-dried and collected afterwards. To remove any unreacted monomers, microparticles were kept in a vacuum oven at RT for 7 days.

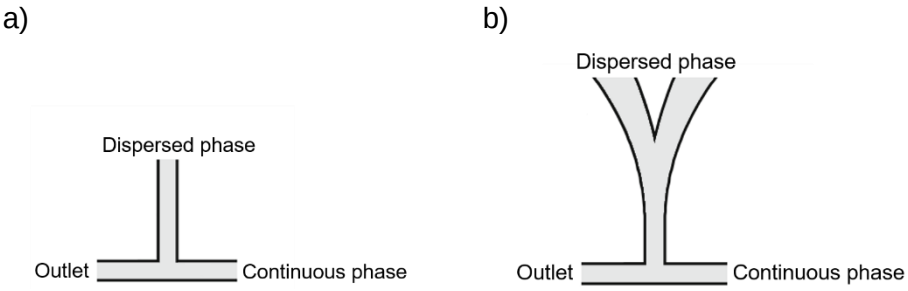


Figure 3.4: Schematic of the planar microfluidic geometries: a) simple T-junction applied for homopolymeric and pre-blended copolymerised particles, b) Y-shaped channel leading to a T-junction used for the production of copolymerised on-chip particles.

General Equipment and Procedure

The experimental setup consisted of a custom-made glass chip (15 × 15 × 3.5 mm) which was assembled in a stainless steel holder. This microfluidic device was connected to syringes via polytetrafluoroethylene (PTFE) tubes (0.8 mm internal diameter, 1.59 mm external diameter) as shown in Figure 3.5. The syringes, made out of glass (Hamilton Company, USA), were filled with the monomer solution and continuous phase and then, placed on syringe pumps (KD Scientific, KDS LEGATO 200). A high-speed video camera (Fastcam-1024PCI, Photron Limited), which was mounted on an upright microscope (Olympus, BX-51), was applied to observe the droplet formation. The microchannels were cleaned in between employing different monomers by introducing and flushing with acetone, ethanol and distilled water.

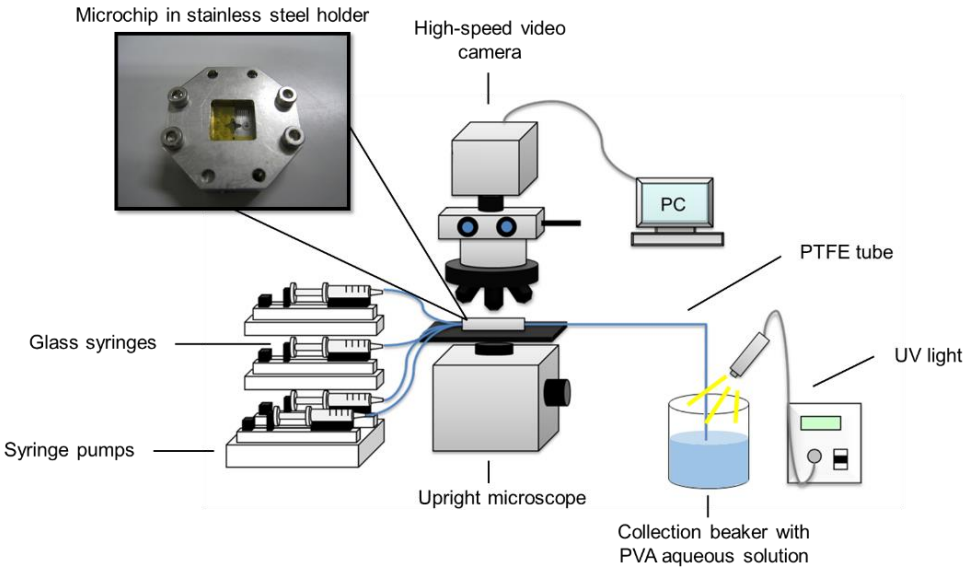


Figure 3.5: Schematic of the experimental microfluidic setup.

3.3. MATERIALS

The photocurable polymerisation solutions used in this work are based on (meth)acrylates, most of which have been shown to be biocompatible [161]. In Figure 3.6, the basic chemical structures of an acrylate (a) and methacrylate (b) are depicted. Additionally, Figure 3.6 c) shows the initiation of a photopolymerisation reaction in which photoinitiator (PI) radicals are formed by absorbing UV energy. These radicals react with acrylate species to create reactive alkyl monomer radicals. An example of a common photoinitiator is 2,2-dimethoxy-2-phenylacetophenone (DMPA) whose chemical structure is presented in Figure 3.6 d). DMPA is a Type I photoinitiator and employed in most of the studies performed within this thesis.

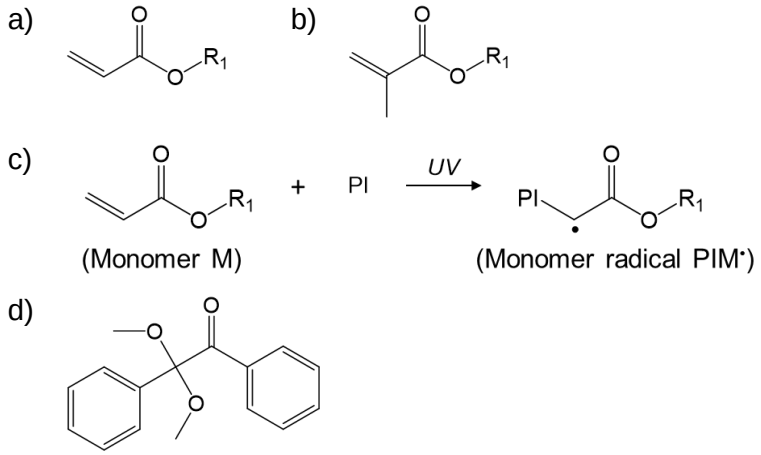


Figure 3.6: Basics of a photopolymerisation reaction are shown: a) chemical structure of an acrylate, b) chemical structure of a methacrylate, c) initiation of the reaction by absorbing UV energy by the photoinitiator (PI), forming radicals and attacking monomers (M) to generate reactive monomer radicals (PIM•), d) chemical structure of the photoinitiator DMPA.

In Table 3.1, all tested monomers with their abbreviations are provided. The molecular structure of each monomer with its corresponding abbreviation are outlined in Figure 3.7.

Table 3.1: All monomers with their corresponding abbreviations tested using the inkjet printer.

Abbr.	Monomer name	Abbr.	Monomer name
BACOEA	2-[[(Butylamino)carbonyl]oxy]ethyl acrylate	MBAm	N,N'-Methylenebisacrylamide
BDDA	1,3-Butanediol diacrylate	MBMAm	N,N'-Methylenebismethacrylamide
BMA	Butyl methacrylate	MHMB	Methyl 3-hydroxy-2-methylene-butyrate
CMAOE	Caprolactone 2-(methacryloyloxy) ethyl ester	MMA	Methyl methacrylate
DEGDA	Di(ethylene glycol) diacrylate	MOPAm	N-(3-Methoxypropyl) acrylamide
DEGDMA	Di(ethylene glycol) dimethacrylate	MTEMA	2-(Methylthio)ethyl methacrylate
DEGMA	Di(ethylene glycol) methyl ether methacrylate	PEGDA250	Poly(ethylene glycol) diacrylate (Mn-250)
DFHA	2,2,3,3,4,4,5,5,6,6,7,7-Dodecafluoroheptyl acrylate	PEGDA575	Poly(ethylene glycol) diacrylate (Mn-575)
DMAPA	3-(Dimethylamino)propyl acrylate	pEGMA	Poly(ethylene glycol) methacrylate
DMPAm	N-[3-(Dimethylamino)propyl] acrylamide	pEGMEMA	Poly(ethylene glycol) methyl ether methacrylate
EG3DMA	Tri(ethylene glycol) dimethacrylate	pEGPhEA	Poly(ethylene glycol) phenyl ether acrylate
EG4DMA	Tetra(ethylene glycol) dimethacrylate	PFPA	2,2,3,3,3-Pentafluoropropyl acrylate
EGDA	Ethylene glycol diacrylate	PhMA	Phenyl methacrylate
EGdPEA	Ethylene glycol dicyclopentenyl ether acrylate	pPGA	Poly(propylene glycol) acrylate
EGMEA	Ethylene glycol methyl ether acrylate	pPGDA	Poly(propylene glycol) diacrylate
EGMMA	Ethylene glycol methyl ether methacrylate	pPGMEA	Poly(propylene glycol)methyl ether acrylate
EGPEA	Ethylene glycol phenyl ether acrylate	SMA	Stearyl methacrylate
EGPhMA	Ethylene glycol phenyl ether methacrylate	tBCHA	4-tert-Butylcyclohexyl acrylate
F6BMA	2,2,3,4,4,4-Hexafluorobutyl methacrylate	TCDMDA	Tricyclo[5.2.1.$0^{2,6}$]decanedimethanol diacrylate
FuMA	Furfuryl methacrylate	TEGDA	Tetra(ethylene glycol) diacrylate
HA	Hexyl acrylate	TMCHMA	3,3,5-Trimethylcyclohexyl methacrylate
HDMPDA	3-Hydroxy-2,2-dimethylpropyl 3-hydroxy-2,2-dimethylpropionate diacrylate	TMPETA	Trimethylolpropane ethoxylate triacrylate
HFiPA	1,1,1,3,3,3-Hexafluoroisopropyl acrylate	TMPOTA	Trimethylolpropane propoxylate triacrylate
HMDA	1,6-Hexanediol diacrylate	TMPTA	Trimethylolpropane triacrylate
HPhOPA	2-Hydroxy-3-phenoxypropyl acrylate	TMSA	Trimethylsilyl acrylate
iBMA	Isobornyl methacrylate	TPGDA	Tri(propylene glycol) diacrylate
iBuMA	Isobutyl methacrylate	A4	IIA4, 1,3-BDDA 35%, DMPA 2%
iOA	Isooctyl acrylate	CA-2	IIpC4-2, TPGDA 20%, DMPA 2%

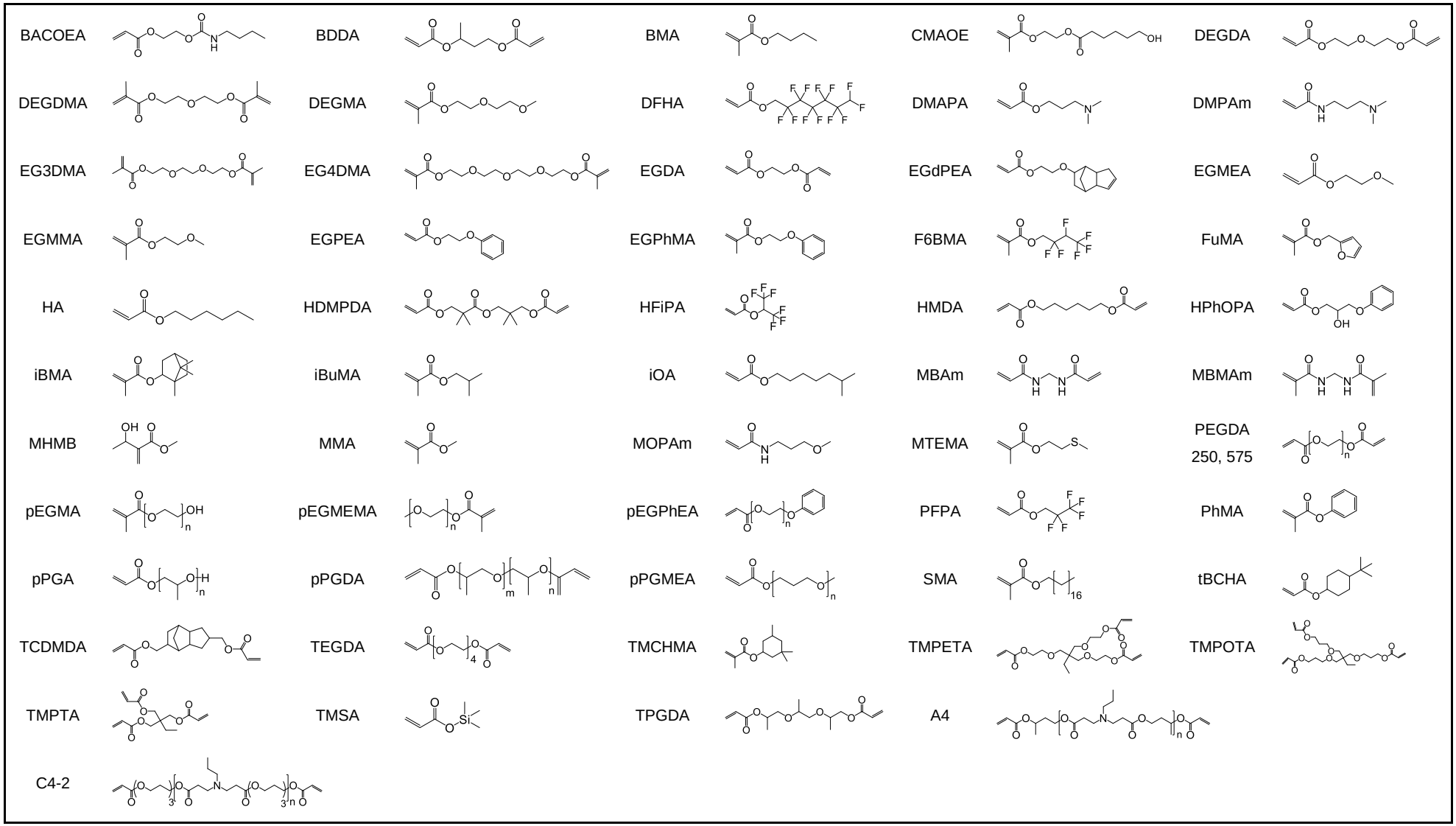


Figure 3.7: Chemical structures of all monomers tested with the inkjet printer.

3.4. Material Characterisation Techniques

3.4.1. Viscosity Measurement

Viscosity and surface tension are two of the fluid physical characteristics which are significant for achieving optimum printing performance. For the purpose of this work, a rotational viscometer was used to measure the flow parameters of different fluids (Kinenux Pro rheometer, Malvern, USA). This method deduces viscosity from the force required to turn an object in a fluid [228]. For most of the measurements performed, the cone and plate measuring system was employed. In this system, a cone of very shallow angle in the range of 0.5-4° is contacting a flat plate where the fluid to be measured fills the gap between the upper and lower parts. This system is preferred as it requires small sample volumes (<1 ml) and can be used on materials having a viscosity of about 10 cP and higher. A schematic of the cone system can be seen in Figure 3.8 a). A photo of the system is shown in Figure 3.8 b). The viscosity values were directly exported from the software which graphically displayed shear stress against shear rate.

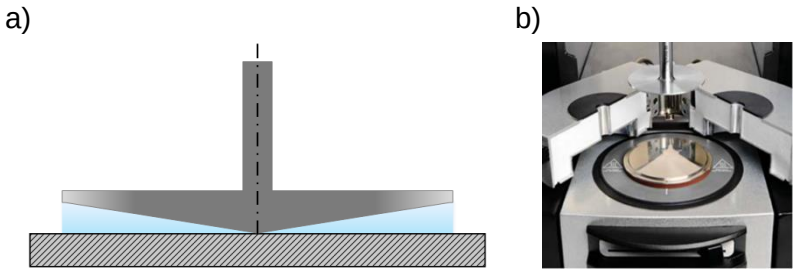


Figure 3.8: Cone and plate measuring system used for rheological measurements on materials with small sample volumes (<1 ml) and/or viscosities of 10 cP and higher: a) schematically drawn, b) photograph.

Some low viscosity fluids, which caused difficulties when applying the cone and plate system, were analysed using a DIN standard coaxial cylinder in the cup and bob measuring system. A schematic and a photograph of this measuring system are shown in Figure 3.9. A relatively large amount of material (~3 ml) is required for this measurement process, hence it was only used when absolutely essential. In this system, the torque needed to achieve a certain rotational speed is measured under the assumption of knowing the exact fluid volume to be sheared [228].

a) b)

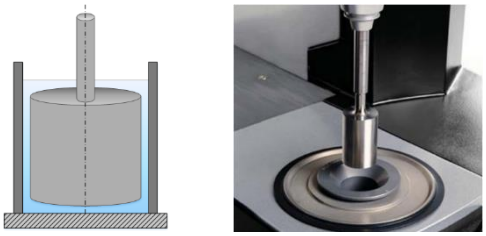


Figure 3.9: Coaxial cylinder in the cup and bob measuring system used to study the rheological behaviour of low viscosity fluids: a) schematically sketched, b) photograph.

Independent of the measuring system, viscosity versus shear rate were studied with shear rates from 10 to 1000 s^{-1} at 25ºC to a temperature corresponding to a viscosity value in the range of 8-15 cP or maximal 70ºC.

3.4.2. SURFACE TENSION MEASUREMENT

In order to predict the printability of a selected monomer solution, viscosity and surface tension need to be known so that adjustments can be performed to achieve ranges of 10-12 cP and 28-33 mN/m, respectively. These values are stated for optimal performance in the jettable fluid formulation guidelines [229]. A Krüss Drop Shape Analyzer DSA100 was used to determine the surface properties of the monomer solutions and collection fluids. The pendant drop method was applied, in which a droplet is suspended from a needle in air as shown in Figure 3.10. The shape of the drop is governed by the surface tension and gravity. According to the Young-Laplace equation (Eq. 3.2), the Laplace pressure difference (Δp) is caused by the surface tension (σ) of the interface between a gas and liquid region:

$$\Delta p = \sigma * \left(\frac{1}{r_1} + \frac{1}{r_2}\right) \qquad \text{Eq. 3.2}$$

where r_1 and r_2 are the radii of curvature. Consequently, the surface tension of a liquid is determined by applying a Young-Laplace fit to the contour of a shadow image of the pendant drop at its equilibrium state with known image scale using drop shape analysis [230]. The magnification of the image is previously calibrated by the first two blue lines, as illustrated in Figure 3.10, which are placed close to the needle end. The third blue line, which is placed below the needle tip, defines the border below which the shape of the drop will be determined.

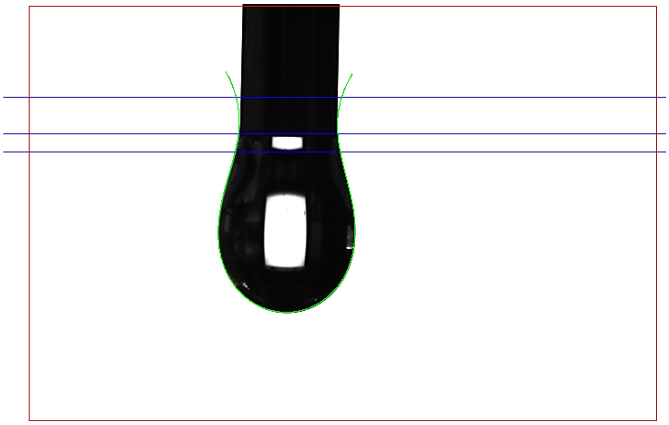


Figure 3.10: Measuring surface tension on a pendant drop. Red region defines the analysis zone, whereas the first two blue lines are used for the magnification calibration. The third blue line, which is below the needle tip, defines the border below which the shape of the drop will be determined. The green line represents the Young-Laplace fit.

3.4.3. PHOTO-DIFFERENTIAL SCANNING CALORIMETRY (PHOTO-DSC)

A photo-DSC is a differential scanning calorimetry (DSC) with some changes in the design which enables the irradiation of samples with light. The basic principle of this technique comprises monitoring heat effects associated with chemical reactions and phase transitions as a function of temperature [231,232]. The heat flow is recorded as the difference of heat measured in a sample compared to a reference cell.

In this thesis, the UV curing of monomer solutions was monitored using a Perkin-Elmer DSC8500 accessory with nitrogen as the purge gas. The UV source was equipped with a 200 W mercury lamp (OminCure 200 curing system with fiber-optic light guide). Two quartz windows were directly positioned over the sample and reference cells. The intensity at the distance of sample and reference cells was 10 mW/cm^2 in the wavelength range of 250 to 450 nm. Each sample was placed in an open aluminium pan. The experiments were performed for 360 s under isothermal conditions at 25°C of which 180 s (2 × 90 s) were baseline measurements. The baseline measurements were performed without light input before and after the exposure time. The UV light was applied continuously for 180 s in-between the baseline measurements. In order to eliminate possible baseline displacements, a second measurement was subtracted from the first. The data reported for each ink is an average of two separate photopolymerisation reactions. The analysis was performed in both Pyris Manager (PerkinElmer, version 11.1.0.0488) and MATLAB (R2016b, version 9.1.0.441655).

PREPARATION OF MONOMER SOLUTIONS FOR PHOTO-DSC

Monomer solutions were prepared by dissolving 1 wt% DMPA in (meth)acrylates. All tested monomers with their abbreviations and chemical structures are shown in Figure 3.11.

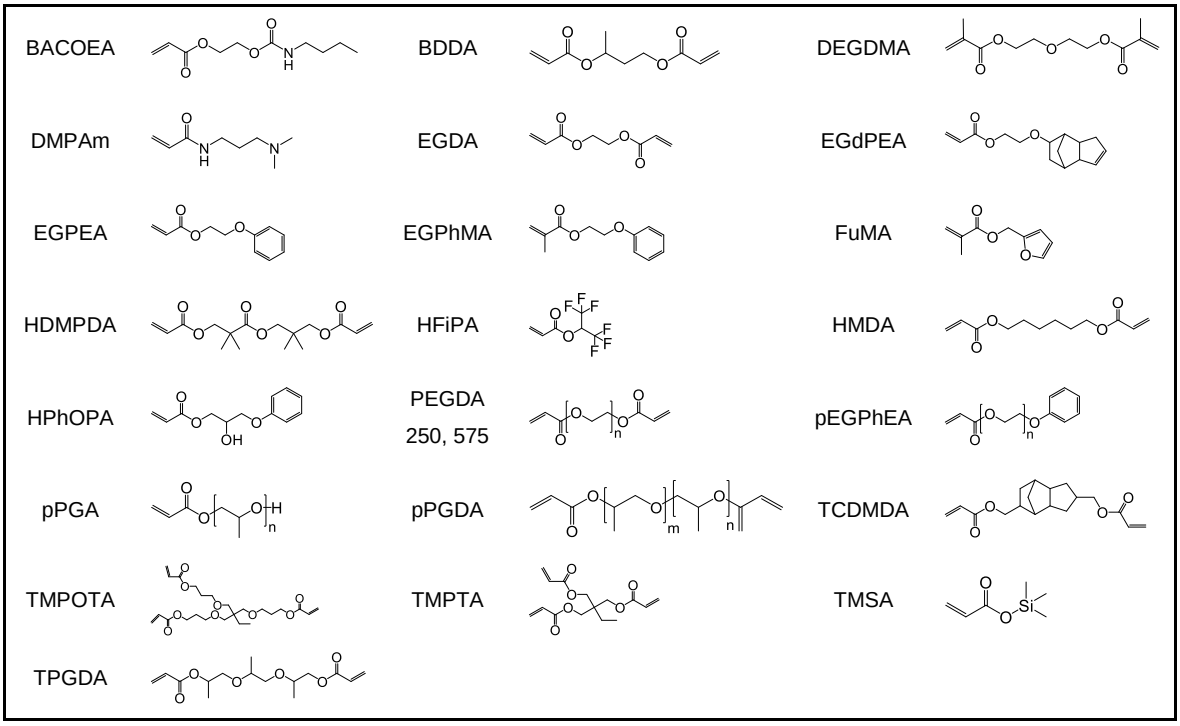


Figure 3.11: (Meth)acrylates analysed for their curing kinetics using Photo-DSC.

3.4.4. FOURIER TRANSFORM INFRARED SPECTROSCOPY

Fourier transform infrared spectroscopy (FTIR) is one of the preferred methods to determine various specific compositions and molecular structures. FTIR has been reported to be a powerful analytical technique that allows to study UV-initiated curing processes [233]. In other words, the kinetics of photopolymerisation reactions occurring within a fraction of a second but also the actual degree of conversion of specific reactive functional groups can be monitored [234]. Attenuated total reflectance (ATR) is a standard accessory that makes it possible to measure solid and liquid samples without any preparation and hence, it was exclusively used for all sample measurements within this work. A beam of infrared (IR) light is directed onto an optically dense crystal with a high refractive index in such a way that the beam reflects internally at the interface between the crystal and the sample as shown in Figure 3.12 [235]. The fraction of light extending into the sample forms an evanescent wave. This wave is attenuated or altered in spectral regions where energy is absorbed by the

sample. After hitting the IR detector, these changes are measured and converted to an infrared spectrum [236].

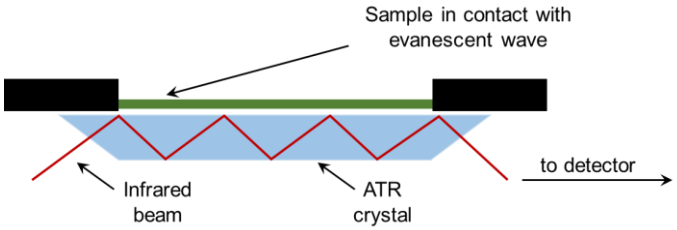


Figure 3.12: Multiple internal reflection of a beam of infrared light at the interface between the ATR crystal and sample.

FTIR-ATR was conducted on a Perkin Elmer Frontier instrument in order to characterise and identify chemical bonds present in a specimen. Scans were conducted from 4000 to 650 cm^{-1}, at a resolution of 4 cm^{-1}. The analysis was conducted in the 'PerkinElmer Spectrum' software (PerkinElmer, version 10.4.4.449).

3.5. Particle Characterisation Techniques

3.5.1. Optical Microscopy

The size and size uniformity of inkjet printed microparticles were analysed by acquiring brightfield images using an Olympus IX51 microscope with a 40x objective lens together with a Smart Imaging System (IMSTAR S.A.). Brightfield images of the microfluidic produced particles were acquired on an Olympus BX-51 upright microscope (Olympus, Japan) with a 50x objective lens. The printed samples were imaged in a 24-well plate and the mean diameter of representative particles was measured applying the software IMSTAR array. A small aliquot of the dried microfluidic particles was re-suspended in 2 wt% aqueous PVA solution for imaging. The dimensions of the microparticles were examined off the fluidic module by using ImageJ, an image analysis software package.

3.5.2. Scanning Electron Microscopy

Scanning electron microscopy (SEM) is an imaging technique that produces images by rastering a focused beam of electrons across the sample. When electrons hit the specimen, various electron-sample interactions may occur like elastic scattering of electrons, secondary electron emission, ionisation of inner shell electrons and excitation of photons [237]. The most common type of SEM imaging is the secondary

electron imaging (SE) which involves the collection of displaced secondary electrons using a secondary electron detector. This type of detection is heavily dependent on specimen topography as the emitted electrons emerge from near the surface areas. Therefore, by collecting the secondary electrons an image representative of the surface topography is created.

SEM imaging was performed using a JEOL JSM-6060LV in order to obtain information about the shape and surface morphology of the polymeric microspheres. The inkjet printed particles were placed onto aluminium sample holders by pipetting 100 µl of particle suspension whereas the dried microfluidic produced particles were sprinkled, using a spatula, onto a double-sided adhesive carbon tape. Prior to SEM analysis, the samples were sputter-coated for 4-5 minutes at 25 mA with a thin gold layer in an argon atmosphere utilising a Leica EM SCD005 sputter coater (Leica Microsystems GmbH, Wetzlar, Germany) to give approximately a 25 nm thick coating.

3.5.3. Particle Sizing

3.5.3.1. Measuring the Size Distribution of Microfluidic Particles

For quantifying the particle size distribution of the microfluidic produced particles, a Coulter LS230 (Beckman Coulter, UK) equipped with a laser light of 750 nm was applied. This instrument utilises light diffraction to measure particles from 0.04 to 2000 µm. After passing through a spatial filter and projection lens, the laser radiation forms a beam of light. The beam passes through a sample cell in which a representative number of particles was moderately stirred in deionised water applying a pre-set speed level of 5. In order to be able to start a size distribution measurement, the particle suspension had to reach an obscuration of 8 to 12% while maintaining a total chamber volume of 18 ml. These particles scatter the incident light onto a Fourier lens, as schematically displayed in Figure 3.13. This lens focuses the diffracted light onto a single annular area on its plane of focus, the Fourier plane. An image from the collected scattered light data, also called diffraction pattern, is formed and can be accurately sensed by a detector array.

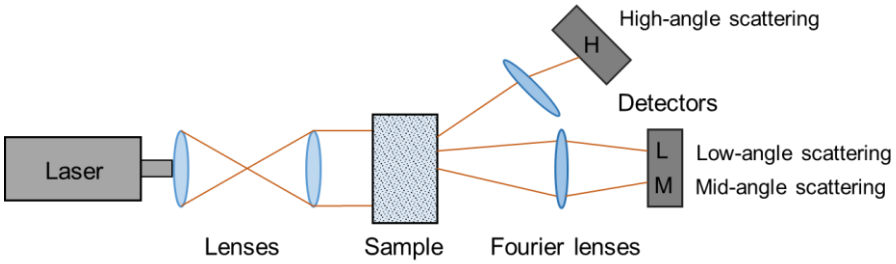


Figure 3.13: Schematic of the laser diffraction: laser beam passes through a sample cell where particles scatter the light onto Fourier lenses. The Fourier lenses focus the diffracted light and the scattered light is accurately recorded by detectors.

Particle size distributions were determined by measuring the composite, time-averaged diffraction patterns which are the sum of individual diffraction patterns from particles. The sizes were computed based on the Fraunhofer model of light scattering, where the relative amplitude of each pattern was used to determine the relative volume of particles in each size classification. More background information about dynamic light scattering is provided in Appendix A.

3.5.3.2. Measuring the Size Distribution of Printed Particles

Although the inkjet printed particles (d ~ 20 µm) were within the measuring range of the Coulter LS230 (0.04-2000 µm), a complementary technique had to be used for size distribution evaluation due to limitations in sample quantity. A centrifugation-based method required smaller amounts of sample than the Coulter LS230 (~20 mg).

The particle size distribution of inkjet printed particles was measured on a CPS disc centrifuge (Model DC24000, CPS Instruments Inc.) equipped with a 405 nm light source. This instrument measures particles between 0.02 and 30 microns, however the system has its maximum capability in the range of 0.01 to 40 microns. The size distributions were measured using centrifugal sedimentation within an optically clear spinning disc. This spinning disc was filled with a sucrose density gradient, formed by adding varying density solutions in steps, to stabilise the sedimentation of particles. 0.5 ml dodecane (anhydrous, ≥ 99%) was added as a final step to prevent gradient evaporation. All fluids were injected into the spinning disc through an injection point, as shown in Figure 3.14 a), using syringes. The sucrose density gradients were prepared in distilled water based on the density of the particle material:

- Gradient 1 for densities between 1.0 and 1.1 g/ml: 2-8 wt% sucrose
- Gradient 2 for densities between 1.1 and 1.3 g/ml: 4-12 wt% sucrose

Aqueous suspensions containing the microspheres (0.1 ml each) were sized after calibrating the instrument prior to each test. The instrument was calibrated with 1.27 µm polyvinyl chloride (PVC) particles dispersed in deionised water. The concentration of particles at each size was quantified by measuring the turbidity of the fluid near the outside of the rotating disc. Schematics of the disc are presented in Figure 3.14. As the particles reach the outer edge of the disc, they pass through the detector light beam and scatter a portion of light. The change in the light intensity is continuously recorded and converted by the operating software into a particle size distribution. In this conversion, the Stokes law is applied with the assumption that the particles are spherical [238].

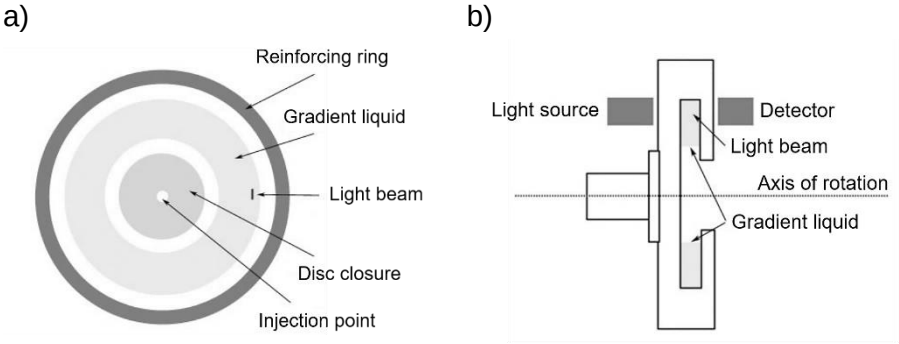


Figure 3.14: Schematic of the spinning disc: a) front view, b) cross section view. Images adapted from CPS Instruments Europe [239].

The simplified Stokes equation, which is presented in Eq. 3.3, reveals that the particle diameter (D) is proportional to the inverse of the square root of time (t) required for the particle to move a defined distance:

$$D = \frac{K}{\sqrt{t}} \qquad \text{Eq. 3.3}$$

where K is a combination of constants.

3.5.4. Time-of-Flight Secondary Ion Mass Spectrometry

Time-of-Flight secondary ion mass spectrometry (ToF-SIMS) is an ideal technique for detailed surface chemical analysis due to its ability to provide specific chemical information with good depth resolution (~1-2 nm). The working principle is described in full detail in Appendix B. ToF-SIMS measurements were conducted utilising an IONTOF IV instrument (ION-TOF GmbH, Munster, Germany) using a Bi_3^+ primary ion source operated at 25 kV in 'high current bunched' mode. The primary ions exhibited a pulsed target current of ~1 pA. Sample areas of 500 × 500 µm were acquired at a

resolution of 256 × 256 pixels by rastering the primary ion beam over the substrate surface in a 'random raster' path sequence. An ion dose of 2.45×10^{11} ions per cm^2 was applied to each sample area in order to ensure that the static conditions were maintained throughout. Both positive and negative secondary ion spectra were collected (mass resolution of >7000) over an acquisition period of 20 scans (the data from which was summed). In order to compensate for charge build-up due to the non-conductive nature of the polymeric samples, low energy electrons (20 eV) were delivered via a flood gun. Data analysis was carried out using the 'IONTOF SurfaceLab 6' software.

3.5.5. Atomic Force Microscopy

Atomic force microscopy (AFM) is a surface characterisation technique which is outlined in Appendix C. For topographical characterisation of inkjet printed and microfluidic produced microparticles, a Dimension FastScan with ScanAsist AFM scanning probe microscope (Bruker, UK) was used. The particles, attached to a double-sided carbon tape on a silicon wafer, were studied in air using PeakForce QNM mode. Within a sample aliquot 3 × 3 µm areas of 5 randomly chosen particles were analysed for their roughness while high resolution images were acquired. Bruker RTESPA-150 0.01-0.025 Ω cm antimony doped silicon (Bruker, UK) were the cantilevers selected. The analysis was conducted with the 'NanoScope Analysis' software (Bruker, version 1.50).

3.6. Bacterial Attachment Assays

3.6.1. Bacteria and Growth Conditions

P. aeruginosa PAO1-N mCherry (Nottingham strain) was obtained from stocks held within the university from the group of Professor Paul Williams. PAO1-N is a specific lab strain representative of *P. aeruginosa* (PA) that was genetically modified to express the red fluorescent protein mCherry. Small amounts of *P. aeruginosa* were routinely plated out on LB (Luria-Bertani, Oxoid, UK) agar plates and incubated overnight at 37°C. Following, a single colony was selected, transferred into 10 ml of LB medium and incubated at 37°C with 200 rpm. The bacterial suspension was centrifuged for 5 min at 9500 rpm the next day. After replacing the LB medium by RPMI-1640 medium (R0883, Sigma, UK), the bacterial suspension was vortexed and centrifuged again for

5 min at 9500 rpm. The RPMI-1640 medium, which contained some residues of the LB medium, was replaced by fresh RPMI-1640 prior to optical density measurements. The optical density (OD) of PAO1-N mCherry was measured at a wavelength of 600 nm using an Evolution 60S UV-Visible spectrophotometer (Thermo Fisher, UK). The bacterial suspension was diluted with fresh RPMI-1640 until an OD_{600} of 0.01 was achieved. Prior to the incubation with the bacteria, all samples were washed with phosphate buffer saline (PBS) solution, air-dried and UV sterilised for 30 min. Empty wells in Falcon® non-tissue culture 48-well plates (polystyrene) and pieces of a silicone catheter served as references which attracted high levels of bacterial attachment. Each sample was incubated in 1000 µl bacterial suspension which was taken from the prepared diluted stock (OD_{600} = 0.01). The incubation was performed at 37°C with 60 rpm for 24 h. After incubating the well plate for 24 hours, the samples were washed three times with 600 µl of sterile PBS prior to analysis. The washing steps were conducted as carefully as possible using a pipette to remove non-adhesive bacteria but not to damage the biofilm.

QUANTIFYING COLONY FORMING UNITS

The number of colony forming units (CFU) was determined with serial dilutions after 24 h. This was done by diluting the bacterial suspension from overnight cultures to an optical density of OD_{600} = 0.01 in RPMI-1640. This bacterial suspension corresponded to the starting concentration from which further dilutions were conducted in PBS. Afterwards, 100 µl of the diluted bacterial suspensions were plated onto LB agar plates and grown for 24h at 37°C. The next day, the colonies were counted and the colony forming units per millilitre (CFU/ml) were calculated using the following formula (Eq. 3.4):

$$\frac{CFU}{ml} = \frac{Number\ of\ colonies \times dilution\ factor}{plated\ volume} \qquad \text{Eq. 3.4}$$

An average of 1.5×10^7 CFU/ml were counted after 24h using a starting bacterial suspension of OD_{600} = 0.01.

3.6.2. CONFOCAL MICROSCOPE IMAGE ACQUISITION

The biofilm coverage on microparticles, pipetted thin films and control samples were observed using a ZEISS LSM 700 laser confocal microscope. Fluorescence images were acquired representing an area of 639 × 639 µm with a resolution of 512 × 512 pixels at 8-bit colour depth. Image acquisition was conducted with 2 light channels,

mCherry and T-PMT, and consisted of optical cross-sections which were evenly spaced by vertical steps of 4.0, 1.5 and 1.0 µm for films, microfluidic produced and inkjet printed particles, respectively. The microscope was operated as follows: excitation at a wavelength of 555 nm with a power of 10%, 10x/0.30 M27 EC Plan-Neofluar objective at an Airy disc setting of 1 Airy unit (AU) which corresponds to 34 µm.

3.6.3. BIOFILM QUANTIFICATION

Confocal laser scanning microscopy (CLSM) is able to reconstruct high-resolution 3D images of biofilm grown on any surfaces; more information is available in Appendix D. However, the quantification of bacterial attachment is currently limited to microbes grown on flat surfaces [240]. Recently developed, more sophisticated image processing algorithms, such as COMSTAT [241] and PHLIP [242], facilitate the quantification of three-dimensional biofilm structures. Moreover, the quantitative output from CLSM images has been enhanced by introducing methods, like objective threshold selection (OTS), which allow for automated determination of threshold levels [243]. Despite recent advances, there are no reports about quantification of biofilm-associated bacteria on 3D surfaces (here, particles) in the literature.

As a consequence, a new algorithm was developed to determine bacterial attachment on microparticles using an in-built MATLAB shape recognising function combined with adapted scripts from the COMSTAT program [244]. A schematic description of the biofilm quantification method using inkjet printed particles is provided in Figure 3.15.

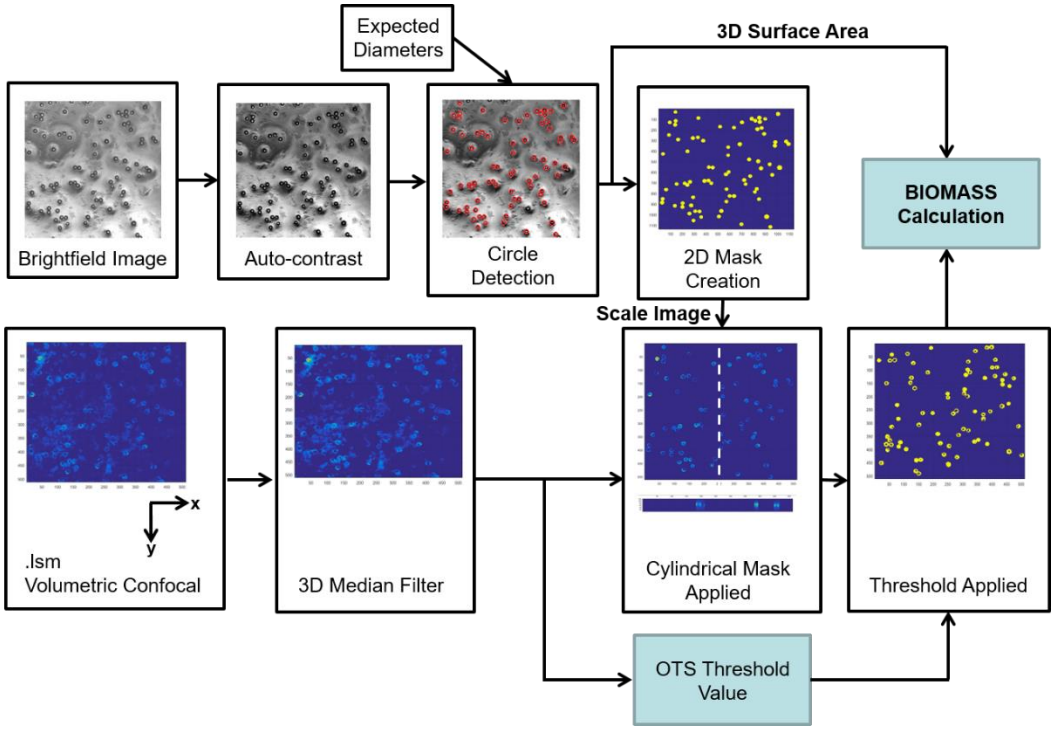


Figure 3.15: Schematic description of the developed algorithm to quantify biofilm on 3D surfaces.

In more detail, the observed biomass on the pipetted films, microparticles and control samples was calculated using MATLAB (R2016b, version 9.1.0.441655). The volumetric fluorescence images were directly imported into MATLAB and the in-built 3D median filter (*medfilt3*) was applied to filter noise present in the confocal data. Automatic thresholding and segmentation of volumes were statistically determined for the confocal microscopy images using the OTS procedure proposed by Xavier et al. [243]. This provides a consistent method selecting the threshold value without requiring manual intervention. In Figure 3.16, a cross-section through the confocal volumes of inkjet printed particles is presented before applying a volumetric filter (a) and after applying the 3D median filter (b). These two cross-sections were further modified by applying a threshold, illustrating the thresholded cross-sections before applying a filter (c) and after applying the 3D median filter (d). The substrate is highlighted as a dashed line in Figure 3.16 c) and d).

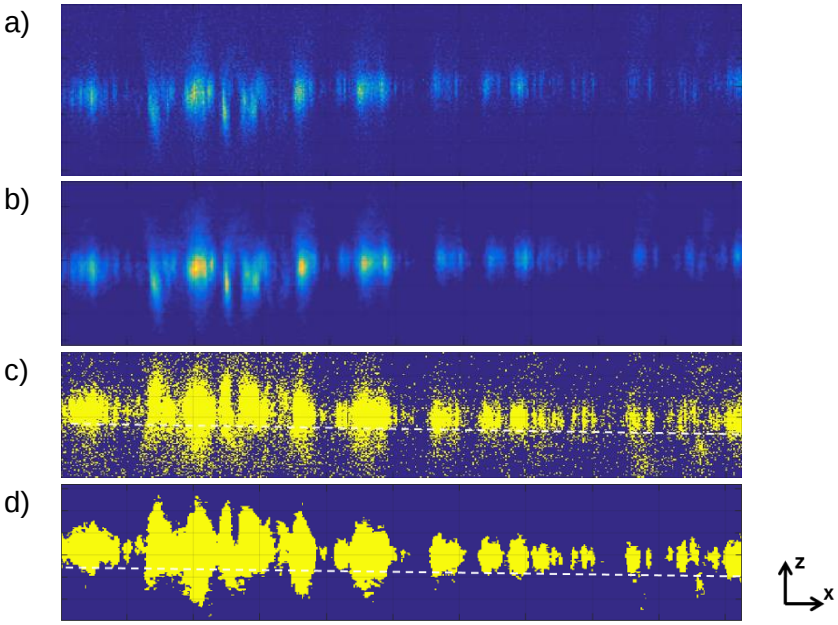


Figure 3.16: Images highlighting the effect of applying both a volumetric filter and a threshold on confocal data. A cross-section through confocal volumes of inkjet printed particles is shown for: a) before applying a filter, b) after applying the MATLAB in-built 3D median filter, c) after applying a threshold on unfiltered data, d) after applying a threshold on noise-filtered data.

In order to quantify the biofilm on the surface of microparticles, the particle centres and radii were automatically determined by detecting circular shapes in the optical image. Circle detection was performed with the in-built MATLAB function (*imfindcircles*), as shown in Figure 3.17 a). Using these geometries, a cylindrical mask was projected vertically and applied to the volumetric fluorescence images. This enables the quantification of the biomass only present on the selection of detected particles, shown in Figure 3.17 b).

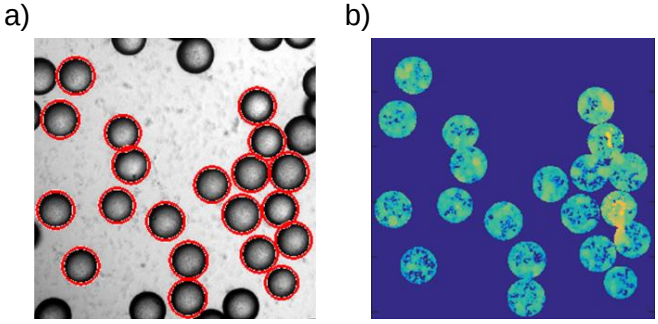


Figure 3.17: Biomass quantification on microparticles: a) successful circle detection (red) of microparticles present in the optical brightfield image, b) biomass captured on particles after applying the cylindrical mask to the volumetric images.

The new algorithm was validated against the COMSTAT program using pipetted thin films. In general, the biomass was calculated analogously to COMSTAT [241]. The overall biofilm on microspheres was quantified by summing the thresholded fluorescence pixels in all images of a stack multiplied by the voxel size $[pixel\ size_x \times pixel\ size_y \times pixel\ size_z]$ and dividing by the total spherical surface area

of the particles detected. Similarly, the biomass of the films and control samples was calculated by summing the thresholded volumes and dividing by the planar area of the image. This calculation was automatically repeated throughout all samples relevant for this work, with the particle detection validated visually.

3.7. SUMMARY

In this chapter, an overview of methodologies used throughout the thesis was given. Firstly, the microparticle fabrication techniques including piezoelectric inkjet printing and microfluidics were described. Furthermore, the materials, which were used for producing particles, were outlined. Material characterisation methods were presented which were used to predict the printability but also to provide insight as to the reasons for a successful particle formation in certain monomers. Additionally, analysis techniques, which were employed to characterise microspheres in this work, were outlined. Finally, details about the confocal laser scanning microscopy and biofilm quantification were provided with the intention to gain further understanding of the material-performance relationships, as discussed in Chapter 6.

4. RESULTS - GENERATION OF A PARTICLE LIBRARY

4.1. INTRODUCTION

Successful particle fabrication is a complex process, which depends on multiple parameters such as solubility, viscosity, surface tension; each playing a crucial role. A need has been identified for new and optimised fabrication techniques that circumvent the issues related to the lack of control over shape, size and size distribution. This lack of control has been commonly associated with conventional production techniques. Furthermore, optimised fabrication techniques offer access to material combinations in a controlled fashion, an important development for particle generation.

Inkjet printing has become attractive because it is capable of precisely depositing picolitre volumes of fluid in well-defined patterns without the need for masks [7,8]. In contrast, microfluidics is already a well-established methodology for producing particles of complex design and composition [27,30]. Both manufacturing methodologies show potential for commercialisation and production on a big scale.

This chapter presents the development of a combinatorial microparticle library of (meth)acrylate based monomers using two methodologies, inkjet printing and microfluidics. Firstly, macroscopic pipetting experiments were performed in order to gain understanding of the droplet formation process and to find suitable monomer-collecting fluid combinations in a high throughput manner. Monitoring the UV curing of the selected monomers assisted in determining the reason for successful particle formation in certain monomers. The macroscopic particle formation was transferred into microscopic dimensions using inkjet printing and microfluidics, which is outlined in Section 4.3.3 and 4.3.4, respectively. Finally, both techniques were compared and evaluated in terms of microparticle production and production rate which is described in Section 4.3.5.

4.2. Experimental

4.2.1. Preliminary Experiments

4.2.1.1. Optimal Solution Ratio of Isopropanol in Deionised Water

The effect of changing the polarity and density of the collecting fluid on droplet formation was studied using a manual pipetting setup. Solutions were prepared using isopropanol (IPA) and deionised water (DIW) with the following chosen weight percentages: 0, 1, 3, 7, 10, 13, 15, 17, 20, 23, 25, 30, 40, 50, 100 wt% IPA/DIW. 5 µl of two different inks were pipetted from 10 mm above into a glass beaker filled with the prepared collecting fluids. The generated droplets were visualised and captured using a USB2-Micro-200x USB microscope (optical zoom up to 50x, digital zoom up to 200x) and the software MicroCapture as shown in Figure 4.1. The inks applied in this work were a commercially available ink, Solsys EMD6415 (Sun Chemical Ltd, UK), and poly(ethylene glycol) diacrylate (PEGDA250) with 1 wt% DMPA. Both inks were tested with and without adding rhodamine B, a fluorescent dye, for improving the visualisation of the droplets.

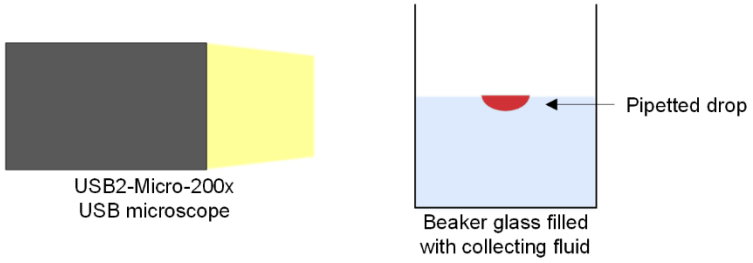


Figure 4.1: Schematic drawing of the experimental setup to visualise the ink droplet (5 µl) behaviour in the collecting fluid after being pipetted from 10 mm above the collecting fluid.

4.2.1.2. Manuel Pipetting Experiments

In order to find suitable monomers for generating a combinatorial library of microparticles, pipetting of monomers into collecting fluids was combined with stimulated polymerisation as illustrated in Figure 4.2.

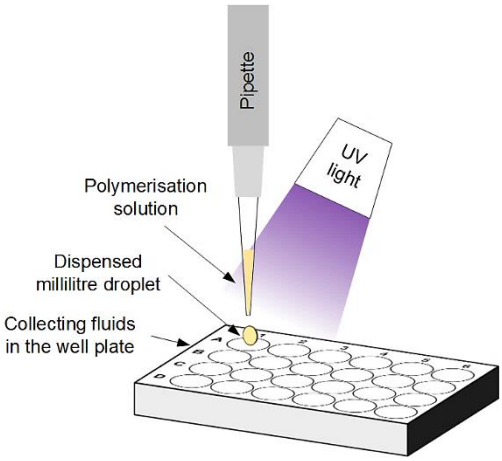


Figure 4.2: Schematic representation of the macroscopic pipetting experiment.

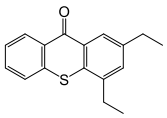
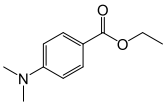
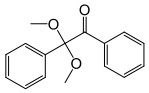
Four aqueous solutions with different polarity indices were selected as collecting fluids: deionised water (DIW), 17 wt% isopropanol in deionised water (IPA/DIW), dimethyl sulfoxide (DMSO) and hexane. The physiochemical properties of the collecting fluids are listed in Table 4.1.

Table 4.1: Collecting fluids with their physiochemical properties.

Collecting fluid	**Density [g/cm^3]**	**Viscosity [cP]**	**Surface tension [mN/m]**	**Hildebrand solubility [MPa$^{1/2}$]**	**Relative polarity** [245]
DIW	1.00	1.00	72.80	48.00	1.00
17 wt% IPA/DIW	0.96	1.14	37.07	IPA: 23.80 DIW: 48.00	IPA: 0.55 DIW: 1.00
DMSO	1.10	1.99	42.90	26.40	0.44
Hexane	0.66	0.31	18.40	14.90	0.01

The ability to form droplets was investigated by pipetting 15 µl of monomer solution into each collecting fluid with subsequent exposure to UV light (Blak-Ray® XX-15L UV Bench Lamp, 365 nm) for 1 min. The experiment was performed at room temperature in air and under argon atmosphere both with pipetting from above the collecting fluids and with the tip submerged in the collecting fluids. These two configurations were chosen to analyse the impact of the liquid-gas interface on the drop shape preservation. Depending on the environment, the monomer solutions consisted of (meth)acrylate based monomers, listed in Figure 3.7 in Section 3.3, with either a photoinitiator or a photoinitiator combined with an accelerator, as outlined in Table 4.2.

Table 4.2: Additives dissolved in monomers depending on the test environment.

Environment	Photoinitiator	Accelerator
Air	2,4-diethyl-9H-thioxanthen-9-one (DETX, 3 wt%) 	Ethyl 4-(dimethylamino)benzoate (EDB, 3 wt%) 
Reduced oxygen (argon, nitrogen)	2,2-dimethoxy-2-phenylacetophenone (DMPA, 1 wt%) 	

24-well plates were used as substrates because they allow for efficient testing of several monomers and collecting fluids at the same time. Each collecting fluid was placed into a different row, whereas the monomer solutions were tested along columns as is shown in the schematic in Figure 4.3.

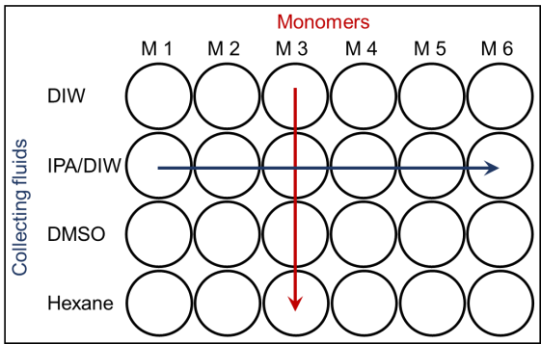


Figure 4.3: Schematic of the testing array in a 24-well plate.

4.2.1.3. High Speed Imaging of Pipetting

In order to determine the factors influencing the droplet formation, high speed videos of pipetting 5 µl of a monomer solution into collecting fluids were recorded utilising a Photron FASTCAM APX RS High-speed camera (frame rate: 3000 fps; shutter speed: 1/104000 s). The monomer solution consisted of PEGDA250 with 3 wt% of both photoinitiator DETX and accelerator EDB. The selected collecting fluids were deionised water, 17 wt% IPA/DIW and 1-octanol. Pipetting in air served as a reference. Two different jetting arrangements, pipetting from above the collecting fluid and submerged, were employed as schematically shown in Figure 4.4. A comparison of the two configurations was conducted to investigate the impact of the liquid-gas interface on the drop shape preservation.

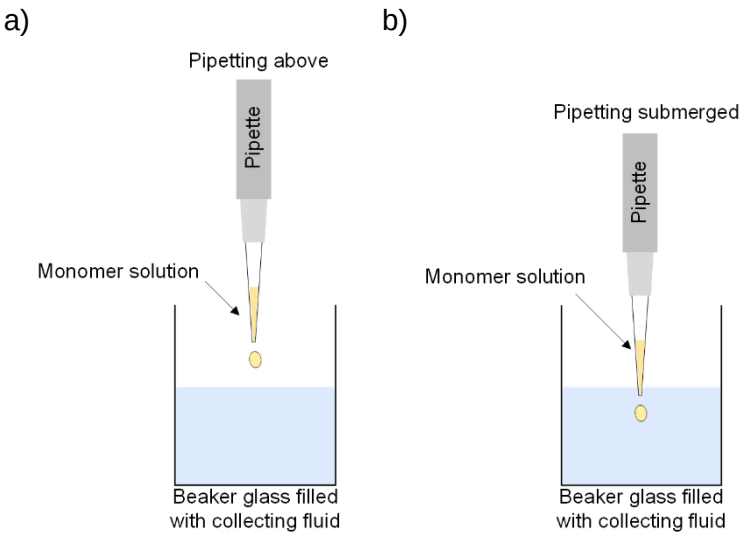


Figure 4.4: Schematic representation of the two different jetting arrangements: a) pipetting from above the collecting fluid, b) pipetting with the tip submerged in the fluid.

4.2.2. Interfacial Tension Measurement

The interfacial tension between the monomers and the PVA aqueous phase were measured at room temperature (RT) by using a tensiometer (CBVP-Z, Kyowa Interface Science) according to the Wilhelmy plate method. Prior to each measurement, the Wilhelmy plate was rinsed several times in acetone followed by flaming the plate over a Bunsen burner until it glowed red.

In this method, an extremely thin plate is partially immersed vertically below the interface of the two test fluids [246]. When the plate touches the liquid interface, a force F, which relates the interfacial tension γ to the contact angle θ, acts on the plate according to the following equation (Eq. 4.1):

$$\gamma = \frac{F}{L * cos\theta} \qquad \text{Eq. 4.1}$$

where L is the wetted length of the plate. The force F is measured by attaching the plate to a force sensor of a tensiometer. A schematic representation of the measurement setup is provided in Figure 4.5.

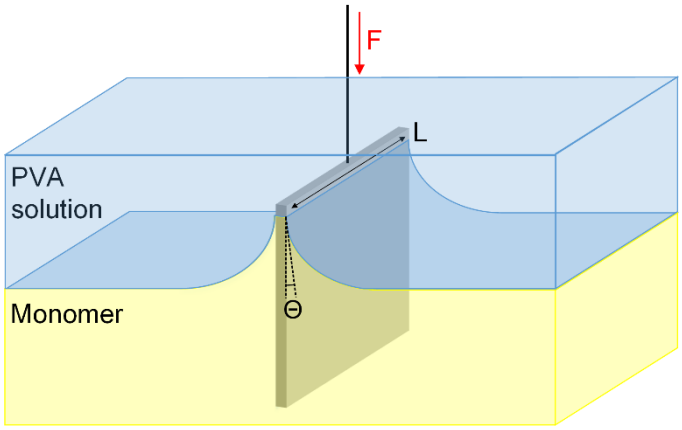


Figure 4.5: Schematic of the Wilhelmy plate method for measuring the interfacial tension at the monomer-PVA solution interface.

4.2.3. Preparation of Fluids for Particle Formation

4.2.3.1. Preparation of Fluids for Inkjet Printing

The monomers prepared for inkjet printing are mainly based on the monomers which successfully formed particles in the manual pipetting experiments under reduced oxygen atmosphere. Additionally, the monomer 2,2,3,4,4,4-hexafluorobutyl methacrylate (F6BMA) was selected, which did not result in particulate formation during manual testing. This selection was made to investigate how transferable the results are from the manual pipetting study. Besides these monomers, the monomers di(ethylene glycol) dimethacrylate (DEGDMA) and methyl methacrylate (MMA) were also added to the testing material due to similarities in chemical structures to some monomers able to produce particles. All monomers with their abbreviations and chemical structures, used in this study, are presented in Figure 4.6. For crosslinking, 1 wt% DMPA was dissolved in the monomers. Stirring at elevated temperatures up to 50°C was applied for dissolving the photoinitiator in case it was needed. Afterwards, the inks were purged with nitrogen for 15 minutes and left overnight in the fridge for oxygen removal.

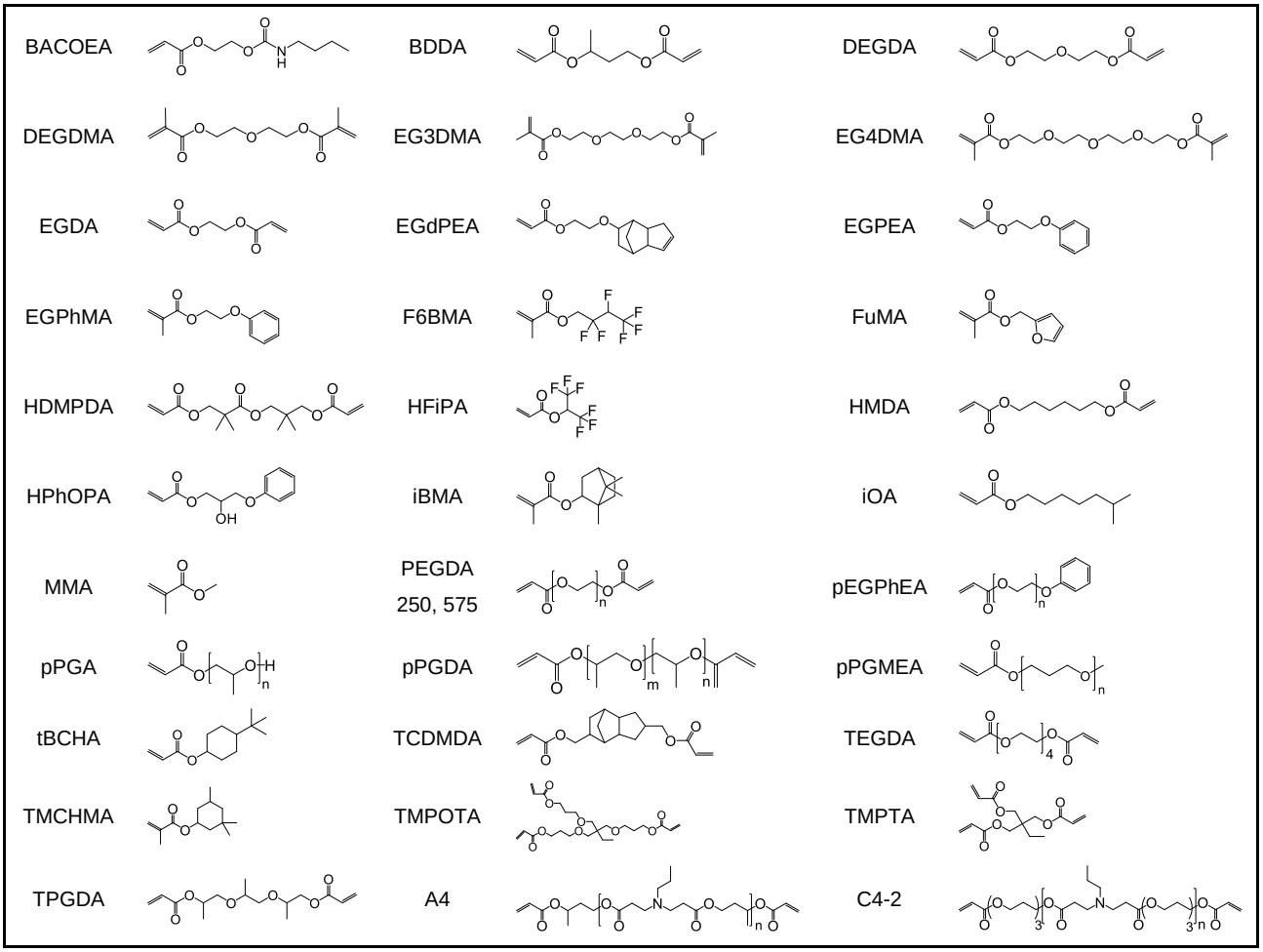


Figure 4.6: Abbreviation and chemical structure of each monomer tested using the Dimatix printer.

Deionised water, 17 wt% IPA/DIW and hexane were selected as collecting fluids in order to find a universal collecting fluid for optimised particle formation. The physiochemical properties of the fluids are outlined in Table 4.1. Prior to usage, the collecting fluids were degassed for 15 minutes using an ultrasonic bath.

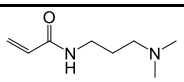
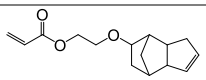
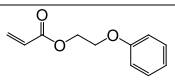
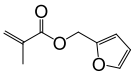
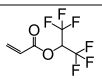
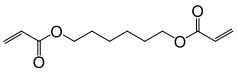
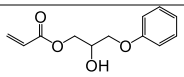
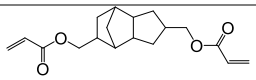
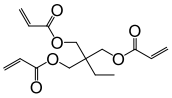
4.2.3.2. FREEZE-PUMP-THAW CYCLING

Degassing liquids by freeze-pump-thaw cycling is one of the most effective method for solvent degassing. The monomer solution was placed in a Schlenk flask and frozen by immersion in liquid nitrogen (N_2 (l)). When the fluid was completely frozen, the stopcock to the vacuum line was opened on the Schlenk flask. The flask atmosphere was pumped off for three minutes while the flask was still immersed in N_2 (l). Afterwards, the flask was sealed and warmed up until the monomer solution was completely melted using a warm water bath. This process was repeated three times. At the end of the last cycle, the flask was backfilled with nitrogen gas.

4.2.3.3. PREPARATION OF FLUIDS FOR MICROFLUIDICS

A small selection from the library generated for inkjet printing was chosen for particle fabrication using microfluidics. The monomers, including their abbreviations, chemical structures and comments found in the literature, are listed in Table 4.3. For crosslinking of each monomer, 1 wt% of the photoinitiator DMPA was dissolved in the monomer. The monomer solutions were degassed for 15 min using an ultrasonic bath to remove any air bubbles. For the continuous aqueous phase, distilled water was heated up to 75 ± 5°C before poly(vinyl alcohol-co-vinyl acetate) (PVA, 88% hydrolysed, Mw 300) was added in order to generate a 2 wt% solution. The PVA solution was cooled down to room temperature prior to use. When filling the glass syringes (Hamilton Company, USA) with monomer solution and aqueous PVA phase, it had to be assured that no air bubbles were present in the syringes since they cause instabilities in the system.

Table 4.3: Monomers employed for microparticle production using microfluidics.

Abbr.	Monomer	Structure	Comments
DMPAm	N-[3-(dimethylamino)propyl]acrylamide		Supports Calu3 and MRC5 cell attachment [157]
EGdPEA	Ethylene glycol dicyclopentenyl ether acrylate		Resistant to bacterial attachment [163,172]
EGPEA	Ethylene glycol phenyl ether acrylate		Low bacterial attachment [172]
FuMA	Furfuryl methacrylate		Low bacteria attachment [172], supports OCT4 cell [247] and hESC-CM [248] attachment
HFiPA	1,1,1,3,3,3-Hexafluoroisopropyl acrylate		Resistant to bacterial attachment [172]
HMDA	1,6-hexanediol diacrylate		Low bacterial attachment [172], supports OCT4 cell attachment [247]
HPhOPA	2-Hydroxy-3-phenoxypropyl acrylate		High bacterial attachment [163]
TCDMDA	Tricyclo[5.2.1.0^{2,6}]decanedimethanol diacrylate		Medium bacterial attachment [172]
TMPTA	Trimethylolpropane triacrylate		Resistant to bacterial attachment [163], supports OCT4 cell attachment [247]

4.2.4. PRINTING IN AIR

Dispensing inks in air was performed on a custom-built printer developed by Craig Sturgess (PhD student, Centre for Additive Manufacturing). This printing setup was

built similar to the Dimatix DMP-2800 printer employing the same printer cartridges. The main components include a waveform generator, printhead controller, Dimatix cartridge and an air-cooled FireFly UV light with a wavelength of λ = 365 nm. The printed monomer solution was comprised of the monomer PEGDA250, the photonitiator DETX (3 wt%) and of the accelerator EDB (3 wt%), as listed in Table 4.2. A simple waveform with a period of 15 µs and a trigger interval of 1 ms were used for printing the PEGDA250 ink into an empty petri dish. The waveform applied for printing in air is presented in Figure 4.7.

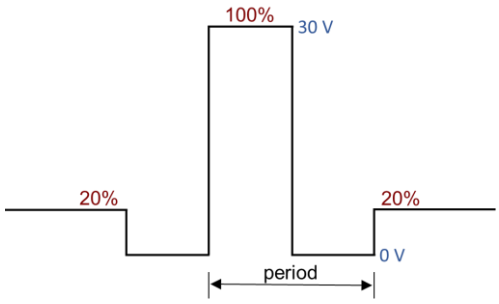


Figure 4.7: Simple waveform with a period of 15 µs was applied for printing in air.

A schematic representation of the experimental printing setup is given in Figure 4.8. The printhead controller with integrated display enabled to set temperatures for heating the nozzles and to individually switch the 16 nozzles on and off, respectively.

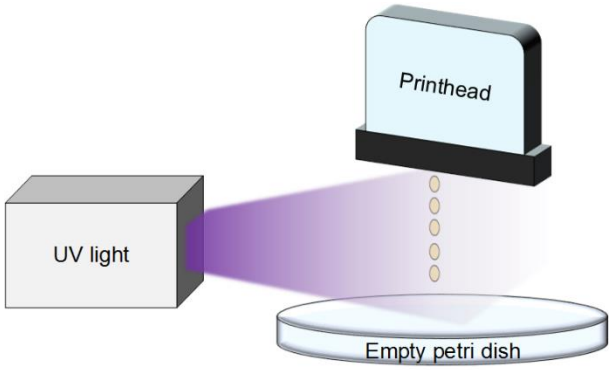


Figure 4.8: Schematic illustration of the experimental setup employed for ejecting a monomer solution into an empty petri dish in air while being exposed simultaneously to UV light.

4.2.5. Focused Ion Beam Measurement

In order to analyse the interior of microparticles, focused ion beam measurements (FIB) were performed using a Zeiss NVision 40 CrossBeam machine equipped with a Ga source. Sectioning of the particles was conducted at 30 kV with a probe current of 1.5 nA. Prior to FIB measurements, the microparticles were placed onto sample holders and sputter-coated for 4-5 minutes at 25 mA with a thin gold layer in an argon atmosphere.

4.3. Results and Discussion

4.3.1. Preliminary Experiments

In order to optimise the discovery of suitable monomer-collecting fluid combinations, the droplet formation process with all its interdependent parameters should be investigated. Herein, macroscopic pipetting experiments were performed in order to discover materials, which are able to form particles upon dropping 5 µl of monomer solution into a liquid, in a quick and efficient way. Additionally, forming particles macroscopically might illustrate the principle applied in droplet formation more clearly, resulting in better understanding of the process. This knowledge can assist in predicting and discovering new fluid combinations.

Poly(ethylene glycol) diacrylate (PEGDA) was chosen as the first monomer for the pipetting experiment due to its appropriate viscosity and surface tension for printing. Furthermore, this monomer had been extensively investigated in previous work where it had been shown that UV crosslinked PEGDA is an applicable material for biomedical applications [27,249]. Therefore, PEGDA was used as a model ink to illustrate the droplet formation process and served as an initial proof of concept to prepare UV cured microspheres using piezoelectric inkjet printing.

4.3.1.1. Optimal Solution Ratio of Isopropanol in Deionised Water

In order to test the usability of deionised water, isopropanol and a mixture of both solvents as a collecting fluid, two different inks (Solsys EMD6415, PEGDA250-DMPA) were pipetted from above into a glass beaker filled with isopropanol in deionised water (IPA/DIW) with varied weight percentages. Both inks shared spreading of the ink at low IPA concentrations whereas sinking followed by immediate dissolution of the pipetted drop was observed at high IPA concentrations. Droplets were only formed in the transition range of 13-23 wt% and 15-20 wt% IPA/DIW in case of Solsys EMD6415 and PEGDA250-DMPA, respectively. These results, which are described in more detail in Appendix E.1, led to the usage of 17 wt% IPA/DIW as a test collecting fluid in the manual pipetting experiments.

4.3.1.2. MANUAL PIPETTING EXPERIMENTS

Manual pipetting experiments were performed in order to test for suitable monomers that can be employed in a high throughput printing scheme. Due to similarities between pipetting and printing, it can be assumed that these monomers can be directly transferred to piezoelectric inkjet printing to generate a combinatorial particle library.

Manual pipetting of monomer solutions into collecting fluids was transferred into a glovebox with reduced oxygen atmosphere (argon, O_2 concentration: <500 ppm) after observing 69.2% of the inks incapable of generating particles in air. 55.4% of monomers, however, were able to form particles under argon atmosphere. These succeeding monomers with their abbreviations and chemical structures are listed in Figure 4.9. The full list of the 56 tested monomers with their performance in air and under argon atmosphere is outlined in Appendix F.

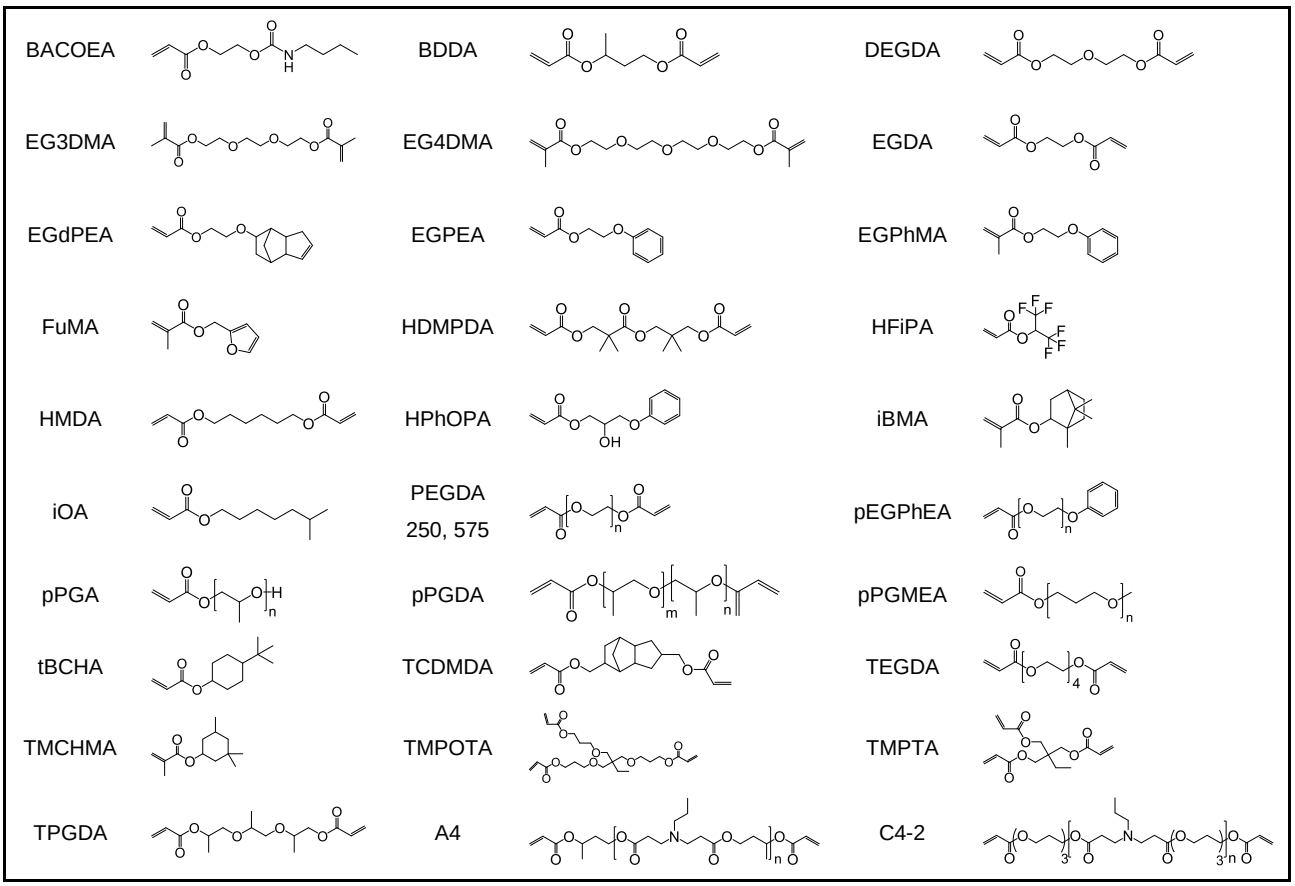


Figure 4.9: (Meth)acrylates capable of forming particles when pipetting a small volume (5 µl) into 17 wt% IPA/DIW under argon atmosphere.

The reason for obtaining more particles under reduced oxygen atmosphere is that oxygen acts as an inhibitor for the polymerisation by quenching free radicals. However, despite changing to a reduced oxygen atmosphere, some monomer solutions still did not lead to particles independent of the degree of hydrophilicity of the collecting fluid. The inability of some monomers to form particles is explained by an insufficiently high

polymerisation rate which will be discussed in Section 4.3.2. Furthermore, forming particles in a fluid requires also an appropriate combination of density, surface tension, viscosity and solubility.

Spherical particles are presented in Figure 4.10, which were the results of pipetting 1,6-hexanediol diacrylate (HMDA)-DMPA and tri(ethylene glycol) dimethacrylate (EG3DMA)-DMPA from above and below 17 wt% IPA/DIW under argon atmosphere.

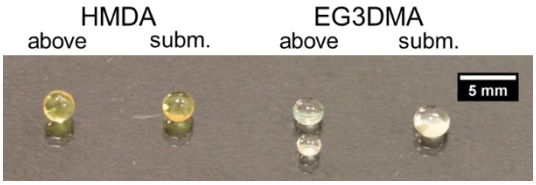


Figure 4.10: Image showing spherical particles on a glass slide. These particles were obtained by manually pipetting 5 µl of the monomer solutions, HMDA and EG3DMA with 1 wt% DMPA each, from above and below 17 wt% IPA/DIW under argon atmosphere.

The results showed that there is no significant difference between pipetting above and below the collecting fluid. High speed footage of pipetting an ink, in this case PEGDA250-DETX-EDB, into deionised water, 17 wt% IPA/DIW and 1-octanol confirmed the same outcome (Appendix E.2). However, the monomer EG3DMA dispensed from above the collecting fluid resulted in two particles. This might have happened due to separation at the interface.

4.3.2. Characterisation of Photopolymerisation Kinetics

The curing kinetics of monomer solutions play a significant role for successful particle formation, as already mentioned in Section 4.3.1.2. Free radical polymerisation rates of (meth)acrylates need to be sufficiently high. Otherwise, the monomer solution drop loses its spherical shape or dissolves in the collecting fluid in the case of sufficient miscibility. Furthermore, not fully crosslinked particles can affect the biological response because radicals trapped inside the particles leak out, destabilising bacterial membranes [250]. In this subchapter, the photopolymerisation reactivity of various commercially available (meth)acrylates is discussed based on data gathered by Photo-DSC.

4.3.2.1. Monitoring of Radiation Curing by Photo-DSC

In this study, the free radical polymerisation rates were investigated for 23 different monomer solutions in order to probe the significance of curing kinetics on successful microparticle formation. The results obtained by applying photo-DSC, however, cannot be directly correlated to the actual inkjet printing because the UV intensity (10 mW/cm^2) and the wavelengths (250-450 nm) of the DSC do not fully match the UV intensity (~6000 mW/cm^2) and wavelength (365 nm) of the Dimatix printer, respectively. Despite these limitations, this study provides a comparison of the reactivity between the monomers and, hence, explains why some monomers are incapable of producing particles.

Exothermic Heat Flow versus Time

Free radical photopolymerisation reactions are exothermic which means that heat is generated during the experiment. The entire heat released is attributed to the monomer acrylate, methacrylate or acrylamide C=C bond opening [251,252]. Therefore, by measuring the exothermic heat flow, information relating to polymerisation kinetics can be determined. Herein, the heat flow of 23 monomer solutions was measured. Data, displaying the heat flow normalised to sample weight versus time, is shown for a small selection of seven chemically similar monomers in Figure 4.11. These monomers differ in the composition of repeat unit, chain length, number of double bonds and acrylate/methacrylate functional groups. Therefore, the effect of these alterations on the exothermic heat generated during polymerisation is pointed at. Although each experiment was conducted for 360 s, data is only shown up to 180 s because the amount of heat released after that point was below 1% and not critical for this analysis.

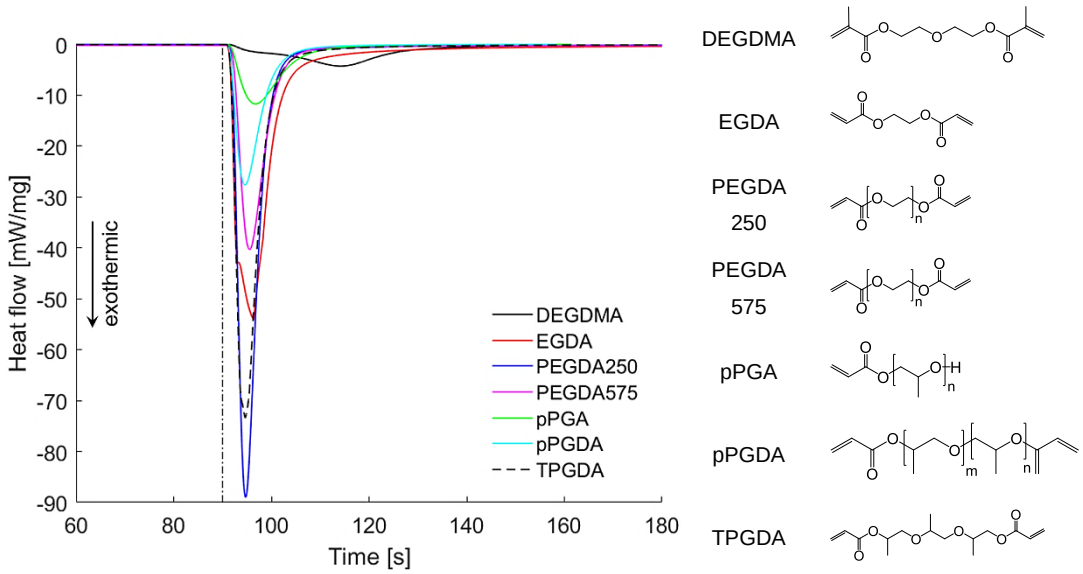


Figure 4.11: Normalised heat flow is plotted against time for seven chemically similar monomers (chemical structures shown right). The samples were exposed to UV light for 180 s starting at 90 s (dash-dot line).

The majority of the monomer solutions, which are displayed in Figure 4.11, except di(ethylene glycol) dimethacrylate (DEGDMA)-DMPA, succeeded in particulate formation. Comparing the heat flow curves, it can be discerned that the monomer DEGDMA released less heat during photopolymerisation coupled with a shift in time for the peak maximum. This is shown in Table 4.4, which tabulates the heat released and time of maximum heat flow.

Table 4.4: Amount of heat released during photopolymerisation and time at which the peak maximum occurred are listed for seven chemically similar monomers.

Monomer	Heat released [mJ]	Peak [s]	Particle formation
DEGDMA	-123.2	114	unsuccessful
EGDA	-519.6	96	successful
PEGDA250	-462.7	95	successful
PEGDA575	-328.9	96	successful
pPGA	-114.7	97	successful
pPGDA	-163.6	95	successful
TPGDA	-428.7	95	successful

This delayed polymerisation is explained by the greater steric hindrance to polymerisation in the case of methacrylates. Methacrylates form tertiary radicals whereas acrylates generate secondary radicals in a free radical polymerisation. Tertiary radicals are more stable resulting in lower reactivity.

Polymerisation Rate versus Time

Due to the fact that polymerisation rate is one of the parameters affecting the feasibility to produce particles, the curing rates of 23 monomers are calculated and compared

with each other. The photopolymerisation rate (R_P) is determined from the measured heat flow by the following equation (Eq. 4.2):

$$R_P = \frac{dH}{dt} * \frac{1}{n * \Delta H_P * m} \qquad \text{Eq. 4.2}$$

where dH/dt is the heat flow measured by the DSC, n is the number of C=C bonds per monomer, ΔH_P is the standard enthalpy of reaction for the C=C double bond (acrylate: 86.2 kJ/mol [253], methacrylate: 54.81 kJ/mol [254,255], acrylamide: 81.6 kJ/mol [256]) and m is the moles of the monomer in the sample. Figure 4.12 shows the curing rates as a function of time for the 7 chemically similar compounds. The rise and fall in the polymerisation rates, which is seen in all monomers, outline the auto-acceleration and auto-deceleration phases of the reaction, respectively. The time at which the highest polymerisation rate was observed is referred as the 'gel-point' [233]. At this point, a loose network of polymers is formed and, hence, a significant change in the viscosity can be observed. As seen from Figure 4.12, the monomer solution DEGDMA-DMPA exhibited its gel-point approximately 19 s later compared to the other inks. In addition, the polymerisation rate of DEGDMA-DMPA was significant lower (93.0%) compared to PEGDA575-DMPA which exhibited the highest curing rate among the seven chemically similar compounds.

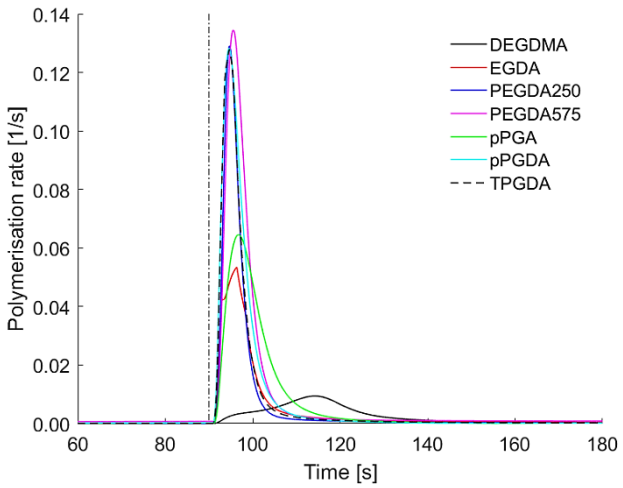


Figure 4.12: Photopolymerisation rates are displayed against time for seven chemically similar inks. The exposure to UV light occurred for 180 s starting at 90 s (dash-dot line).

The effect of chain length and number of acrylate C=C double bonds on the photopolymerisation rates is presented in Figure 4.13 a). For the monomers with varying chain lengths, the chain length does not affect the curing rates as seen from comparing the peaks of tri(propylene glycol) diacrylate (TPGDA) and poly(propylene glycol) diacrylate (pPGDA). However, the number of C=C double bonds influences the curing kinetics significantly. Poly(propylene glycol) acrylate (pPGA), which exhibit only

one acrylate, polymerised 49.7% slower than pPGDA having a diacrylate. The reason for this is that the overall effectiveness of UV initiated polymerisation can be assessed by the number of C=C double bonds polymerised per photon absorbed also known as quantum yield [257]. Therefore, the more acrylate double bonds available in a compound, the higher is the chance for a free radical to attack which results in a faster propagation of the polymer chain.

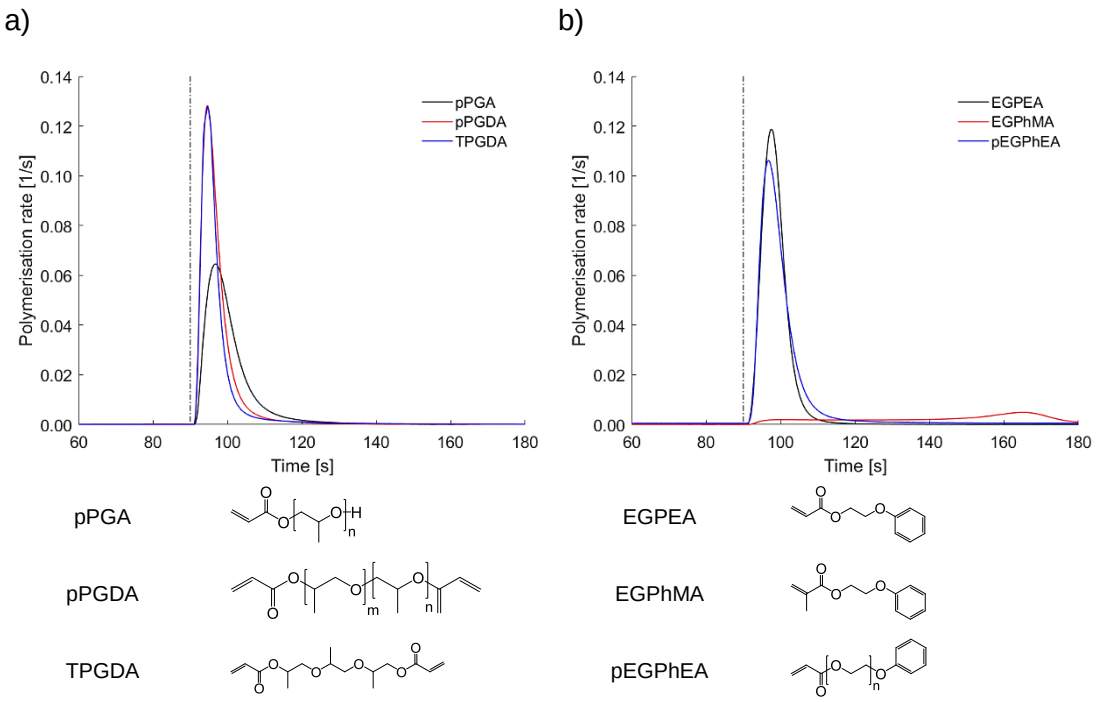


Figure 4.13: The effect of chain length and number of C=C double bonds on polymerisation rates are shown. The chemical structures of the monomers are shown at the bottom. The dash-dot line at 90 s represents the starting point of UV exposure.

Figure 4.13 b) shows the polymerisation rates of three monomer solutions that differ in chain length and functional group (acrylate, methacrylate). Comparing the results of ethylene glycol phenyl ether acrylate (EGPEA) and poly(ethylene glycol) phenyl ether acrylate (pEGPhEA), pEGPhEA revealed a 10.6% lower polymerisation rate. This is explained by deceleration of polymerisation due to steric hindrance. Exchanging the acrylate C=C double bond by a methacrylate, the monomer solution ethylene glycol phenyl ether methacrylate (EGPhMA) showed a significant decrease in polymerisation rate of 95.9% and 95.4% compared to EGPEA and pEGPhEA, respectively. These results confirm the findings outlined in Figure 4.12, that more stable radicals result in lower curing rates.

Monomer Conversion

The extent of polymerisation of a monomer solution can be calculated since the acrylate/methacrylate/acrylamide C=C bond breakages are the only source releasing

heat during the reaction process. Therefore, the monomer conversion in percentage (α_c) was calculated by summing up the exothermic heat flow up to a time t and dividing by the expected heat of polymerisation (Eq. 4.3):

$$\alpha_c(t) = \frac{\Delta H_{sample}(t)}{\Delta H_P * m} * 100 \qquad \text{Eq. 4.3}$$

The conversion was calculated for all 23 monomers both at the 'gel-point' and at 360 s, the end of the experiment. Comparisons of monomer conversions coupled with the times between onset and peak can be used to determine differences in speed of polymerisation. Consequently, it was assumed that a low conversion at the gel-point and a large time difference between onset and peak would not succeed in particle formation. The reason for this is that the printed ink drops dissolve or lose their shape in the collecting fluid in the meantime. Inks, that are capable of forming microspheres, are depicted in Figure 4.14 and Figure 4.15 as solid symbols (e.g. ■) whereas inks, which did not lead to particles, are displayed as hollow symbols (e.g. □). The majority of the inks (93.8%), which resulted in uniform particles, exhibited the maximal curing rate between 0 to 7.2 s after exposure to UV light and revealed a monomer conversion at the gel-point of 15.5-37.1% (Figure 4.14). In contrast, HDMPDA and BACOEA, which are positioned in this specified region, were not able to fabricate particles. Surprisingly though, the ink EGPhMA, which was polymerised to 16.8% at 72.8 s after turning on the UV light, generated microspheres.

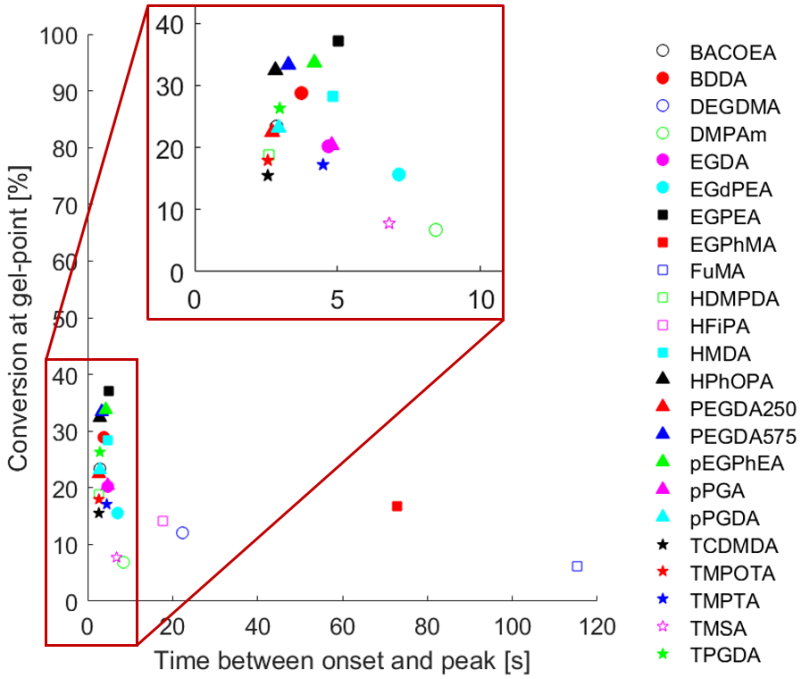


Figure 4.14: Conversion of monomer (%) was calculated for 23 monomers at the gel-point as a function of time between onset and peak of maximal curing rate. The inks capable of forming particles are illustrated with solid symbols (e.g. ■) and the ones that did not succeed with hollow symbols (e.g. □).

Comparing the conversion for each monomer from the gel-point (Figure 4.14) to the end of the experiment (Figure 4.15), it can be seen that all monomers exhibited an increase in conversion. Most notably, the monomers highlighted in the red boxes in both figures showed the biggest change in conversion from the gel-point (6.8-37.1%) to the end of experiment (45.3–97.6%). A conversion of 100% can hardly be reached by any monomer due to the formation of the crosslink network and subsequent gelification. This leads to an increase in viscosity and hence, reduces the segmental mobility of both the growing polymer chain and unreacted functional double bonds [258]. Consequently, this restriction in mobility makes it harder for the propagating polymer chains and unreacted monomers to react with each other terminating the reaction.

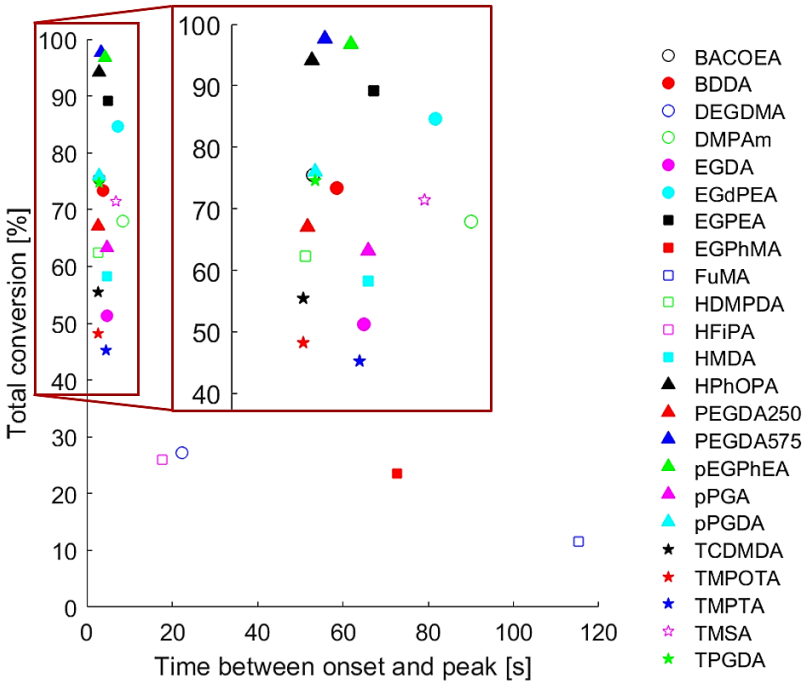


Figure 4.15: Total conversion in percentage was computed for 23 monomers as a function of time to reach maximal curing rate. The inks succeeding in particulate formulation are displayed with solid symbols (e.g. ■) and the ones that did not form spheres with hollow symbols (e.g. □).

The ink EGPhMA extended its degree of polymerisation from the gel-point (163 s) with 16.8% to the end of the measurement (360 s) with 23.5%. Both the small increase and the eventually low conversion indicate that EGPhMA did not fully cure. This finding was confirmed by the particles being in a soft and sticky state.

From the data presented, it can be seen that the rate of polymerisation affects the particulate formation process. Despite that, the interplay of parameters such as viscosity, surface tension and solubility are more significant for producing particles successfully than the individual parameters themselves.

4.3.3. Generation of Particles using Inkjet Printing

In this subchapter, photopolymerisation is combined with piezoelectric inkjet printing with the intention of forming (meth)acrylate based microspheres with precisely controllable size distribution. Initially, the promising monomer solutions received from the manual pipetting experiments were transferred to the Dimatix printer and tested for their ability to produce microspheres. Afterwards, diverse parameters such as additives, printing velocity, photoinitiator concentration were varied and examined with focus on improvement on particulate formation. Finally, printing in air is presented as an alternative route to produce microparticles without using any solvents and surfactants. A detailed characterisation of these particles is provided in Chapter 5.

4.3.3.1. Comparison with the Manual Pipetting Experiment

Promising photocrosslinkable inks obtained from manual pipetting under reduced oxygen atmosphere were inkjet printed into three collecting fluids. As seen from Figure 4.16, microspheres with a diameter in the range of 8.5-23.5 microns were only obtained when printing PEGDA250-DMPA into 17 wt% IPA/DIW. In case of deionised water and hexane as collecting fluids, polymer agglomerations were found at the bottom of the well. Moreover, hexane was an impractical collecting fluid due its rapid evaporation. Therefore, high consumption of hexane would be required in case of high throughput particle fabrication.

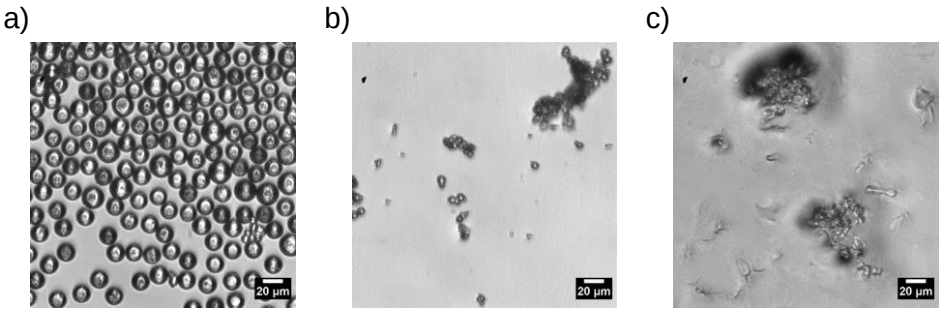


Figure 4.16: Brightfield micrographs acquired after printing PEGDA250-DMPA into a) 17 wt% IPA/DIW, b) deionised water and c) hexane. Scale bars are 20 µm.

The inkjet printed polyPEGDA250 particles were uniform and exhibited a smooth surface containing some pores (Figure 4.17 a)). However, particles trapped in a polymeric network were also found as depicted in Figure 4.17 b). A few smaller microspheres were also present, which were likely formed by breaking up of the droplets while touching the liquid-gas interface. Satellites, which are usually

significantly smaller than the particles, were also observed in the printing experiment (Figure 4.16 b)).

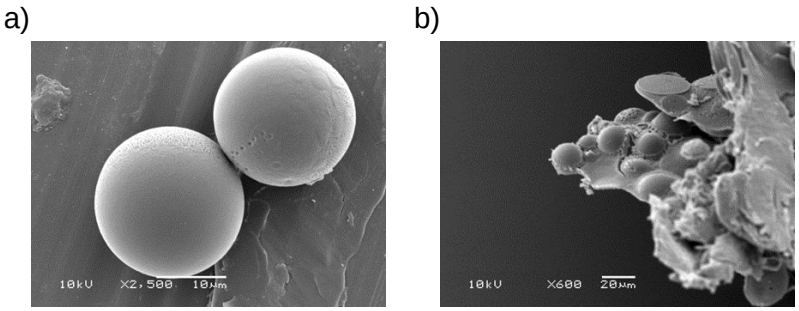


Figure 4.17: SEM pictures taken after jetting PEGDA250-DMPA into 17 wt% IPA/DIW under reduced oxygen atmosphere: a) particles exhibiting few surface pores, b) polymeric network entrapping microspheres.

Spheres trapped in a polymeric network and pores might have resulted from partially cured particles. Incomplete curing could have happened if the remaining oxygen in the nitrogen atmosphere or in the collecting fluid was sufficient to inhibit the polymerisation. Consequently, it was postulated that the interior of the particles cured fully whereas a liquid layer remained on the particle surfaces. These liquid layers caused polymeric networks by coalescence of uncured monomers. A visualisation of this supposition is given in Figure 4.18.

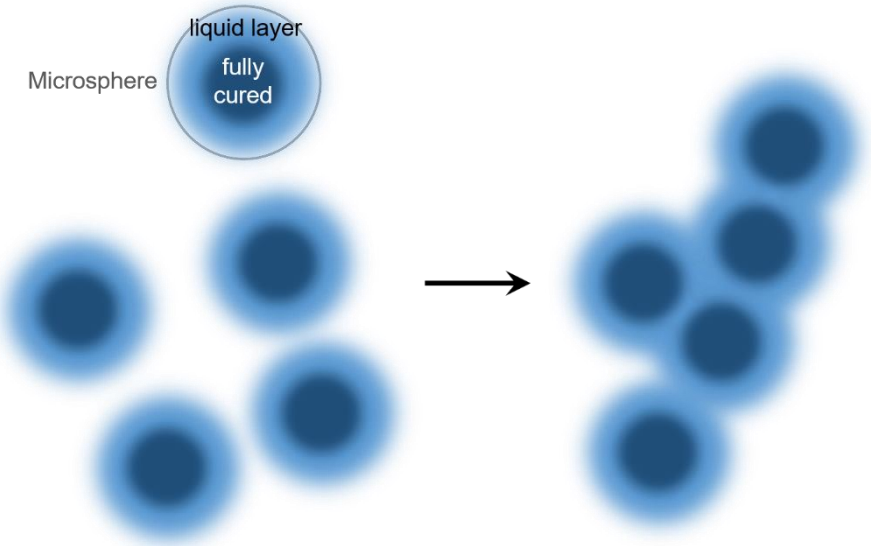


Figure 4.18: Schematic representing the proposed process of multiple particle coalescence due to incomplete cured outer layers of particles.

The interior of the polyPEGDA250 particles was analysed by slicing the microspheres in half using FIB. The inkjet printed particles were solid throughout as seen in Figure 4.19. Therefore, the results suggest that neither air nor collecting fluid was trapped inside the particles.



Figure 4.19: FIB images showing an inkjet printed polyPEGDA250 particle: a) before sectioning, b) after sectioning top view, c) after sectioning side view. Scale bars are 2 µm.

After repeatedly obtaining spherical microparticles with the monomer PEGDA250, all monomers, presented in Figure 4.6, were tested for their ability to form particles using the Dimatix printer. 24 out of 34 monomers (71%) formed particles in 17 wt% IPA/DIW. Few particles were observed in deionised water whereas none of the monomers succeeded in producing particles in hexane. The monomers capable of generating particles using the Dimatix printer are shown in Figure 4.20. Besides free-flowing particles, however, these monomers also resulted in polymer agglomerations which reduced their usability. Furthermore, four out of these monomers, namely tetra(ethylene glycol) dimethacrylate (EG4DMA), tri(ethylene glycol) dimethacrylate (EG3DMA), di(ethylene glycol) dimethacrylate (DEGDMA) and furfuryl methacrylate (FuMA), yielded only some particles with high amounts of agglomerations. Attempts to improve their performance by changing parameters like adding a surfactant and modifying the monomer solution preparation will be discussed in Section 4.3.3.3.

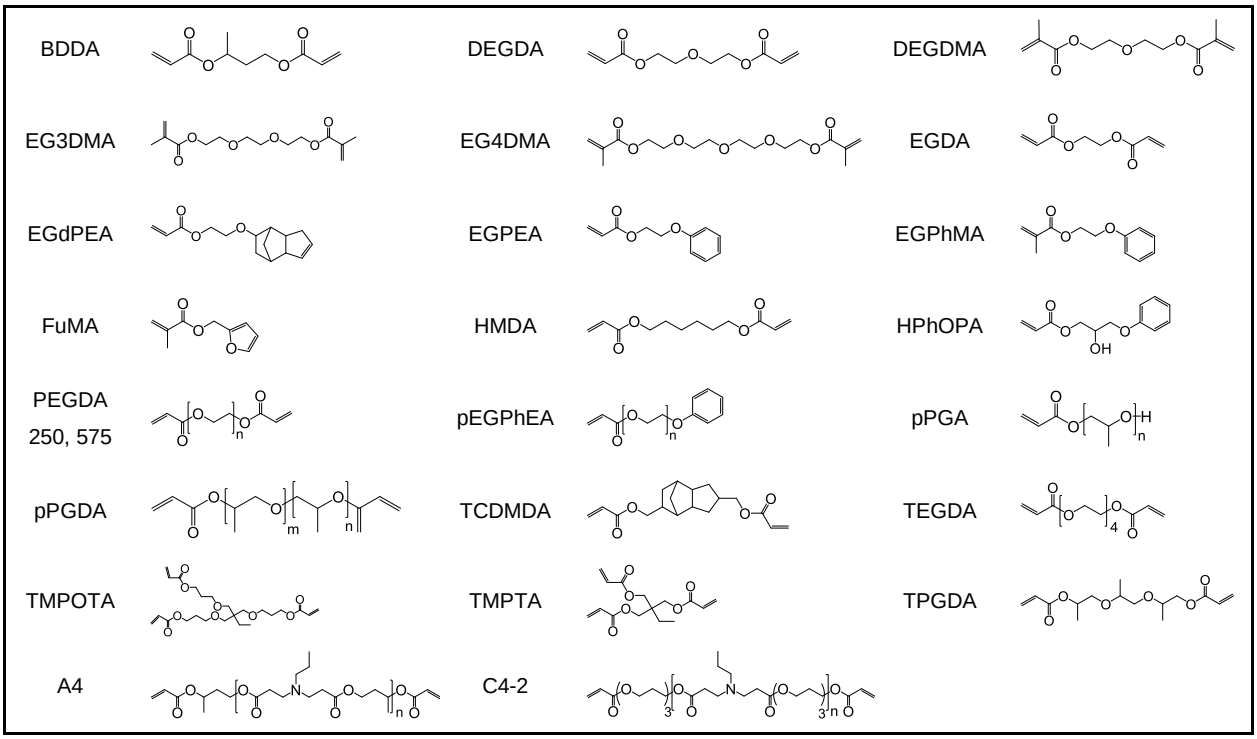


Figure 4.20: Monomers capable of forming microspheres, independent on the actual yield, using the Dimatix printer.

Jetting monomer solutions into collecting fluids using a piezoelectric inkjet printer reflected the observations made in the manual pipetting experiment to a large extent. Reducing the volume from pipetting (µl) to printing (pl), made it harder to fully understand the parameters affecting the particle formation. The reason is that factors related to the surface such as surface energy and surface charge become more important the smaller the volume and consequently the smaller the particles.

4.3.3.2. Interdependency Analysis of Monomers and Collecting Fluids

Droplet formation into collecting fluids was affected by a number of parameters which are individually described below. First of all, the density of the monomer solution should ideally be in the same order as the collecting fluid (as mentioned in Section 4.3.1.1). If the monomer solution has a lower density, the droplet will 'swim' at the surface of the collecting fluid, resulting in elliptic shapes due to unbalanced intermolecular forces. However, in the case of a higher density, the monomer drop will sink and eventually form a hemisphere at the bottom of the substrate, assuming that the droplet has not cured beforehand. Viscosity and surface tension determine the performance of printing and hence, play an important role for successful droplet formation. In the case of the Dimatix printer, optimal performances are achieved with inks exhibiting viscosities and surface tensions in the range of 10-12 cP and 28-33 mN/m, respectively, at jetting temperatures. Viscosity of the printable fluid, which is a function of the molar mass, can be adjusted by heating the printhead up to 70°C. As a result of heating the monomer solution, a decreased surface tension is normally obtained. Additionally, adding surfactants also modifies the surface tension.

Besides density, surface tension and viscosity, solubility of the monomer solution in the collecting fluid also affects the particle formation outcome. Solubility can be expressed as partition coefficient which defines the ratio of the concentrations of a compound in two immiscible solvents, normally 1-octanol and water, at equilibrium. This coefficient is useful to predict the ability of the printed drop to dissolve in the collecting fluid since the droplets hit the collecting fluid in a negligibly partially cured state. Therefore, the photopolymerisation kinetics of the inks, including the curing rate and the corresponding monomer conversion, are the main crucial factors influencing the particle fabrication. As described in Section 4.3.2, the polymerisation rate is affected by the number of functional C=C double bonds, functional groups

(methacrylate / acrylate / acrylamide), chain length and also bulkiness of the monomer (steric hindrance).

Last but not least, the printing height, which defines the distance between the nozzle plate and the well plate, particularly the collecting fluid, also determines the success of particle formation. An enlarged distance promotes curing to a larger extent before hitting the collecting fluid. As a consequence, less deformation and reduced numbers of smaller particles and polymeric agglomerations are expected in case the droplets are almost completely polymerised. On the contrary, if the droplets are not sufficiently cured, the particle shapes will be distorted on a bigger scale as a result of the more severe impact at the gas-liquid interface. Furthermore, ejected droplets spread more with distance which increases the likelihood of not collecting them.

4.3.3.3. Effect of Different Parameters on Particle Formation

In order to improve the output of the microspheres, different parameter scenarios were tested in order to compare relative improvements to microsphere formation.

Addition of a Fluorescent Dye to the Monomer Solution

Rhodamine B (0.1 wt%) was co-dissolved into the PEGDA250-DMPA solution in order to investigate the effect of a fluorescent dye on particle formation as well as to improve the droplet visualisation. Optical microscopy revealed that rhodamine B did not influence the size or the shape of the microspheres. However, an improved visualisation was achieved since the contrast between the particles and collecting fluid was enhanced. By analysing the particles under SEM (Figure 4.21), both polymeric agglomerations enclosing particles and free-flowing particles were visualised as already observed with the undyed particles. However, the amount of surface pores increased vastly on the rhodamine B containing spheres as illustrated in Figure 4.21 b). Moreover, some particles showed evidence of being hollow inside whereas the polyPEGDA250 particles without additives proved to be homogeneous throughout.

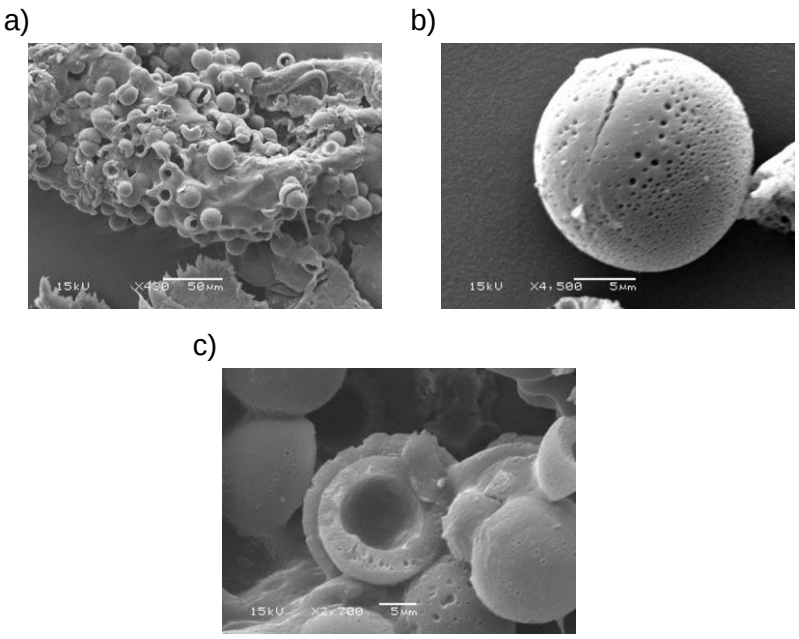


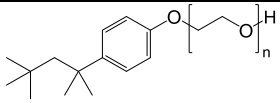
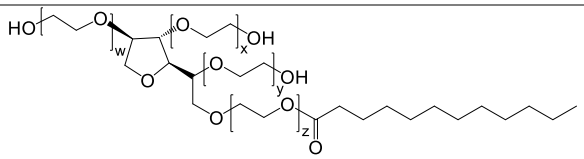
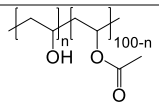
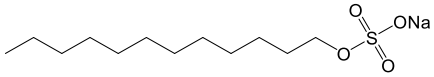
Figure 4.21: SEM images of polyPEGDA250 particles containing rhodamine B: a) polymer network capturing particles, b) free-flowing particle showing increased surface porosity, c) fractured particle revealing a hollow structure.

Adding a fluorescent dye only improved the visualisation to a small extent in the optical brightfield microscopy while simultaneously resulting in increased surface porosity and hollow particles. Consequently, rhodamine B was not incorporated into the standard conditions for printing from here onwards.

Modification of the Collecting Fluid using Different Surfactants

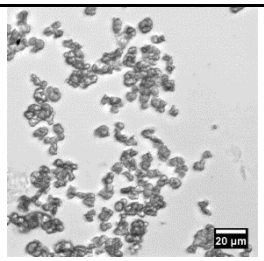
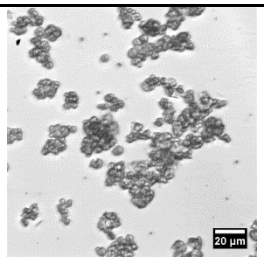
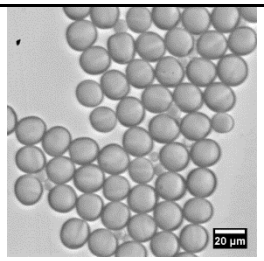
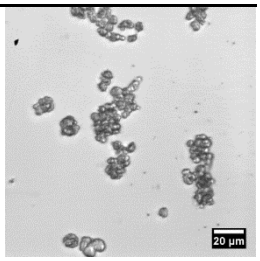
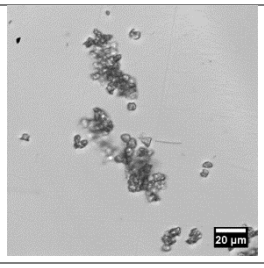
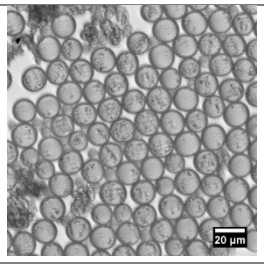
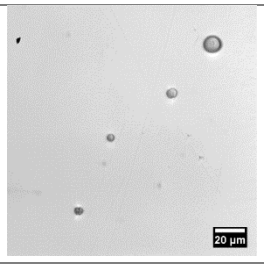
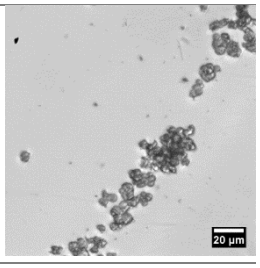
Different surfactants were examined for improvement in droplet formation by dissolving them into the collecting fluid, 17 wt% IPA/DIW. Surfactants are well known for stabilising droplets and hence, preventing them from coagulation. Four different surfactants with hydrophile-lipophile balance (HLB) values larger than 10 were chosen. These surfactants, which reveal affinity for water, are outlined with their chemical structure and HLB value in Table 4.5.

Table 4.5: Summary of the four different surfactants, which were dissolved into the collecting fluid (17 wt% IPA/DIW), with their chemical structure and HLB value.

Surfactant	Structure	HLB
Triton X-100		13.5 [259]
Tween 20		16.7 [259]
PVA		18 [260]
SDS		40 [261]

Printing the monomers 1,3-butanediol diacrylate (BDDA) and poly(ethylene glycol) phenyl ether acrylate (pEGPhEA) into collecting fluids supplemented with PVA and also Tween 20 showed no successful particle formation. In both cases, polymer agglomerations were observed as illustrated in Table 4.6. Particles were obtained when ejecting BDDA- and pEGPhEA-DMPA into the collecting fluid containing Triton X-100 and sodium dodecyl sulfate (SDS), respectively. However, as seen from Table 4.6, the particle yield, shape and topography of the particles were not optimal; polyBDDA particles were aspherical in shape whereas polypEGPhEA microspheres presented dimples on the surface.

Table 4.6: Brightfield images showing the results of printing BDDA- and pEGPhEA-DMPA into 17 wt% IPA/DIW supplemented with 0.1 wt% surfactant (PVA, SDS, Triton X-100 and Tween 20). Scale bars are 20 µm.

Monomer	PVA	SDS	Triton X-100	Tween 20
BDDA				
pEGPhEA				

The dimples in the microspheres, presented in Figure 4.22, might arise from dissolving the particle material when it is not fully cured.

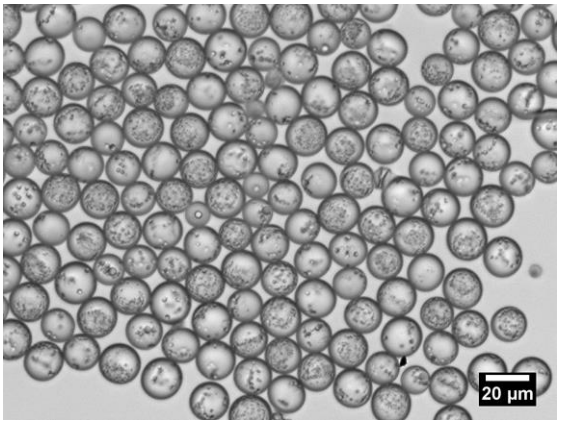


Figure 4.22: Microparticles with dimpled surfaces were observed when printing pEGPhEA-DMPA into 0.1 wt% SDS dissolved in 17 wt% IPA/DIW.

By testing all monomers capable of forming particles using the Dimatix printer, as outlined in Figure 4.20, the majority of the monomer solutions (17 out of 24) performed better when dissolving 0.1 wt% Triton X-100 into 17 wt% IPA/DIW. One monomer, pEGPhEA, showed improved results when applying SDS as a surfactant. Moreover, the microspheres generated using the monomers PEGDA250 and PEGDA575 showed quality reduction when adding surfactants. The performance of the monomers EG4DMA, EG3DMA, DEGDMA and FuMA, which was mentioned in Section 4.3.3.1 to yield few particles with mostly polymer agglomerations, did not improve independent of the surfactant added.

Adding the surfactant Triton X-100 to the collecting fluid showed improved particle formation with the majority of inks. Therefore, Triton X-100 was implemented into the standard printing conditions. A surface chemistry analysis of the inkjet printed particles was performed at a later point indicating residual surfactant at the surface (Appendix G).

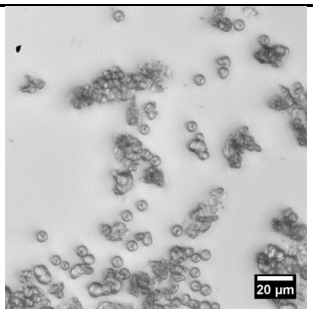
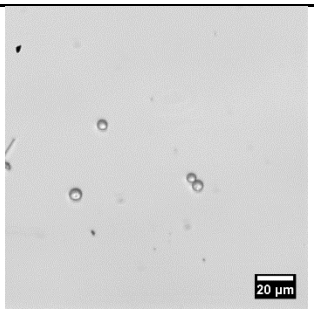
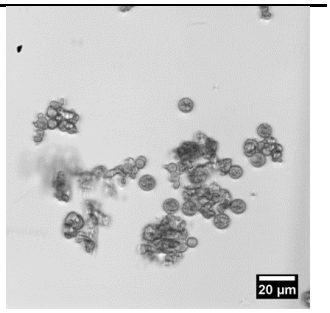
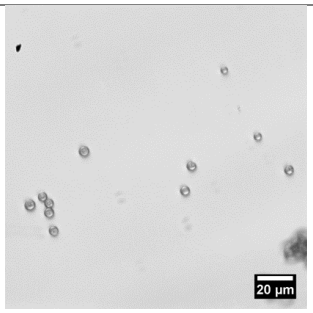
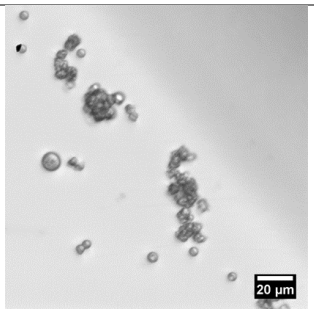
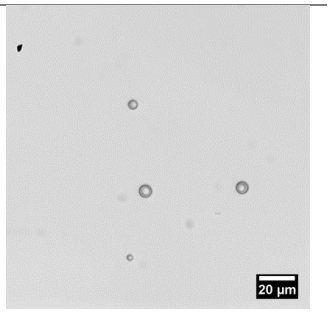
FREEZE-PUMP-THAW VERSUS PURGING AN INK

A possible reason for weak performance in droplet generation is that the monomer solutions still contain oxygen either from ambient air or oxygen dissolved in raw materials. Oxygen is able to inhibit the polymerisation reaction through all polymerisation stages. In this way, even small amounts of oxygen can have a considerable effect on curing. Herein, the monomers EG4DMA, EG3DMA and DEGDMA were examined for improved performance in droplet fabrication by comparing two different oxygen removal methods; substitution by an inert gas (standard) and freeze-pump-thaw cycling.

The monomer solutions, of which the reactive oxygen gas was removed by two different ways, were printed into three collecting fluids: 17wt% IPA/DIW, 17wt%

IPA/DIW with 0.1 wt% SDS and 17wt% IPA/DIW with 0.1 wt% Triton X-100. In Table 4.7, the results of dispensing ink droplets into 17 wt% IPA/DIW supplemented with Triton X-100 are presented, using either purging with nitrogen gas or freeze-pump-thaw cycling. It can be seen that only a few particles with mostly polymer agglomerations were obtained independent on the degassing procedure. However, fewer agglomerations were found when the monomer solutions were degassed using the freeze-pump-thaw cycles. Furthermore, the observed particles were 4-7 µm in diameter which is more than three times smaller than normally produced (~20-23 µm). This finding indicates that the curing rates of the monomer solutions are most likely not sufficiently high as already shown for DEGDMA in Section 4.3.2. Consequently, most of the printed droplets dissolve in the collecting fluid prior to complete polymerisation. This also explains the small number of free-flowing particles found in the wells. Also, the length of time to reach a loose network of polymer (gel-point) is extended enabling the drops to move around and coalescence resulting in polymeric agglomerations.

Table 4.7: Brightfield images were taken after printing three different inks (EG4DMA-, EG3DMA- and DEGDMA-DMPA) into 0.1 wt% Triton X-100 dissolved in 17 wt% IPA/DIW. Prior to printing, the monomer solutions were degassed by either bubbling with nitrogen gas or by freeze-pump-thaw cycling.

Methods	EG4DMA-DMPA	EG3DMA-DMPA	DEGDMA-DMPA
Purging with nitrogen gas			
Freeze-pump-thaw cycling			

The tested monomers were excluded from the actual library of (meth)acrylates since the efficiency could not be enhanced despite efficient removal of the reactive oxygen gas from the monomer solutions. In addition, furfuryl methacrylate (FuMA) was also excluded due to insufficient photopolymerisation rate as already observed during photo-DSC measurements (Section 4.3.2). By doing this, the updated library consisting of 20 particle forming monomers is shown in Figure 4.23.

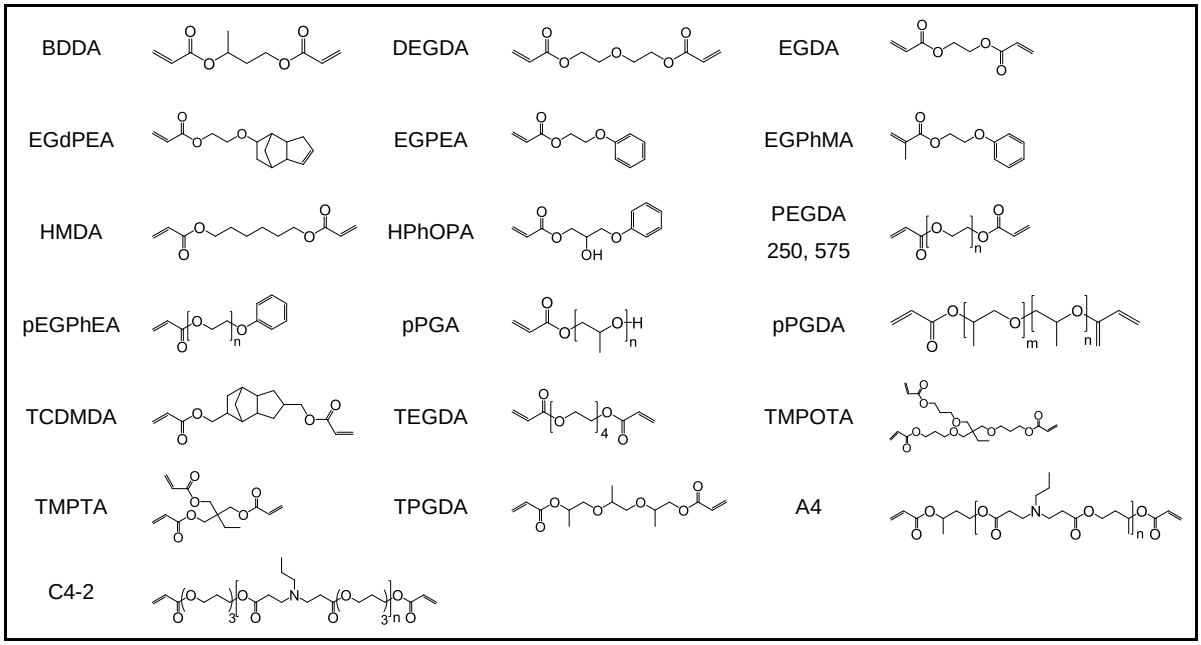
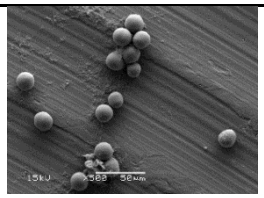
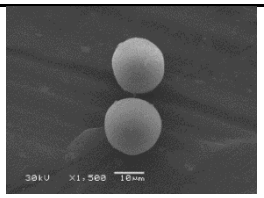
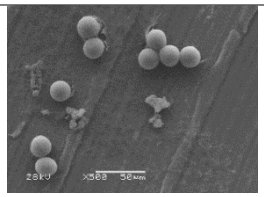
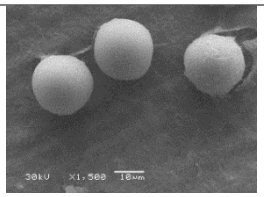
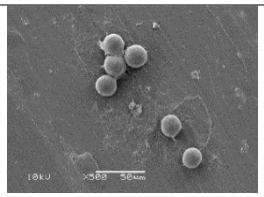
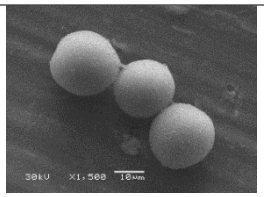
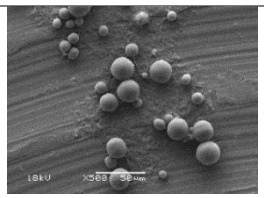
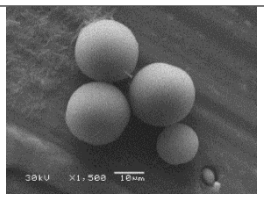
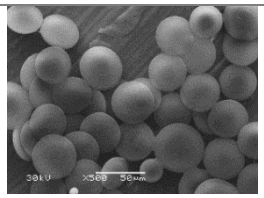
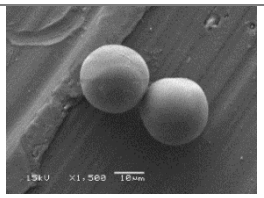


Figure 4.23: The updated library of (meth)acrylates capable of producing microparticles using the Dimatix printer.

VARYING THE PRINTING VELOCITY

The effect of changing the printing velocity on particle formation was studied by printing the monomer solution tricyclo[5.2.1.$0^{2,6}$]decanedimethanol diacrylate (TCDMDA) containing 1 wt% DMPA into the collecting fluid 17 wt% IPA/DIW concentrated with Triton X-100 (0.1 wt%). The printing velocity was adjusted by changing the voltage applied to a nozzle whilst checking the distance travelled at a strobe delay of 100 µm using the Drop Watcher camera. By increasing the voltage to obtain greater printing speed, the ejected drop volume decreases and hence, also the final particle diameter. SEM images of particles printed at 2, 4, 6, 8 and 10 m/s were taken and depicted in Table 4.8.

Table 4.8: SEM images showing polyTCDMDA particles ejected at a velocity of 2, 4, 6, 8 and 10 m/s. The images were taken at a magnification of 500x (left, scale bar: 50 µm) and 1500x (right, scale bar: 10 µm), respectively.

Printing velocity [m/s]	Image (500x)	Image (1500x)
2		
4		
6		
8		
10		

Analysing the particles dispensed at different speeds revealed that monodisperse particles with a spherical shape were only obtained up to a printing velocity of 6 m/s. Ejecting droplets at speeds exceeding 6 m/s resulted in higher asphericity with satellite drops. At a rate of 10 m/s, three separate particle shapes were observed: spheres, flattened shapes up to hemispheres and disc-like shapes. Flattened particles, hemispheres and disc-like shapes are depicted in Figure 4.24.

a) b) c)

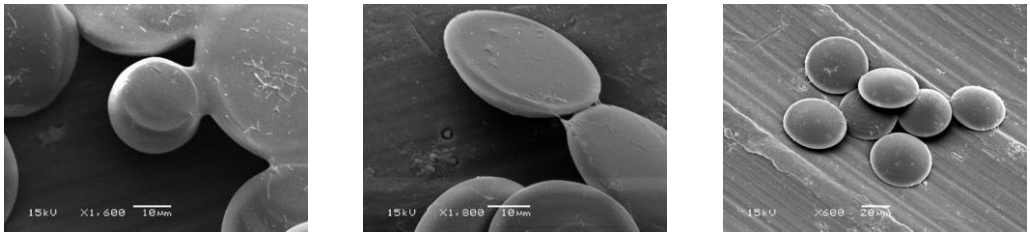


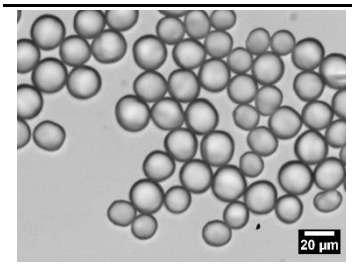
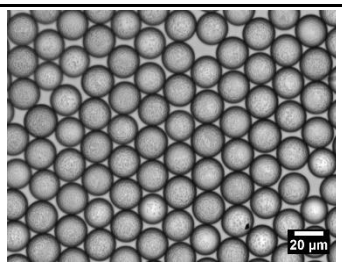
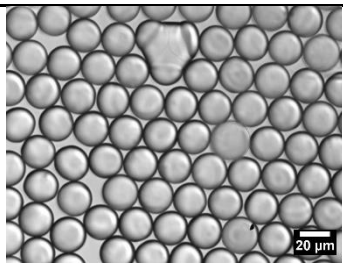
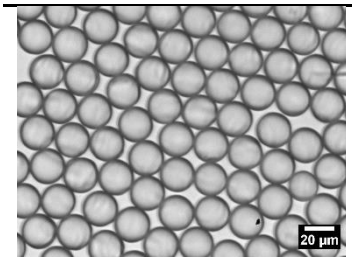
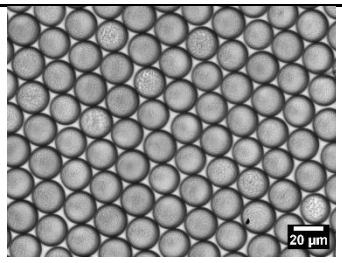
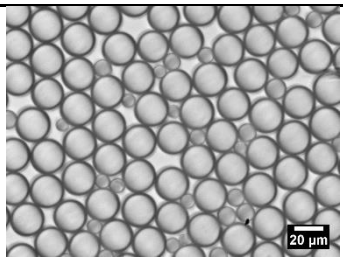
Figure 4.24: SEM images of particle shapes observed at a printing velocity of 10 m/s: a) flattened particles, b) hemispheres, c) disc-like shapes.

An explanation for obtaining flattened shapes varying towards hemispheres at high velocity is that they become deformed due to the strong impact occurring when entering the collecting fluid. Additionally, it is speculated that the microparticles only fully cured at the bottom of the substrate, thus, resulting in hemispheres. Due to the higher dispensing rates, the droplets in flight were exposed to UV light for a shorter amount of time until reaching both the collecting fluid and the bottom of the substrate. Consequently, the droplets can easily be deformed because they are still in a partially cured state as already ascertained by the curing kinetic studies (Section 4.3.2). Disc-like shapes may occur when droplets float at the interface due to unbalanced intermolecular forces while being polymerised. After performing this experiment, a velocity of 6 m/s was employed for standardised printing of (meth)acrylate based monomer solutions. This printing velocity was selected to achieve the optimum relation between sphericity in shape and production rate.

INCREASED PHOTOINITIATOR CONCENTRATION

Standard (1 wt%) and increased photoinitiator concentrations (3-5 wt%) were dissolved into three different monomers, tricyclo[5.2.1.$0^{2,6}$]decanedimethanol diacrylate (TCDMDA), ethylene glycol dicyclopentenyl ether acrylate (EGdPEA) and trimethylolpropane triacrylate (TMPTA). These prepared monomer solutions were printed into 17 wt% IPA/DIW containing 0.1 wt% Triton X-100 and compared with respect to particle shape, size and yield. Brightfield images of the particles produced are presented in Table 4.9.

Table 4.9: Comparison of microparticles printed with three different inks (TCDMDA, EGdPEA and TMPTA) containing standard (1 wt%) and increased DMPA concentration (3-5 wt%), respectively, into Triton X-100 (0.1 wt%) dissolved in 17 wt% IPA/DIW. Scale bars are 20 µm.

	TCDMDA-DMPA (1 wt%)	**EGdPEA-DMPA (1 wt%)**	**TMPTA-DMPA (1 wt%)**
Standard			
	TCDMDA-DMPA (4 wt%)	**EGdPEA-DMPA (5 wt%)**	**TMPTA-DMPA (3 wt%)**
Increased photoinitiator			

The results revealed that raising the amount of photoinitiator helped to improve the sphericity in case of the monomer TCDMDA due to faster curing. Additionally, the sizes of the microparticles became more monodisperse. However, no significant changes were observed for the monomers EGdPEA and TMPTA. Smaller particles, which are best seen in the image taken for TMPTA-DMPA (3 wt%), occurred independent of the photoinitiator concentration. Such smaller particles are formed by break-up of a ligament formed from the mass of two interacting drops pinching off the remaining portions of the drops [262] or by detachment of liquid when impacting on the surface of the collecting fluid. Therefore, both the stability of jetting and polymerisation kinetics are the critical factors for emerging these secondary drops. Furthermore, it was assumed that a higher concentration of photoinitiator results in faster curing, thus forming less polymeric agglomerations. No significant reduction in polymeric agglomerations, however, was observed in this study. Increasing the photoinitiator concentration can also lead to generation of more free photoinitiating radicals. Consequently, as the polymerisation reaction continues, the free photoinitiating radical concentration keeps increasing while the concentration of the unreacted monomer decreases resulting in augmented termination. This effect can cause a higher number of particles but at smaller sizes. Due to the combination of the vicinity of the particles and high surface contact areas, particles can agglomerate with ease.

Based on the fact that no remarkable improvements were achieved by increasing the amount of photoinitiator, the standard concentration of 1 wt% DMPA was retained for subsequent testing.

4.3.3.4. PRINTING IN AIR

The idea of dispensing a monomer solution into an empty collection substrate in air was tested to explore a route of producing microparticles without using any solvents or surfactants. In this way, the particles could be collected and hence, analysed quickly without the need of washing, filtration and/or centrifugation in advance. Solvent-free production under ambient air would contribute to scale-up of the microparticle fabrication due to reduced costs and production time. Moreover, the particle chemistries would be as prepared without exhibiting contamination induced by surfactants and solvent residues.

The monomer solution containing PEGDA250, photoinitiator DETX and accelerator EDB were printed with a frequency of 1 kHz into an empty petri dish. The ejected

droplets were simultaneously polymerised by exposure to a UV source. The particles collected in the petri dish were analysed using SEM (Figure 4.25).

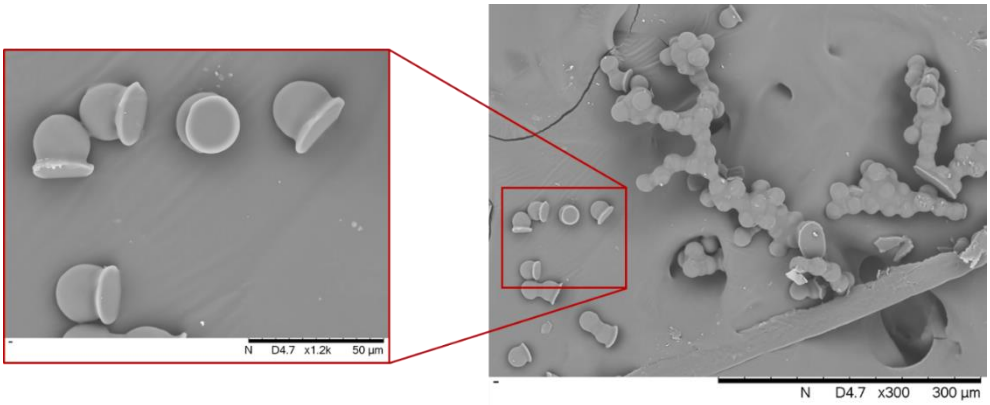


Figure 4.25: SEM images presenting particles obtained from printing PEGDA250-DETX-EDB into an empty petri dish under ambient air. Zoomed image reveals the impacted spherical shape of particles.

SEM analysis revealed that particles with an impacted spherical shape were formed by printing in ambient air. The particles were approximately 25 µm in height and 20 µm in width. The shape is explained by deformation that occurred due to the strong impact of the partially cured drop upon the petri dish. However, there seems to be notably more material in the base than deformation alone would produce. This suggests some particle settling on the surface before complete solidification - possibly aided by favourable surface-monomer wetting. The UV light not only cured the droplets but also blocked the nozzle plate. By inserting a collimated lens as shown in Figure 4.26, the issue of blocking the nozzles was solved but microparticles were no longer obtained. The polymerisation only took place when the droplets fell through the collimated light, which happened in a relatively short time. By employing a fixed working distance between the UV source and the lens to successfully collimate the light, the UV source had to be adjusted further back resulting in a reduced intensity. The UV light intensity is inversely proportional to the square of the distance from the source. Both factors, reduced light intensity and the resulting shorter exposure time, led to incomplete curing.

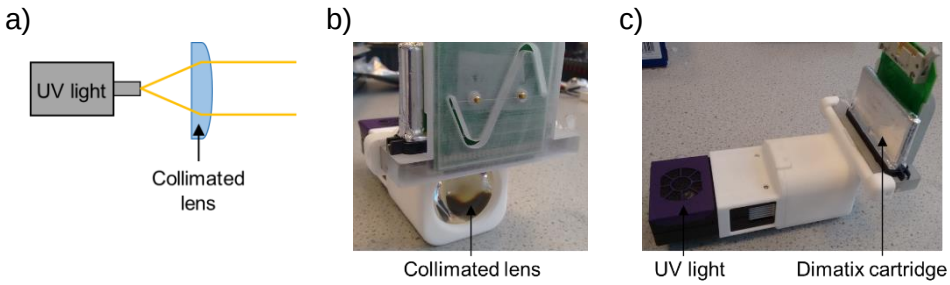


Figure 4.26: Collimating the UV light by inserting a specific lens: a) sketch illustrating how the light will propagate after passing the collimated lens, b) front view showing the collimated lens incorporated into the printing setup, c) side view of the experimental setup.

Obtaining spherical particles in air could be possible by increasing the distance between the Dimatix cartridge and collection substrate combined with exposing the droplets to UV light during the entire flight in consideration of shielding the nozzle plate.

4.3.4. Generation of Particles using Microfluidics

An alternative manufacturing process to inkjet printing, microfluidic particle synthesis, is introduced in this subchapter. First, some results are presented showing the production of homopolymeric microparticles. Following, copolymerised particles were fabricated by applying two different co-polymerisation routes, blending-before and on-chip copolymerisation. These copolymerisation methods were compared by considering pros and cons in Section 4.3.5. In terms of microparticle characteristics, the physical and chemical properties of the microfluidic produced particles are compared with the properties of the inkjet printed particles in Chapter 5.

4.3.4.1. Formation of Homopolymeric Droplets in a T-junction

Monodisperse microparticles were successfully formed from 6 out of 9 tested monomers in a reproducible manner in a simple glass T-junction by adjusting the flow rates of the dispersed (Q_d, monomer solution) and continuous (Q_c, aqueous 2 wt% PVA solution) phase. One of these monomers, HPhOPA, required the addition of a solvent to reduce the viscosity in order to allow for particle formation. Ethyl acetate was added in the concentration of 10, 33.5 and 50 wt% to the monomer solution in order to probe their particle performance. Adding 33.5 and 50 wt% ethyl acetate resulted in monodisperse microspheres whereas polydisperse particles were obtained with 10 wt% ethyl acetate. By diluting HPhOPA with 50 wt% ethyl acetate, however, uniform particles with sizes up to 52 µm were fabricated only. Therefore, a concentration of 33.5 wt% ethyl acetate was employed for further polyHPhOPA particle production. Furthermore, the surfactant was seen to be crucial for the droplet formation because a minimum of 2 wt% PVA resulted in stable droplet generation, as displayed in Figure 4.27 a). A PVA concentration lower than 2 wt% led to no or instable droplet formation (Figure 4.27 b)).

a) b)

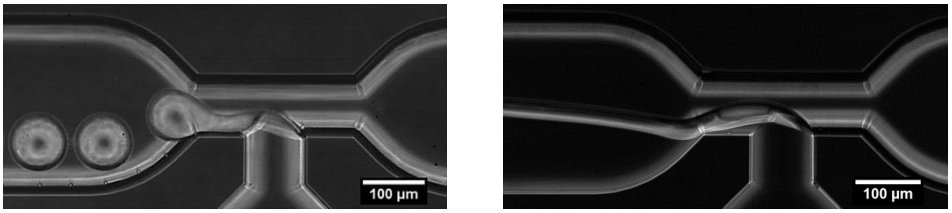


Figure 4.27: Images taken at a glass T-junction: a) stable monomer droplets observed using 2 wt% PVA, b) constant monomer stream seen in the microfluidic chip without adding PVA as a surfactant.

The monomers 1,1,1,3,3,3-hexafluoroisopropyl acrylate (HFiPA) and furfuryl methacrylate (FuMA), presented in Table 4.3, formed droplets in the microchannel but did not fully cure even after purging with nitrogen gas. The monomer N-[3-(dimethylamino)propyl]acrylamide (DMPAm) did not succeed in droplet formation most likely due to a surface and/or interfacial tension problem between the monomer and the continuous PVA phase. By changing the glass chip to a hydrophobically coated cross-junction glass chip, the monomer stream still did not break up into droplets at any tested flow rates (Figure 4.28 a)). Furthermore, no droplet formation was observed when exchanging PVA in the continuous phase with more hydrophobic surfactants like SDS, Triton X-100 and Tween 80, as displayed in Figure 4.28 b).

a) b)

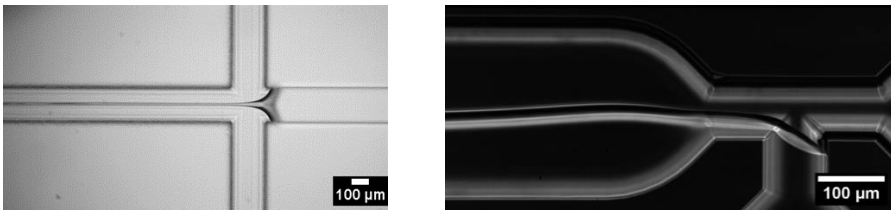


Figure 4.28: Images showing the inability of the monomer DMPAm to form droplets: a) in a hydrophobically coated cross-junction glass chip, b) in a glass T-junction using SDS as the surfactant in the continuous phase.

Consequently, the monomer DMPAm was excluded from fabricating homopolymeric microparticles due to its inability to generate droplets. Additionally, the relatively high monomer viscosity of 65 cP did not simplify manufacture. Besides DMPAm, the monomers HFiPA and FuMA, which were unable to form particles using piezoelectric inkjet printing, were also not included in the library to form homopolymeric particles using microfluidics. However, these three monomers were retained for trying to fabricate co-polymerised spheres as outlined in Sections 4.3.4.2 and 4.3.4.3. A comparison of success of the monomers used in both particle fabrication techniques is listed in Table 4.10.

Table 4.10: Comparison of the monomers employed in microfluidics and piezoelectric inkjet printing with respect to microparticle fabrication. Successful particle formation is highlighted in green whereas the inability to form particles is highlighted in red. Monomers, which failed to produce homopolymeric particles but were retained for trying to fabricate co-polymerised particles, are highlighted in purple.

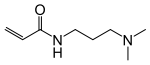
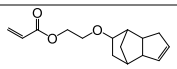
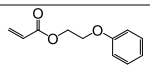
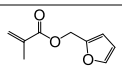
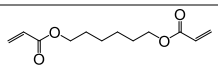
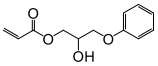
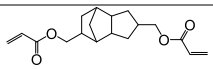
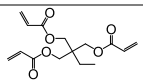
Monomers	Structure	Microfluidics	Inkjet printing
DMPAm		Surface and/or interfacial tension problem	
EGdPEA			
EGPEA			
FuMA		Curing issues	
HFiPA		Curing issues	
HMDA			
HPhOPA		Required addition of solvent	
TCDMDA			
TMPTA			

Figure 4.29 illustrates flow pattern diagrams of three monomers with different viscosity values: a) HMDA with 6 cP, b) EGdPEA with 20 cP and c) TCDMDA with 140 cP. A flow diagram shows the flow conditions under which monodisperse droplets can be generated in a T-junction. When the flow rate of the continuous phase (Q_c) is too low, droplets cannot be formed since the viscous shearing force is too weak resulting in continuous laminar streams of the dispersed and continuous phase. In contrast, when Q_c is too high, polydisperse droplets are irregularly formed in the jetting regime [263]. Uniform microparticles were only generated with flow conditions complying to be below the 'mountain-shaped' area. As reported by Nisisako et al. [124], the capillary number Ca should be low and in the range from 10^{-4} to 10^{-2}. The capillary number, representing the relative effect of viscous forces versus surface tension acting across an interface, is defined in Eq. 4.4:

$$Ca = \frac{\eta v}{\gamma} \qquad \text{Eq. 4.4}$$

where η is the viscosity of the continuous phase, v is the velocity and γ is the interfacial tension between the dispersed and continuous phase. In addition, it can be seen that the higher the viscosity of the monomer, the flatter the 'mountain-shaped' curve and consequently, the smaller the range to produce droplets.

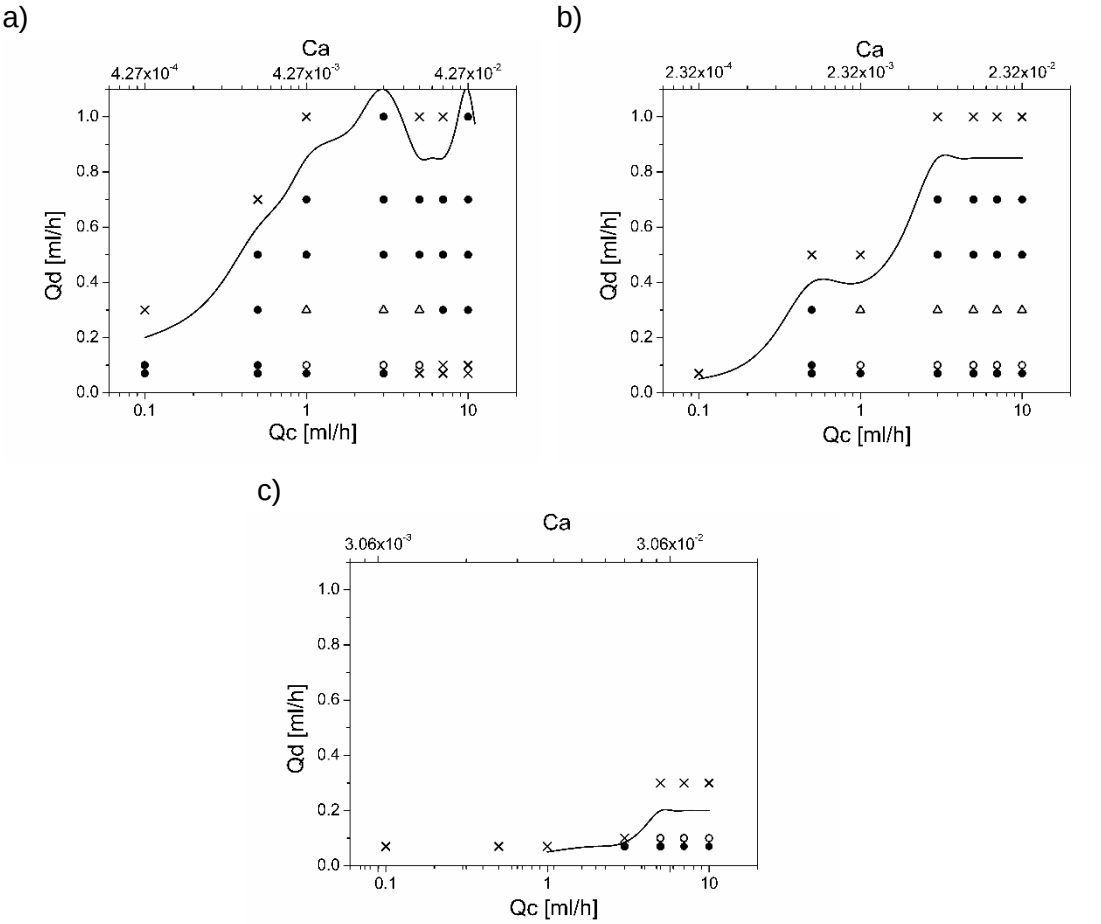


Figure 4.29: Flow pattern diagrams of three monomers with different viscosities indicating the regions where monodisperse particles were formed: a) HMDA with 6 cP, b) EGdPEA with 20 cP, c) TCDMDA with 140 cP. Qd is the flow rate of the dispersed phase whereas Qc is the flow rate of the continuous phase. The upper horizontal axis represents the capillary number Ca. The crosses (x) indicate the conditions under which monodisperse droplets were not formed reproducibly. All other symbols (●, Δ, ○) represent the conditions under which monodisperse particles were reproducibly generated. The hollow circles (○, Qd = 0.1 ml/h) and the hollow triangles (Δ, Qd = 0.3 ml/h) show the conditions where the particle size was measured. The boundary between the two regimes, represented as a line, was estimated empirically.

A relation between the particle diameter and the continuous phase flow rate is depicted for the same three monomers, as in Figure 4.29, at a fixed dispersed phase flow rate (Q_d) of 0.1 and 0.3 ml/h, respectively. Figure 4.30 shows that a higher continuous flow rate results in smaller particles. The reason for this trend is that the shear stresses become greater, the higher the flow rate. Therefore, the droplets break up faster resulting in a smaller volume. Furthermore, a higher dispersed phase flow rate pushes more liquid through the microchannel to the T-junction generating bigger droplets.

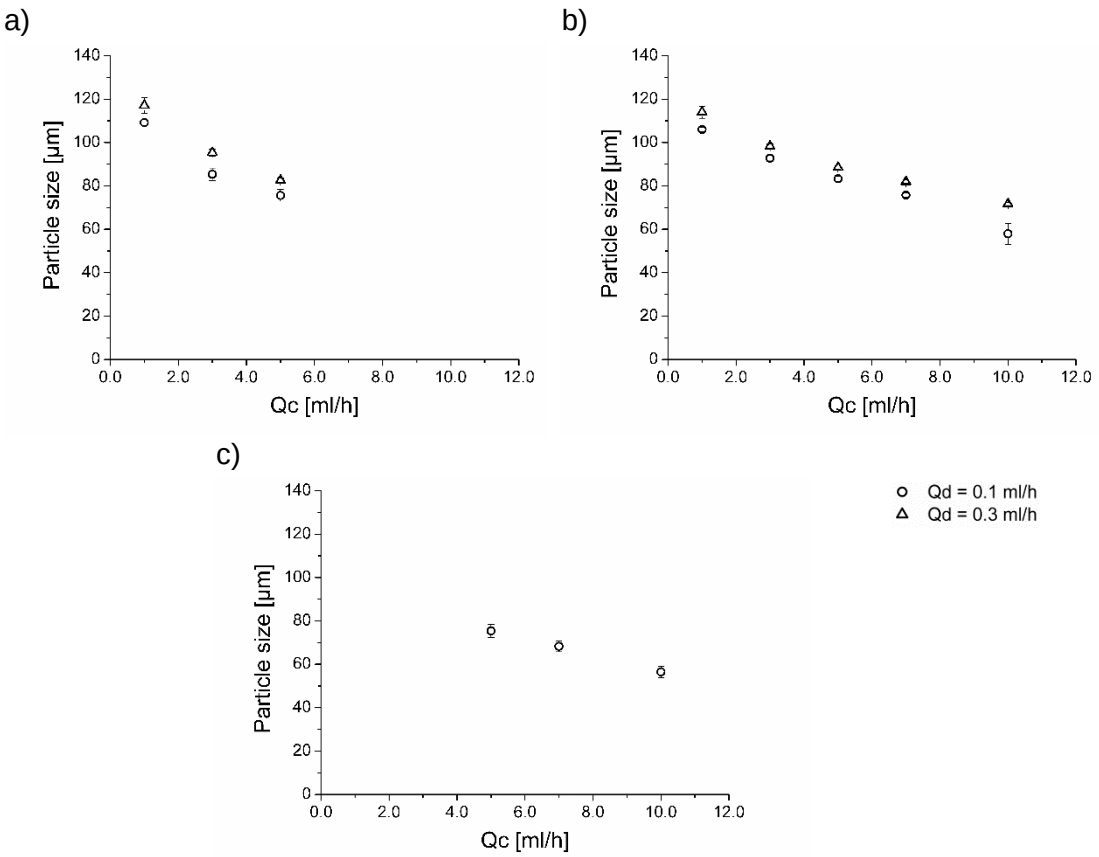


Figure 4.30: Effect of the continuous phase (Qc) and monomer stream (Qd) flow rate on particle size is presented for three monomers with different viscosities: a) HMDA with 6 cP, b) EGdPEA with 20 cP, c) TCDMDA with 140 cP. The particle diameters were measured at two fixed Qd. The hollow circles (○) and the hollow triangles (Δ) indicate the dispersed flow rate of 0.1 and 0.3 ml/h, respectively. The error bars represent the standard deviation of the measured particle sizes.

All homopolymeric particles generated from the small library of 6 functioning acrylates were formed to have an average diameter of 80 µm by adjusting the flow rates accordingly.

4.3.4.2. Formation of Pre-blended Co-polymerised Particles in a T-junction

Monodisperse particles consisting of two different monomers, which were pre-blended to a ratio of 70 to 30 wt%, were obtained in a simple glass T-junction. Figure 4.31 shows images of microparticles made from the pre-blended monomer solution consisting of 70 wt% EGdPEA and 30 wt% HMDA with 1 wt% DMPA.

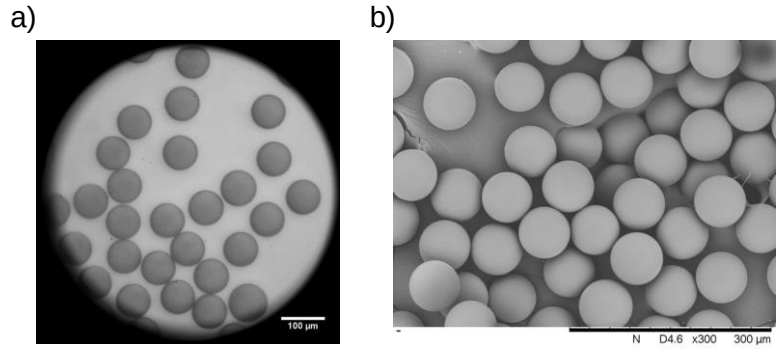


Figure 4.31: Uniform microparticles were generated from the monomer combination 70 wt% EGdPEA - 30 wt% HMDA: a) brightfield image with a scale bar of 100 µm, b) SEM image with a scale bar of 300 µm.

The droplets were formed in a one-step process, which is illustrated with the monomer combination 70 wt% EGdPEA – 30 wt% HMDA in Figure 4.32. The monomer mixture was injected at 0.1 ml/h into the stream of PVA solution at 5.0 ml/h. The process consists of growth of a forefront of the monomer stream, formation of a pinched neck, detachment of the droplet and formation of a satellite drop. The satellite droplet is generated from a thin filament because of interfacial instability and could be eliminated by applying a branching structure at the downstream of the droplet generator [264].

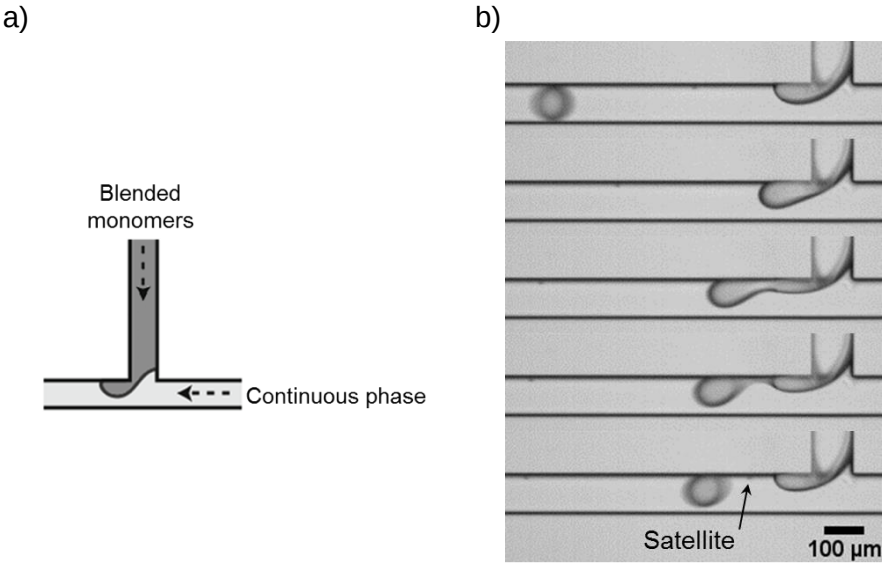


Figure 4.32: Formation of droplets from pre-blended photocurable monomers: a) schematic of a simple T-junction, b) five sequential images illustrating the one-step process of generating droplets at a T-junction. The flow rates of the dispersed and continuous phase are 0.1 and 5.0 ml/h, respectively.

By testing different monomer combinations, it was observed that even when the summed viscosity value of the two monomers was lower than the viscosity value of the more viscous monomer ($0.7 \times \eta_1 + 0.3 \times \eta_2 < \eta_1$ with $\eta_1 > \eta_2$), the range of flow rates to produce particles was smaller. A plausible explanation is that besides viscosity, surface and interfacial tension play a crucial role in the droplet formation process.

Co-polymerised particles made from pre-blended monomers were fabricated to obtain an average particle diameter of 80 µm by controlling the flow rates of the dispersed and continuous phase. Combinations of monomers were selected in consideration of not exceeding values of 100 cP for the summed viscosity of the pre-blended solutions. In Table 4.11, a summary of the fabricated pre-blended co-polymerised particles with the applied flow rates and the obtained particle sizes are provided. Each monomer combination was produced in two batches because the aqueous PVA solution needed to be refilled after a certain time in order to obtain a yield large enough to perform biological testing afterwards.

Table 4.11: Summary of the produced pre-blended co-polymerised microspheres with the applied flow rates and the measured particle sizes.

Pre-blended monomers (70 – 30 wt%)	**Monomer / PVA phase flow rate [ml/h]**	**Particle size [µm]**
EGdPEA - HMDA	0.1 / 5.0	78.3 ± 1.0, 76.6 ± 2.5
EGPEA - EGdPEA	0.1 / 5.0	76.9 ± 6.3, 75.6 ± 2.5
EGPEA - TMPTA	0.1 / 5.0	63.8 ± 3.1, 72.1 ± 1.4
EGdPEA - HPhOPA	0.09 / 5.5	70.0 ± 6.5, 67.3 ± 0.9
TCDMDA - EGPEA	0.1 / 5.0	77.0 ± 1.5, 72.0 ± 1.1
HMDA - FuMA	0.3 / 4.0	87.7 ± 2.6, 88.3 ± 3.3
FuMA - TMPTA	0.1 / 5.0	74.1 ± 5.6, 74.3 ± 8.6
TMPTA - HMDA	0.09 / 5.0	76.2 ± 1.1, 76.6 ± 0.8
TMPTA - EGdPEA	0.1 / 4.0	74.9 ± 1.9, 78.2 ± 1.1

The following pre-blended co-monomer solutions (70-30 wt%) containing the monomer HFiPA and DMPAm were tried out and did not result in particle formation: TMPTA-HFiPA, HMDA-DMPAm and EGPEA-DMPAm. The co-monomer combination TMPTA-HFiPA was not able to generate droplets, not even at flow rates of 0.07 and 10.0 ml/h for the monomer and aqueous PVA phase, respectively (Figure 4.33 a)). The co-monomer solution behaved as a highly viscous fluid even though the summed viscosity should be lower than the viscosity of TMPTA alone. The monomer TMPTA was capable of producing homopolymeric microspheres. Figure 4.33 b) shows the instable flow of HMDA-DMPAm at flow rates of Q_d = 0.1 ml/h and Q_c = 5.0 ml/h which resulted in polydisperse droplets. In addition, it was observed that DMPAm leaked out from the co-monomer solution.

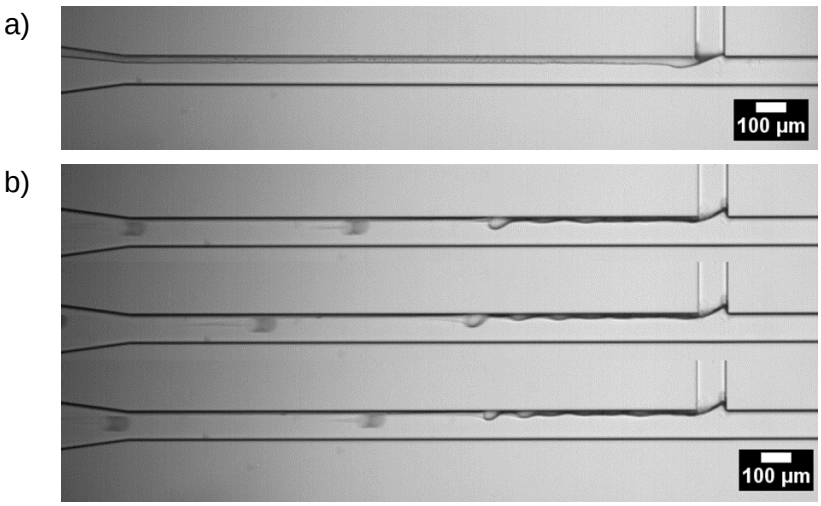


Figure 4.33: Examples of unsuccessful droplet formation: a) break-up into droplets did not occur within the channel length when using TMPTA-HFiPA at Q_d= 0.07 ml/h and Q_c= 10.0 ml/h, b) instable flow happened when testing HMDA-DMPAm at Q_d= 0.1 ml/h and Q_c= 5.0 ml/h.

4.3.4.3. Formation of On-chip Co-polymerised Particles in a Y-shaped Channel Leading to a T-junction

By mixing the two monomers directly on the glass chip (on-chip), displayed in Figure 4.34, monodisperse microparticles were obtained with average sizes of 80 µm. A summary of the on-chip co-polymerised particles including the applied flow rates and measured particle diameters are outlined in Appendix H. The particle diameters were controlled by adjusting the appropriate flow rates of the two organic phases (Q_d = $Q_{Monomer1}$ + $Q_{Monomer2}$) and the continuous stream (Q_c). The droplets were also generated in a one-step process as explained in Section 4.3.4.2.

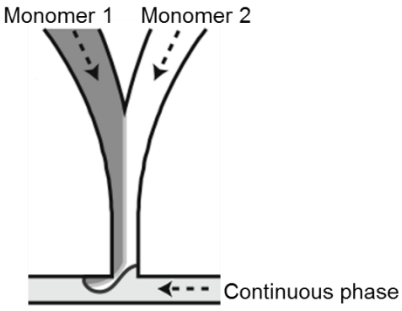


Figure 4.34: Schematic of the on-chip copolymerisation method.

In contrast to the pre-blended co-polymerised particles, the ratio to which the monomers were effectively blended together during the on-chip copolymerisation is not fully under control and can only be analysed by surface chemistry techniques. Given that pre-blending can also result in phase separation, the surface composition

of such co-polymerised particles should also be verified. By modifying the flow rates of the monomers independently, particles with different monomer ratios can be produced using on-chip copolymerisation. Nevertheless, the degree of homogeneity throughout the particle or whether phase separation occurred within the particle, basically depends on the extent of miscibility between the monomers. It is known, however, that mixing is enhanced by steady flow recirculation within droplets [265], by introducing wavy microchannels as outlet channels and by lengthening the outlet tube to extend the time for diffusion.

The droplet formation process is shown for two different monomer combinations, EGdPEA-EGPEA (a) and EGPEA-TMPTA (b), in Figure 4.35. In both cases, the monomer solutions were injected at the same flow rate (Q_{M1} = Q_{M2} = 0.05 ml/h) into the stream of PVA aqueous solution at 3.0 ml/h. The monomers in Figure 4.35 a) are both ethylene glycol acrylates and hence, exhibit similar properties that lead to good miscibility. However, Figure 4.35 b) shows two monomers, an ethylene glycol acrylate and a triacrylate, with dissimilar properties. The blending does not occur readily amongst the monomers which is best seen in b) ii). The image sequences b) ii) – iv) suggest phase separation which occurred most likely due to the large difference in viscosity. No conclusions can be reached, however, from the image b) v) because the droplet is out of focus.

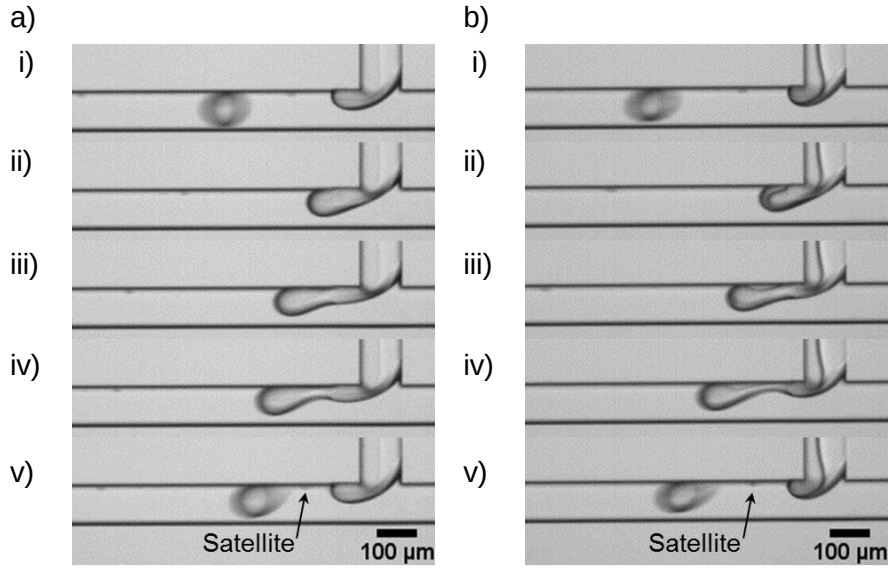


Figure 4.35: Formation of on-chip co-polymerised droplets from two different photocurable monomers. All the monomers were injected at the same flow rate of 0.05 ml/h into the stream of aqueous PVA solution at 3.0 ml/h: a) sequence of images showing the generation of droplets from two similar monomers (EGdPEA-EGPEA) - good miscibility, b) five sequential images illustrating the one-step process of two dissimilar monomers (EGPEA-TMPTA) - to a lesser extent miscible.

The same monomer combinations were tested on-chip as already studied as pre-blended co-monomer solutions. Particles were successfully formed with the same 9

out of 12 co-monomers as already described for blended-before copolymerisation. A summary of the co-monomers tested for their ability to generate particles using the two copolymerisation approaches is provided in Table 4.12.

Table 4.12: Summary of the monomer combinations tested for their ability to fabricate microparticles using blended-before and on-chip copolymerisation: successful particle formation (green) and inability to generate particles (red).

Monomer combination	On-chip copolymerisation	Blended-before copolymerisation
EGdPEA - HMDA		
EGdPEA - HPhOPA		
EGPEA - DMPAm	Instable flow followed by blocked microchannel; DMPAm phase-separated and leaked out from co-monomer solution	No droplet formation, behaved like high viscous fluid; DMPAm leaked out from co-monomer solution
EGPEA - EGdPEA		
EGPEA - TMPTA		
FuMA - TMPTA		
HMDA - DMPAm	Instable flow resulted in polydisperse droplets; DMPAm phase-separated and leaked out from co-monomer solution	Instable flow resulted in polydisperse droplets; DMPAm leaked out from co-monomer solution
HMDA - FuMA		
TCDMDA - EGPEA		
TMPTA - EGdPEA		
TMPTA - HFiPA	No droplet formation, behaved like high viscous fluid	No droplet formation, behaved like high viscous fluid
TMPTA - HMDA		

The co-monomer HMDA-DMPAm did repeatedly reveal instabilities in the flow as already determined with the pre-blended co-monomer solution. However, using the on-chip blending setup, it can be seen in Figure 4.36 that the monomers did not fully mix, resulting in phase separation.

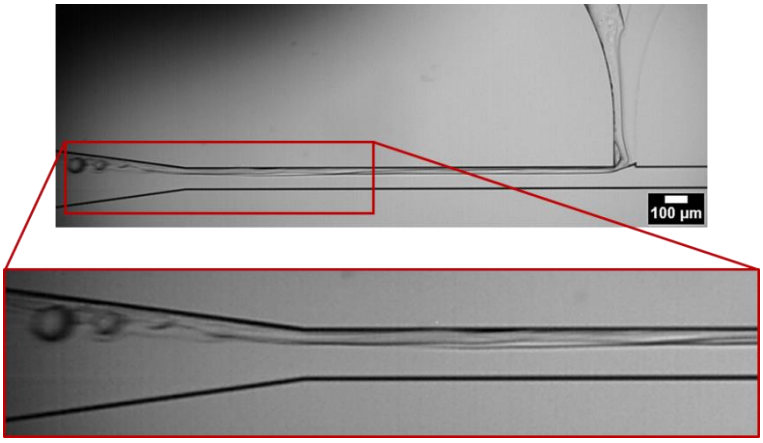


Figure 4.36: Instability of HMDA-DMPAm flow resulting in polydisperse droplets using on-chip copolymerisation. Zoomed image shows the phase separation of the monomers.

The polydisperse particles, obtained from blending the two monomers, HMDA and DMPAm, on-chip in the vicinity of a 2 wt% aqueous PVA solution, are depicted in Figure 4.37. The microspheres exhibited some circular features, which emerged from the immiscibility of the two monomers. The circular features observed are thought to be on top of the particles due to the differences in densities of both monomers (microspheres: HDMA, ρ: 1.01 g/ml; circular features: DMPAm, ρ: 0.95 g/ml), resulting in the features to float. The yield of these particles was very low as the PTFE tube, transporting the DMPAm solution from the glass syringe to the microfluidic chip, was blocked repeatedly.

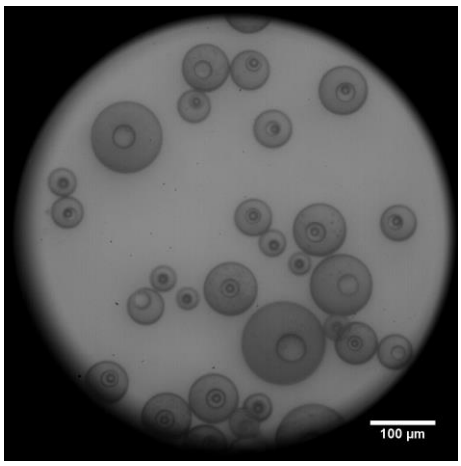


Figure 4.37: Polydisperse microparticles were generated by blending the monomers HMDA and DMPAm in the glass chip. Phase-separation of the monomers resulted in circular features on the particles.

By comparing on-chip blending with blending-before, both methods showed that not only viscosity but also surface and interfacial tension are crucial for successful droplet generation. Furthermore, single monomers that did not form particles, should not be discarded immediately from the library because they can still be used in copolymerisation. In case of on-chip copolymerisation less preparation was needed. In addition, the on-chip copolymerisation exhibits a larger range to modify the flow rates

since the monomer flow rates can be adjusted independently. This is advantageous for fabricating particles with different monomer ratios, such as phase separation into small domains or complete separation as seen in Janus particles, in limited production runs. However, the specific properties of the monomers affect the results in the on-chip copolymerisation more compared to the mixed properties in blended-before copolymerisation (Figure 4.38). In order to obtain particles with a well-defined monomer ratio, blending-before copolymerisation is the technique to choose in manufacture. Although better control of droplet formation is achieved with blending-before, phase separation might occur with some monomer combinations in the syringe.

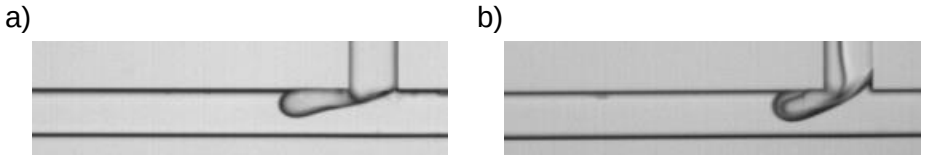


Figure 4.38: Formation of co-polymerised droplets from the monomer combination EGPEA-TMPTA using two different copolymerisation approaches: a) blended-before copolymerisation, b) on-chip copolymerisation. The specific properties of the monomers affect the results in on-chip copolymerisation more compared to the mixed properties in blended-before copolymerisation – phase separation might have occurred in on-chip copolymerisation.

4.3.5. Comparison between Inkjet Printing and Microfluidics

Comparing inkjet printing and microfluidics in terms of microparticle production and production rate, microfluidics was less sensitive to input parameters and resulted in higher yields in this study. The process of forming microspheres using microfluidics is better developed since it is mainly controlled by the ratio of flow rates, capillary and Reynolds number. In contrast, parameters inter-dependently affect the formation of droplets in inkjet printing where a partially cured liquid droplet must pass a gas-liquid interface into the collecting fluid. Moreover, comparing the particle formation success rate for both fabrication techniques based on the small selection of the library generated for inkjet printing, it was shown that 6 out of 9 monomers worked for both production methods. However, reasons why the monomers 1,1,1,3,3,3-hexafluoro-isopropyl acrylate (HFiPA), furfuryl methacrylate (FuMA) and N-[3-(dimethylamino)propyl] acrylamide (DMPAm) failed using the Dimatix printer is partially known. Employing microfluidics though, it was demonstrated that both HFiPA and FuMA formed droplets in the channel but particles were not obtained due to insufficient curing. The inability to form particles in a microfluidic device using the monomer DMPAm could not be explained even after conducting further tests. Nevertheless, microfluidics is a well-established technique that has been applied for producing

various particle shapes [27,124]. Less literature has been found on diversity of shapes fabricated using piezoelectric inkjet printing.

Both manufacturing techniques are summarised in Table 4.13 by comparing materials, production rate, sizes, shapes, costs and scalability.

Table 4.13: Summary showing a comparison between inkjet printing and microfluidics with respect to materials, production rates, sizes, shapes, costs and scalability.

Process	Materials	Production rate	Sizes and shapes	Costs	Scalability
Inkjet printing	Polymer [33,77,95]; composites [8,94,266]; ceramics [76,108]; metals [94,267]	Calculated for printing frequency of 3 kHz and diameter of 20 µm: Continuous printing: 86'400'000 drops per 8h (= 45.2 mg/h); DOD printing: 230'400 drops per 8h (= 0.1 mg/h)	Sizes: nano- to micrometre (50-200 nm [268], 2-500 µm [33,95,98]) Shapes: simple spheres [31,32,95]; core-shell particles [269]; circles, grids, honey combs, rings [33]	Low material wastage, reduction in manufacturing costs [8,75,94]; in case of Dimatix expenses due to disposable cartridges	Ease to scale-up [75,270]; unable to readily access library of materials in case of Dimatix but possible e.g. for sciFlexarrayer
Microfluidics	Polymers [124,271,272]; composites [27,273]	Calculated for flow rates of Q_d = 0.1 ml/h, Q_c = 5.0 ml/h and diameter of 80 µm: Microfluidics: 2'985'100 drops per 8h (= 100.0 mg/h)	Sizes: nano- to micrometer (0.005 - 500 µm [15,30,110,274]) Shapes: spheres [109,273]; flattened spheres [29]; disc, rods [27,275]; Janus particles [273]; various shapes [69]	Low cost experimental setup, low material wastage	Possible to scale-up using different approaches: parallelisation, membrane emulsification [112,276–278]; difficult to readily access library of materials

As seen from Table 4.13, inkjet printing offers the flexibility of dispensing a wider palette of functional materials than microfluidics. However, in microfluidic-based techniques the spectrum of possible sizes is larger since the size can simply be

controlled by adjusting the ratio of flow rates, channel widths and depths. Unlike microfluidics, the drop sizes of printed particles are adjusted by controlling the dispense voltage and time. Additionally, the sizes are limited by the nozzle orifice. Furthermore, microfluidics facilitates the fabrication of various shapes ranging from hemispheres via spheres to discs and rods. Recently, an advanced technique called optofluidics has been reported on, which allows for creation of an infinite set of 3D-shaped particles by combining geometry-induced flow deformation and orthogonal masked UV polymerisation [69]. The variety of particle shapes, reported for inkjet printing, is smaller because modifying the shape poses difficulties. In terms of costs, both techniques have initial expenses for the experimental setup, but apart from that exhibit low material wastage and small manufacturing expenses in general. The Dimatix printer is an exception, though, because the cartridges are disposable and require replacement for testing different materials, increasing the cost for consumables. In respect to the number of droplets formed within 8 hours, a continuous printer would produce ~86'400'000 drops (= 45.2 mg/h at 20 µm) when applying a printing frequency of 3 kHz assuming a steady state condition. A drop-on-demand printer, like the Dimatix printer, could theoretically fabricate ~468'700 drops in 8 hours (= 0.2 mg/h at 20 µm), assuming that a print pattern of 30 × 30 drops is repeatedly printed into a well plate using a frequency of 3 kHz. However, in practice, time is required for setting the print starting point and adjusting the nozzles which results in a feasible yield of ~230'400 drops (= 0.1 mg/h). Eventually, fewer droplets were obtained as some will not have reached the well due to the movement of the printhead. In addition, the impact of incompletly cured droplets on the liquid-gas interface led to shape deformation and polymeric agglomerations instead of free-flowing particles. Alternative to printing, microfluidics is able to generate 2'985'100 particles in 8 hours (= 100.0 mg/h at 80 µm) when applying flow rates of 0.1 and 5.0 ml/h for the dispersed and continuous phase, respectively. Consequently, submerged continuous printing would be the most suitable technique due to the highest yield in microparticles without the issue of shape deformation occurring at a liquid-gas interface. This technique is followed by microfluidics, which is only able to fabricate 3.45% (number of particles) of the continuous printing outcome. Scaling-up the particle fabrication for large-scale industrial production seems feasible for both techniques. However, the ability to readily access a library of materials is lacking for both microfluidics and pre-loaded inkjet printing such as the Dimatix printer. Printers that come with nozzles capable of aspirating and dispensing fluids, for instance the sciFLEXARRAYER developed by Scienion AG, enable production of particles with different chemistries. A schematic of a sciFLEXARRAYER printer is presented in Figure 4.39.

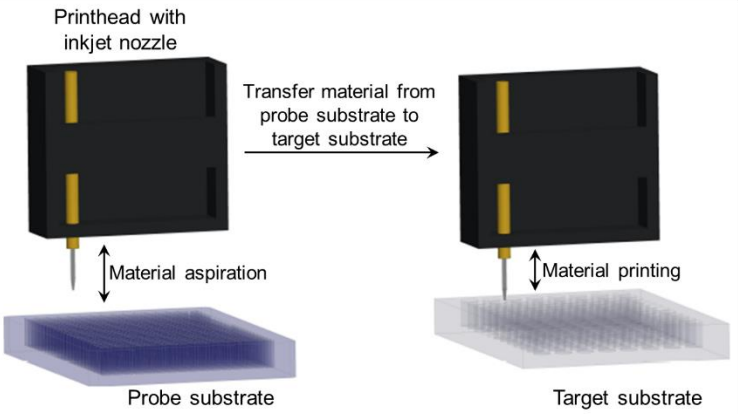


Figure 4.39: Schematic representation of the workflow, aspiring and dispensing material, enabled by the sciFLEXARRAYER printer.

4.4. SUMMARY

The aim of this chapter was to generate a combinatorial library of microparticles composed of (meth)acrylates using photopolymerisation in combination with either piezoelectric inkjet printing or microfluidics. In search of a universal collecting fluid, 17 wt% IPA/DIW gave the most promising results in respect to particle formation. Pipetting different monomer solutions into different collecting fluids in air revealed that oxygen caused polymerisation inhibition by quenching free radicals. Overcoming the oxygen inhibition problem by changing to reduced oxygen atmosphere improved the monomer success rate upon 13.1%.

Polymerisation kinetic studies performed on 23 different monomer solutions demonstrated that the number of functional C=C double bonds affects the curing rate. Moreover, methacrylates cure slower than acrylates because the generated tertiary radical is more stable than a secondary radical resulting in lower photopolymerisation rates. Curing rates are also influenced by steric hindrance that can arise from increased chain lengths or from the physical size of the monomers. Due to increased monomer bulkiness, hence decreased flexibility, approaching a free radical becomes more difficult.

Transferring the macro-pipetting experiment into micro scale using the Dimatix printer, a piezoelectric inkjet printer, presented great similarities. However, reducing the volume by a million-fold challenged the understanding of parameters affecting the particle formation. Factors related to the surface such as surface energy and surface charge become more dominant with a larger surface-to-volume ratio. Printing monomer solutions into the collecting fluid resulted in monodisperse free-flowing particles with 20 µm in size, particle and polymeric agglomerations. It was postulated

that particle agglomerations emerged due to coalescence of incompletely cured particles. The microspheres did not trap any gas or collecting fluid, which was confirmed by FIB measurements, presenting solid particles throughout the bulk. By modifying the inks, collecting fluids and process conditions, it was found that adding 0.1 wt% Triton X-100 as a surfactant helped to improve the particle outcome. Moreover, uniform microspheres were obtained up to a printing velocity of 6 m/s, whereas higher rates led to increased aspherical shapes with satellite droplets. After gaining control over the printing process, a library of 20 (meth)acrylates capable of producing particles was generated using the Dimatix printer.

A representative range of the library created for inkjet printing was tested using microfluidics. A surfactant concentration of 2 wt% PVA in the continuous phase was perceived to be crucial for droplet formation. By exploring the flow conditions, under which monodisperse droplets can be produced in a simple glass T-junction, it was observed that uniform microspheres were only generated with flow conditions in a 'mountain-shaped' area. This mountain-like curve encloses a maximal dispersed phase flow rate range (Q_d on y-axis) at an intermediate continuous phase flow rate (Q_c on x-axis) under low capillary number (Ca) ranging from 10^{-4} to 10^{-2}. In this area, a laminar flow is prevalent enabling to predict the manner of fluid transport and the shearing force is strong enough to form droplets. In addition, a higher viscosity of the dispersed phase (monomer) resulted in a smaller range to form droplets recognisable by a flattened 'mountain-shaped' curve. The droplets were formed in a one-step process independent of the microfluidic chip geometry. Besides homopolymeric spheres, co-polymerised particles were fabricated in two different ways: by blending the monomer solutions either beforehand (blended-before) or directly on the microfluidic chip (on-chip). The on-chip copolymerisation method exhibited advantages regarding the range of flow rates to be tested since the monomer flow rates can be adjusted independently. This can be deployed for fabricating particles with different monomer ratios allowing for phase separation into small partitions or complete separation such as seen in Janus particles. However, blending-before copolymerisation is the technique to choose in order to obtain particles with a well-defined monomer ratio for the purpose of greater process stability. Furthermore, both methods revealed that besides viscosity, surface and interfacial tension play a key role for successful droplet generation.

Comparing both fabrication methodologies, piezoelectric inkjet printing and microfluidics, microfluidics was shown to be eminently suitable for producing particles. Microfluidics was easier to control due to the technique already having been well

established for particle fabrication. Consequently, a larger yield was acquired. In theory, continuous printing would achieve an even higher yield compared to both drop-on-demand printing and microfluidics. If the printing process could be optimised to allow for submerged continuous printing, this technique might be the better choice for producing large-scale simple particles. However, in consideration that inkjet printing is far from reaching a stable, steady state printing condition, microfluidics offers a greater potential for various applications due to its feasibility in scaling-up particles in all sizes, shapes and compositions.

5. RESULTS - MICROPARTICLE CHARACTERISATION

5.1. INTRODUCTION

The performance of particles for drug delivery, for instance, is determined by its physiochemical properties amongst others [64]. It has been reported that particle size, size distribution and carrier geometry affect the encapsulation efficiency, route of administration and release kinetics for drug delivery [33,67,279]. Moreover, it has been demonstrated that both the surface chemistry and topography are of great importance for bacterial interactions because biomolecules of biological systems interact with only the surfaces of materials [163,280,281]. Recently, R. Helbig et al. [210] have shown that dimensions of periodically structured polymeric substrates have profound effects on initial bacterial cell attachment during biofilm formation. Therefore, it is important to perform comprehensive surface chemical and structural characterisation of the microparticles produced in this thesis in order to elucidate relationships between surface properties and a specific biological phenomenon of interest. These structure-performance relationships facilitate a move towards the rational design of biomaterials. Within this rational design, new or optimised materials can be identified for specific applications involving interfacial contact between the material and its surrounding environment.

This chapter focuses on a thorough physical and chemical characterisation of inkjet printed and microfluidic produced microparticles. Imaging approaches, such as optical and scanning electron microscopy, were employed as an initial, rapid assessment of particle size, shape and surface morphology. Complementary ensemble analysis techniques, dynamic light scattering and centrifugation, were used to examine the particle size distribution along with optical and electron microscopy. For detailed chemical analysis of the uppermost 1-2 nm of the surface, time-of-flight secondary ion mass spectrometry (ToF-SIMS) was employed. Atomic force microscopy (AFM) was utilised allowing for comprehensive topographical analysis of the polymeric microparticles. The surfaces of inkjet printed and microfluidic produced particles were assessed extensively due to its key role in controlling the bacterial attachment and biofilm formation, which will be discussed using the bacterial strain *Pseudomonas aeruginosa* (*P. aeruginosa*) in Chapter 6.

5.2. EXPERIMENTAL

This subsection discusses the experimental methods employed in this chapter. The fundamentals of the majority of the techniques with their operating parameters used are presented in Chapter 3. Particle defect assessment methods can be found in Section 5.2.1, which describes a quantitative method to compare defects on SEM images. Furthermore, post-treatment methods of microparticles are presented in Section 5.2.2.

5.2.1. PARTICLE DEFECT ASSESSMENT METHOD

In order to be able to compare defects on the obtained microfluidic produced microparticles, SEM micrographs were analysed quantitatively. Ten micrographs of particles of each monomer (homopolymer) or monomer combination (co-polymer) were investigated for defects: surface porosity, surface cracking, detachment marks, polymer residues, asphericity, waviness and particle agglomeration. The full defect list including defect name, defect cause and example is discussed in Section 5.3.1.2.

The amount of the different types of defects was noted, and a performance score was associated for each. The scaling ranges from 0 to 1; 0 indicating no defect present and 1 indicating poor performance with a defect present on every particle.

5.2.2. POST-TREATMENT OF MICROPARTICLES

5.2.2.1. WASHING OF PARTICLES FOR REMOVAL OF SILICON-BASED CONTAMINATION

With the aim of removing any silicon (Si) based contaminations, on-chip co-polymerised EGPEA-TMPTA microparticles were washed extensively with the following four different solvents: hexane, methylated industrial spirits, Dow Corning® DS-2025 Silicone Cleaning Solvent (‘Dow Corning’) and Techsil® Silstrip Liquid (‘Silstrip Liquid’). The chemical components of the trade products, Dow Corning and Silstrip Liquid, including their concentration are listed in Table 5.1.

Table 5.1: Trade products, Dow Corning and Silstrip Liquid, are listed with their chemical components and their appropriate concentrations.

Trade name	Chemical components	Concentration [wt%]
Dow Corning® DS-2025 Silicone Cleaning Solvent	distillates (petroleum), hydrotreated light	70-90
	dodecylbenzene sulfonic acid	25-30
Techsil® Silstrip Liquid	distillates (petroleum), hydrotreated light	>90
	dodecylbenzene sulfonic acid	1-10

Small aliquots of particles were washed by performing three wash cycles. A wash cycle consisted of sonicating the microspheres in one of the mentioned Si-removal solvents for 10 min, followed by another sonication in isopropanol for 10 min. At the end of the third wash, the particles were sonicated two more times in isopropanol for 10 min in order to remove any residues of the Si-removal solvents. Afterwards, the on-chip co-polymerised EGPEA-TMPTA particles were dried in an oven at 37°C for 48 h.

5.2.2.2. Washing of Particles for PVA Coverage Removal

In order to assess whether the PVA surfactant was physically adsorbed or crosslinked into the microfluidic produced polymer particles, aliquots of particles were washed varying the number of wash cycles. The number of wash cycles ranged from 0, 1, 3, 5, 7 to 10. A wash cycle involved sonicating the microspheres in isopropanol for 5 min, followed by another sonication in distilled water for 5 min. Prior to ToF-SIMS analysis, the microparticles were dried in a vacuum oven at RT for 48 h.

5.3. Results and Discussion

5.3.1. Characterisation of Inkjet Printed and Microfluidic Produced Particles

5.3.1.1. Particle Size and Size Distribution

The average particle size and size distribution of inkjet printed and microfluidic produced particles were measured using disc centrifuge and laser light diffraction, respectively. These two techniques were selected according to their size measuring range and required sample quantity.

INKJET PRINTED HOMOPOLYMERIC PARTICLES

The inkjet printed particles were approximately 20 µm in size due to limitations of the Dimatix cartridge used for printing, which has nozzle orifices of 21 µm. The particle diameter plotted against the normalised relative weight are shown for the inkjet printed polyTCDMDA (a) and polyTMPTA (b) microparticles in Figure 5.1.

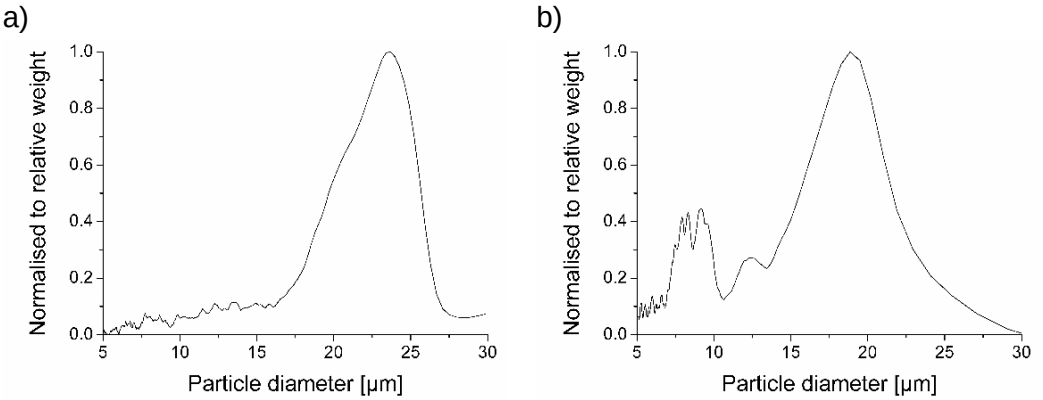


Figure 5.1: Particle size distribution of inkjet printed microparticles measured using centrifugal sedimentation stabilised by a sucrose density gradient. Particle diameter plotted against normalised relative weight are shown for inkjet printed polyTCDMDA (a) and polyTMPTA (b) microparticles.

Both monomer solutions showed narrow size distribution with an average particle diameter of 21.4 ± 4.2 µm and 17.2 ± 4.9 µm for polyTCDMDA and polyTMPTA, respectively. However, particles produced from TMPTA-DMPA also revealed smaller particles with sizes ranging from 7.5-12.5 µm, as seen in Figure 5.1 b). These smaller particles are either satellite droplets or appear to arise from impacting onto the gas-liquid interface of the collecting fluid splitting incomplete polymerised drops into smaller droplets. Monomer solutions consisting of a triacrylate like TMPTA with a photoinitiator showed a low conversion at the gel-point (outlined in Section 4.3.2) due to low degree of flexibility of the bulky monomer resulting in steric hindrance. This affirms that TMPTA droplets were polymerised only to a small extent when hitting the collecting fluid and hence, deformation and separation of droplets were likely to occur. Any particle agglomerates that formed were excluded from the measurements since size distribution evaluations were only conducted up to 30 µm.

MICROFLUIDIC PRODUCED HOMOPOLYMERIC PARTICLES

The microparticles produced in a microfluidic glass T-junction were approximately 80 µm in size. It was tuned to give this particle size range by adjusting the flow rates of the dispersed and continuous phase determined in the flow pattern experiments, presented in Section 4.3.4.1. Average particle diameters of 81.5 ± 5.1 µm and 68.6 ± 7.3 µm were measured for polyTCDMDA and polyTMPTA particles, respectively, with a narrow size distribution as illustrated in Figure 5.2. Any particles including satellites,

smaller than 20 µm were removed during particle collection by filtering the yield through a nylon mesh as described in Section 3.2.2.

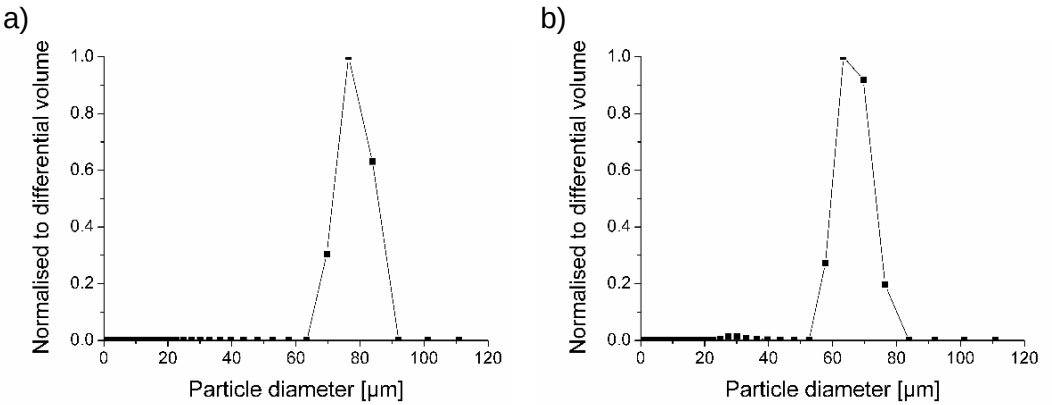


Figure 5.2: Particle size distribution shown for microfluidic produced particles measured utilising the Coulter LS230. The particle diameter versus normalised differential volume is plotted for microfluidic produced polyTCDMDA (a) and polyTMPTA (b) particles.

A low number of particles with sizes ~30 µm were detected when measuring polyTMPTA microparticles. This might be explained by an instability of the flow conditions which resulted in less fluid being temporarily pushed through the channels. A probable source for this lies in the channel of the dispersed phase, where smaller amounts of a monomer solution at the T-junction result in smaller particles. However, in case of instabilities in the channel of the continuous phase, larger particles are expected due to reduced shear forces acting on the stream of monomer solution. Instabilities can originate from air bubbles, dust or any other contaminations in the microfluidic setup. Blockages, which most likely occurred at the T-junction itself and at the outlet tube, also resulted in instabilities of the microfluidic system. Particle agglomerations were not detected in polyHMDA, polyTCDMDA and polyTMPTA particle manufacture. In contrast, microparticles made from HPhOPA-, EGdPEA- and EGPEA-DMPA could not be measured due to the inability to re-suspend large particle agglomerations in water, which were visible by eye. These agglomerations emerged only after drying the particles. Consequently, since these monomers share a low glass transition temperature (shown in Appendix I), it was assumed that a glass transition temperature below RT promoted agglomerations between the particles.

Comparison of Homopolymeric Particles

A summary of the data obtained from the particle sizing measurements are listed for inkjet printed and microfluidic produced polyTCDMDA and polyTMPTA particles in Table 5.2. As seen from Table 5.2, the particles exhibited a standard deviation of approximately 5 µm irrespective of the fabrication methodology. Comparing the coefficients of variation, it can be observed that the inkjet printed particles were

dispersed almost twice as much as the microfluidic particles. The relative span, which is defined as follows (Eq. 5.1):

$$Span = \frac{d_{v0.9} - d_{v0.1}}{d_{v0.5}} \qquad \text{Eq. 5.1}$$

is an additional parameter to show the breadth of the size distribution by indication how far the 10th ($d_{v0.1}$) and 90th ($d_{v0.9}$) percentile are apart, normalised with the 50th percentile of particles ($d_{v0.5}$) [282]. The span confirms that the microfluidic produced particles exhibited an up to three times narrower size distribution compared to the inkjet printed particles.

Table 5.2: Summary of the particle sizing data obtained for polyTCDMDA and polyTMPTA microparticles produced by piezoelectric inkjet printing (inkjet) and microfluidics (mf). Disc centrifuge and laser light diffraction were used to measure the particle size distribution of inkjet printed and microfluidic produced particles, respectively.

Particle	Average diameter [µm]	Standard deviation [µm]	Coefficient of variation [%]	Span
TCDMDA inkjet	21.4	4.2	19.9	0.4
TMPTA inkjet	17.2	4.9	28.7	0.8
TCDMDA mf	81.5	5.1	6.2	0.2
TMPTA mf	68.6	7.3	10.7	0.2

MICROFLUIDIC PRODUCED CO-POLYMERIC PARTICLES

In order to compare the two copolymerisation routes applied in microfluidics, blended-before and on-chip copolymerisation, particle size distributions were measured using the Coulter LS230 size analyser. In Figure 5.3, the particle diameter is plotted against the normalised differential volume for EGPEA-TMPTA blended-before (a) and on-chip (b) co-polymerised particles. These samples were a good representation of all co-polymerised samples measured.

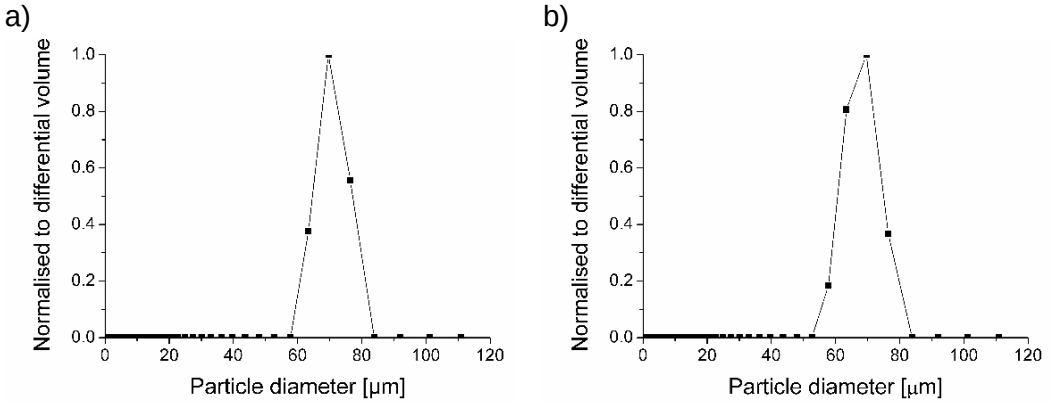


Figure 5.3: The size distribution of co-polymerised microparticles was determined using the Coulter LS230. The particle diameter is plotted against the normalised differential volume for the microfluidic produced blended-before (a) and on-chip (b) co-polymerised EGPEA-TMPTA particles.

Both samples showed an average particle diameter of 70 ± 5 µm, as listed in Table 5.3. Any particles smaller than 20 µm were removed during particle collection by filtering through a nylon mesh. Furthermore, the blended-before co-polymerised samples (span ~ 0.2) revealed overall a smaller polydispersity than the on-chip co-polymerised particles (span ~ 0.3). A potential reason is that the on-chip copolymerisation was more susceptible to the specific physiochemical properties of the monomers themselves rather than the mixed properties in the blending-before copolymerisation. Therefore, the on-chip route resulted in flow instabilities more often, arising from insufficient miscibility of monomers with dissimilar properties such as viscosity values. Moreover, having three inlet channels, instead of two as in the case of blended-before copolymerisation, predispose the process to more failures resulting in larger particle size variations.

Table 5.3: Summary of the particle sizing data obtained for blended-before (bb) and on-chip (on) co-polymerised EGPEA-TMPTA microparticles.

Particle	Average diameter [µm]	Coefficient of variation [%]	Span
EGPEA – TMPTA bb	73.7	6.4	0.20
EGPEA – TMPTA on	70.9	7.7	0.24

5.3.1.2. PARTICLE SHAPE

After applying particle sizing techniques to study the average particle diameter and size uniformity within a sample chemistry, SEM imaging was employed to analyse the shape and surface morphology of the inkjet printed and microfluidic produced microparticles.

INKJET PRINTING PARTICLES

The inkjet printed particles were mostly spherical and revealed smooth surfaces as shown in Figure 5.4. Some small line-like surface features were observed on inkjet printed polyHMDA particles (Figure 5.4 a)), which might be caused by a gold coating that was too thick and began to crack. Analysing microparticles with diameters around 20 µm and smaller presented difficulties to strike the right balance between sufficient resolution and not overcharging the samples as highlighted in Figure 5.4 b).

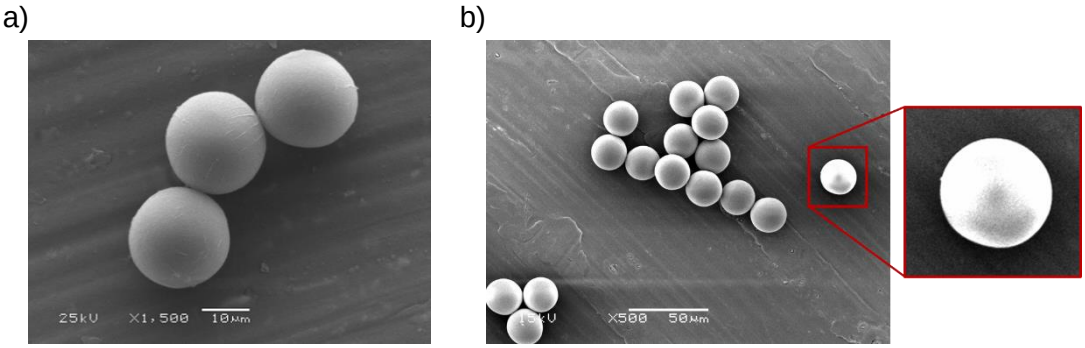


Figure 5.4: SEM images of inkjet printed microparticles revealing smooth surfaces with mostly spherical shapes: a) printed polyHMDA particles exhibited some line-like features on the surface, b) sample charge build-up caused some difficulties during SEM analysis. Microparticles were gold sputter-coated prior to the analysis.

Rather than free-flowing microparticles with smooth surfaces, inkjet printing also resulted in polymeric agglomerations, particle agglomerations and smaller particles as depicted in Figure 5.5. An overall surface roughness was observed on printed polyEGdPEA particles (Figure 5.5 a)) which can be caused by an inhomogeneous gold sputter-coating. Below the particle, polymeric agglomerations were observed, which were cured monomer residues originating from either partially dissolved monomer drops or droplet break-up pieces. In Figure 5.5 b) particle coalescence is shown. The printed polyEGPEA particles coalesced prior to complete curing and obtained their wrinkled surface as a result of shrinkage. Agglomeration of particles, as illustrated in Figure 5.5 c), was observed frequently when inkjet printing a monomer solution into 17 wt% IPA/DIW with 0.1wt% Triton X-100. This is explained in the majority of cases by attachment of partially polymerised microparticles. However, agglomeration of particles can also emerge from sticky or rubbery surfaces of monomers with a glass transition temperature (T_g) below 25°C. Above their T_g, polymer molecules start to move around and finally change from an amorphous rigid to a flexible structure when enough heat is absorbed. Smaller microparticles were also commonly observed using piezoelectric inkjet printing, as outlined in Figure 5.5 d). These smaller particles originated either from break-up of the fluid jet into secondary droplets (satellites) or from droplet split-up when hitting the collecting fluid.

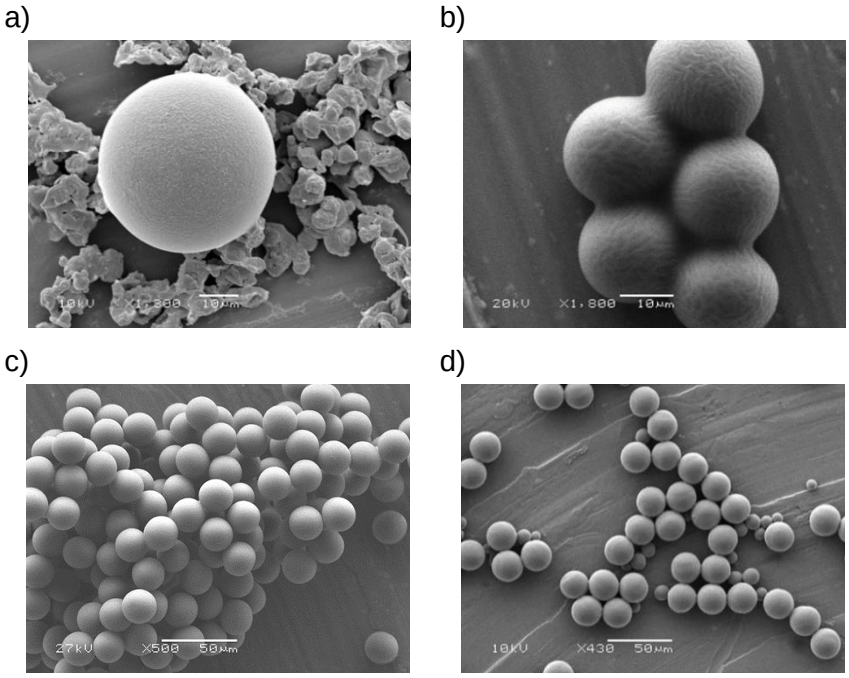


Figure 5.5: SEM micrographs of observations frequently made using inkjet printing: a) polymeric agglomerations with microparticles exhibiting rough features on the surface, b) particles coalesced prior to curing and shrinkage caused a wrinkled appearance, c) particle agglomeration of partially cured microparticles, d) presence of smaller particles emerged from break-up of droplets at the gas-liquid interface.

MICROFLUIDIC PRODUCED PARTICLES

Pushing monomer solutions, prepared from a single monomer, through a microfluidic glass T-junction led to mostly smooth surfaces on perfectly spherical particles. In Figure 5.6, SEM images of microspheres made from the monomers EGdPEA (a) and TMPTA (b) are presented.

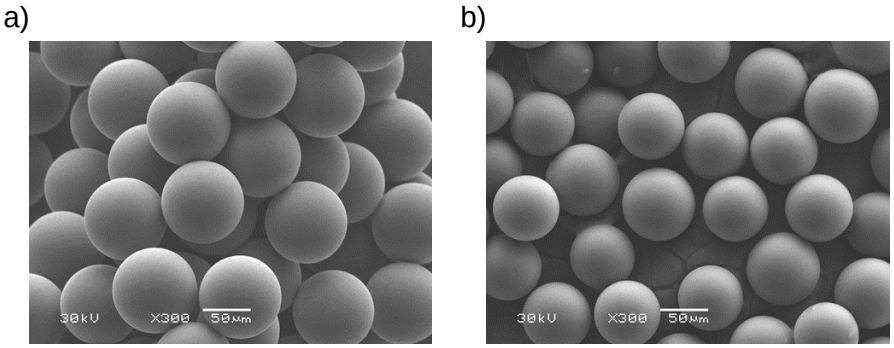


Figure 5.6: SEM images of microfluidic produced particles. The majority of the homopolymeric particles were perfectly spherical in shape and exhibited smooth surfaces as shown for polyEGdPEA (a) and polyTMPTA (b) microspheres.

When analysing the co-polymerised particles for their shape and surface morphology, more imperfections were observed compared to the homopolymeric particles formed by microfluidics. Most of the defects identified are outlined in Figure 5.7 and listed in more detail in Table 5.4. A certain degree of particle asphericity with some surface cracking are presented in Figure 5.7 a). These defects are explained by variation in

curing rates and shrinkage during photopolymerisation. Particle agglomerations (Figure 5.7 b)) and detachment marks (Figure 5.7 c)) were results of coalesced, partially cured particles, which remained either attached or detached leaving an imprint behind. Another common imperfection observed using the microfluidic system were deviation in sizes, leading to smaller (b) or larger particles (c), arisen by flow instabilities. Particle breakages, as illustrated in Figure 5.7 d), only occurred with the monomer combination HMDA-FuMA when co-polymerised directly in the microfluidic chip (on-chip).

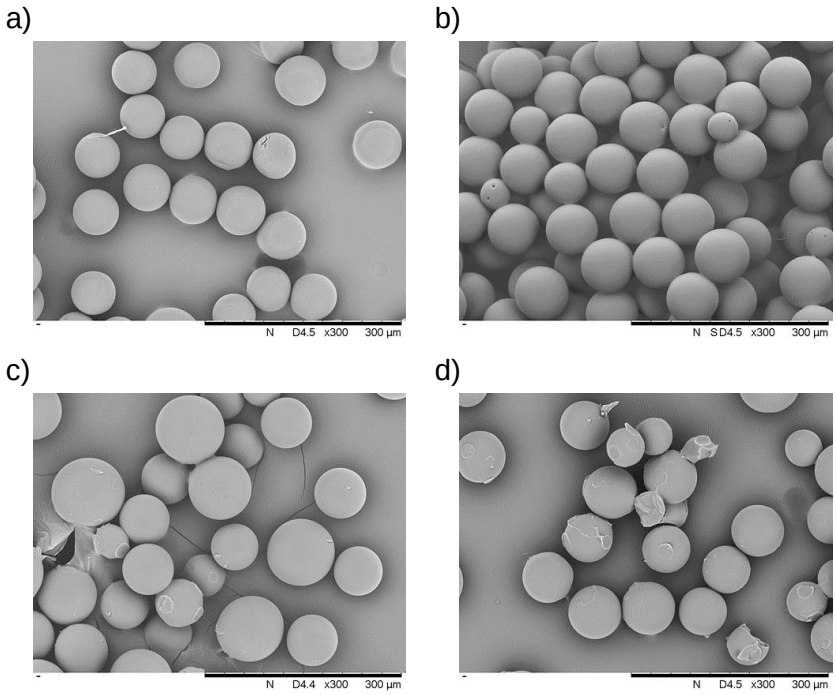
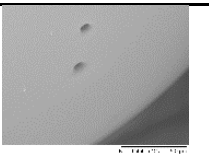
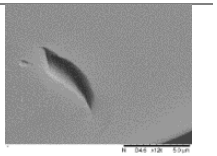
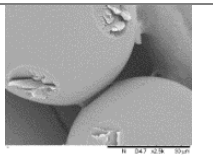
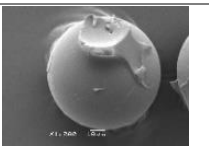
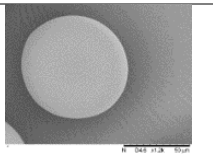
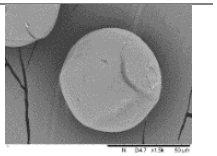
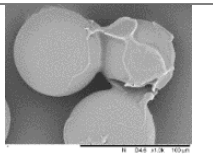


Figure 5.7: SEM micrographs of different defects observed mostly on co-polymerised particles fabricated utilising glass microfluidic chips: a) some degree of asphericity and surface cracking, b) particle agglomeration with few smaller particles revealing surface holes, c) polydispersity and some detachment marks visible on particle surfaces, d) broken microspheres and particles with polymeric residues attached.

All defects observed on microfluidic produced particles are summarised with a defect description, cause and an image by way of illustration in Table 5.4.

Table 5.4: Summary of possible defects observed on microfluidic produced microparticles and their origin.

Defect	Defect Cause	Example
Surface porosity	Caused by air bubbles in monomer solution	
Surface cracking	Caused by solvent evaporation or shrinkage	
Detachment marks	Caused by detachment of partially cured particles or monomers with T_g below 25°	
Polymer residues	Curing issue: agglomerated particles break apart and leave behind a larger amount of material	
Asphericity	Caused by inhomogeneous curing or anisotropic solvent evaporation	
Waviness	Caused by a volume shrinkage due to solvent evaporation or curing	
Particle agglomeration	Caused by attachment of incomplete polymerised samples or monomers with T_g below 25°C	

In order to find correlations between defects and monomer solutions, the incidence of defects were plotted using radar graphs as shown in Figure 5.8. The number of defects present is represented on the normalised scale as discussed in Section 5.2.1. Microspheres made from the monomer HPhOPA revealed throughout the most defects. As seen from Figure 5.8, detachment marks and surface pores were detected most, followed by asphericity. Furthermore, imperfections such as detachment marks, pores and particle agglomerations were also detected frequently on microfluidic produced polyEGdPEA and polyEGPEA particles. Due to the fact that most defects were observed on polyHPhOPA particles, which required 33.5 wt% ethyl aceteate for successful particle fabrication, uncontrollable solvent evaporation was thought to be the main cause for defect development. Moreover, the monomers HPhOPA, EGdPEA and EGPEA are all monoacrylates, presenting only one functional acrylate C=C bond, and they also exhibit a T_g below 25°C. The number of functional acrylate C=C bonds affected the curing kinetics as discussed in Section 4.3.2. Having only one functional acrylate C=C group resulted in lower polymerisation rates compared to similar compounds with two C=C groups. In addition, presenting a low T_g does not have a favourable effect on particle formation since polymers become rubbery at elevated temperatures (>25°C) promoting particle agglomeration even after manufacture.

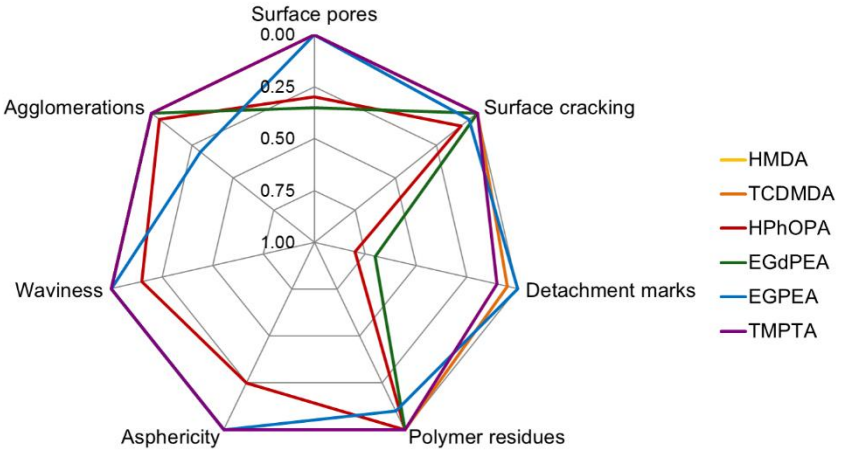


Figure 5.8: The relation between incidence of defects and monomer identity is plotted for homopolymeric microparticles fabricated using microfluidics. The scale is based on 0 indicating no defects and 1 containing a defect on every particle.

In order to check whether the monomers HPhOPA, EGdPEA and EGPEA also promoted defects when being co-polymerised, radar graphs were also generated for the two different copolymerisation routes. From Figure 5.9, it can be seen that 50% and 33.3% of all co-polymerised particles containing HPhOPA, EGdPEA and EGPEA revealed defects in case of blended-before and on-chip copolymerisation, respectively. A monomer solution was only included into the percentage calculation if defects were present (>0.25) in the sample range of ten micrographs. Furthermore, accumulations

of imperfections were detected on co-polymerised blended-before FuMA-TMPTA and on-chip HMDA-FuMA microparticles. These generated particles share an amount of 50% or more FuMA that presented curing issues as already outlined in Section 4.3.4.1. In contrast, on-chip co-polymerised FuMA-TMPTA microspheres, which were formed applying a flow rate of 0.05 ml/h for both monomers (Appendix H), exhibited only a few detachment marks. Consequently, the triacrylate monomer (TMPTA) was able to increase the overall crosslinking density of the co-monomer compound due to several unsaturated double bonds leading to faster curing. It was concluded that a higher tendency to crosslink resulted in fewer defects.

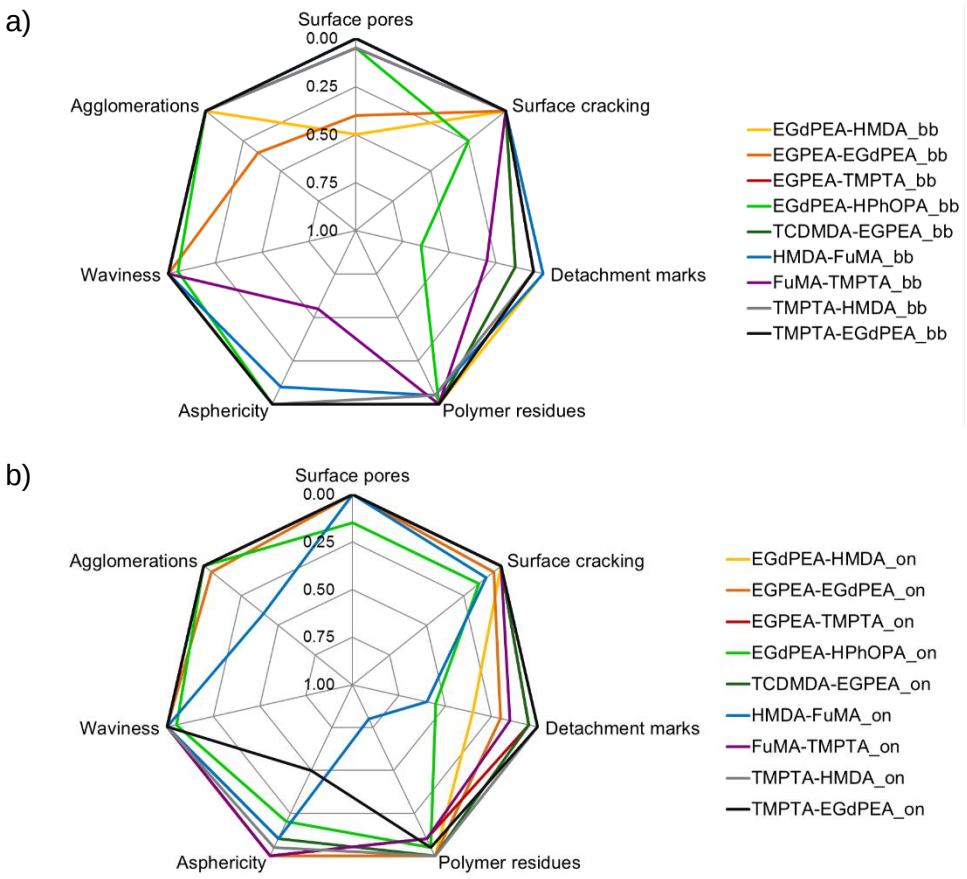


Figure 5.9: The relations between incidence of defects and monomer identity are plotted for blended-before (a) and on-chip (b) co-polymerised microparticles fabricated using microfluidic glass chips. The scale is based on 0 indicating no defects and 1 containing a defect on every particle.

5.3.1.3. Surface Roughness

Homopolymeric Microparticles

AFM analysis was employed to characterise differences in topography between inkjet printed and microfluidic produced microparticles but also between the various particle

chemistries. In Figure 5.10, the average roughness is shown for six different particle chemistries fabricated using piezoelectric inkjet printing and microfluidics.

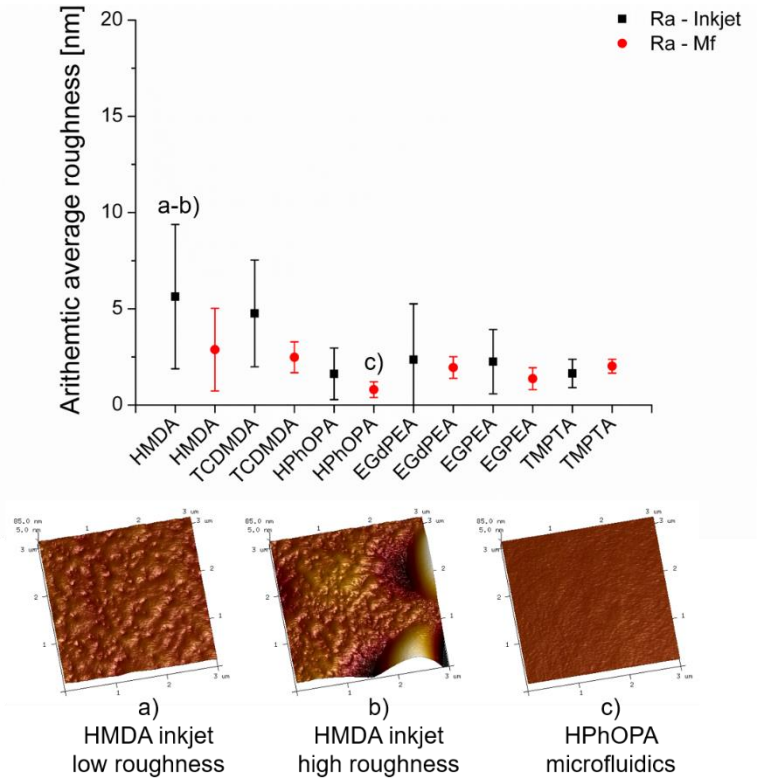


Figure 5.10: Arithmetic average roughness derived from AFM measurements is presented for inkjet printed (black) and microfluidic produced (red) microparticles. Roughness values were calculated from 5 randomly selected particles within a sample aliquot, whereas areas of 3 × 3 µm were analysed on top of the particles. 3D topographical images (z-axis range: 160 nm) are shown for the highlighted letters.

The microfluidic produced particles exhibited fewer topographical features throughout all chemistries compared to the printed particles. This finding was expected since microfluidic droplets, unlike inkjet printed droplets, did not cross any phase boundaries causing severe disruptions. In microfluidics, particles were formed at the T-junction by shear forces followed by transporting them through the channel by means of continuous flow. Inkjet printed droplets, on the contrary, were formed by breaking up of a stream of fluid due to instabilities in surface tension. The ejected droplets travelled through a gaseous environment until hitting the collecting fluid at which point impact forces acted upon microspheres inducing viscoelastic deformation. The extent of deformation depends on the dimension of acting forces and curing state at the time of impact. Both parameters were variable which might explain the broad roughness distribution within most samples as illustrated by the printed polyHMDA particles in Figure 5.10 a-b). The images, a) and b), clarify that the broad roughness deviation within a sample chemistry emerged from single features on the surface rather than from the overall surface roughness. This is reinforced by the relatively low averaged roughness values but broad deviations. In addition, particles consisting of

polyHPhOPA, polyEGdPEA or polyEGPEA, on which most imperfections were detected (described in Section 5.3.1.2), did not reveal significantly higher roughness values compared to particles with less defects. Therefore, it was concluded that the arithmetic average roughness is mainly affected by the predominant surface roughness. Single features on particles did not significantly influence the average but affected the width of the standard deviation in this work. The reason is that the area of analysis and sample quantities were small and predefined by the AFM tip geometry. Therefore, in order to get a complete overview of the surface topographies on particles, SEM imaging should be used as a complementary technique as it allows for a relatively fast and large-scale characterisation of microparticles exhibiting micrometre-sized imperfections. AFM analysis should be selected as the primary technique since SEM imaging exhibits limitations for detecting subtle topographies. The limitations arise from the gold coating and the analysis depth of the electron beam (~3 µm).

CO-POLYMERISED MICROPARTICLES

Comparing the surface topographies of blended-before and on-chip co-polymerised microfluidic particles, graphically shown in Figure 5.11, the blended-before co-polymerised particles had lower surface roughness throughout all six studied chemistries. This observation is explained by better mixing of the monomer solutions when pre-blended compared to blended directly in the microfluidic glass chip. Blending in the chip was limited to some extent because it occurred by diffusion and flow recirculation. Recirculation of the flow was caused by shearing interactions of the dispersed phase with the stationary channel wall [265]. Moreover, it needs to be considered that the monomer ratios in microparticles produced on-chip did not always match the 70-30 wt% ratio maintained in blended-before particles due to differently adjusted flow rates (Appendix H). However, as seen from Figure 5.10, the arithmetic average roughness of the six homopolymers did not differ significantly. Consequently, it was assumed that deviations in monomer ratio did not cause the obtained differences in roughness.

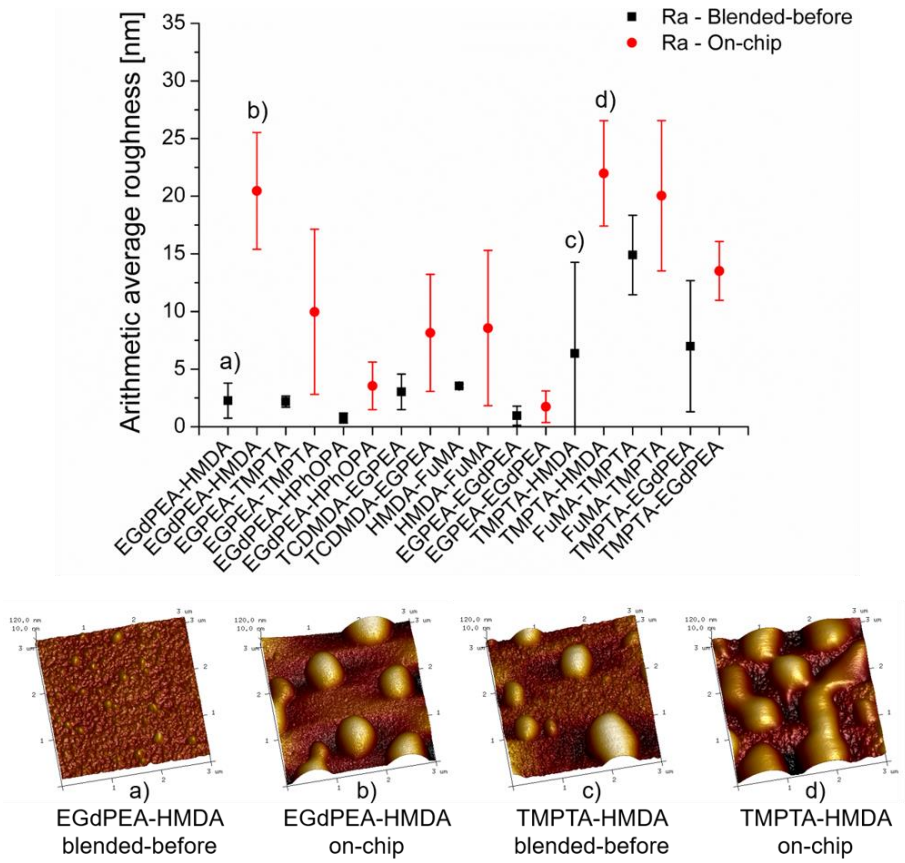


Figure 5.11: AFM derived arithmetic average roughness is illustrated for blended-before (black) and on-chip (red) co-polymerised microfluidic microparticles. Roughness values were calculated from 5 randomly selected particles within a sample aliquot, whereas areas of 3 × 3 µm were analysed on top of the particles. 3D topographical images (z-axis range: 220 nm) are shown for the highlighted letters.

Heterogeneous surfaces were only observed on blended-before TMPTA-HMDA, TMPTA-EGdPEA and FuMA-TMPTA co-polymerised particles which indicated phase separated morphologies. By studying the relation between occurrence of phase separation and co-monomer properties, a trend was found which indicates that co-monomers with large differences in the molecular descriptor parameter α resulted in continuous and discontinuous phase separated morphologies (Figure 5.12). The parameter α is defined as follows (Eq. 5.2):

$$\alpha = 0.44 \times n\mathrm{RoTB} - c\log P \qquad \text{Eq. 5.2}$$

where $n\mathrm{RoTB}$ is the number of rotatable bonds and $c\log P$ is the calculated log octanol/water partition coefficient (measure of hydrophilicity) [283]. The molecular physiochemical properties of the monomers are listed in Appendix J.

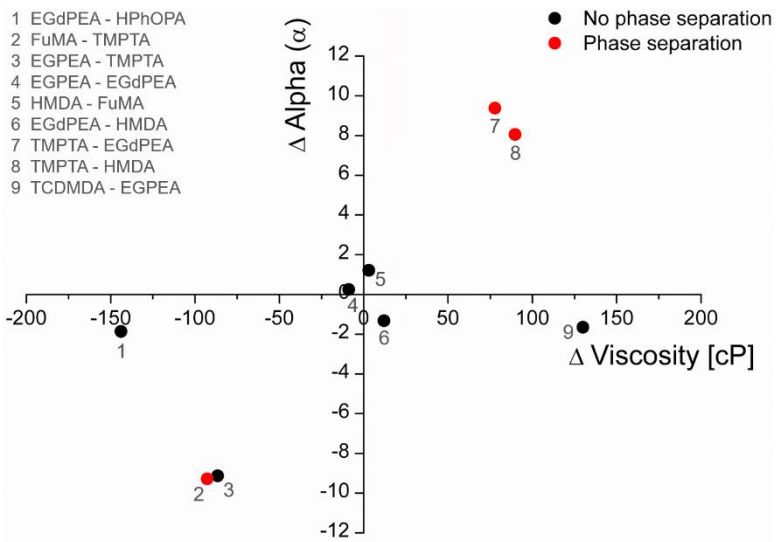


Figure 5.12: Graph revealing a trend that pre-blended co-monomers with large differences in the molecular descriptor parameter α exhibited continuous and discontinuous phase separated morphologies.

Blended-before co-polymerised EGPEA-TMPTA microparticles constituted an exception to this trend; the co-monomer exhibited a large difference in the molecular descriptor parameter α but did not result in phase separation. Therefore, it was hypothesised that phase separated morphologies are associated to pre-blended co-monomers containing TMPTA due to its large α value but only when TMPTA predominantly determined the curing kinetics. Variations in the dimensions of the bump-like features are the reason for the broader roughness distribution.

Employing the on-chip copolymerisation route, 88.9% of the produced particles revealed continuous and discontinuous phase separated morphologies. However, particles made from HMDA-FuMA and EGdPEA-HPhOPA exhibited partially smooth and partially heterogeneous surfaces. The only on-chip co-polymerised particles, which did not show any surface heterogeneities, were fabricated from the two monomers with similar properties, EGPEA-EGdPEA. A list of the monomer combinations used in both copolymerisation approaches is given in Table 5.5, where the occurrence of phase separation is highlighted as red.

Table 5.5: List of the monomer combinations and their occurrence of continuous and discontinuous phase separated morphologies using blended-before and on-chip copolymerisation: no phase separation (green), phase separation (red) and partial phase separation (purple).

Monomer combination	Blended-before copolymerisation	On-chip copolymerisation
EGdPEA - HMDA		
EGPEA - EGdPEA		
EGPEA - TMPTA		
EGdPEA - HPhOPA		
TCDMDA - EGPEA		
HMDA - FuMA		
FuMA - TMPTA		
TMPTA - HMDA		
TMPTA - EGdPEA		

It was concluded that the phase separated morphologies most likely originated from partial miscibility of the monomers applied. The images provide an exaggerated view of the surfaces for improved visibility in representation. Generally, the circular features were relatively flat with a maximum height of ~120 nm.

5.3.2. Assessment of Microparticle Surface Chemistries

5.3.2.1. Removal of Silicon-based Contamination

The surface chemistry of inkjet printed and microfluidic produced microparticles was assessed using ToF-SIMS. Overall the ToF-SIMS spectra revealed a significant peak at m/z = 73 in the positive ion spectra which is representative of $[Si(CH_3)_3]^+$ [284]. This peak arises from any kind of PDMS contamination when seen with m/z = 147 in the positive polarity which is characteristic for $[Si(CH_3)_3OSi(CH_3)_2]^+$. These findings are illustrated for on-chip co-polymerised EGPEA-TMPTA microparticles in Figure 5.13.

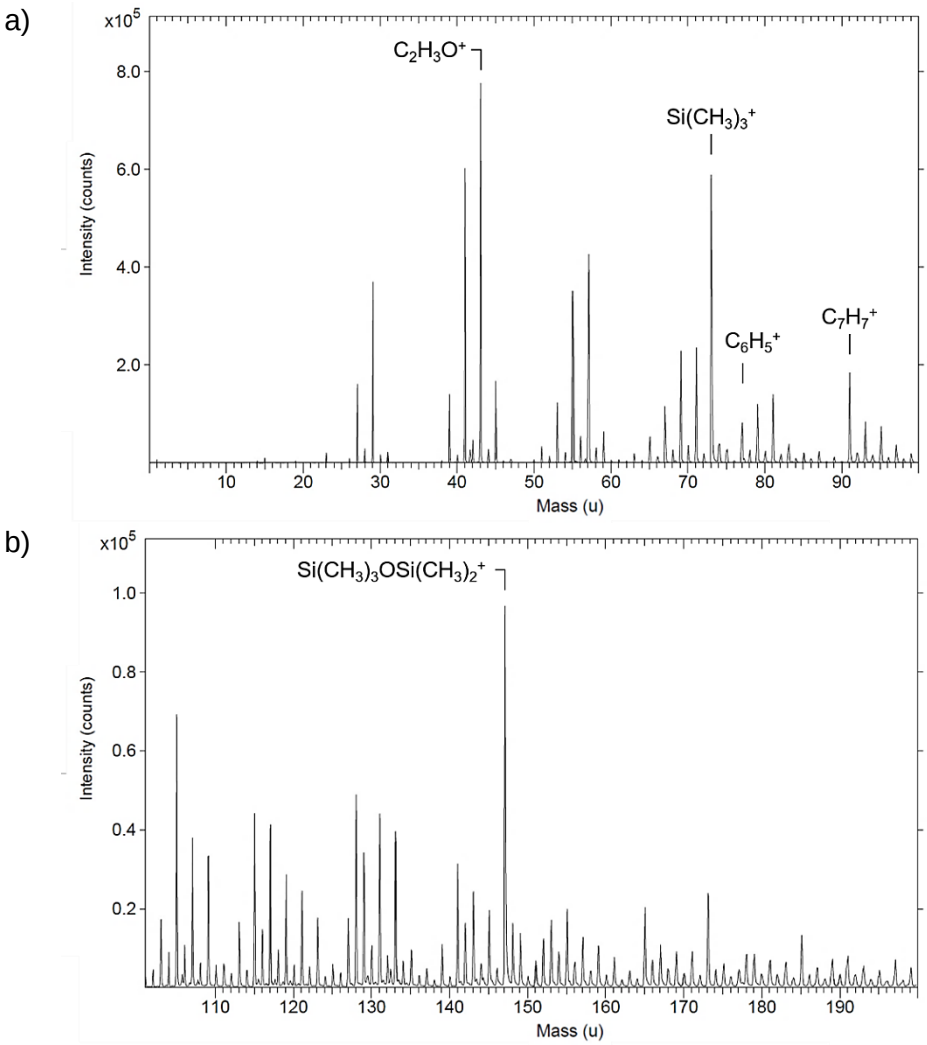


Figure 5.13: Positive ToF-SIMS spectra of the surface of on-chip co-polymerised EGPEA-TMPTA microparticles from a mass of: a) 0-100 u, b) 101-200 u. Peaks used in the subsequent analysis are labelled.

CAUSE OF SILICONE CONTAMINATION

By searching for the underlying cause of the silicone contamination within both fabrication methodologies, it was determined that plastic syringes were used for filtration of monomer solutions and for transporting inks to the cartridges in case of inkjet printing. FTIR-ATR studies were performed on a cross-linked PDMS sample (reference), evaporated acetone after being shaken in a plastic syringe and unwashed on-chip co-polymerised EGPEA-TMPTA microparticles in order to evaluate and compare chemical groups present. The spectra obtained are illustrated in Figure 5.14.

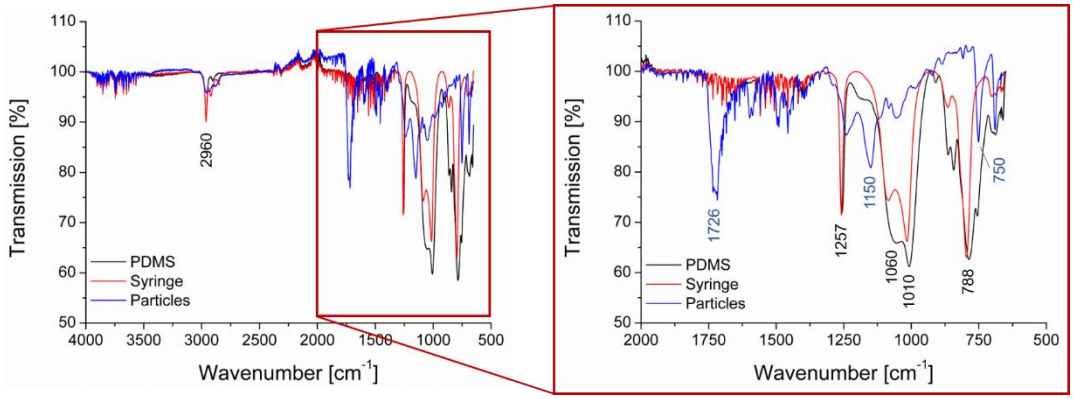


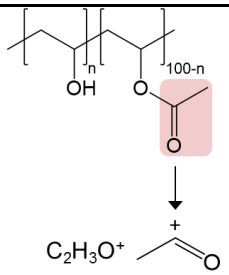
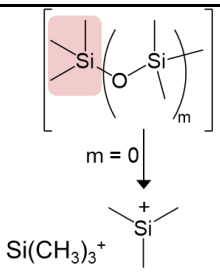
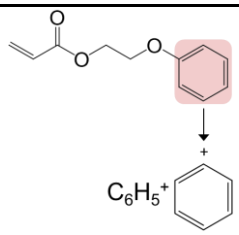
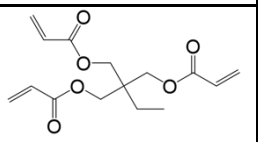
Figure 5.14: FTIR-ATR spectra of crosslinked PDMS (reference, black), evaporated acetone after being shaken in plastic syringe (red) and unwashed on-chip co-polymerised EGPEA-TMPTA particles (blue) are shown for wavenumbers ranging from 4000-500 cm^{-1}. Zoomed-in image displays a section of the spectra ranging from 2000-500 cm^{-1}.

PDMS sample displayed characteristic infrared bands at 2960 cm^{-1} (asymmetric CH_3 stretch), 1257 cm^{-1} (CH_3 symmetric bending), 1060 cm^{-1} and 1010 cm^{-1} doublet (Si-O-Si stretching vibrations) and 788 cm^{-1} (Si-C stretching, CH_3 rocking). Substances measured from the plastic syringe interior were characterised by the same major peaks as detected for PDMS. In case of the unwashed on-chip co-polymerised EGPEA-TMPTA particles, characteristic major peaks were identified at 1726 cm^{-1} (ester C=O bond stretching), 1150 cm^{-1} (ester C-O stretching) and 750 cm^{-1} (monosubstituted benzene C-H bending). Minor characteristic infrared bands, though, were seen at 2960 cm^{-1}, 1240 cm^{-1}, 1052 cm^{-1} and 690 cm^{-1} (monosubstituted benzene C-H bending). The minor peaks at 2960 cm^{-1}, 1240 cm^{-1} and 1052 cm^{-1} were most likely derived from the silicone contamination. These observations provided further evidence that plastic syringes were the origin of contamination due to their lubricant coating in the interior.

Extensive Washing of Microfluidic Produced Particles

Microfluidic particles generated on-chip from EGPEA-TMPTA were extensively washed and assessed for a reduction in the peak intensity of the fragments obtained from the PDMS fingerprint. The chemical compounds and their fragmentation into the diagnostic ions of PVA, the monomers and silicone contamination are presented in Table 5.6. The phenylium ion $[C_6H_5]^+$ fragmented from both the monomer EGPEA and photoinitiator DMPA, hence, characteristic for the monomer solution. In case of monomer TMPTA, it was difficult to find a unique ion because the SIMS spectra were characterised by ions derived from the acrylate group and short hydrocarbon fragments. These fragments could likely also be assigned to the PVA compound. The tropylium ion $[C_7H_7]^+$, prominent at m/z=91 in Figure 5.13, fragmented also from the photoinitiator.

Table 5.6: Structure of the monomers (EGPEA, TMPTA), stabiliser PVA, silicone contamination and their representative ions emerged during ToF-SIMS analysis.

PVA	Silicone contamination	Monomer EGPEA	Monomer TMPTA
			
n = % hydrolysis from poly(vinyl acetate)	m = 0, 1, 2, 3 m/z: 73, 147, 221, 295		

In Figure 5.15, the proportion of total counts (%) of three representative ions is illustrated for the washing solvents utilised. It can be seen that the peak intensity of the contamination fragment trimethylsilyl ion ($[Si(CH_3)_3]^+$) was larger compared to the intensity obtained for the PVA and monomer fragment. However, the appearance of the phenylium, which is characteristic for the monomer EGPEA and photoinitiator DMPA, indicated that the silicone contamination did not completely cover the co-polymer itself. Washing the microparticles led to a decrease in the intensity of the acetyl cation ($[C_2H_3O]^+$) up to 12.8% when applying the solvent Silstrip Liquid, as shown in Figure 5.15 a). This observation indicated a partial removal of the PVA surfactant layer. In contrast, the trimethylsilyl ion intensity increased up to 9.5% when sonicating in solvents, as depicted in Figure 5.15 b). Due to the inability to remove the contamination from the particle surfaces, regardless of the solvent used, it was concluded that the contamination was entangled into the co-polymer structure. The increase of the trimethylsilyl ion total counts is explained by the well-known silicone contamination problem [285]. Oligomeric components of crosslinked PDMS are able to spread, hence increase the amount of contamination by migration from the bulk to surrounding surfaces because of the high mobility of PDMS oligomers.

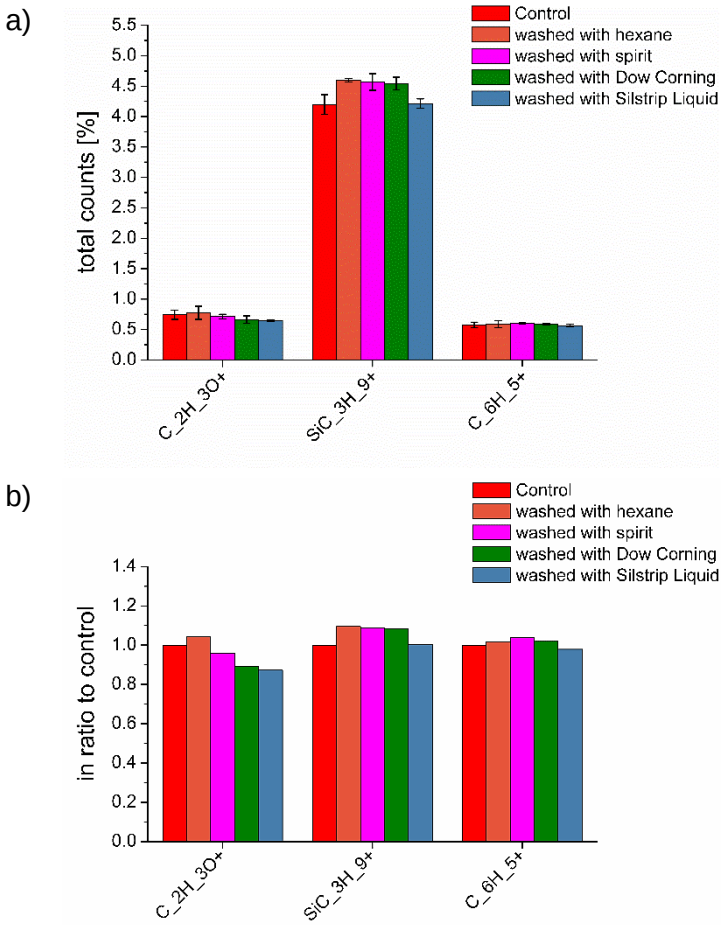


Figure 5.15: Microfluidic on-chip co-polymerised EGPEA-TMPTA particles were washed with four different solvents (hexane, methylated spirit, Dow Corning, Silstrip Liquid) and assessed for their surface chemistry in the positive polarity: a) proportion of total counts [%] with its standard deviation and b) proportion of total counts in relation to the unwashed sample (control) are shown for three representative ions: $C_2H_3O^+$ (PVA), $Si(CH_3)_3^+$ (contamination), $C_6H_5^+$ (monomer).

Utilising the representative ions mentioned above, the ToF-SIMS spectra were reconstructed as images to analyse the distribution of PVA, silicone contamination and co-polymer at the surface of microfluidic produced particles. Figure 5.16 exhibits ToF-SIMS overlay images of PVA (red), silicone contamination (green) and co-polymer (blue) for unwashed (a) and washed by sonicating in Silstrip Liquid (b) on-chip co-polymerised EGPEA-TMPTA microparticles. Focusing on the unwashed particles (Figure 5.16 a)), a small spot of red is visible which indicates that PVA coverage was most likely inhomogeneous. In contrast, the washed microparticles did not reveal any accumulation of PVA on the surface, as illustrated in Figure 5.16 b). A possible reason is the partial removal of PVA through washing. Both images shared an almost complete coverage of silicone contamination at the surface. Both facts, the entanglement of the silicone contamination into the co-polymer structure and being present as an almost complete layer, indicated that the contamination must have occurred before droplet generation.

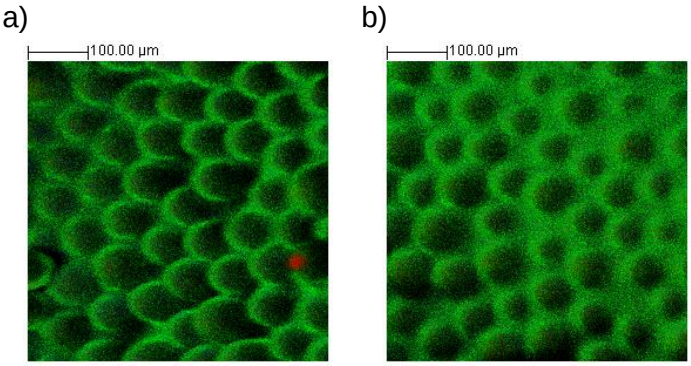


Figure 5.16: ToF-SIMS images displaying an overlay of the characteristic cations ($C_2H_3O^+$ (red, PVA), $Si(CH_3)_3^+$ (green, contamination), $C_6H_5^+$ (blue, monomer)) identified within the ToF-SIMS spectra for: a) unwashed on-chip co-polymerised EGPEA-TMPTA particles, b) on-chip co-polymerised EGPEA-TMPTA microparticles washed with Silstrip Liquid.

SEM images were taken of each sample after extensive washing. The particles appeared unchanged when washing with hexane, methylated spirits and Dow Corning. However, sonicating in Silstrip Liquid resulted in dimpling of particles as depicted in Figure 5.17 b). A SEM image of the unwashed on-chip co-polymerised EGPEA-TMPTA microparticles is provided for comparison in Figure 5.17 a). These dimples in the particle surfaces may arise by dissolution of the co-polymer caused by the hydrotreated light distillate. This substance constituted more than 90% in Silstrip Liquid whereas Dow Corning, which did not cause any particle alterations, composed of 70-90% of hydrotreated light distillate.

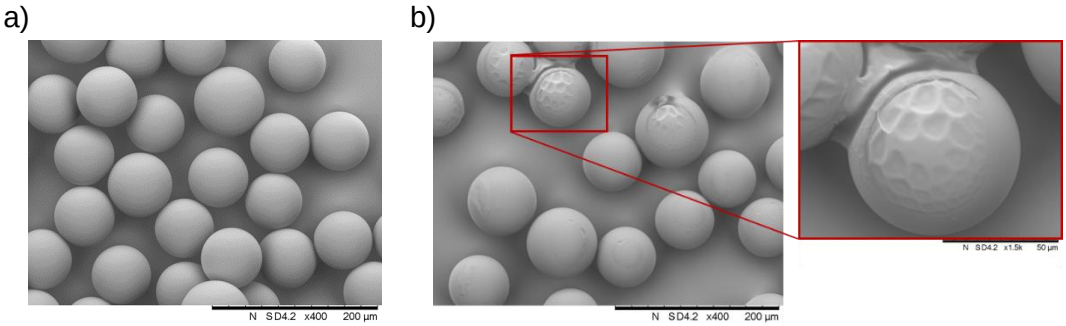


Figure 5.17: SEM micrographs presenting on-chip co-copolymerised EGPEA-TMPTA particles: a) unwashed as a control, b) after extensive washing applying Silstrip Liquid.

5.3.2.2. PVA Coverage on Particles

ToF-SIMS analysis was used to characterise microfluidic produced EGdPEA particles for presence of PVA surfactant on their surfaces. In order to assess whether PVA was physically adsorbed or crosslinked into the polymer particles, aliquots of particles were washed varying the number of wash cycles. Initially, SIMS spectra of PVA powder and pipetted thin film made of polyEGdPEA were acquired which served as a reference for PVA and a control for the polymer itself, without containing PVA, respectively. The

secondary ions which were most dominant for tracking PVA arose from the unhydrolysed vinyl acetate component within the 88% hydrolysed PVA (Mw 25,000) used as control and particle surfactant in this work. In the negative ion spectrum, the peak found at m/z = 59 corresponded to the acetate anion $[CH_3COO]^-$ whose fragmentation is illustrated in Figure 5.18 a). The base peak in the positive ion spectrum was observed at m/z = 43 representing the acetyl cation $[CH_3CO]^+$ which had previously been reported as a diagnostic peak for PVA [286]. Both peaks, however, can not only be attributed to the acetate anion and acetyl cation from the PVA surfactant, respectively, but also to secondary ions derived from the polymer itself. This was confirmed by the polyEGdPEA film which exhibited peaks at the same m/z positions, as shown to be representative for the PVA surfactant, in both secondary ion polarities. In Figure 5.18 b), the proportion of total counts of the acetate anion are plotted against the polyEGdPEA particles varying in wash cycles and its corresponding pipetted thin film.

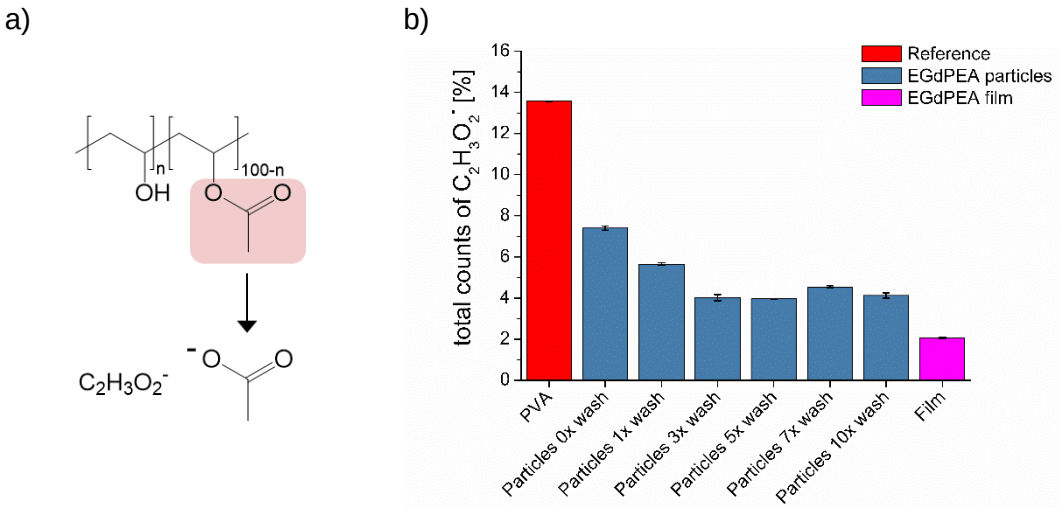


Figure 5.18: ToF-SIMS data acquired in the negative ion polarity are showing: a) the fragmentation of the poly(vinyl alcohol-co-vinyl acetate) (PVA) compound into the acetate anion (CH_3COO^-, m/z = 59), b) the proportion of total counts [%] of the acetate anion with its standard deviation for the polyEGdPEA particles varying in wash cycles and its corresponding pipetted thin film. PVA (Mw 25,000) with a hydrolysis degree of 88% was used as control and particle surfactant.

The graph revealed a reduction in intensity of the acetate anion with increased washing. A gradual decrease of 45.7% was noticed from particles as produced (Particles 0x wash) to the third wash cycle. From the 3rd to the 10th wash cycle, the normalised counts (%) of the PVA characteristic secondary ion remained reasonably constant without any significant changes. Slightly increased values, however, were found on microparticles after the 7th wash. One of the reasons maybe is that particles, which were agglomerated during washing, became separated in the sample preparation for the ToF-SIMS study. Consequently, not all particles were washed with the same efficiency leaving a higher amount of surfactant behind. The same

observations were made when considering the acetyl cation in the positive ion SIMS spectra.

A secondary ion specific to the EGdPEA polymer, $C_5H_5^-$, was selected and its fragmentation is depicted in Figure 5.19 a). By showing the percentage of total counts of the cyclopentadienyl anion ($C_5H_5^-$) in ratio to the percentage of total counts for the acetate anion (m/z = 59), an increase of 264.2% was observed for the cyclopentadienyl anion when washing the microparticles three times (Figure 5.19 b)). The increase of the anion characteristic for the EGdPEA fragment was inversely proportional to the decrease found in the PVA compound, confirming that the PVA surfactant was removed from the particle surfaces. However, since the intensity of the EGdPEA polymer specific fragment after extensive washing did not match the intensity obtained for the polyEGdPEA film (control), only a partial reduction was observed. Consequently, it was postulated that most of the PVA surfactant was embedded into the polymeric particle surface preventing its complete removal.

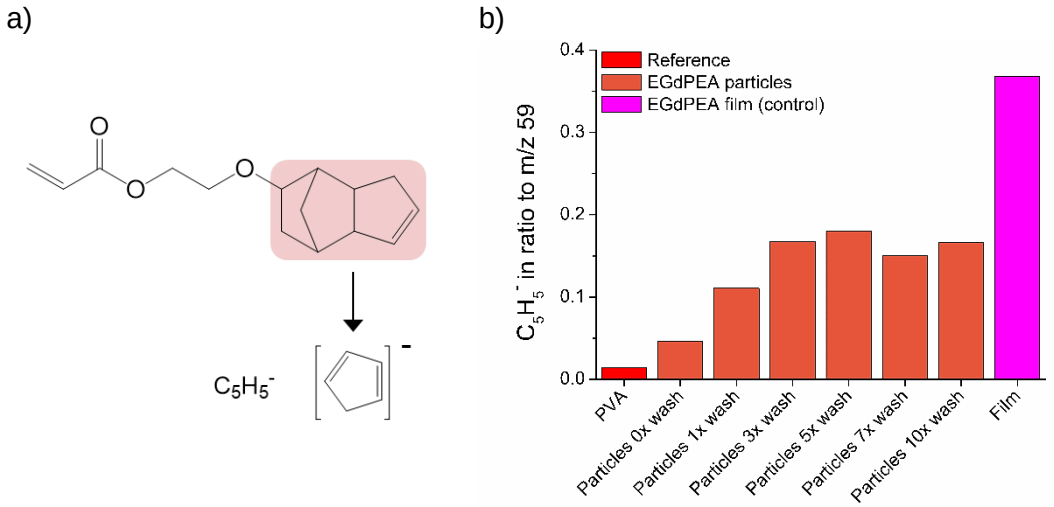


Figure 5.19: ToF-SIMS data acquired in the negative ion polarity are showing: a) the fragmentation of the monomer EGdPEA into the cyclopentadienyl anion ($C_5H_5^-$), b) the ratio of the cyclopentadienyl anion to the acetate anion (m/z = 59) for the polyEGdPEA particles varying in wash cycles and its corresponding pipetted thin film.

Applying the characteristic ions, $C_2H_3O_2^-$ and $C_5H_5^-$, the ToF-SIMS spectra were reconstructed as images to analyse the distribution of PVA and EGdPEA on the surfaces. Figure 5.20 shows the overlay of PVA (red) and EGdPEA (blue) for the pipetted thin film (a), particles as produced (b) and after 10 washes (c). The pipetted thin film revealed a homogeneous distribution of the two diagnostic ions across the surface. In contrast, the untreated EGdPEA particle surfaces (no washing) were almost fully covered by the PVA surfactant such that the $C_5H_5^-$ characteristic ion ratio to the PVA was only 0.05. There were only a few spots were EGdPEA appeared in the image indicating that the PVA was a discontinuous layer (Figure 5.20 b)). Comparing the ToF-

SIMS image of the microparticles as produced (b) with the image of the extensively washed particles (c), a significant reduction in PVA was observed which resulted in increased detection of the cyclopentadienyl anion derived from the EGdPEA polymer.

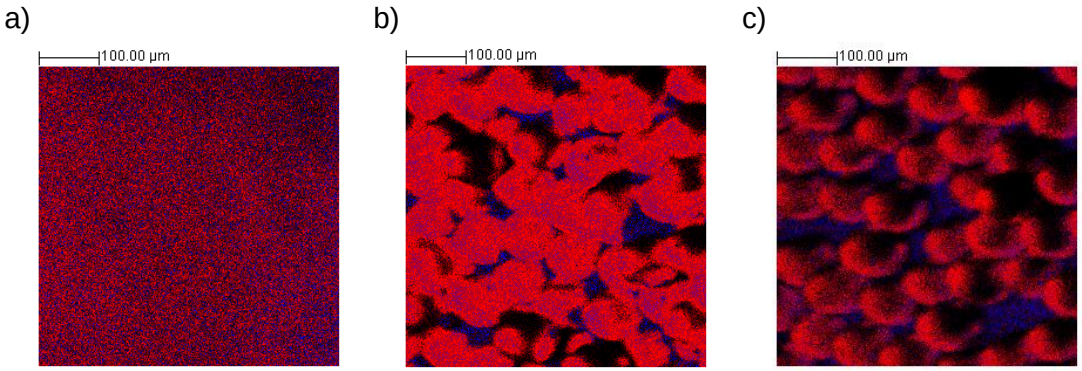


Figure 5.20: Negative ToF-SIMS imaging showing the overlay of CH_3COO^- (red, PVA) and $C_5H_5^-$ (blue, EGdPEA) for: a) pipetted thin film, b) untreated microspheres, c) particles after performing 10 wash cycles.

The distribution of PVA was further examined on microparticles after the first wash because microfluidic produced particles were normally washed once with PBS before being tested for bacterial attachment. As illustrated in Figure 5.21, the concentration of PVA surfactant varied within a sample aliquot.

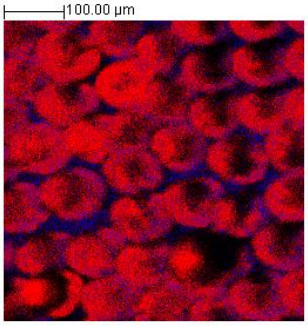


Figure 5.21: Negative ToF-SIMS imaging revealing the inhomogeneous distribution of PVA surfactant on microparticles after the first wash. An overlay of CH_3COO^- (red, PVA) and $C_5H_5^-$ (blue, EGdPEA) is shown.

5.3.3. Comparison between Inkjet Printing and Microfluidics

The two particle fabrication techniques, piezoelectric inkjet printing and microfluidics, are mainly compared in terms of their particle characteristics. A few pros and cons of the methods themselves are also listed in Table 5.7 for gaining a better understanding of the results obtained.

Table 5.7: Comparison between piezoelectric inkjet printing and microfluidics in terms of the methods and particle characteristics (particle size, size distribution, shape, surface topography and chemistry). Advantages and disadvantages are highlighted in green and red, respectively.

Characteristics	Piezoelectric inkjet printing	Microfluidics
Method	limited to printing from above which leads to phase boundary crossing by droplets	larger particle yield; greater chemical diversity due to feasibility of on-chip copolymerisation
Particle size	limited to ~20 µm due to nozzle orifice	wider range of sizes possible by adjusting phase flow rates or employing chips with different channel dimensions; particles with ~80 µm in size produced
Size distribution	up to three times broader size distributions due to print instabilities (satellites) and collecting fluid perturbations	narrow size distribution; instabilities in flow conditions may result in smaller or larger particles
Shapes	microparticles mostly spherical but some degree of asphericity detected; besides free-flowing particles, particle agglomerations and polymeric agglomerations observed	majority of particles spherical; defects including pores, surface cracking, detachment marks, particle agglomerations mostly found on co-polymerised particles
Surface topography	broader roughness distribution due to variability in viscoelastic deformation	smoother surfaces with narrower roughness distribution; continuous and discontinuous phase separated morphologies revealed on some co-polymerised particles
Surface chemistry	silicone contamination from plastic syringe; residues of Triton X-100 (surfactant) detected	silicone contamination from plastic syringe; discontinuous PVA surfactant layer detected

By comparing the two techniques, microfluidics proved to be the superior method for fabricating particles. Microparticles produced by microfluidics revealed better particle properties than the inkjet printed particles. Moreover, greater process stability was achieved, resulting in larger particle yield. Another merit of microfluidics is that a greater chemical diversity can be achieved by blending monomer solutions not only beforehand (blending-before) but also at the actual state of droplet generation (on-chip). Inkjet printing allows only blending-before copolymerisation, which has not been conducted due to its instability of particle manufacture.

5.4. SUMMARY

The focus of this chapter was an in-depth physical and chemical characterisation of the generated inkjet printed and microfluidic produced microparticles. Specifically, the surface chemistry and topography were of great interest due to the key role of the outermost layers of the surface in biological-material interactions. Particle sizing data showed average diameters of 20 ± 5 µm and 75 ± 5 µm for printed and microfluidic particles, respectively. Microparticles produced with the Dimatix printer exhibited up to three times broader size distributions compared to microfluidics, which was calculated by using the relative span. Surface morphology studies performed utilising SEM imaging revealed mostly spherical particles for both fabrication methodologies. However, printed particles presented some degree of asphericity whereas particles formed in the microfluidic glass chip were perfectly spherical. Furthermore, piezoelectric inkjet printing often also resulted in polymer and particle agglomerations including both smaller and larger microparticles. Some defects, such as surface porosity, cracking, detachment marks and particle agglomerations, were also detected on microfluidic produced particles, especially on co-polymerised microparticles. By assessing the relations between the incidence of defects and monomer identity using radar graphs, mono-functional monomers with a T_g below RT were found to be susceptible to imperfections. This observation was explained by insufficient photopolymerisation rate due to low numbers of functional C=C double bonds and also by unfavourable rubbery properties at elevated temperatures ($T > T_g$). Therefore, it was concluded that materials with a higher tendency to crosslink showed fewer defects. Surface topography characterisation (AFM analysis) of microparticles revealed less topographical features on microfluidic produced particles compared to inkjet printed particles. It was shown that the arithmetic average roughness was mainly affected by the predominant surface roughness rather than by single surface features. However, surface imperfections contributed to broaden the width of the standard deviation. Comparing the blended-before with the on-chip co-polymerised microfluidic particles, lower surface roughness was observed on blended-before co-polymerised particles. Surface features, which look like continuous and discontinuous phase separated morphologies, were detected on 33.3% of the blended-before and 88.9% of the on-chip co-polymerised particles which most likely arose from partial miscibility of the monomers applied. In the case of the pre-blended co-polymerised microparticles, a trend was discovered which suggests that co-monomers with large differences in the molecular descriptor parameter α resulted in heterogeneous surfaces (phase separation). For gaining a complete overview of the surface topographies, SEM

imaging should be used as a complementary technique allowing for a fast and meso-scale characterisation of microparticles.

ToF-SIMS analysis was performed in order to assess the surface chemistry of the particles. SIMS spectra revealed the presence of silicone contaminant peaks. It was demonstrated that the contamination was caused from a lubricant coating lining the interior of plastic syringes. Therefore, it is advisable to utilise only glass syringes to avoid such contaminations. Moreover, this contamination did not fully cover the underneath polymer but is thought to be homogeneously entangled into the polymer structure. Besides detecting silicone, a discontinuous layer of PVA surfactant was also found on the surfaces of microfluidic produced particles. The surfactant residues were only partially removed by extensive washing which implies that most of the PVA surfactant was embedded into the polymeric particle surface preventing its complete removal. Furthermore, the concentration of PVA surfactant varied within a sample aliquot.

By comparing the two manufacturing techniques, it can be stated that inkjet printed particles showed inferior properties to microfluidic produced particles. The reason is that inkjet printed droplets crossed a gas-liquid interface which resulted in collecting fluid perturbations. These perturbations caused droplet deformation and even damage as the droplets cured. As a result of the smaller particle yield and unfavourable properties of inkjet printed particles, microfluidics is proposed as the main manufacturing technique and focus of this work will take this into account.

6. Results - Bacteria Biofilm Assays on Inkjet Printed and Microfluidic Produced Particles

6.1. Introduction

Novel materials that can control bacterial attachment and subsequent biofilm formation are in high demand to reduce device-centred infections in the fight against antimicrobial resistance [287]. Furthermore, bio-fouling also poses a global problem in the marine industry [288,289]. To tackle the problem at the earliest possible stage, surfaces need to be adapted to prevent bacterial adhesion. This can be done by applying materials known to resist bacterial attachment [163,207,208] or by modifying the surface topography. Helbig et al. [210] have recently reported that substrates with periodical structures of sub-cell sized dimensions restricted attachment whereas cell-sized dimensions increased initial bacterial attachment independent of the contact time and the surface hydrophobicity. Despite these advances, there is still a lack of information on parameters governing the cell response to surfaces and hence, hindering rational materials design.

The goal of this chapter is to study the effect of particle chemistry, architecture and size on bacterial biofilm formation. *P. aeruginosa* was selected as a representative of Gram-negative pathogens that is frequently found in medical device-associated infections [9]. Initially, the effect of PVA surfactant on bacterial activity was tested on microfluidic produced polyEGdPEA microparticles and on pipetted thin films prepared from four different acrylates. Inkjet printed and microfluidic produced microparticles made from six different chemistries were studied for their bacterial attachment and compared to their 2D equivalent pipetted thin films. The quantification of biofilm-associated bacteria on particles involved developing a new algorithm for enabling quantification of the biomass exclusively on the particles. The algorithm was designed to determine the bacterial biofilm on microparticles using a MATLAB shape recognising function combined with adapted scripts from the COMSTAT program [241].

6.2. EXPERIMENTAL

This section presents the preparation of pipetted thin films (2D surfaces) intended to be used as references for the chemically identical microparticles (3D surfaces) in bacterial biofilm studies. Moreover, the preparation of PVA embedded films, which were utilised for investigating the effect of PVA surfactant on bacterial attachment, is outlined in Section 6.2.1. The microbial cell viability assay is discussed in Section 6.2.2. A detailed description of the bacterial attachment assays, which includes bacterial growth conditions, confocal microscope image acquisition and biofilm quantification, is provided in Section 3.6.

6.2.1. PREPARATION OF PIPETTED THIN FILMS

To remove unreacted monomers, all pipetted films were exposed to UV light for 30 min under an argon atmosphere followed by sample washing. The sample washing was performed with PBS for 20 min prior to bacterial testing.

6.2.1.1. PREPARATION OF CONTROL FILMS

Control films were produced by pipetting 40 µl of a monomer solution onto the bottom of a well in a Falcon® non-tissue culture 48-well plate (Corning Inc.). Non-tissue culture well plates made from polystyrene do not undergo a surface treatment to render hydrophilic surfaces and, hence, the substrates remain hydrophobic. The well plate was subsequently exposed to UV light (Blak-Ray® XX-15L UV Bench Lamp, 365 nm) for 30 min under argon atmosphere. Monomer solutions were composed of acrylate based monomers, listed in Figure 6.1, with 1 wt% DMPA as the photoinitiator.

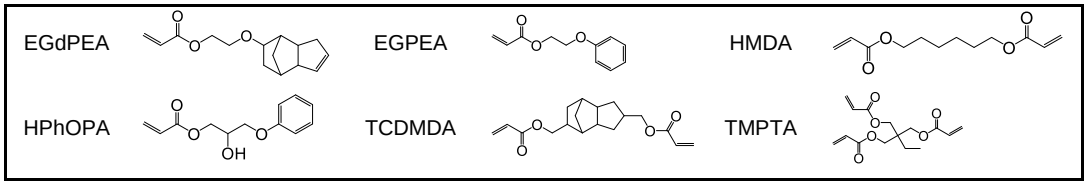


Figure 6.1: Monomers, used to prepare the pipetted control films, are shown with their abbreviations and chemical structures.

6.2.1.2. Preparation of PVA 'Embedded' Films

Polymeric films with PVA molecules physically entangled into the surface, referred to as 'PVA embedded films', were fabricated identically to the control films up until the UV exposure phase. The monomers applied are presented in Figure 6.2.

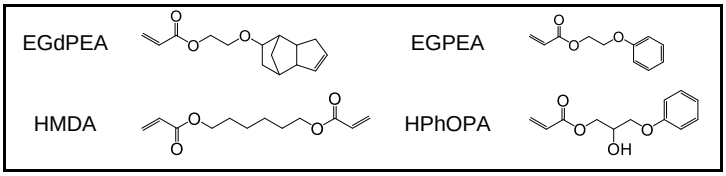


Figure 6.2: Monomers, used to prepare the PVA embedded films, are shown with their abbreviations and chemical structures.

Prior to photopolymerisation, 1000 µl of a 2 wt% aqueous PVA solution was placed on top of the pipetted monomer solutions. Immediately afterwards, the well plate was irradiated with a UV source for 30 min under argon atmosphere. Following the exposure to UV light, residues of the PVA solution were removed from the wells using a pipette. A schematic drawing of the preparation of pipetted control and PVA embedded films is depicted in Figure 6.3.

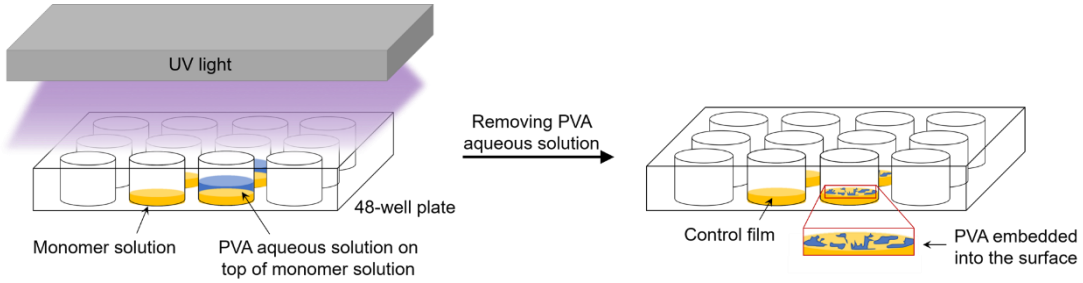


Figure 6.3: Schematic illustration of the preparation of pipetted control and PVA embedded films.

6.2.1.3. Preparation of pHEMA Films

Falcon® non-tissue culture 48-well plates (polystyrene) were oxygen plasma etched for 5 min at an O_2-pressure of 1.0×10^{-2} mbar and with an input power of 50 W. Immediately after oxygen plasma activation, the well bottoms of the 48-well plates were coated with 30 µl of a previously prepared poly(2-hydroxyethyl methacrylate) (pHEMA) ethanolic solution to generate homogeneous pHEMA films completely covering the well bottoms. The pHEMA coating acted both as a low-fouling background and as an adhesive layer for the physical entrapment of pipetted monomer solutions [159]. The pHEMA solution was composed of 4% (w/v) pHEMA solution in 95% ethanol solution. The oxygen plasma-treated well plates coated with pHEMA solution were dried at RT for 48 h followed by 48 h in a vacuum oven kept at 50°C. The chemical structure of pHEMA is presented in Figure 6.4.

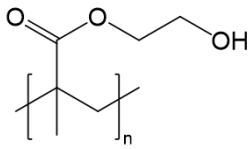


Figure 6.4: Chemical structure of poly(2-hydroxyethyl methacrylate) (pHEMA).

Monomer solutions were pipetted on top of the dried pHEMA films to create polymer films on pHEMA coated backgrounds. Wells, which were completely covered with pHEMA films but not further modified, were referred to 'pHEMA on polystyrene' in Section 6.3.2.3.

6.2.1.4. Preparation of Pipetted Films with Different Thicknesses

Pipetted films composed of EGdPEA were prepared as the control films, described in Section 6.2.1.1, except different quantities of monomer solution were pipetted onto the well bottoms in Falcon® non-tissue culture 48-well plates (Corning Inc.). The pipetted volumes of the EGdPEA-DMPA solution and their resultant computed film thicknesses are listed in Table 6.1.

Table 6.1: Different volumes of the EGdPEA-DMPA solution, which were pipetted into 48-well plates, and their resultant computed polymer thicknesses.

Pipetted volume [µl]	Film thickness [µm]
25	263
40	421
55	579
100	1053

6.2.2. Microbial Cell Viability Assays

To quantify bacterial attachment on microparticles, BacTiter-Glo™ assays (Promega, Madison, WI, USA) were carried out following manufacturer's instructions: 5 mg of microfluidic produced microparticles were loaded in triplicate in an opaque-walled 96-well plate and UV sterilised for 10 min. 100 µl of a suspension (OD_{600} = 0.01) of *P. aeruginosa* PAO1-N pME6032::mCherry in FAB medium [241] supplemented with 20 mM glucose were inoculated in each of the wells and incubated at 37ºC with 60 rpm. After 24 hours, planktonic cells were removed from the wells and particles were washed with 100 µl of PBS. Finally, microspheres were re-suspended with 50 µl of PBS and 50 µl of BacTiter-Glo™ reagent. Contents were mixed briefly on an orbital shaker and incubated for five minutes before the luminescence was recorded in a

TECAN Genios Pro spectrophotometer (Tecan, UK). Control wells containing medium without cells were also prepared to obtain a value for background luminescence.

6.3. Results and Discussion

6.3.1. Bacterial Attachment Assays - Effect of PVA Surfactant

Studying the role of PVA surfactant on bacterial attachment was essential since residues of PVA were detected at the surface of microfluidic produced particles even after extensive washing (Chapter 5). Therefore, bacterial biofilm studies were performed on microfluidic produced polyEGdPEA particles and on pipetted thin films prepared from four different acrylates: EGdPEA, EGPEA, HMDA and HPhOPA. The results, which show the level of biofilm-associated bacteria on the tested specimens, are presented in the following pages.

6.3.1.1. Bacterial Attachment on Washed Microparticles

Biofilm Quantification using Custom Matlab Algorithm

In order to assess the relationship between residual PVA surfactant on particles and bacterial resistance, 5 mg each of microparticle varying in the number of wash cycles were tested with *P. aeruginosa* PAO1-N mCherry for 24 hours under agitation (shaking at 60 rpm) and analysed using confocal microscopy. The biofilm quantification was performed exclusively on the surfaces of microparticles and pipetted thin films by using the custom Matlab algorithm, shown in Figure 6.5 a). The overall biomass was plotted versus the identity of tested samples, whereas non-tissue culture polystyrene (bottom of well) and pieces of silicone catheter were selected as references of high bacterial attachment surfaces. A significantly lower bacterial attachment (90.7%) was observed on PVA compared to polystyrene. The PVA sample consisted of 5 mg of loose PVA powder in a well that dissolved during sample washing and testing (Figure 6.5 a)). This observation revealed the low-fouling properties at well surfaces when being covered with dissolved bulk PVA as recently reported by Salman et al. on PVA (5 wt%) films cast on glass and plastic plates [290]. Focusing on the microfluidic produced polyEGdPEA microparticles, a gradual increase of biofilm was determined from zero

up to three wash cycles. However, after performing five wash cycles, the level of bacterial attachment remained unaltered. These results were inversely proportional to the amount of PVA detected on the particle surfaces using ToF-SIMS as shown in Figure 5.18 b), discussed in Section 5.3.2.2, indicating an anti-adhesive effect of the surfactant. Moreover, these findings were reinforced when considering the reduction of 44.6% in biofilm-associated bacteria on the PVA embedded polyEGdPEA films compared to the control films with no PVA.

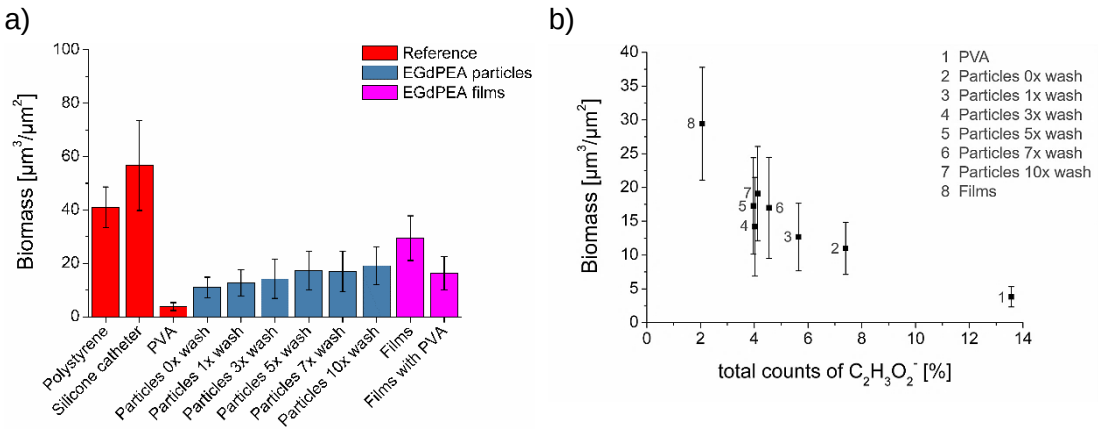


Figure 6.5: Quantification of biomass on polyEGdPEA microparticles varying in repeats of wash cycles and pipetted polyEGdPEA films: a) biomass volume divided by surface area ($\mu m^3/\mu m^2$) and its standard deviation is plotted against the tested samples, whereas non-tissue culture polystyrene and pieces of silicone catheter served as references of high bacterial attachment surfaces, b) correlation between the biomass captured on surfaces and the percentage of total counts of the acetate anion $[CH_3COO]^-$ detected by ToF-SIMS.

The relationship between bacterial attachment and PVA is shown by plotting the biomass captured on PVA, polyEGdPEA particles and films against the proportion of total counts of the ToF-SIMS acetate ion representative for PVA (Figure 6.5 b)). From the graph, it can be seen that having more PVA on the surface resulted in less biofilm formation. The amount of biofilm determined on microparticles and films was higher than the amount observed on bulk PVA. This could be explained by two possible reasons: first, differences in the low-attachment mechanism for PVA bulk samples and PVA surfactant physically entrapped at polymerised surfaces; second, differences in the surface area of PVA exposed to bacterial cells. It was hypothesised that PVA in the bulk works by dissolution of the PVA followed by sloughing off the bacterial biofilm from the weak interfacial layer. However, in the case of the PVA surfactant, which cannot be fully removed from the particle surfaces, the suggested mechanism for the bulk PVA would not be applicable. PVA crosslinked into the surface (surfactant) is considered as a water-soluble polymer that can induce surface hydration via hydrogen bonding. A tightly bound layer of water molecules near the surface is known to generate a physical and energetic barrier able to prevent stable bacterial attachment [206].

The biofilm quantification method allowed assessment of the variance of biomass within a sample. The successful particle detection on optical brightfield images and the captured biomass resulting from applying the mask throughout the volumetric images is depicted in Figure 6.6 for microfluidic produced polyEGdPEA particles as produced (a) and after 10 wash cycles (b); wash cycles were conducted before incubation in medium inoculated with PAO1-N mCherry.

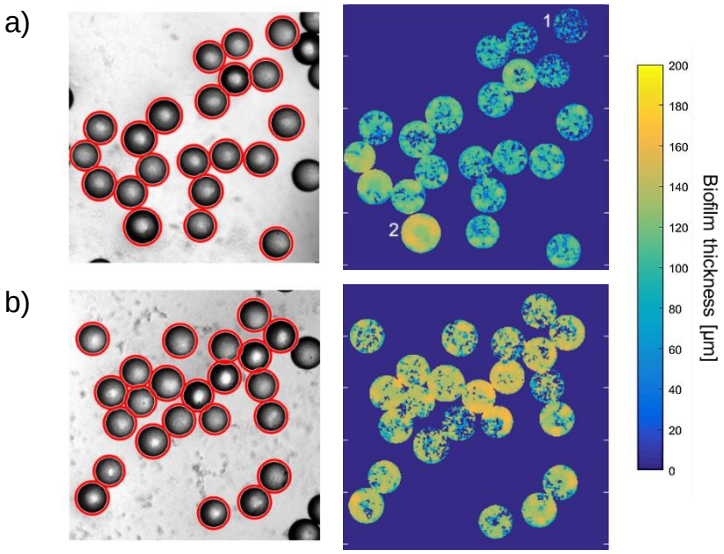


Figure 6.6: Biofilm assessment on polyEGdPEA microparticles showing the successful circle detection on acquired brightfield images (left) and the determined biomass (right) for: a) particles as produced (no washing), b) particles washed 10 times prior to bacterial incubation.

The biomass volume detected across the particle surfaces varied which is best seen in Figure 6.6 a). The particle numbered 2 had considerably more bacterial cells attached compared to the particle numbered 1. These differences in biofilm thickness may have emerged due to variations in PVA surface coverage (an observation made in Section 5.3.2.2) or due to heterogeneity of colonisation across microparticles within a test aliquot. Moreover, alterations in surface topography lead to different levels of bacterial attachment as reported by Feng et al. [291]. Their study demonstrated that the bacterial attachment was reduced on anodic alumina surfaces with pore sizes of 15 and 25 nm as compared to surfaces with larger pores. The bacteria-repelling effect was observed across several bacteria strains and attributed to densely distributed pores exerting increased repulsive forces on the bacteria found in the proximity of the surfaces [291]. In contrast to Feng et al., the microfluidic produced polyEGdPEA particles exhibited mostly detachment marks and only few surface pores on some particles, as presented in Figure 6.7.

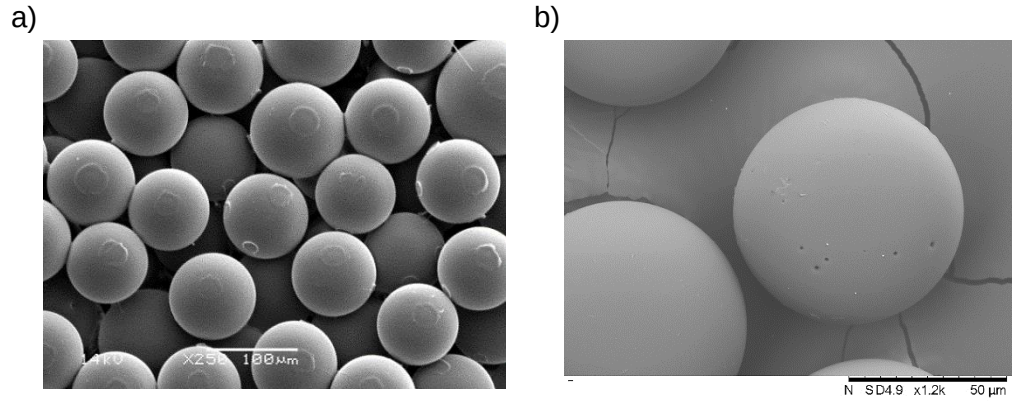


Figure 6.7: SEM micrographs showing two different defects detected on the surfaces of microfluidic produced polyEGdPEA microparticles: a) detachment marks, b) surface porosity.

Microbial Cell Viability Assays

The low-attachment activity of PVA was retested when studying the microbial cell viability using the BacTiter-Glo™ assay. This assay allowed determination of the number of viable planktonic cells by quantifying the amount of adenosine triphosphate (ATP). The amount of ATP was directly proportional to a luminescence signal generated from lysing the microbes. The number of viable planktonic cells is plotted against the test samples in Figure 6.8.

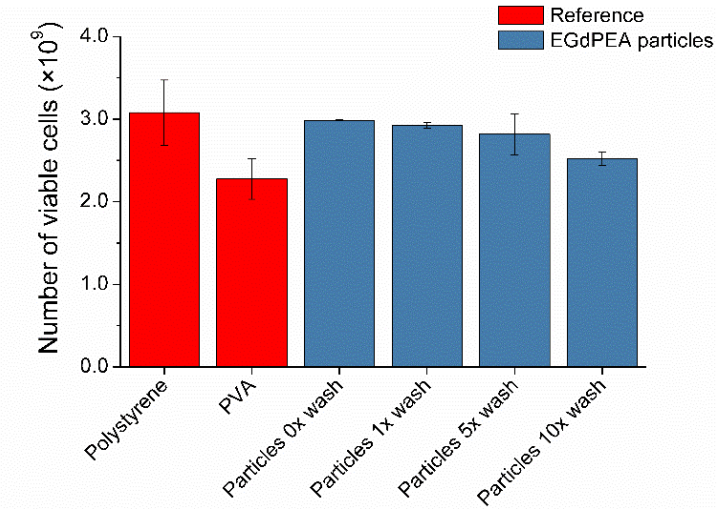


Figure 6.8: Microbial cell viability assays performed on microfluidic produced polyEGdPEA particles, PVA and polystyrene (reference). The average number of viable *P. aeruginosa* cells with its standard deviation, which was determined based on quantification of the ATP present, is shown.

A reduction in bacterial attachment from polystyrene (bottom of the well) to PVA was reconfirmed as illustrated in Figure 6.8. As opposed to the trend seen for the biofilm microscopy quantification studies in Figure 6.5 a), less biofilm on particles was observed with increased washing in this assay. An average of 2.5 to 3.0 × 10^9 viable planktonic cells was quantified for all tested microparticles made from EGdPEA. A paired sample t-test indicated a statistically significant difference ($p < 0.5$) between as-produced and 10 wash cycles. No significant difference was seen between the

individual wash cycles. A possible explanation for the deviation in the level of bacterial attachment between the viability assays and the biofilm microscopy quantification studies, is that the luminescence signal was detected from the entire well due to the implementation of the BacTiter-Glo™ assay. As a result, the number of viable planktonic cells determined cannot be solely attributed to the microparticles but also to the well acting as a background. This indicated that the BacTiter-Glo™ assay was prone to distortion of results when deviations in sample quantity occurred, so it was not used subsequently.

6.3.1.2. Bacterial Attachment on Pipetted Films

Pipetted thin films composed of four different acrylate monomers were photo-polymerised in the presence of a 2 wt% aqueous PVA solution. This was done in order to mimic the microfluidic process of crosslinking PVA surfactant into particle surfaces as confirmed by ToF-SIMS analysis (Section 5.3.2.2). These pipetted films were then incubated with *P. aeruginosa* PAO1-N mCherry to study the relationship between PVA covered acrylates and bacterial attachment. For comparative purposes, polystyrene and pieces of a silicone catheter were included in this study as references of high bacterial attachment surfaces. Figure 6.9 presents a decrease of biomass throughout all films with PVA crosslinked into their surfaces irrespective of the film chemistry. However, the pipetted films prepared from HPhOPA, which strongly promoted bacterial attachment, did not differ significantly. The possible reasons are twofold: first, the antibacterial effect of PVA was not significant in the presence of a strongly microbial promoting material; second, the physiochemical properties of HPhOPA, such as the relatively high viscosity, prevented PVA permeating into the monomer structure prior to polymerisation.

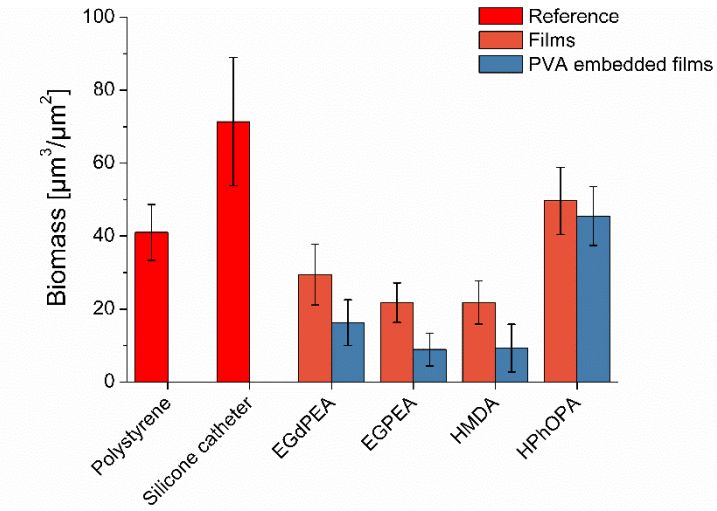


Figure 6.9: The biofilm of PAO1-N mCherry was quantified on pipetted thin films from the volumetric images acquired using confocal microscopy. The effect of PVA surfactant on bacterial attachment was assessed by comparing polymer films with PVA embedded films applying four different acrylates. Polystyrene and pieces of a silicone catheter were included as references of high bacterial attachment surfaces.

By searching for correlations between surface chemistry of the PVA-free pipetted thin films and bacterial attachment, similar trends were found as previously reported by Sanni et al. [283] and Hook et al. [172]. Their research demonstrated that poly(meth)acrylates, which contain both hydrophilic ester groups and rigid hydrophobic chemical moieties, had been correlated to decreased bacterial attachment. The monomer EGdPEA, which was discovered as a 'hit' material able to resist high levels of bacteria [163,172], did not perform best in the presented work within this thesis. The anti-attachment mechanism involved is still not fully understood for this class of materials. However, it is thought that EGdPEA surfaces are able to prevent bacterial cell attachment due to entropic shielding which is outlined in Section 2.6.4. Using PVA as a stabiliser revealed that the polymer surfaces are almost completely covered by the surfactant. Consequently, the contaminated surfaces exhibited the same interfacial chemistry as pure PVA which is significant in controlling cell-material association. Therefore, it is assumed that PVA-contaminated surfaces also prevent bacteria attachment via surface hydration as reported for hydrophilic surfaces.

The level of PAO1-N mCherry quantified on all tested pipetted films, with and without PVA embedded, was significantly higher in ratio to the control samples than previously published by Hook et al. [163,172] and Sanni et al. [283]. As a consequence, it was speculated that changes in the testing procedure have caused these differences in bacterial response. Possible factors causing the differences in the bacterial attachment are discussed in Section 6.3.2.3.

6.3.2. Bacterial Attachment Assays - Comparison from 2D to 3D

In this section, bacterial biofilm studies were conducted with the intention of comparing 2D to 3D surfaces, whereas pipetted thin films served as 2D equivalents to the microparticles (3D) produced from the same monomer. By doing this, the relationship between bacterial response and particle properties, such as chemistry, architecture and size, was explored. As a preliminary remark, the intended direct comparison between chemically identical 2D and 3D surfaces was rendered impossible due to the presence of PVA surfactant at the surface of all particles (outlined in Section 5.3.2.2). Additionally, to correct for mass transport effects [292,293], the pipetted thin films should have only been compared to the upper hemispheres of microparticles. However, the biofilm quantification method could not be adjusted accordingly due to difficulties in determining the centres of particles in the confocal data. Consequently, the biofilm quantified on microparticles included the entire surface of the spheres. The bacterial results obtained from the pipetted thin films are compared to the results published on polymer spots in microarrays, made from the same material, by Hook et al. and Sanni et al. [163,172,283].

6.3.2.1. Bacterial Attachment on Microparticles and Pipetted Thin Films

Pipetted thin films, inkjet printed (~20 µm) and microfluidic produced (~80 µm) microparticles were tested for their prevention of *P. aeruginosa* PAO1-N mCherry attachment in order to study the effect of particle chemistry, shape and size on bacterial behaviour. Polystyrene and pieces of silicone catheter were used as comparators exhibiting high bacterial attachment and represent the performance of a commonly used medical device material. The captured biomass on pipetted films and microparticles prepared from six different acrylate chemistries is presented in Figure 6.10.

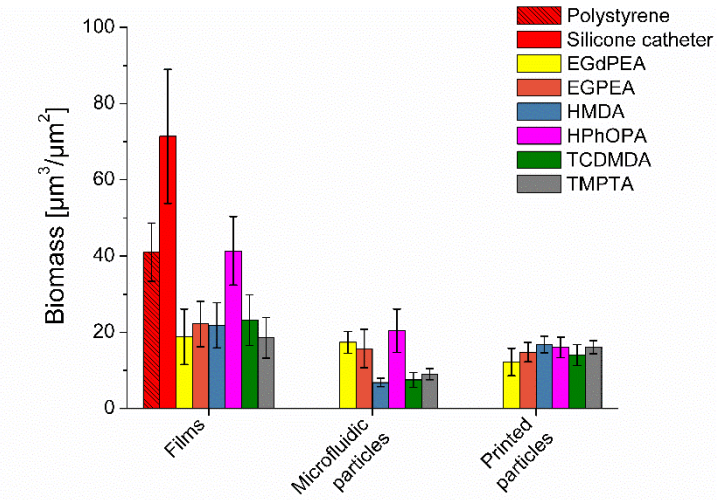


Figure 6.10: The biomass of PAO1-N mCherry was quantified on pipetted thin films, inkjet printed and microfluidic produced particles prepared from six different acrylates. By comparing 2D to 3D surfaces, the effect of surface chemistry, shape and size on bacterial attachment was assessed. Polystyrene and pieces of a silicone catheter were included as references of high bacterial attachment surfaces.

Figure 6.10 shows that the monomer HPhOPA, which has been shown to promote bacterial attachment in microarray and scale-up experiments under agitated culture [163], also exhibited the greatest amount of biomass on the surfaces of pipetted films and microfluidic produced particles under negligibly weak flows. However, in the case of printed particles, no significant difference in bacterial attachment was observed between the different acrylate chemistries. Irrespective of the particle chemistries, some inkjet printed particles were embedded in the biofilm grown on polystyrene well bottoms (substrate) whereas some other particles exhibited only the biofilm grown on the particles themselves. This, however, led to distortion of the results since the biofilm captured in the cylindrical mask could not be differentiated accordingly. An example for clarifying this issue best is given with inkjet printed polyHMDA particles which exhibited the highest level of *P. aeruginosa* at the surfaces, as shown in Figure 6.10. However, by comparing the fluorescence images of polyHMDA (Figure 6.11 a)) to the images obtained for printed polyHPhOPA particles (Figure 6.11 b)), PAO1-N mCherry preferred the polyHPhOPA particles to the polystyrene background, whereas the printed polyHDMA particles and polystyrene background were both similarly inhabited by bacteria.

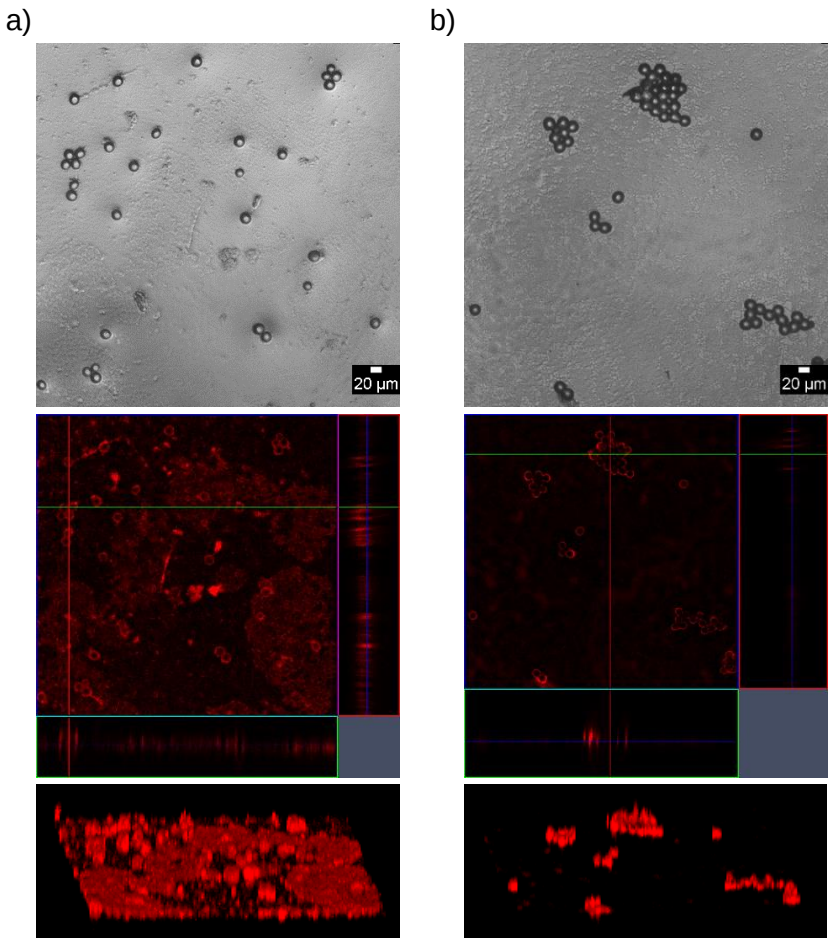


Figure 6.11: Biofilm quantified on inkjet printed particles after 24 h incubation in polystyrene wells of 48-well plates. Brightfield (top row) and fluorescence images are shown in orthogonal (middle row) and 3D (bottom row) view for: a) polyHMDA particles, b) polyHPhOPA microparticles.

A plausible explanation for these findings is that differences detected in the bacterial behaviour were affected by both mass transport effects and particle surface chemistry. The printed particles, hence, had to be excluded from the bacterial attachment assays. Consequently, it was not possible to study the effect of particle size on bacterial response.

By focusing on pipetted thin films and microfluidic produced particles to evaluate the effect of surface chemistry and particle shape on bacterial attachment, it became apparent that a direct comparison between chemically identical 2D and 3D surfaces was rendered impossible due to the presence of PVA surfactant at the particle surfaces.

6.3.2.2. Effect of Shape on Bacterial Attachment

By preparing PVA embedded films containing the same amount of PVA as detected on microparticles, the effect of particle shape on bacterial attachment could be

explored assuming that the surface chemistry was alike. In Figure 6.12, the biomass captured on pipetted films and microfluidic produced microparticles is depicted for four different acrylate chemistries: EGdPEA, EGPEA, HDMA and HPhOPA.

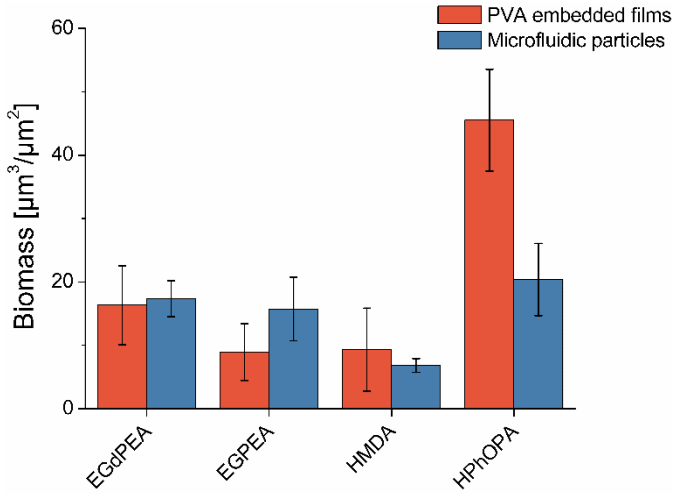


Figure 6.12: The biomass of PAO1-N mCherry was captured on PVA embedded thin films and microfluidic particles. The biofilm quantification involved the custom MATLAB algorithm. The effect of particle shape on bacterial attachment was assessed by comparing PVA embedded films with microfluidic particles applying four different acrylates.

No significant difference in bacterial attachment was observed for the monomers EGdPEA and HMDA when comparing 2D to 3D surfaces. In case of the monomer EGPEA, the microfluidic produced particles revealed 55.0% more biofilm-associated bacteria on the surfaces. A possible reason for this difference is that particle agglomerations, which were detected using SEM imaging (discussed in Section 5.3.1.2), promoted bacterial attachment. In this case, spaces between agglomerated particles potentially act as shelters preventing shear forces, which emerged by fluid agitation, acting on the bacteria. In contrast to polyEGPEA, PVA embedded films prepared from the monomer HPhOPA showed a notably higher level of bacterial attachment (76.3%) compared to the corresponding microparticles. The higher *P. aeruginosa* level can be explained by differences in the concentration of PVA surfactant at the surface of the films and particles repelling bacteria to a variable extent. Furthermore, another possible explanation is that the surface properties of the microfluidic polyHPhOPA particles changed to be less favourable to bacterial cells. The change in the surface properties could have been induced by the required addition of the solvent ethyl acetate to the monomer solution resulting in rearrangements of surface molecules.

Within the particle radii studied, no significant difference in bacteria behaviour was observed, suggesting that at diameters >75 µm the bacterial response is independent of the radius of curvature. Due to the very large difference in length scale between the

microfluidic produced microparticles (~80 µm) and the *Pseudomonas* bacteria (~1-5 µm), it is speculated that the bacteria do not easily sense the shape at all – they may perceive that the surface on which they reside is flat. Moreover, surface topographical features such as defects and periodical structures (as discussed in Section 2.6.3), need to be considered as a parameter influencing the bacterial response.

6.3.2.3. Other Parameters affecting the Bacteria Attachment

Besides PVA surfactant, particle shape and surface topography, there are a few other parameters that were considered to have an effect on bacterial attachment. By comparing the results of the pipetted thin films with the results of their analogue polymer spots in microarrays reported in the literature [163,172], higher levels of biofilm-associated bacteria were quantified on all pipetted thin films. As a result, the bacterial attachment studies were compared and investigated thoroughly for differences in the materials and test conditions applied.

Effect of pHEMA

In combinatorial polymer microarrays, glass slides were coated with pHEMA because of its low-fouling properties and ability to act as an adhesion layer for the printed polymer spots [159]. It has been reported that pHEMA was detected on some surfaces of polymer islands which indicated that pHEMA diffused through the above polymer layer during or before curing the monomer [248]. As a result, the effect of pHEMA on bacterial attachment was assessed. The biofilm, which was quantified on pipetted thin films with and without having a pHEMA coated background, is shown for six different chemistries in Figure 6.13: EGdPEA, EGPEA, HDMA, HPhOPA, TCDMPA and TMPTA.

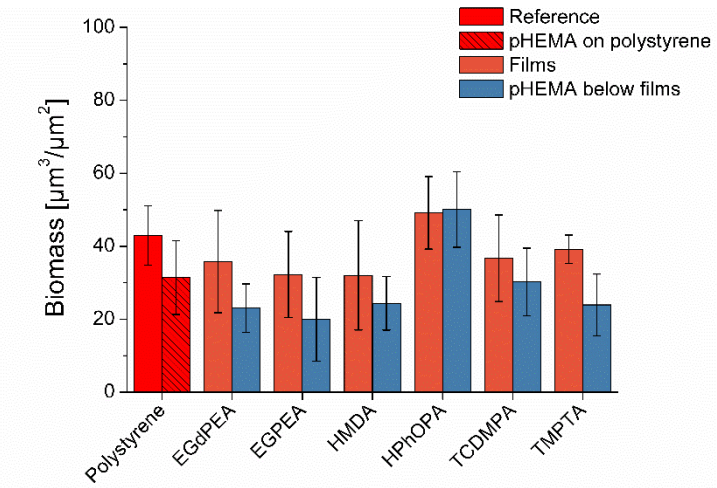


Figure 6.13: The biomass of PAO1-N mCherry was quantified on pipetted thin films from the volumetric images acquired using confocal microscopy. The effect of pHEMA on bacterial attachment was assessed by comparing polymer films prepared from six different acrylates with and without having a thin, homogeneous pHEMA film underneath. Polystyrene was included as a reference of a high bacterial attachment surface.

By comparing the bacterial attachment data captured on pipetted thin films with and without having a pHEMA coated background, a trend was observed which revealed less bacterial attachment on 85.7% of all tested films with pHEMA coated wells underneath. A reduction of up to 39% in biomass was observed. The pHEMA background layer did not affect films made from the monomer HPhOPA. This finding showed remarkable similarities to the results presented with the PVA surfactant in Section 6.3.1.2. Consequently, it is assumed that the bacterial behaviour is explained by the same reasons as already outlined previously. This involved the outperformance of the antibacterial activity of pHEMA by the strongly microbial promoting monomer and also the inability of pHEMA to diffuse through the HPhOPA layer because of its physiochemical properties.

The mechanism for the low-fouling properties of PVA and pHEMA is thought to be correlated since both materials are of hydrophilic nature. It has been reported that the non-fouling ability is associated to a hydration layer near the surface which excludes biomolecules from the surfaces [283]. This exclusion of biomolecules is caused by a physical and energetic barrier which is formed by a surface-bound water layer [206]. More information about this proposed mechanism of action is provided in Section 2.6.4.

By testing the microfluidic produced particles in well plates as received and previously oxygen plasma-treated directly followed by pHEMA coating, the effect of a low-fouling background on bacterial attachment was assessed at the particle surfaces using the biofilm quantification algorithm. The biovolume quantified at the particle surfaces of three different particle chemistries is presented in Figure 6.14.

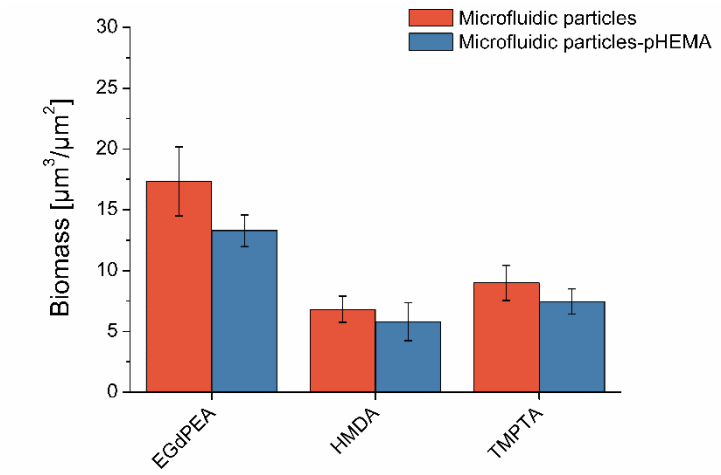


Figure 6.14: The biovolume of PAO1-N mCherry was assessed at the particle surfaces of three different particle chemistries. The effect of pHEMA on bacterial attachment at particle surfaces was studied by comparing microfluidic polymer particles in untreated and oxygen plasma-activated pHEMA coated wells in 48-well plates.

Figure 6.14 shows lower levels of biofilm-associated bacteria on microparticles tested on pHEMA coated substrates. The largest decrease in biomass of 23.5% was observed on polyEGdPEA microparticles, whereas a reduction of 17.1% and 14.9% was quantified on microfluidic polyTMPTA and polyHMDA particles, respectively. The difference in the level of PAO1-N mCherry on polyEGdPEA and polyTMPTA microparticles was statistically significant ($p < 0.05$) between the substrates as received and pHEMA-coated wells. No statistically significant difference, however, was found for microfluidic produced polyHMDA particles. These variations in bacterial attachment received throughout the majority of tested particle chemistries indicate that the bacterial behaviour at the contact sites between particles and substrate influences the actual results. This is the case because the biofilm quantification algorithm employed in this work involved particle shape recognition combined with vertical projection of cylindrical masks through the volumetric fluorescence images. Consequently, the biofilm grown between the substrate and particles is included in the calculation that could lead to distortion of bacterial attachment results. To circumvent these issues, the test substrates can be treated with non-fouling materials. Another option includes the alteration of the biofilm quantification algorithm in such a way that the biovolume is quantified only at the upper hemisphere of the particle surfaces. The latter proposed improvement is more favourable since less time and material is required for preparing the test substrates.

Effect of Flow Conditions

Differences in the flow conditions, which could occur during sample washing after samples being removed from the bacteria-inoculated media and prior to analysis, may affect the extent of the bacterial cells captured at the surfaces. No specific information

was provided in the papers published by Hook et al. [163,172] and Sanni et al. [283] regarding the washing procedures applied. However, it was ascertained at a later stage that Hook et al. and Sanni et al. performed their sample washing in petri dishes using a rotating platform at 60 rpm three times for five minutes. This leads to significant flow, whereas in this thesis, samples were carefully washed in wells (48-well plates) by pipetting, inducing weak flow only.

In order to study the impact of variations in flow conditions during post-incubation sample washing on bacterial attachment, the following two washing procedures were selected: manual pipetting ('Pipetting', standard procedure mentioned in Section 3.6.1) was compared to applying linear shake movements for five minutes at an amplitude of 3 mm (corresponds to a frequency of 218 rpm) using a TECAN Genios Pro spectrophotometer followed by removal of the fluids using a pipette ('Shaking'). These two methods, which were applied three times, differed in the magnitude of shear forces acting during washing. Therefore, the effect of flow conditions on the PAO1-N mCherry attachment was studied for pipetted thin films and microfluidic produced particles composed of polyEGdPEA. The data from these tests is shown graphically in Figure 6.15. EGdPEA was selected as the monomer to investigate thoroughly since it had been reported as a hit homopolymer exhibiting the lowest surface coverage for *P. aeruginosa* [163,172].

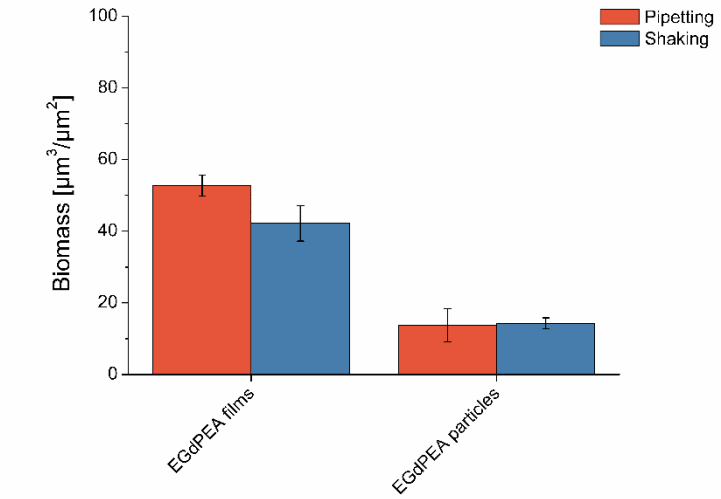


Figure 6.15: The biofilm was quantified on pipetted thin films and microfluidic produced particles composed of polyEGdPEA after 24 h incubation in PAO1-N mCherry suspension under agitation (shaking at 60 rpm). The influence of flow conditions on biofilm-associated bacteria was analysed by washing the samples three times in two different ways, manual pipetting ('Pipetting') and applying linear shake movements for five minutes prior to removal of the fluids using a pipette ('Shaking').

A decrease of 20.0% in bacterial attachment was observed at the surfaces of pipetted polyEGdPEA films when stronger shear forces acted upon the surface during post-incubation washing. In contrast, the biofilm quantified on the polyEGdPEA microparticles remained unchanged irrespective of the washing procedure applied.

These differences in their biological performance are explained by the relative movement of the specimens to the washing fluid in the test system. In the case of the pipetted thin films, they remain static in respect to the well plate leading to greater impact of shear forces at the surfaces through the washing fluid moving over the surfaces. As a result, it is assumed that biofilm-associated bacteria are carried away to some extent. However, loose microparticles act as dynamic systems moving with the flow. In this way, assuming contact and abrasion are insignificant for the suspended particles, microparticles are likely to be exposed to less shear forces overall, hence, minimal removal of biomass is expected.

Considering that biofilms are formed by bacterial communities embedded within a matrix of self-secreted extracellular polymeric substances, much stronger forces are required to remove these bacteria from the surface compared to planktonic bacterial cells [294]. Suspended bacteria, which are close enough to allow initial contact with the surface, are weakly bound to the surface and, thus, can be easily removed by fluid shear forces [295]. As a consequence, it is hypothesised that variations in the flow conditions during sample incubation result in greater differences in the level of bacterial attachment compared to variations in the flow condition occurring during post-incubation sample washing.

The flow conditions, which are affected by the level of agitation but also by the choice of substrate type and size, directly impact on the number of bacterial cells attaching to the surface, hence, resulting in changes in biofilm quantity. An in-depth study on the effects of flow conditions during the incubation stage on biofilm growth is beyond the scope of this thesis. However, this is recommended to be investigated in the near future, and is discussed in the future work section.

Effect of Film Thickness

The polymer films tested in this work differ in dimensions compared to the polymer spots reported in literature [163,172,283]. Hook et al. reported that homopolymeric EGdPEA spots with an average height of 20 µm revealed a surface coverage for *P. aeruginosa* of 11.6 ± 1.5% [163]. As a result, film thickness was identified as another parameter which could determine the antibacterial efficacy. In this study, pipetted polyEGdPEA films varying in film thickness were analysed for their bacterial performance after being incubated for 24 hours under agitation (shaking at 60 rpm). The biomass, which was quantified on surfaces of polyEGdPEA films prepared with 25, 40, 55 and 100 µl of EGdPEA-DMPA solution, is illustrated in Figure 6.16.

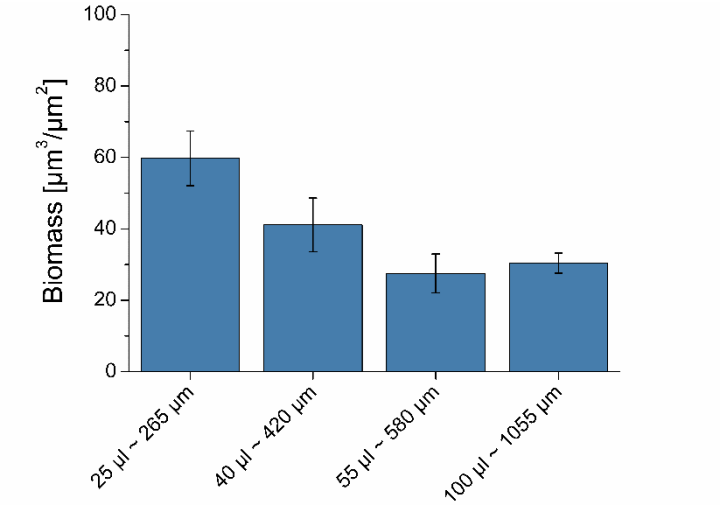


Figure 6.16: The biovolume per surface area was quantified on pipetted polyEGdPEA films which were prepared by pipetting different quantities of monomer solution (25, 40, 55 and 100 µl) onto the well bottoms of 48-well plates. The effect of film thickness on anti-adhesive efficacy was analysed by testing the polyEGdPEA films varying in thickness with PAO1-N mCherry for 24 h under agitation (shaking at 60 rpm).

Figure 6.16 shows a decrease in the biovolume captured per surface area on pipetted polyEGdPEA films fabricated with increasing volumes of monomer solution, consequently, increasing resultant film thicknesses. The films with the overall lowest bacterial attachment were prepared with 55 µl of EGdPEA-DMPA solution, resulting in an average reduction in biomass of 53.9% compared to the polyEGdPEA films with the highest degree of biofouling (25 µl). This bacterial attachment data indicates that the likelihood of incomplete curing rises with increasing film thickness. A possible explanation for lower levels of bacterial attachment involves fragments such as cyclopentadienyl which could diffuse to the film surface where they remain due to their hydrophobic nature. In this way, hydrophobic interactions can result in destabilisation of bacterial membranes. Moreover, it is also possible that unreacted monomers could reduce the bacterial doubling rates. Therefore, polymer constituents and unreacted monomers affect the mechanism for reduction in bacterial attachment to some extent.

6.4. SUMMARY

To tackle the problem of biofilm formation at surfaces, bacterial attachment and biofilm formation needs to be prevented through material design and manufacture optimisation. This, however, requires a full understanding of material-function relationships in order to design surfaces accordingly. Herein, the focus of this chapter was to enable screening from 2D to 3D surfaces by studying the effect of particle chemistry, architecture and size on bacterial attachment of *P. aeruginosa* PAO1-N mCherry.

Assessing the effect of PVA surfactant on bacterial attachment, a strong anti-adhesive activity was demonstrated for bulk PVA. Microparticles, which were tested with PAO1-N mCherry, as-produced and after a varying number of wash cycles to remove PVA, did not show significant changes in bacterial attachment. However, a trend was observed which revealed greater prevention of bacterial attachment for particles with increased amount of PVA surfactant at particle surfaces. The difference in the low-fouling efficacy between bulk PVA and PVA surfactant could be explained by two possible reasons: first, differences in the mechanism of preventing *Pseudomonas* attachment for PVA bulk samples and PVA surfactant physically entrapped at polymerised surfaces; second, differences in the surface area of PVA exposed to bacterial cells.

The low-fouling properties of PVA were confirmed by testing pipetted thin films, which were prepared from four different acrylates and crosslinked in the presence of a 2 wt% PVA solution. A decrease in biomass throughout all films with PVA entangled into their surfaces was detected irrespective of the film chemistry. Correlating the surface chemistry of the PVA-free pipetted thin films to the bacterial attachment, it was found that polyacrylates containing both hydrophilic ester groups and rigid hydrophobic chemical moieties showed lower levels of *P. aeruginosa* attachment. Similar observations were previously reported by Sanni et al. [283] and Hook et al. [172]. The underlying mechanism that reduces bacterial attachment is believed to be different for amphiphilic polyacrylates and PVA-contaminated surfaces; polyacrylates probably involve entropic shielding whereas PVA-contaminated surfaces prevent attachment via surface hydration.

The effect of particle chemistry, shape and size on bacterial behaviour was investigated by conducting bacterial biofilm studies on pipetted thin films, inkjet printed (~20 µm) and microfluidic produced (~80 µm) microparticles. Due to the small size of the inkjet printed particles, mass transport effects and surface chemistries led to differences in the level of *P. aeruginosa* attachment within sample aliquots but also within different materials, distorting the results. Therefore, the inkjet printed particles were excluded from the bacterial biofilm studies. With respect to particle shape, no significant difference in bacteria behaviour was observed, suggesting that at diameters >75 µm the bacterial response is independent of the radius of curvature.

By conducting a comparison of the bacterial results received from testing pipetted thin films with results published by Hook et al. [163,172], higher levels of biofilm-associated bacteria were observed on all pipetted thin films in this work. Searching for differences

in the bacterial testing procedures including microarray and scale-up polymer coupon assays, three main parameters (pHEMA, flow conditions, film thickness) were identified and tested for their bacterial outcome. Films on top of pHEMA coated wells exhibited less bacterial attachment compared to control films (without pHEMA). However, polyHPhOPA films were not affected by the pHEMA background layer. These observations bore resemblance to the PVA study. Consequently, the mechanism for preventing bacterial attachment of PVA and pHEMA contaminated surfaces is thought to be tightly correlated and associated to a hydration layer near the surface. This surface hydration leads to exclusion of biomolecules such as proteins which would normally adsorb [206,283,296]. By evaluating the biomass on particles using the custom biofilm quantification algorithm, less biofouling of PAO1-N mCherry was observed on microparticles tested on pHEMA coated substrates. This indicated that the contact sites between particles and substrate had a determining influence on the bacterial performance.

Moreover, variations in flow conditions, which result in different shear forces acting on surfaces during post-incubation sample washing, affected the biological performance. In static test systems (pipetted films) the performance was affected greatly but barely in dynamic systems (microparticles). The reason is that loose microparticles overall were exposed to less shear forces since they were set into motion by the washing fluid movements. Furthermore, it is hypothesised that variations in the flow conditions during sample incubation result in greater differences in the level of bacterial attachment compared to variations in the flow conditions occurring during sample washing prior to analysis.

With respect to the film thickness, lower bacterial attachment was detected on pipetted films prepared with increasing volumes of monomer solution, hence, increasing resultant film thickness. These results pointed towards incomplete curing with increased film thickness. The reduction in PAO1-N mCherry attachment was believed to be caused by polymer constituents diffusing to the surface, destabilising bacterial membranes, and by unreacted monomers reducing the bacterial doubling rates.

7. CONCLUSIONS

7.1. GENERAL CONCLUSIONS

Over the last decades, research has focused on discovery of new materials for biomedical applications. Recently, exciting advances have been made, mostly in two-dimensional materials development, through both hypotheses relating material properties to cell response, and discovery of new materials via high throughput screening. This research field, however, is still hindered by the lack of knowledge on the physicochemical parameters controlling the range of cellular responses – the material-function relationships. As it is well recognised that 3D structures can behave differently compared to 2D materials, the overall aim of this thesis is to perform a step change from formation and screening of 2D to 3D surfaces.

The first objective was to generate a combinatorial library of microparticles using photo-induced polymerisation in combination with either piezoelectric inkjet printing or microfluidics. In Chapter 4, 31 (out of 56 tested) (meth)acrylates capable of forming spheres and a universal collecting fluid, 17 wt% IPA/DIW, were discovered by performing preliminary experiments. Both particle agglomerations and free-flowing microparticles were obtained by inkjet printing these monomers, blended with 1 wt% DMPA (photoinitiator), into 17 wt% IPA/DIW under nitrogen atmospheres. The inkjet printing process and, hence, the microparticle output were optimised by adding 0.1 wt% surfactant (Triton X-100) to the collecting fluid and printing at a velocity of 6 m/s. In this way, a library of 20 (meth)acrylates, able to fabricate particles using the Dimatix printer, was successfully generated. Polymer kinetic studies assisted in the explanation of the inability of certain monomers to form particles by demonstrating that smaller numbers of functional C=C double bonds, increased steric hindrance (increased chain length, monomer bulkiness) and more stable radicals resulted in decreased curing rates. By employing microfluidics as an alternative particle fabrication technique, a PVA surfactant concentration of 2 wt% in the collecting fluid was found to be crucial for a reproducibly stable droplet formation. Monodisperse microparticles were only generated within a limited combination of dispersed and continuous flow rates under low capillary numbers ranging from 10^{-4} to 10^{-2}. To fabricate co-polymerised particles with a well-defined monomer ratio, blending-before co-polymerisation was found to be the superior technique due to greater process stability.

The second objective was to conduct an in-depth chemical and physical characterisation on microparticles generated using inkjet printing and microfluidics. In Chapter 5, particle sizing measurements demonstrated average diameters of 20 ± 5 µm and 75 ± 5 µm for printed and microfluidic produced particles, respectively. However, microparticles produced with the Dimatix printer exhibited up to three times broader size distributions compared to microfluidics. Surface morphology studies revealed that microfluidic produced particles were perfectly spherical whereas inkjet printed particles exhibited asphericity. In microfluidics, defects such as surface porosity, surface cracking, detachment marks and particle agglomerations, were mainly detected on particles made from mono-functional monomers with a T_g below RT. Consequently, it was concluded that materials with a higher tendency to crosslink showed fewer defects. AFM analysis showed that microfluidic produced particles exhibited overall lower average roughness values combined with less topographical features than inkjet printed particles. Results showed that 33.3% of blended-before and 88.9% of on-chip co-polymerised particles exhibited heterogeneous surfaces in the form of phase separation. These phase separations most likely occurred from partial miscibility of the monomers applied. In the case of the pre-blended co-polymerised microparticles, a trend was discovered which indicated that co-monomers with large differences in the molecular descriptor parameter α resulted in continuous and discontinuous phase separated morphologies. ToF-SIMS spectra indicated the presence of silicone contaminant peaks on all measured particle aliquots. This silicone contamination was caused by a lubricant coating lining the interior of plastic syringes. This contamination was homogeneously entangled into the polymer structures, hence, rendered the removal impossible. Furthermore, a discontinuous layer of PVA surfactant was detected at the surfaces of microfluidic produced particles which was partially removed by extensive washing. Comparing both particle fabrication methodologies, microfluidics was shown to be the superior technique for fabricating particles. Inkjet printed particles exhibited unfavourable properties due to collecting fluid perturbations, which emerged from droplets crossing a phase boundary from gas to liquid. In consideration that inkjet printing is far from reaching a stable, steady state printing condition, microfluidics offers a greater potential for various applications since scaling-up of particles in all sizes, shapes and compositions is feasible.

The final objective was to achieve a change in screening from 2D to 3D surfaces by examining the effect of particle chemistry, architecture and size on bacterial attachment using *P. aeruginosa* PAO1-N mCherry. In Chapter 6, a strong anti-adhesive activity was observed in case of bulk PVA. A similar but smaller effect was

observed for microparticles with increased amount of PVA surfactant at the surfaces. The difference in low-fouling efficacy between PVA bulk and PVA surfactant could be explained by either differences in the mechanism of preventing *Pseudomonas* attachment for PVA bulk samples and PVA surfactant physically entrapped at polymerised surfaces or by differences in the surface area of PVA exposed to bacterial cells. Polyacrylates containing both hydrophilic ester groups and rigid hydrophobic chemical moieties exhibited lower levels of *P. aeruginosa* attachment which was previously reported by Sanni et al. [283] and Hook et al. [172]. The low-fouling interactions of bacteria with material surfaces were most likely governed by two different mechanisms, entropic shielding and surface hydration in case of polyacrylates and PVA-contaminated surfaces, respectively. The study of evaluating the effect of particle size on bacterial attachment could not be performed since biomass results quantified on inkjet printed particles were distorted. In respect of particle shape, no significant difference in bacteria behaviour was observed, suggesting that at diameters >75 µm the bacterial response is independent of the radius of curvature due to the very large difference in length scale between microparticles and bacteria. Moreover, by examining other parameters, including pHEMA, flow conditions and film thicknesses, on bacterial response, it was found that pipetted films on pHEMA coated substrates presented less biofilm compared to control films without pHEMA. Similar results were obtained with PVA contaminated surfaces and, therefore, the mechanism for the low-fouling activity is thought to be tightly correlated and associated to surface hydration preventing attachment of biomolecules [206,283,296]. Less biofilm-associated bacteria were captured on microparticles tested on pHEMA coated substrates which clarified the determining influence of the contact sites, between particles and substrate, on the bacterial performance. Differences in fluid flows during post-incubation sample washing affected the biological performance greatly in case of static test systems (pipetted films) but barely in case of dynamic systems (microparticles).

The differences in the attachment of biofilm-associated bacteria between the pipetted thin films tested within this work and their analogue polymer spots in microarrays reported in literature are thought to be induced by the low-fouling pHEMA and variations in flow conditions occurring both during incubation stage and sample washing prior to analysis.

7.2. RECOMMENDATIONS FOR FUTURE WORK

Several areas of future work have been identified through the work conducted in this thesis.

Whilst ToF-SIMS analysis was successfully employed to probe the surface chemistry of inkjet printed and microfluidic produced microparticles, its capabilities were not fully exploited. Surface spectrometry could be conducted on PVA embedded films to quantify the PVA surfactant content at the surfaces. This would clarify whether the same amount of PVA was achieved on both pipetted films and microfluidic produced particles. Based on the results, the effect of particle shape on *P. aeruginosa* biofilm formation can either be directly examined or after adjusting the PVA concentration in order to neglect the surface chemistry. In addition, by quantifying the PVA content, it can be ascertained that less PVA surfactant permeated into the HPhOPA structure prior to curing due to its physiochemical properties. For the same reason, pipetted films on pHEMA coated substrates could be chemically analysed in order to confirm the smaller amount of pHEMA on polyHPhOPA films due to the limited diffusion of pHEMA oligomers. The bacterial attachment results, which were obtained for both polyHPhOPA films with and without a pHEMA background layer, showing little to no difference, could thereby be explained with a higher degree of confidence. Moreover, ToF-SIMS depth profiling or X-ray photoelectron spectroscopy (XPS) could be utilised for two reasons: firstly, to confirm that PVA surfactant is only present as an overlayer at the surfaces and not throughout the microfluidic produced particles; secondly, to analyse the thickness of the PVA layer.

In this work, a biofilm quantification method was applied which captured the biofilm at the entire surfaces of particles. Bacterial biofilm results revealed, however, that the contact sites between particles and substrate affected the bacterial performance. Therefore, to correct for mass transport effects, the biofilm should only be quantified on the upper hemisphere of particles allowing for a direct comparison between chemically identical 2D and 3D surfaces. This can generally be done by adjusting the algorithm accordingly through further development. Confocal volumetric data, however, need to be acquired in such a way that the centre of particles can easily be determined afterwards. If this suggestion is not feasible, well plates (substrates) could be coated with pHEMA to reduce the bacterial attachment at the contact sites.

Polyacrylates, which contained both hydrophilic ester groups and rigid hydrophobic chemical moieties, have been discovered as a new class of polymers resistant to *P. aeruginosa* attachment [172,283]. These observations were also made within the

bacterial biofilm assays performed in this thesis. Based on the fact that PVA demonstrated low-fouling properties, copolymerisation of (meth)acrylates with PVA should be considered and tested for improved prevention of bacterial cells. This copolymerisation might have synergistic effects in case of 2D surfaces since the underlying mechanisms of action of the different materials may complement each other resulting in greater reduction of bacterial attachment. However, in case of forming particles in an aqueous continuous phase, micelles are likely formed due to self-assembly of the macromolecules consisting of PVA and (meth)acrylates. PVA, which is more hydrophilic than (meth)acrylates, would spontaneously form the outer shell, hence, controlling solely the attachment of bacterial cells. Moreover, the OH groups of the PVA surfactant (residues) at the surface of microparticles could be used as initiator for attaching compounds of interest to the microparticles.

Despite these recent advances, the involved anti-attachment mechanism is not yet fully understood. Consequently, to fully understand the biological performance, extended combinatorial particle libraries should be tested for their bacterial attachment. Material-function relationships could be induced as a result of testing different substrates by varying the shape, size, composition and morphology for their resistance to bacteria with different physiochemical properties. Moreover, the suspending liquid medium, including for instance its surface tension, pH and ionic strength, should be considered as another crucial factor mediating the bacterial attachment. In terms of particle sizes, the same particle fabrication technique should be used to produce particles with different sizes in order to exclude any other parameters affecting the bacterial attachment. Moreover, to directly compare the level of bacteria on complex 3D surfaces with 2D surfaces (microarrays), previously published by Hook et al. [163,172] and Sanni et al. [283], research should strive for particle formation without employing surfactants. In consequence of changing the substrate type and size to adapt to the implementation of the biofilm assays, an in-depth study should be conducted on the effects of variations in flow conditions present during the incubation stage on biofilm growth.

In the future, biological testing could also be transferred from bacterial to human cell interactions to discover materials suitable for specific biomedical applications. The vision is to mature this effort for applications that require acceptance into body such as low-fouling coatings, drug delivery and cell carriers in regenerative medicine strategies.

8. REFERENCES

[1] Riahi R, Tamayol A, Shaegh SAM, Ghaemmaghami AM, Dokmeci MR, Khademshosseini A. Microfluidics for advanced drug delivery systems. Curr Opin Chem Eng 2015;7:101–12. doi:10.1016/j.coche.2014.12.001.

[2] Chau DYS, Agashi K, Shakesheff KM. Microparticles as tissue engineering scaffolds: Manufacture, modification and manipulation. Mater Sci Technol 2008;24:1031–44. doi:10.1179/174328408X341726.

[3] Oliveira MB, Mano JF. Polymer-based microparticles in tissue engineering and regenerative medicine. Biotechnol Prog 2011;27:897–912. doi:10.1002/btpr.618.

[4] Rosca ID, Watari F, Uo M. Microparticle formation and its mechanism in single and double emulsion solvent evaporation. J Control Release 2004;99:271–80. doi:10.1016/j.jconrel.2004.07.007.

[5] Haase MF, Stebe KJ, Lee D. Continuous fabrication of hierarchical and asymmetric bijel microparticles, fibers, and membranes by solvent transfer-induced phase separation (STRIPS). Adv Mater 2015;27:7065–71. doi:10.1002/adma.201503509.

[6] Schafroth N, Arpagaus C, Jadhav UY, Makne S, Douroumis D. Nano and microparticle engineering of water insoluble drugs using a novel spray-drying process. Colloids Surfaces B Biointerfaces 2012;90:8–15. doi:10.1016/j.colsurfb.2011.09.038.

[7] Perelaer J, Schubert US. Ink-jet printing of functional polymers for advanced applications. In: Matyjaszewski K, Möller M, editors. Polym. Sci. A Compr. Ref., Elsevier; 2012, p. 147–75. doi:http://dx.doi.org/10.1016/B978-0-444-53349-4.00205-3.

[8] Tekin E, Smith PJ, Schubert US. Inkjet printing as a deposition and patterning tool for polymers and inorganic particles. Soft Matter 2008;4:703–13. doi:10.1039/b711984d.

[9] Hidron AI, Edwards JR, Patel J, Horan TC, Sievert DM, Pollock DA, et al. NHSN annual update: Antimicrobial-resistant pathogens associated with healthcare-associated infections: Annual summary of data reported to the National Healthcare Safety Network at the Centers for Disease Control and Prevention,

2006-2007. Infect Control Hosp Epidemiol 2008;29:996–1011. doi:10.1086/591861.

[10] Kawaguchi H. Functional polymer microspheres. Prog Polym Sci 2000;25:1171–210. doi:10.1016/S0079-6700(00)00024-1.

[11] Tang J, Shen D, Caranasos TG, Wang Z, Vandergriff AC, Allen TA, et al. Therapeutic microparticles functionalized with biomimetic cardiac stem cell membranes and secretome. Nat Commun 2017;8:1–9. doi:10.1038/ncomms13724.

[12] He Z, Santos JL, Tian H, Huang H, Hu Y, Liu L, et al. Scalable fabrication of size-controlled chitosan nanoparticles for oral delivery of insulin. Biomaterials 2017;130:28–41. doi:10.1016/j.biomaterials.2017.03.028.

[13] Lopes M, Aniceto D, Abrantes M, Simões S, Branco F, Vitória I, et al. In vivo biodistribution of antihyperglycemic biopolymer-based nanoparticles for the treatment of type 1 and type 2 diabetes. Eur J Pharm Biopharm 2017;113:88–96. doi:10.1016/j.ejpb.2016.11.037.

[14] Tagaya A, Ishii S, Yokoyama K, Higuchi E, Koike Y. The advanced highly scattering optical transmission polymer backlight for liquid crystal displays. Jpn J Appl Phys 2002;41:2241–8. doi:10.1143/JJAP.41.2241.

[15] Nisisako T, Ando T, Hatsuzawa T. Capillary-assisted fabrication of biconcave polymeric microlenses from microfluidic ternary emulsion droplets. Small 2014;10:5116–25. doi:10.1002/smll.201401269.

[16] Komazaki Y, Hirama H, Torii T. Electrically and magnetically dual-driven Janus particles for handwriting-enabled electronic paper. J Appl Phys 2015;117:34–9. doi:10.1063/1.4917379.

[17] Jiang T, Zukoski CF. Role of particle size and polymer length in rheology of colloid-polymer composites. Macromolecules 2012;45:9791–803. doi:10.1021/ma301184t.

[18] Dendukuri D, Doyle PS. The synthesis and assembly of polymeric microparticles using microfluidics. Adv Mater 2009;21:4071–86. doi:10.1002/adma.200803386.

[19] Gilchrist SE, Rickard DL, Letchford K, Needham D, Burt HM. Phase separation behavior of fusidic acid and rifampicin in PLGA microspheres. Mol Pharm

2012;9:1489–501. doi:10.1021/mp300099f.

[20] Tinsley-Bown AM, Fretwell R, Dowsett AB, Davis SL, Farrar GH. Formulation of poly(D,L-lactic-co-glycolic acid) microparticles for rapid plasmid DNA delivery. J Control Release 2000;66:229–41.

[21] Kawashima Y, Yamamoto H, Takeuchi H, Hino T, Niwa T. Properties of a peptide containing DL-lactide/glycolide copolymer nanospheres prepared by novel emulsion solvent diffusion methods. Eur J Pharm Biopharm 1998;45:41–8. doi:10.1016/S0939-6411(97)00121-5.

[22] Sinha VR, Trehan A. Biodegradable microspheres for protein delivery. J Control Release 2003;90:261–80. doi:10.1016/S0168-3659(03)00194-9.

[23] Jain RA. The manufacturing techniques of various drug loaded biodegradable poly(lactide-co-glycolide) (PLGA) devices. Biomaterials 2000;21:2475–90. doi:10.1016/S0142-9612(00)00115-0.

[24] Zhang W, He X. Encapsulation of living cells in small (approximately 100 microm) alginate microcapsules by electrostatic spraying: A parametric study. J Biomech Eng 2009;131:74515. doi:10.1115/1.3153326.

[25] Beck-Broichsitter M, Schweiger C, Schmehl T, Gessler T, Seeger W, Kissel T. Characterization of novel spray-dried polymeric particles for controlled pulmonary drug delivery. J Control Release 2012;158:329–35. doi:10.1016/j.jconrel.2011.10.030.

[26] Tracy MA. Development and scale-up of a microsphere protein delivery system. Biotechnol Prog 1998;14:108–15. doi:10.1021/bp9701271.

[27] Kim JH, Jeon TY, Choi TM, Shim TS, Kim S-H, Yang S-M. Droplet microfluidics for producing functional microparticles. Langmuir 2014;30:1473–88. doi:10.1021/la403220p.

[28] Hosokawa M, Hoshino Y, Nishikawa Y, Hirose T, Yoon DH, Mori T, et al. Droplet-based microfluidics for high-throughput screening of a metagenomic library for isolation of microbial enzymes. Biosens Bioelectron 2015;67:379–85. doi:10.1016/j.bios.2014.08.059.

[29] Nisisako T, Torii T. Formation of biphasic Janus droplets in a microfabricated channel for the synthesis of shape-controlled polymer microparticles. Adv Mater 2007;19:1489–93. doi:10.1002/adma.200700272.

[30] Lim J-M, Bertrand N, Valencia PM, Rhee M, Langer R, Jon S, et al. Parallel microfluidic synthesis of size-tunable polymeric nanoparticles using 3D flow focusing towards in vivo study. Nanomedicine 2014;10:401–9. doi:10.1016/j.nano.2013.08.003.

[31] Radulescu D, Schwade N, Wawro D. Uniform paclitaxel-loaded biodegradable microspheres manufactured by ink-jet technology. Control. Release Soc. 11th Int. Symp. Recent Adv. Drug Deliv. Syst., Salt Lake City, Utah: 2003.

[32] Böhmer MR, Schroeders R, Steenbakkers JAM, de Winter SHPM, Duineveld PA, Lub J, et al. Preparation of monodisperse polymer particles and capsules by ink-jet printing. Colloids Surfaces A Physicochem Eng Asp 2006;289:96–104. doi:10.1016/j.colsurfa.2006.04.011.

[33] Lee BK, Yun YH, Choi JS, Choi YC, Kim JD, Cho YW. Fabrication of drug-loaded polymer microparticles with arbitrary geometries using a piezoelectric inkjet printing system. Int J Pharm 2012;427:305–10. doi:10.1016/j.ijpharm.2012.02.011.

[34] Saunders RE, Gough JE, Derby B. Delivery of human fibroblast cells by piezoelectric drop-on-demand inkjet printing. Biomaterials 2008;29:193–203. doi:10.1016/j.biomaterials.2007.09.032.

[35] Fonseca AC, Ferreira P, Cordeiro RA, Mendonça P V., Góis JR, Gil MH, et al. Drug delivery systems for predicitive medicine: Polymers as tools for advanced applications. In: Mozaffari MS, editor. New Strateg. to Adv. Pre/Diabetes Care Integr. Approach by PPPM, vol. 3, Dordrecht: Springer Netherlands; 2013, p. 399–455. doi:10.1007/978-94-007-5971-8.

[36] Maa YF, Hsu C. Microencapsulation reactor scale-up by dimensional analysis. J Microencapsul 1996;13:53–66. doi:10.3109/02652049609006803.

[37] Li GL, Möhwald H, Shchukin DG. Precipitation polymerization for fabrication of complex core-shell hybrid particles and hollow structures. Chem Soc Rev 2013;42:3628–46. doi:10.1039/c3cs35517a.

[38] Hou Q, De Bank PA, Shakesheff KM. Injectable scaffolds for tissue regeneration. J Mater Chem 2004;14:1915–23. doi:10.1039/B401791A.

[39] Park K, Yeo Y. Microencapsulation technology. In: Swarbrick J, editor. Encycl. Pharm. Technol. Third Edit, Informa Healthcare USA, Inc.; 2007, p. 2315–27. doi:10.1081/E-EPT-120028567.

[40] Jalil R, Nixon JR. Biodegradable poly(lactic acid) and poly(lactide-co-glycolide) microcapsules: Problems associated with preparative techniques and release properties. J Microencapsul 1990;7:297–325. doi:10.3109/02652049009021842.

[41] Arshady R. Preparation of biodegradable microspheres and microcapsules: 2. Polyactides and related polyesters. J Control Release 1991;17:1–21. doi:10.1016/0168-3659(91)90126-X.

[42] Radulescu D. Method for forming polymer microspheres. US 6,998,074 B1, 2006.

[43] Tewes F, Boury F, Benoit J-P. Biodegradable microspheres: Advances in production technology. In: Benita S, editor. Microencapsul. Methods Ind. Appl. Second Edi, Informa Healthcare; 2005, p. 1–53. doi:doi:10.1201/9781420027990.pt1.

[44] Thomasin C, Nam-Trân H, Merkle HP, Gander B. Drug microencapsulation by PLA/PLGA coacervation in the light of thermodynamics. 1. Overview and theoretical considerations. J Pharm Sci 1998;87:259–68. doi:10.1021/js970047r.

[45] Thomasin C, Merkle HP, Gander B. Drug microencapsulation by PLA/PLGA coacervation in the light of thermodynamics. 2. Parameters determining microsphere formation. J Pharm Sci 1998;87:269–75. doi:10.1021/js970048j.

[46] Edelman R, Russell RG, Losonsky G, Tall BD, Tacket CO, Levine MM, et al. Immunization of rabbits with enterotoxigenic E. coli colonization factor antigen (CFA/I) encapsulated in biodegradable microspheres of poly (lactide-co-glycolide). Vaccine 1993;11:155–8. doi:10.1016/0264-410X(93)90012-M.

[47] Augustin MA, Hemar Y. Nano- and micro-structured assemblies for encapsulation of food ingredients. Chem Soc Rev 2009;38:902–12. doi:10.1039/b801739p.

[48] Thomasin C, Merkle HP, Gander BA. Physico-chemical parameters governing protein microencapsulation into biodegradable polyesters by coacervation. Int J Pharm 1997;147:173–86. doi:10.1016/S0378-5173(96)04810-7.

[49] Ruiz JM, Tissier B, Benoit JP. Microencapsulation of peptide: A study of the phase separation of poly(D,L-lactic acid-co-glycolic acid) copolymers 50/50 by silicone oil. Int J Pharm 1989;49:69–77. doi:10.1016/0378-5173(89)90154-3.

[50] Dong ZJ, Touré A, Jia CS, Zhang XM, Xu SY. Effect of processing parameters on the formation of spherical multinuclear microcapsules encapsulating peppermint oil by coacervation. J Microencapsul 2007;24:634–46. doi:10.1080/02652040701500632.

[51] Strand BL, Gaserod O, Kulseng B, Espevik T, Skjak-Baek G. Alginate-polylysine-alginate microcapsules: Effect of size reduction on capsule properties. J Microencapsul 2002;19:615–30. doi:10.1080/02652040210144243.

[52] Koch S, Schwinger C, Kressler J, Heinzen C, Rainov NG. Alginate encapsulation of genetically engineered mammalian cells: Comparison of production devices, methods and microcapsule characteristics. J Microencapsul 2003;20:303–16. doi:10.1080/0265204021000058438.

[53] Xie J, Wang CH. Electrospray in the dripping mode for cell microencapsulation. J Colloid Interface Sci 2007;312:247–55. doi:10.1016/j.jcis.2007.04.023.

[54] van de Weert M, Hennink WE, Jiskoot W. Protein instability in poly(lactic-co-glycolic acid) microparticles. Pharm Res 2000;17:1159–67. doi:10.1023/A:1026498209874.

[55] Bodmeier R, Chen H. Preparation of biodegradable poly(+/-)lactide microparticles using a spray-drying technique. J Pharm Pharmacol 1988;40:754–7. doi:10.1111/j.2042-7158.1988.tb05166.x.

[56] Elversson J, Millqvist-Fureby A. Particle size and density in spray drying - Effects of carbohydrate properties. J Pharm Sci 2005;94:2049–60. doi:10.1002/jps.20418.

[57] Makadia H, Siegel S. Poly lactic-co-glycolic acid (PLGA) as biodegradable controlled drug delivery carrier. Polym 2011;3:1377–97. doi:10.3390/polym3031377.

[58] Yurteri CU, Hartman RPA, Marijnissen JCM. Producing pharmaceutical particles via electrospraying with an emphasis on nano and nano structured particles - A review. KONA Powder Part J 2010;28:91–115. doi:10.14356/kona.2010010.

[59] Wang J, Li Y, Wang X, Wang J, Tian H, Zhao P, et al. Droplet microfluidics for the production of microparticles and nanoparticles. Micromachines 2017;8:22. doi:10.3390/mi8010022.

[60] Berkland C, Kipper MJ, Narasimhan B, Kim K, Pack DW. Microsphere size, precipitation kinetics and drug distribution control drug release from biodegradable polyanhydride microspheres. J Control Release 2004;94:129–41. doi:10.1016/j.jconrel.2003.09.011.

[61] Han FY, Thurecht KJ, Whittaker AK, Smith MT. Bioerodable PLGA-based microparticles for producing sustained-release drug formulations and strategies for improving drug loading. Front Pharmacol 2016;7:185. doi:10.3389/fphar.2016.00185.

[62] Tirella A, La Marca M, Brace L-A, Mattei G, Aylott JW, Ahluwalia A. Nano-in-Micro self-reporting hydrogel constructs. J Biomed Nanotechnol 2015;11:1451–60. doi:10.1166/jbn.2015.2085.

[63] Adams JM. Particle size and shape effects in material science: Examples from polymer and paper systems. Clay Miner 1993;28:509–30. doi:10.1180/claymin.1993.028.4.03.

[64] Sen Gupta A. Role of particle size, shape, and stiffness in design of intravascular drug delivery systems: Insights from computations, experiments, and nature. Wiley Interdiscip Rev Nanomedicine Nanobiotechnology 2016;8:255–70. doi:10.1002/wnan.1362.

[65] Canelas DA, Herlihy KP, DeSimone JM. Top-down particle fabrication: Control of size and shape for diagnostic imaging and drug delivery. Wiley Interdiscip Rev Nanomedicine Nanobiotechnology 2009;1:391–404. doi:10.1002/wnan.40.

[66] Champion JA, Katare YK, Mitragotri S. Particle shape: A new design parameter for micro- and nanoscale drug delivery carriers. J Control Release 2007;121:3–9. doi:10.1016/j.jconrel.2007.03.022.

[67] Berkland C, Kim K, Pack DW. Fabrication of PLG microspheres with precisely controlled and monodisperse size distributions. J Control Release 2001;73:59–74. doi:10.1016/S0168-3659(01)00289-9.

[68] Champion J a, Katare YK, Mitragotri S. Making polymeric micro- and nanoparticles of complex shapes. Proc Natl Acad Sci U S A 2007;104:11901–4. doi:10.1073/pnas.0705326104.

[69] Paulsen KS, Di Carlo D, Chung AJ. Optofluidic fabrication for 3D-shaped particles. Nat Commun 2015;6:6976. doi:10.1038/ncomms7976.

[70] Gupta MK, Meng F, Johnson BN, Kong YL, Tian L, Yeh YW, et al. 3D printed programmable release capsules. Nano Lett 2015;15:5321–9. doi:10.1021/acs.nanolett.5b01688.

[71] Gillen G, Najarro M, Wight S, Walker M, Verkouteren J, Windsor E, et al. Particle fabrication using inkjet printing onto hydrophobic surfaces for optimization and calibration of trace contraband detection sensors. Sensors 2015;15:29618–34. doi:10.3390/s151129618.

[72] Gao M, Li L, Song Y. Inkjet printing wearable electronic devices. J Mater Chem C 2017;5:2971–93. doi:10.1039/C7TC00038C.

[73] Mitra KY, Sternkiker C, Martínez-Domingo C, Sowade E, Ramon E, Carrabina J, et al. Inkjet printed metal insulator semiconductor (MIS) diodes for organic and flexible electronic application. Flex Print Electron 2017;2:15003.

[74] Murphy S V, Atala A. 3D bioprinting of tissues and organs. Nat Biotechnol 2014;32:773–85. doi:10.1038/nbt.2958.

[75] Singh M, Haverinen HM, Dhagat P, Jabbour GE. Inkjet printing - Process and its applications. Adv Mater 2010;22:673–85. doi:10.1002/adma.200901141.

[76] Calvert P. Inkjet printing for materials and devices. Chem Mater 2001;13:3299–305. doi:10.1021/cm0101632.

[77] de Gans B-J, Duineveld PC, Schubert US. Inkjet printing of polymers: State of the art and future developments. Adv Mater 2004;16:203–13. doi:10.1002/adma.200300385.

[78] Song H, Spencer J, Jander A, Nielsen J, Stasiak J, Kasperchik V, et al. Inkjet printing of magnetic materials with aligned anisotropy. J Appl Phys 2014;115:17E308. doi:10.1063/1.4863168.

[79] Lee H, Tentzeris MM, Markondeya P, Raj MKP, Kawahara Y. Inkjet-printed ferromagnetic nanoparticles for miniaturization of flexible printed RF inductors. IEEE Antennas Propag. Soc. Int. Symp., Orlando: 2013, p. 994–5. doi:10.1109/APS.2013.6711157.

[80] Saleh E, Woolliams P, Clarke B, Gregory A, Greedy S, Smartt C, et al. 3D inkjet-printed UV-curable inks for multi-functional electromagnetic applications. Addit Manuf 2016;13:143–8. doi:10.1016/j.addma.2016.10.002.

[81] Fox CB, Nemeth CL, Chevalier RW, Cantlon J, Bogdanoff DB, Hsiao JC, et al.

Picoliter-volume inkjet printing into planar microdevice reservoirs for low-waste, high-capacity drug loading. Bioeng Transl Med 2017:1–8. doi:10.1002/btm2.10053.

[82] Sandler N, Preis M. Printed drug-delivery systems for improved patient treatment. Trends Pharmacol Sci 2017;38:317–27. doi:10.1016/j.tips.2016.10.002.

[83] Christensen K, Xu C, Chai W, Zhang Z, Fu J, Huang Y. Freeform inkjet printing of cellular structures with bifurcations. Biotechnol Bioeng 2015;112:1047–55. doi:10.1002/bit.25501.

[84] Trombetta R, Inzana JA, Schwarz EM, Kates SL, Awad HA. 3D printing of calcium phosphate ceramics for bone tissue engineering and drug delivery. Ann Biomed Eng 2017;45:23–44. doi:10.1007/s10439-016-1678-3.

[85] Zhang YS, Yue K, Aleman J, Mollazadeh-Moghaddam K, Bakht SM, Yang J, et al. 3D bioprinting for tissue and organ fabrication. Ann Biomed Eng 2017;45:148–63. doi:10.1007/s10439-016-1612-8.

[86] Derby B. Inkjet printing of functional and structural materials: Fluid property requirements, feature stability, and resolution. Annu Rev Mater Res 2010;40:395–414. doi:10.1146/annurev-matsci-070909-104502.

[87] Antohe B V., Wallace DB. Ink-jet as a manufacturing method for drug delivery applications. Int. Manuf. Sci. Eng. Conf., Evanston, Illinois, USA: ASME; 2008, p. 525–33. doi:10.1115/MSEC_ICMP2008-72248.

[88] Derby B. Bioprinting: Inkjet printing proteins and hybrid cell-containing materials and structures. J Mater Chem 2008;18:5717–21. doi:10.1039/b807560c.

[89] Basaran OA. Small-scale free surface flows with breakup: Drop formation and emerging applications. AIChE J 2002;48:1842–8. doi:10.1002/aic.690480902.

[90] Lin H, Wu H, Shan T, Hwang W. The effects of operating parameters on micro-droplet formation in a piezoelectric inkjet printhead using a double pulse voltage pattern. Mater Trans 2006;47:375–82. doi:10.2320/matertrans.47.375.

[91] Sirringhaus H, Shimoda T. Inkjet printing of functional materials. MRS Bull 2003;28:802–6. doi:10.1557/mrs2003.228.

[92] Wijshoff H. Structure- and fluid-dynamics in piezo inkjet printheads. University of Twente, 2008. doi:10.1016/j.physrep.2010.03.003.

[93] Fuller SB, Wilhelm EJ, Jacobson JM. Ink-jet printed nanoparticle microelectromechanical systems. J Microelectromechanical Syst 2002;11:54–60. doi:10.1109/84.982863.

[94] Yu DG, Zhu L-M, Branford-White CJ, Yang XL. Three-dimensional printing in pharmaceutics: Promises and problems. J Pharm Sci 2008;97:3666–90. doi:10.1002/jps.21284.

[95] Fletcher R, Brazin J, Staymates M, Bennerjr B, Gillen J. Fabrication of polymer microsphere particle standards containing trace explosives using an oil/water emulsion solvent extraction piezoelectric printing process. Talanta 2008;76:949–55. doi:10.1016/j.talanta.2008.04.066.

[96] Wu XS, Wang N. Synthesis, characterization, biodegradation, and drug delivery application of biodegradable lactic/glycolic acid polymers. Part II: Biodegradation. J Biomater Sci Polym Edn 2001;12:21–34.

[97] Visscher GE, Robison RL, Maulding H V, Fong JW, Pearson JE, Argentieri GJ. Biodegradation of and tissue reaction to 50:50 poly(DL-lactide-co-glycolide) microcapsules. J Biomed Mater Res 1985;19:349–65. doi:10.1002/jbm.820190315.

[98] Iwanaga S, Saito N, Sanae H, Nakamura M. Facile fabrication of uniform size-controlled microparticles and potentiality for tandem drug delivery system of micro/nanoparticles. Colloids Surfaces B Biointerfaces 2013;109:301–6. doi:10.1016/j.colsurfb.2013.04.007.

[99] Schwalm R. UV coatings: Basics, recent developments and new applications. Elsevier Science; 2006.

[100] Crivello J V., Reichmanis E. Photopolymer materials and processes for advanced technologies. Chem Mater 2014;26:533–48. doi:10.1021/cm402262g.

[101] Stone HA, Kim S. Microfluidics: Basic issues, applications, and challenges. AIChE J 2001;47:1250–4. doi:10.1002/aic.690470602.

[102] Ong S-E, Zhang S, Du H, Fu Y. Fundamental principles and applications of microfluidic systems. Front Biosci 2008;13:2757–73. doi:10.2741/2883.

[103] Whitesides GM. The origins and the future of microfluidics. Nature 2006;442:368–73. doi:10.1038/nature05058.

[104] Slapar V. Microfluidics. 2008.

[105] Zhang J, Yan S, Yuan D, Alici G, Nguyen N-T, Ebrahimi Warkiani M, et al. Fundamentals and applications of inertial microfluidics: A review. Lab Chip 2016;16:10–34. doi:10.1039/C5LC01159K.

[106] Manz A, Harrison DJ, Verpoorte EMJ, Fettinger JC, Paulus A, Lüdi H, et al. Planar chips technology for miniaturization and integration of separation techniques into monitoring systems. J Chromatogr A 1992;593:253–8. doi:10.1016/0021-9673(92)80293-4.

[107] Bhagat AAS, Bow H, Hou HW, Tan SJ, Han J, Lim CT. Microfluidics for cell separation. Med Biol Eng Comput 2010;48:999–1014. doi:10.1007/s11517-010-0611-4.

[108] Song H, Chen DL, Ismagilov RF. Reactions in droplets in microfluidic channels. Angew Chemie Int Ed English 2006;45:7336–56. doi:10.1002/anie.200601554.

[109] Xu S, Nie Z, Seo M, Lewis P, Kumacheva E, Stone H a., et al. Generation of monodisperse particles by using microfluidics: Control over size, shape, and composition. Angew Chemie Int Ed 2005;44:724–8. doi:10.1002/anie.200462226.

[110] Vasiliauskas R, Liu D, Cito S, Zhang H, Shahbazi M-A, Sikanen T, et al. Simple microfluidic approach to fabricate monodisperse hollow microparticles for multidrug delivery. ACS Appl Mater Interfaces 2015;7:14822–32. doi:10.1021/acsami.5b04824.

[111] Conchouso D, Castro D, Khan S a, Foulds IG. Three-dimensional parallelization of microfluidic droplet generators for a litre per hour volume production of single emulsions. Lab Chip 2014;14:3011–20. doi:10.1039/c4lc00379a.

[112] Kobayashi I, Wada Y, Uemura K, Nakajima M. Microchannel emulsification for mass production of uniform fine droplets: Integration of microchannel arrays on a chip. Microfluid Nanofluidics 2010;8:255–62. doi:10.1007/s10404-009-0501-y.

[113] Ren K, Zhou J, Wu H. Materials for microfluidic chip fabrication. Acc Chem Res 2013;46:2396–406. doi:10.1021/ar300314s.

[114] Elveflow. Microfluidics: A general overview of microfluidics n.d. http://www.elveflow.com/microfluidic-tutorials/microfluidic-reviews-and-

tutorials/microfluidics/ (accessed March 23, 2017).

[115] Roy E, Pallandre A, Zribi B, Horny M-C, Delapierre FD, Cattoni A, et al. Overview of materials for microfluidic applications. In: Yu X-Y, editor. Adv. Microfluid. - New Appl. Biol. Energy, Mater. Sci., InTech; 2016, p. 335–55. doi:10.5772/65773.

[116] Nge PN, Rogers CI, Woolley AT. Advances in microfluidic materials, functions, integration, and applications. Chem Rev 2013;113:2550–83. doi:10.1021/cr300337x.

[117] Rodrigues RO, Lima R, Gomes HT, Silva AMT. Polymer microfluidic devices: An overview of fabrication methods. UPorto J Eng 2015;1:67–79.

[118] Lei KF. Materials and fabrication techniques for nano- and microfluidic devices. In: Labeed FH, Fatoyinbo HO, editors. Microfluid. Detect. Sci. Lab-on-a-chip Technol., Royal Society of Chemistry; 2014, p. 1–28. doi:10.1039/9781849737609-00001.

[119] Iliescu C, Taylor H, Avram M, Miao J, Franssila S. A practical guide for the fabrication of microfluidic devices using glass and silicon. Biomicrofluidics 2012;6:16505–1650516. doi:10.1063/1.3689939.

[120] Gokmen MT, Du Prez FE. Porous polymer particles - A comprehensive guide to synthesis, characterization, functionalization and applications. Prog Polym Sci 2012;37:365–405. doi:10.1016/j.progpolymsci.2011.07.006.

[121] Garstecki P, Fuerstman MJ, Stone H a, Whitesides GM. Formation of droplets and bubbles in a microfluidic T-junction - Scaling and mechanism of break-up. Lab Chip 2006;6:437–46. doi:10.1039/b510841a.

[122] Pit AM, Duits MHG, Mugele F. Droplet manipulations in two phase flow microfluidics. Micromachines 2015;6:1768–93. doi:10.3390/mi6111455.

[123] Nurumbetov G, Ballard N, Bon S a. F. A simple microfluidic device for fabrication of double emulsion droplets and polymer microcapsules. Polym Chem 2012;3:1043–7. doi:10.1039/c2py00605g.

[124] Nisisako T, Hatsuzawa T. A microfluidic cross-flowing emulsion generator for producing biphasic droplets and anisotropically shaped polymer particles. Microfluid Nanofluidics 2010;9:427–37. doi:10.1007/s10404-009-0559-6.

[125] Xuan M, Shao J, Lin X, Dai L, He Q. Self-propelled Janus mesoporous silica

nanomotors with sub-100 nm diameters for drug encapsulation and delivery. ChemPhysChem 2014;15:2255–60. doi:10.1002/cphc.201402111.

[126] Fisher JP, Dean D, Engel PS, Mikos AG. Photoinitiated polymerization of biomaterials. Annu Rev Mater Res 2001;31:171–81. doi:10.1146/annurev.matsci.31.1.171.

[127] Green WA. Industrial photoinitiators: A technical guide. illustrate. CRC Press; 2010. doi:10.1201/9781439827468.

[128] Cai Y, Jessop JLP. Photopolymerization, free radical. Encycl. Polym. Sci. Technol., vol. 10, 2004, p. 807–37. doi:10.1002/0471440264.pst490.

[129] Anseth KS, Burdick JA. New directions in photopolymerizable biomaterials. MRS Bull 2002;27:130–6. doi:10.1557/mrs2002.49.

[130] Amini AA, Nair LS. Injectable hydrogels for bone and cartilage repair. Biomed Mater 2012;7:24105. doi:10.1088/1748-6041/7/2/024105.

[131] Jeuken RM, Roth AK, Peters RJRW, van Donkelaar CC, Thies JC, van Rhijn LW, et al. Polymers in cartilage defect repair of the knee: Current status and future prospects. Polymers (Basel) 2016;8:219–49. doi:10.3390/polym8060219.

[132] Anseth KS, Newman SM, Bowman CN. Polymeric dental composites: Properties and reaction behavior of multimethacrylate dental restorations. In: Peppas NA, Langer RS, editors. Biopolym. II, Berlin, Heidelberg: Springer, Berlin, Heidelberg; 1995, p. 177–217. doi:10.1007/3540587888_16.

[133] Stansbury JW. Curing dental resins and composites by photopolymerization. J Esthet Restor Dent 2000;12:300–8. doi:10.1111/j.1708-8240.2000.tb00239.

[134] Burdick JA, Ward M, Liang E, Young MJ, Langer R. Stimulation of neurite outgrowth by neurotrophins delivered from degradable hydrogels. Biomaterials 2006;27:452–9. doi:10.1016/j.biomaterials.2005.06.034.

[135] Schmidt JJ, Rowley J, Kong HJ. Hydrogels used for cell-based drug delivery. J Biomed Mater Res Part A 2008;87:1113–1122. doi:10.1002/jbm.a.32287.

[136] Lin C, Anseth KS. PEG hydrogels for the controlled release of biomolecules in regenerative medicine. Pharm Res 2009;26:631–43. doi:10.1007/s11095-008-9801-2.

[137] Arceneaux JA, Willard K. UV & EB chemistry and technology. RadTech Printer's Guid n.d.:1–8. http://72.52.184.8/~radtecho/pdfs/PrinterGuideChemistry.pdf

(accessed March 13, 2017).

[138] Allen NS. Photopolymerisation and photoimaging science and technology. illustrate. Springer Netherlands; 2011.

[139] Davidson SR. Polymeric and polyrnerisable free radical photoinitiators. J Photochem Photobiol A Chem 1993;69:263–75.

[140] Pappas PS. Radiation curing: Science and technology. illustrate. Springer Science & Business Media; 2013.

[141] Allen NS. Photoinitiators for UV and visible curing of coatings: Mechanisms and properties. J Photochem Photobiol A Chem 1996;100:101–7. doi:10.1016/S1010-6030(96)04426-7.

[142] Davidson S. Exploring the science, technology and applications of UV and EB curing. Sita Technology; 1999.

[143] Roffey CG. Photopolymerization of surface coatings. New York: Wiley-Blackwell; 1982.

[144] Andrzejewska E. Photopolymerization kinetics of multifunctional monomers. Prog Polym Sci 2001;26:605–65. doi:10.1016/S0079-6700(01)00004-1.

[145] Allen NS, Marin MC, Edge M, Daies DW, Garrett J, Jones F, et al. Photochemistry and photoinduced chemical crosslinking activity of type I & II co-reactive photoinitiators in acrylated prepolymeres. J Photochem Photobiol A Chem 1999;126:135–49.

[146] Arceneaux JA. Mitigation of oxygen inhibition in UV LED , UVA, and low intensity UV cure. RadTech Int. UV EB Technol. Expo Conf. (RADTECH 2014), Rosemont, Illinois, USA: Curran Associates, Inc.; 2014, p. 6–16.

[147] Dendukuri D, Panda P, Haghgooie R, Kim JM, Hatton TA, Doyle PS. Modeling of oxygen-inhibited free radical photopolymerization in a PDMS microfluidic device. Macromolecules 2008;41:8547–56. doi:10.1021/ma801219w.

[148] Lee TY, Guymon CA, Jönsson SE, Hoyle CE. The effect of monomer structure on oxygen inhibition of (meth)acrylates photopolymerization. Polymer (Guildf) 2004;45:6155–62. doi:10.1016/j.polymer.2004.06.060.

[149] Studer K, Decker C, Beck E, Schwalm R. Overcoming oxygen inhibition in UV-curing of acrylate coatings by carbon dioxide inerting, Part I. Prog Org Coatings 2003;48:92–100. doi:10.1016/S0300-9440(03)00120-6.

[150] Ligon SC, Husár B, Wutzel H, Holman R, Liska R. Strategies to reduce oxygen inhibition in photoinduced polymerization. Chem Rev 2014;114:577–89. doi:10.1021/cr3005197.

[151] Fouassier J-P. Photoinitiation, photopolymerization, and photocuring: Fundamentals and applications. Hanser; 1995.

[152] Anderson DG, Bell CA, Davidson RS, Sellars P. Mono and bis substituted polymeric aminobenzoates as amine synergists for UV curing. RadTech Eu. Conf. Proc., 2005, p. 437–43.

[153] Lapin SC, Geiger ZS. Effect of amine synergists on the EB-curing properties of acrylate-based coatings. 2014.

[154] Fouassier J-P, Lalevée J. Three-component photoinitiating systems: Towards innovative tailor made high performance combinations. RSC Adv 2012;2:2621–9. doi:10.1039/c2ra00892k.

[155] Matsushima H, Hait S, Li Q, Zhou H, Shirai M, Hoyle CE. Non-extractable photoinitiators based on thiol-functionalized benzophenones and thioxanthones. Eur Polym J 2010;46:1278–87. doi:10.1016/j.eurpolymj.2010.03.003.

[156] Hook AL, Anderson DG, Langer R, Williams P, Davies MC, Alexander MR. High throughput methods applied in biomaterial development and discovery. Biomaterials 2010;31:187–98. doi:10.1016/j.biomaterials.2009.09.037.

[157] Celiz AD, Harrington HC, Hook AL. High throughput assessment and chemometric analysis of the interaction of epithelial and fibroblast cells with a polymer library. Appl Surf Sci 2014;313:926–35. doi:10.1016/j.apsusc.2014.06.111.

[158] Patel AK, Tibbitt MW, Celiz AD, Davies MC, Langer R, Denning C, et al. High throughput screening for discovery of materials that control stem cell fate. Curr Opin Solid State Mater Sci 2016;20:202–11. doi:10.1016/j.cossms.2016.02.002.

[159] Anderson DG, Levenberg S, Langer R. Nanoliter-scale synthesis of arrayed biomaterials and application to human embryonic stem cells. Nat Biotechnol 2004;22:863–6. doi:10.1038/nbt981.

[160] Ratner BD, Bryant SJ. Biomaterials: Where we have been and where we are

going. Annu Rev Biomed Eng 2004;6:41–75. doi:10.1146/annurev.bioeng.6.040803.140027.

[161] Anderson DG, Tweedie C a., Hossain N, Navarro SM, Brey DM, Van Vliet KJ, et al. A combinatorial library of photocrosslinkable and degradable materials. Adv Mater 2006;18:2614–8. doi:10.1002/adma.200600529.

[162] Anastasaki A, Nikolaou V, Pappas GS, Zhang Q, Wan C, Wilson P, et al. Photoinduced sequence-control via one pot living radical polymerization of acrylates. Chem Sci 2014;5:3536–42. doi:10.1039/C4SC01374C.

[163] Hook AL, Chang C-Y, Yang J, Luckett J, Cockayne A, Atkinson S, et al. Combinatorial discovery of polymers resistant to bacterial attachment. Nat Biotechnol 2012;30:868–75. doi:10.1038/nbt.2316.

[164] Hook AL, Chang C-Y, Yang J, Scurr DJ, Langer R, Anderson DG, et al. Polymer microarrays for high throughput discovery of biomaterials. J Vis Exp 2012:e3636. doi:10.3791/3636.

[165] Cole N, Hume EBH, Vijay AK, Sankaridurg P, Kumar N, Willcox MDP. In vivo performance of melimine as an antimicrobial coating for contact lenses in models of CLARE and CLPU. Investig Ophthalmol Vis Sci 2010;51:390–5. doi:10.1167/iovs.09-4068.

[166] Vasilev K, Cook J, Griesser HJ. Antibacterial surfaces for biomedical devices. Expert Rev Med Devices 2009;6:553–67. doi:10.1586/erd.09.36.

[167] Wisniewski N, Reichert M. Methods for reducing biosensor membrane biofouling. Colloids Surfaces B Biointerfaces 2000;18:197–219. doi:10.1016/S0927-7765(99)00148-4.

[168] Brandwein M, Al-Quntar A, Goldberg H, Mosheyev G, Goffer M, Marin-Iniesta F, et al. Mitigation of biofilm formation on corrugated cardboard fresh produce packaging surfaces using a novel thiazolidinedione derivative integrated in acrylic emulsion polymers. Front Microbiol 2016;7:159. doi:10.3389/fmicb.2016.00159.

[169] Kuliasha CA, Finlay JA, Franco SC, Clare AS, Stafslien SJ, Brennan AB. Marine anti-biofouling efficacy of amphiphilic poly(coacrylate) grafted PDMSe: Effect of graft molecular weight. Biofouling 2017;33:252–67. doi:10.1080/08927014.2017.1288807.

[170] Selim MS, Shenashen MA, El-Safty SA, Higazy SA, Isago H, Elmarakbi A. Recent progress in marine foul-release polymeric nanocomposite coatings. Prog Mater Sci 2017;87:1–32. doi:10.1016/j.pmatsci.2017.02.001.

[171] Patel IS, Seemungal TAR, Wilks M, Lloyd-Owen SJ, Donaldson GC, Wedzicha JA. Relationship between bacterial colonisation and the frequency, character, and severity of COPD exacerbations. Thorax 2002;57:759–64. doi:10.1136/thorax.57.9.759.

[172] Hook AL, Chang CY, Yang J, Atkinson S, Langer R, Anderson DG, et al. Discovery of novel materials with broad resistance to bacterial attachment using combinatorial polymer microarrays. Adv Mater 2013;25:2542–7. doi:10.1002/adma.201204936.

[173] Jamal M, Tasneem U, Hussain T, Andleeb and S. Bacterial biofilm: Its composition, formation and role in human infections. Res Rev J Microbiol Biotechnol 2015;4:1–14.

[174] Flemming H-C, Wingender J. The biofilm matrix. Nat Rev Microbiol 2010;8:623–33. doi:10.1038/nrmicro2415.

[175] Costeron JW, Stewart PS, Greenberg EP. Bacterial biofilms: A common cause of persistent infections. Science 1999;284:1318–22. doi:10.1126/science.284.5418.1318.

[176] Smith AW. Biofilms and antibiotic therapy: Is there a role for combating bacterial resistance by the use of novel drug delivery systems? Adv Drug Deliv Rev 2005;57:1539–50. doi:10.1016/j.addr.2005.04.007.

[177] Lebeaux D, Ghigo J-M, Beloin C. Biofilm-related infections: Bridging the gap between clinical management and fundamental aspects of recalcitrance toward antibiotics. Microbiol Mol Biol Rev 2014;78:510–43. doi:10.1128/MMBR.00013-14.

[178] Belas R. Biofilms, flagella, and mechanosensing of surfaces by bacteria. Trends Microbiol 2014;22:517–27. doi:10.1016/j.tim.2014.05.002.

[179] Ventola CL. The antibiotic resistance crisis, Part 1: Causes and threats. P T 2015;40:277–83.

[180] Hermansson M. The DLVO theory in microbial adhesion. Colloids Surfaces B Biointerfaces 1999;14:105–19. doi:10.1016/S0927-7765(99)00029-6.

[181] Zhang X, Zhang Q, Yan T, Jinag Z, Zhang X, Zuo YY. Quantitatively predicting bacterial adhesion using surface free energy determined with a spectrophotometric method. Env Sci Technol 2015;49:6164–71. doi:10.1021/es5050425.

[182] Kaplan ML, Kaplan L. The Gram stain and differential staining. J Bacteriol 1933;25:309–21.

[183] Beveridge TJ, Graham LL. Surface layers of bacteria. Microbiol Rev 1991;55:684–705.

[184] Schleifer KH, Kandler O. Peptidoglycan types of bacterial cell walls and their taxonomic implications. Bacteriol Rev 1972;36:407–77.

[185] Swoboda JG, Campbell J, Meredith TC, Walker S. Wall teichoic acid function, biosynthesis, and inhibition. Chembiochem 2010;11:35–45. doi:10.1002/cbic.200900557.Wall.

[186] Brown L, Wolf JM, Prados-Rosales R, Casadevall A. Through the wall: extracellular vesicles in Gram-positive bacteria, mycobacteria and fungi. Nat Rev Microbiol 2015;13:620–30. doi:10.1038/nrmicro3480.

[187] Silhavy TJ, Kahne D, Walker S. The bacterial cell envelope. Cold Spring Harb Perspect Biol 2010;2:a000414. doi:10.1101/cshperspect.a000414.

[188] Raetz CRH, Whitfield C. Lipopolysaccharide endotoxins. Annu Rev Biochem 2002;71:635–700. doi:10.1146/annurev.biochem.71.110601.135414.

[189] Beveridge TJ. The bacterial surface: general considerations towards design and function. Can J Microbiol 1988;34:363–72. doi:10.1139/m88-067.

[190] Shai Y. Mode of action of membrane active antimicrobial peptides. Biopolymers 2002;66:236–48. doi:10.1002/bip.10260.

[191] Semmler ABT, Whitchurch CB, Mattick JS. A re-examination of twitching motility in Pseudomonas aeruginosa. Microbiology 1999;145:2863–73. doi:10.1099/00221287-145-10-2863.

[192] O'Toole G, Kaplan HB, Kolter R. Biofilm formation as microbial development. Annu Rev Microbiol 2000;54:49–79.

[193] Skerker JM, Berg HC. Direct observation of extension and retraction of type IV pili. Proc Natl Acad Sci U S A 2001;98:6901–4. doi:10.1073/pnas.121171698.

[194] Horbett TA. Adsorbed proteins on biomaterials. In: Ratner BD, Hoffman AS, Schoen FJ, Lemons JE, editors. Biomater. Sci. An Introd. to Mater. Med. Third Edit, Academic Press; 2013, p. 394–408. doi:10.1016/B978-0-08-087780-8.00036-X.

[195] Dee KC, Puleo DA, Bizios R. Protein-surface interactions. An Introd. to tissue-biomaterial Interact., Wiley-Liss; 2002, p. 37–52.

[196] Van Houdt R, Michiels CW. Role of bacterial cell surface structures in Escherichia coli biofilm formation. Res Microbiol 2005;156:626–33. doi:10.1016/j.resmic.2005.02.005.

[197] Garrett TR, Bhakoo M, Zhang Z. Bacterial adhesion and biofilms on surfaces. Prog Nat Sci 2008;18:1049–56. doi:10.1016/j.pnsc.2008.04.001.

[198] McKenney D, Hübner J, Muller E, Wang Y, Goldmann DA, Pier GB. The ica locus of Staphylococcus epidermidis encodes production of the capsular polysaccharide/adhesin. Infect Immun 1998;66:4711–20.

[199] Unosson E. Antibacterial strategies for titanium biomaterials. Uppsala University, 2015.

[200] Vogler EA. Thermodynamics of short-term cell adhesion in vitro. Biophys J 1988;53:759–69.

[201] Hiemenz PC, Rajagopalan R. Principles of colloid and surface chemistry. Third Edit. CRC Press; 1997.

[202] Hori K, Matsumoto S. Bacterial adhesion: From mechanism to control. Biochem Eng J 2010;48:424–34. doi:10.1016/j.bej.2009.11.014.

[203] van Loosdrecht MCM, Zehnder AJB. Energetics of bacterial adhesion. Experientia 1990;46:817–22. doi:10.1007/BF01935531.

[204] Kuroda K, Caputo GA. Antimicrobial polymers as synthetic mimics of host-defense peptides. Wiley Interdiscip Rev Nanomedicine Nanobiotechnology 2013;5:49–66. doi:10.1002/wnan.1199.

[205] Caillier L, de Givenchy ET, Levy R, Vandenberghe Y, Géribaldi S, Guittard F. Synthesis and antimicrobial properties of polymerizable quaternary ammoniums. Eur J Med Chem 2009;44:3201–8. doi:10.1016/j.ejmech.2009.03.031.

[206] Chen S, Li L, Zhao C, Zheng J. Surface hydration: Principles and applications

toward low-fouling/nonfouling biomaterials. Polymer (Guildf) 2010;51:5283–93. doi:10.1016/j.polymer.2010.08.022.

[207] Banerjee I, Pangule RC, Kane RS. Antifouling coatings: Recent developments in the design of surfaces that prevent fouling by proteins, bacteria, and marine organisms. Adv Mater 2011;23:690–718. doi:10.1002/adma.201001215.

[208] Cheng G, Li G, Xue H, Chen S, Bryers JD, Jiang S. Zwitterionic carboxybetaine polymer surfaces and their resistance to long-term biofilm formation. Biomaterials 2009;30:5234–40. doi:10.1016/j.biomaterials.2009.05.058.

[209] Hochbaum AI, Aizenberg J. Bacteria pattern spontaneously on periodic nanostructure arrays. Nano Lett 2010;10:3717–21. doi:10.1021/nl102290k.

[210] Helbig R, Günther D, Friedrichs J, Rößler F, Lasagni A, Werner C. The impact of structure dimensions on initial bacterial adhesion. Biomater Sci 2016;4:1074–8. doi:10.1039/C6BM00078A.

[211] Chung KK, Schumacher JF, Sampson EM, Burne RA, Antonelli PJ, Brennan AB. Impact of engineered surface microtopography on biofilm formation of Staphylococcus aureus. Biointerphases 2007;2:89–94. doi:10.1116/1.2751405.

[212] Leng C, Hung HC, Sun S, Wang D, Li Y, Jiang S, et al. Probing the surface hydration of nonfouling zwitterionic and PEG materials in contact with proteins. ACS Appl Mater Interfaces 2015;7:16881–8. doi:10.1021/acsami.5b05627.

[213] Harris JM. Poly(ethylene glycol) chemistry: Biotechnical and biomedical Applications. illustrate. Springer Science & Business Media; 1992.

[214] McArthur SL, McLean KM, Kingshott P, St John HAW, Chatelier RC, Griesser HJ. Effect of polysaccharide structure on protein adsorption. Colloids Surfaces B Biointerfaces 2000;17:37–48. doi:10.1016/S0927-7765(99)00086-7.

[215] Mrabet B, Nguyen MN, Majbri A, Mahouche S, Turmine M, Bakhrouf A, et al. Anti-fouling poly(2-hydoxyethyl methacrylate) surface coatings with specific bacteria recognition capabilities. Surf Sci 2009;603:2422–9. doi:10.1016/j.susc.2009.05.020.

[216] Ishihara K, Ishikawa E, Iwasaki Y, Nakabayashi N. Inhibition of fibroblast cell adhesion on substrate by coating with 2-methacryloyloxyethyl phosphorylcholine polymers. J Biomater Sci Polym Ed 1999;10:1047–61. doi:10.1163/156856299X00676.

[217] Amanda A, Mallapragada SK. Comparison of protein fouling on heat-treated poly(vinyl alcohol), poly(ether sulfone) and regenerated cellulose membranes using diffuse reflectance infrared fourier transform spectroscopy. Biotechnol Prog 2001;17:917–23. doi:10.1021/bp0100631.

[218] Chapman RG, Ostuni E, Takayama S, Holmlin RE, Yan L, Whitesides GM. Surveying for surfaces that resist the adsorption of proteins. J Am Chem Soc 2000;122:8303–4. doi:10.1021/ja000774f.

[219] Ostuni E, Chapman RG, Holmlin RE, Takayama S, Whitesides GM. A survey of structure-property relationships of surfaces that resist the adsorption of protein. Langmuir 2001;17:5605–20. doi:10.1021/la010384m.

[220] Sharma S, Johnson RW, Desai TA. Evaluation of the stability of nonfouling ultrathin poly(ethylene glycol) films for silicon-based microdevices. Langmuir 2004;20:348–56. doi:10.1021/la034753l.

[221] Wörz A, Berchtold B, Moosmann K, Prucker O, Rühe J. Protein-resistant polymer surfaces. J Mater Chem 2012;22:19547–61. doi:10.1039/c2jm30820g.

[222] Zheng J, Li L, Tsao H-K, Sheng Y-J, Chen S, Jiang S. Strong repulsive forces between protein and oligo (ethylene glycol) self-assembled monolayers: A molecular simulation study. Biophys J 2005;89:158–66. doi:10.1529/biophysj.105.059428.

[223] Leung BO, Yang Z, Wu SSH, Chou KC. Role of interfacial water on protein adsorption at cross-linked polyethylene oxide interfaces. Langmuir 2012;28:5724–8. doi:10.1021/la204805x.

[224] Jeon SI, Lee JH, Andrade JD, De Gennes PG. Protein-surface interactions in the presence of polyethylene oxide. I. Simplified theory. J Colloid Interface Sci 1991;142:149–58. doi:10.1016/0021-9797(91)90043-8.

[225] Jeon SI, Andrade JD. Protein-surface interactions in the presence of polyethylene oxide. II. Effect of protein size. J Colloid Interface Sci 1991;142. doi:10.1016/0021-9797(91)90044-9.

[226] Brünahl J, Grishin AM. Piezoelectric shear mode drop-on-demand inkjet actuator. Sensors Actuators A 2002;101:371–82. doi:10.1016/S0924-4247(02)00212-1.

[227] Kyser EL, Sears SB. Apparatus for recording with writing fluids and drop

projection means therefor. US4339763 A, 1982.

[228] Rheosys LLC. A basic introduction to viscometers & viscometry 2011. http://www.rheosys.com/intro.html (accessed November 2, 2016).

[229] FUJIFILM Dimatix Inc. Jettable fluid formulation guidelines 2013. http://www.fujifilmusa.com/shared/bin/Dimatix_Materials_Printer_Jettable_Fluid_Formulation_Guidelines_05-13.pdf (accessed January 10, 2017).

[230] GmbH K. Young-Laplace fit n.d. https://www.kruss.de/services/education-theory/glossary/young-laplace-fit/ (accessed December 7, 2016).

[231] Freire E. Differential scanning calorimetry. Protein Stab. Fold. Theory Pract., Totowa, NJ: Humana Press; 1995, p. 191–218. doi:10.1385/0-89603-301-5:191.

[232] Gill P, Moghadam TT, Ranjbar B. Differential scanning calorimetry techniques: Applications in biology and nanoscience. J Biomol Tech 2010;21:167–93.

[233] Kambly K. Characterization of curing kinetics and polymerization shrinkage in ceramic-loaded photocurable resins for large area maskless photopolymerization (lamp). Georgia Institute of Technology, 2009.

[234] Sangermano M, Meier P, Tzavalas S. Infrared spectroscopy as a tool to monitor radiation curing. In: Theophile T, editor. Infrared Spectrosc. - Mater. Sci. Technol. Technol., InTech; 2012, p. 325–36. doi:10.5772/37339.

[235] Bruker Optics. Attenuated total reflection (ATR) mode - Advantages for FT-IR spectroscopy 2012:1–11. http://www.azom.com/article.aspx?ArticleID=5958 (accessed January 15, 2017).

[236] FT-IR spectroscopy attenuated total reflectance (ATR). Shelton, USA: 2005.

[237] Goldstein J, Newbury DE, Echlin P, Joy DC, Romig AD, Lyman CE, et al. Scanning electron microscopy and X-ray microanalysis: A text for biologists, materials scientists, and geologists. Second Edi. Springer Science & Business Media; 2012.

[238] CPS Instruments. CPS disc centrifuge operating manual. Florida, USA: 2004.

[239] CPS Instruments Europe. Disc centrifuge n.d. http://www.cpsinstruments.eu/centrifuge.html (accessed December 8, 2016).

[240] Sommerfeld Ross S, Tu MH, Falsetta ML, Ketterer MR, Kiedrowski MR, Horswill

AR, et al. Quantification of confocal images of biofilms grown on irregular surfaces. J Microbiol Methods 2014;100:111–20. doi:10.1016/j.mimet.2014.02.020.

[241] Heydorn A, Heydorn A, Nielsen AT, Nielsen AT, Hentzer M, Hentzer M. Quantication of biofilm structures by the novel computer program COMSTAT. Microbiology 2000;146:2395–407. doi:10.1099/00221287-146-10-2395.

[242] Mueller LN, de Brouwer JFC, Almeida JS, Stal LJ, Xavier JB. Analysis of a marine phototrophic biofilm by confocal laser scanning microscopy using the new image quantification software PHLIP. BMC Ecol 2006;6:1–15. doi:10.1186/1472-6785-6-1.

[243] Xavier JB, Schnell A, Wuertz S, Palmer R, White DC, Almeida JS. Objective threshold selection procedure (OTS) for segmentation of scanning laser confocal microscope images. J Microbiol Methods 2001;47:169–80. doi:10.1016/S0167-7012(01)00298-6.

[244] Heydorn A, Ersboll BK, Hentzer M, Parsek MR, Givskov M, Molin S. Experimental reproducibility in flow-chamber biofilms. Microbiology 2000;146:2409–15. doi:10.1099/00221287-146-10-2409.

[245] Reichardt C. Solvents and solvent effects in organic chemistry. Third Edit. Weinheim: Wiley-VCH Verlag GmbH & Co. KGaA; 2003.

[246] Ramé E. The interpretation of dynamic contact angles measured by the Wilhelmy plate method. J Colloid Interface Sci 1997;185:245–51. doi:10.1006/jcis.1996.4589.

[247] Celiz AD, Smith JGW, Patel AK, Langer R, Anderson DG, Barrett DA, et al. Chemically diverse polymer microarrays and high throughput surface characterisation: A method for discovery of materials for stem cell culture. Biomater Sci 2014;2:1604–11. doi:10.1039/c4bm00054d.

[248] Patel AK, Celiz AD, Rajamohan D, Anderson DG, Langer R, Davies MC, et al. A defined synthetic substrate for serum free culture of human stem cell derived cardiomyocytes with improved functional maturity identified using combinatorial materials microarrays. Biomaterials 2015;61:257–65. doi:10.1016/j.biomaterials.2015.05.019.

[249] Castro D, Ingram P, Kodzius R, Conchouso D, Yoon E, Foulds IG. Characterization of solid UV cross-linked PEGDA for biological applications.

2013 IEEE 26th Int. Conf. Micro Electro Mech. Syst., Taipei: IEEE; 2013, p. 457–60. doi:10.1109/MEMSYS.2013.6474277.

[250] Michl TD, Coad BR, Hüsler A, Valentin JDP, Vasilev K, Griesser HJ. Effects of precursor and deposition conditions on prevention of bacterial biofilm growth on chlorinated plasma polymers. Plasma Process Polym 2016;13:654–62. doi:10.1002/ppap.201500191.

[251] Brady G a, Halloran JW. Differential photo-calorimetry of photopolymerizable ceramic suspensions. J Mater Sci 1998;33:4551–60. doi:10.1023/a:1004416705140.

[252] Wu KC, Halloran JW. Photopolymerization monitoring of ceramic stereolithography resins by FTIR methods. J Mater Sci 2005;40:71–6. doi:10.1007/s10853-005-5689-y.

[253] Pappas PS. UV curing: Science and technology. Technology Marketing Corp., Pub. Division; 1978.

[254] Anseth KS, Wang CM, Bowman CN. Kinetic evidence of reaction-diffusion during the polymerization of multi(meth)acrylate monomers. Macromolecules 1994;27:650–5. doi:Doi 10.1021/Ma00081a004.

[255] Miyazaki K, Horibe T. Polymerization of multifunctional methacrylates and acrylates. J Biomed Mater Res 1988;22:1011–22. doi:10.1002/jbm.820221105.

[256] Olabisi O, Adewale K. Handbook of thermoplastics. Second Edi. CRC Press; 1997.

[257] Decker C. Kinetic study and new applications of UV radiation curing. Macromol Rapid Commun 2002;23:1067–93. doi:10.1002/marc.200290014.

[258] Fouassier J-P, Rabek JF. Radiation curing in polymer science and technology. illustrate. Springer Science & Business Media; 1993.

[259] Slinde E, Flatmark T. Effect of the hydrophile-lipophile balance of non-ionic detergents (Triton X-series) on the solubilization of biological membranes and their integral b-type cytochromes. Biochim Biophys Acta 1976;455:796–805. doi:10.1016/0005-2736(76)90049-3.

[260] Turk CTS, Oz UC, Serim TM, Hascicek C. Formulation and optimization of nonionic surfactants emulsified nimesulide-loaded PLGA-based nanoparticles by design of experiments. AAPS PharmSciTech 2014;15:161–76.

doi:10.1208/s12249-013-0048-9.

[261] Mohamed A, Mahfoodh ASM. Solubilization of naphthalene and pyrene by sodium dodecyl sulfate (SDS) and polyoxyethylenesorbitan monooleate (Tween 80) mixed micelles. Colloids Surfaces A Physicochem Eng Asp 2006;287:44–50. doi:10.1016/j.colsurfa.2006.03.036.

[262] Brenn G, Kolobaric V. Satellite droplet formation by unstable binary drop collisions. Phys Fluids 2006;18:87101. doi:10.1063/1.2225363.

[263] Nisisako T, Torii T, Higuchi T. Novel microreactors for functional polymer beads. Chem Eng J 2004;101:23–9. doi:10.1016/j.cej.2003.11.019.

[264] Nisisako T, Torii T, Higuchi T. Separation of satellite droplets using branch microchannel configuration. Proc. Micro Total Anal. Syst., Malmo, Sweden: 2004, p. 312–4.

[265] Tice JD, Song H, Lyon AD, Ismagilov RF. Formation of droplets and mixing in multiphase microfluidics at low values of the Reynolds and the Capillary numbers. Langmuir 2003;19:9127–33. doi:10.1021/la030090w.

[266] Inzana JA, Olvera D, Fuller SM, Kelly JP, Graeve OA, Schwarz EM, et al. 3D printing of composite calcium phosphate and collagen scaffolds for bone regeneration. Biomaterials 2014;35:4026–34. doi:10.1016/j.biomaterials.2014.01.064.

[267] Kamyshny A, Ben-Moshe M, Aviezer S, Magdassi S. Ink-jet printing of metallic nanoparticles and microemulsions. Macromol Rapid Commun 2005;26:281–8. doi:10.1002/marc.200400522.

[268] Hauschild S, Lipprandt U, Rumplecker A, Borchert U, Rank A, Schubert R, et al. Direct preparation and loading of lipid and polymer vesicles using inkjets. Small 2005;1:1177–80. doi:10.1002/smll.200500093.

[269] Ma M, Chiu A, Sahay G, Doloff JC, Dholakia N, Thakrar R, et al. Core-shell hydrogel microcapsules for improved islets encapsulation. Adv Healthc Mater 2013;2:667–72. doi:10.1002/adhm.201200341.

[270] Dohnal J, Štěpánek F. Inkjet fabrication and characterization of calcium alginate microcapsules. Powder Technol 2010;200:254–9. doi:10.1016/j.powtec.2010.02.032.

[271] Baah D, Floyd-Smith T. Microfluidics for particle synthesis from

photocrosslinkable materials. Microfluid Nanofluidics 2014;17:431–55. doi:10.1007/s10404-014-1333-y.

[272] Rhee M, Valencia PM, Rodriguez MI, Langer R, Farokhzad OC, Karnik R. Synthesis of size-tunable polymeric nanoparticles enabled by 3D hydrodynamic flow focusing in single-layer microchannels. Adv Healthc Mater 2011;23:79–83. doi:10.1002/adma.201004333.

[273] Shepherd RF, Conrad JC, Rhodes SK, Link DR, Marquez M, Weitz DA, et al. Microfluidic assembly of homogeneous and Janus colloid-filled hydrogel granules. Langmuir 2006;22:8618–22. doi:10.1021/la060759+.

[274] Kang X, Luo C, Wei Q, Xiong C, Chen Q, Chen Y, et al. Mass production of highly monodisperse polymeric nanoparticles by parallel flow focusing system. Microfluid Nanofluidics 2013;15:337–45. doi:10.1007/s10404-013-1152-6.

[275] Gokmen MT, Dereli B, De Geest BG, Du Prez FE. Complexity from simplicity: Unique polymer capsules, rods, monoliths, and liquid marbles prepared via HIPE in microfluidics. Part Part Syst Charact 2013;30:438–44. doi:10.1002/ppsc.201200154.

[276] Mulligan MK, Rothstein JP. Scale-up and control of droplet production in coupled microfluidic flow-focusing geometries. Microfluid Nanofluidics 2012;13:65–73. doi:10.1007/s10404-012-0941-7.

[277] Nisisako T, Torii T. Microfluidic large-scale integration on a chip for mass production of monodisperse droplets and particles. Lab Chip 2008;8:287–93. doi:10.1039/b713141k.

[278] Vladisavljević GT, Williams RA. Recent developments in manufacturing emulsions and particulate products using membranes. Adv Colloid Interface Sci 2005;113:1–20. doi:10.1016/j.cis.2004.10.002.

[279] Decuzzi P, Godin B, Tanaka T, Lee SY, Chiappini C, Liu X, et al. Size and shape effects in the biodistribution of intravascularly injected particles. J Control Release 2010;141:320–7. doi:10.1016/j.jconrel.2009.10.014.

[280] Celiz AD, Smith JGW, Patel AK, Hook AL, Rajamohan D, George VT, et al. Discovery of a novel polymer for human pluripotent stem cell expansion and multilineage differentiation. Adv Mater 2015;27:4006–12. doi:10.1002/adma.201501351.

[281] Unadkat H V, Hulsman M, Cornelissen K, Papenburg BJ, Truckenmüller RK, Carpenter AE, et al. An algorithm-based topographical biomaterials library to instruct cell fate. Proc Natl Acad Sci U S A 2011;108:16565–70. doi:10.1073/pnas.1109861108.

[282] Elversson J, Millqvist-Fureby A, Alderborn G, Elofsson U. Droplet and particle size relationship and shell thickness of inhalable lactose particles during spray drying. J Pharm Sci 2003;92:900–10. doi:10.1002/jps.10352.

[283] Sanni O, Chang C, Anderson DG, Langer R, Davies MC, Williams PM, et al. Bacterial attachment to polymeric materials correlates with molecular flexibility and hydrophilicity. Adv Healthc Mater 2015;4:695–701. doi:10.1002/adhm.201400648.

[284] Briggs D. Analysis of polymer surfaces by SIMS, 3-Preliminary results from molecular imaging and microanalysis experiments. Surf Interface Anal 1983;5:113–8. doi:10.1002/sia.740050307.

[285] Andersson LHU, Johander P, Hjertberg T. Silicone elastomers for electronic applications. II. Effects of noncrosslinked materials. J Appl Polym Sci 2003;90:3780–9. doi:10.1002/app.12966.

[286] Scholes PD, Coombes AGA, Illum L, Davis SS, Watts JF, Ustariz C, et al. Detection and determination of surface levels of poloxamer and PVA surfactant on biodegradable nanospheres using SSIMS and XPS. J Control Release 1999;59:261–78. doi:10.1016/S0168-3659(98)00138-2.

[287] Davies D. Understanding biofilm resistance to antibacterial agents. Nat Rev Drug Discov 2003;2:114–22.

[288] Callow ME, Callow JA. Marine biofouling: A sticky problem. Biologist 2002;49:10–4.

[289] Cao S, Wang J, Chen H, Chen D. Progress of marine biofouling and antifouling technologies. Chinese Sci Bull 2011;56:598–612. doi:10.1007/s11434-010-4158-4.

[290] Salman JAS, Kadhemy MFH, Jaleel MS, Abdal AK. Effect of PVA, PVA/biosurfactant on some pathogenic bacteria in glass and plastic plates. Int J Curr Microbiol Appl Sci 2014;3:301–9.

[291] Feng G, Cheng Y, Wang S-Y, Borca-Tasciuc DA, Worobo RW, Moraru CI.

Bacterial attachment and biofilm formation on surfaces are reduced by small-diameter nanoscale pores: How small is small enough? Npj Biofilms Microbiomes 2015;1. doi:10.1038/npjbiofilms.2015.22.

[292] Beyenal H, Lewandowski Z. Internal and external mass transfer in biofilms grown at various flow velocities. Biotechnol Prog 2002;18:55–61. doi:10.1021/bp010129s.

[293] Busscher HJ, van der Mei HC. Microbial adhesion in flow displacement systems. Clin Microbiol Rev 2006;19:127–41. doi:10.1128/CMR.19.1.127-141.2006.

[294] Palmer J, Flint S, Brooks J. Bacterial cell attachment, the beginning of a biofilm. J Ind Microbiol Biotechnol 2007;34:577–88. doi:10.1007/s10295-007-0234-4.

[295] Marshall KC, Stout R, Mitchell R. Mechanism of the initial events in the sorption of marine bacteria to surfaces. J Gen Microbiol 1971;68:337–48. doi:10.1099/00221287-68-3-337.

[296] Herrwerth S, Eck W, Reinhardt S, Grunze M. Factors that determine the protein resistance of oligoether self-assembled monolayers − Internal hydrophilicity, terminal hydrophilicity, and lateral packing density. J Am Chem Soc 2003;125:9359–66. doi:10.1021/ja034820y.

[297] Barth HG. Modern methods of particle size analysis. illustrate. John Wiley & Sons; 1984.

[298] Thomas JC. The determination of log normal particle size distributions by dynamic light scattering. J Colloid Interface Sci 1987;117:187–92. doi:10.1016/0021-9797(87)90182-2.

[299] Pecora R. Dynamic light scattering: Applications of photon correlation spectroscopy. First Edit. Springer US; 1985. doi:10.1007/978-1-4613-2389-1.

[300] Hahn DW. Light scattering theory. University of Florida, 2009.

[301] Malvern Instruments Ltd. Dynamic light scattering: An introduction in 30 minutes. Worcestershire, UK: n.d.

[302] Ferber J, Luther J. Computer simulations of light scattering and absorption in dye-sensitized solar cells. Sol Energy Mater Sol Cells 1998;54:265–75. doi:Computer simulations of light scattering and absorption in dye-sensitized solar cells.

[303] Belu AM, Graham DJ, Castner DG. Time-of-flight secondary ion mass

spectrometry: Techniques and applications for the characterization of biomaterial surfaces. Biomaterials 2003;24:3635–53. doi:10.1016/S0142-9612(03)00159-5.

[304] Ion-tof GmbH. Time-of-flight secondary ion mass spectrometry n.d. https://www.iontof.com/tof-sims-secondary-ion-mass-spectrometry.html (accessed November 20, 2016).

[305] Physical Electronics USA. Time-of-flight secondary ion mass spectrometry. 2012.

[306] Wagner MS, Castner DG. Characterization of adsorbed protein films by time-of-flight secondary ion mass spectrometry with principal component analysis. Langmuir 2001;17:4649–60. doi:10.1021/la001209t.

[307] Bertrand P. Static SIMS for analysis of molecular conformation and orientation. Appl Surf Sci 2006;252:6986–91. doi:10.1016/j.apsusc.2006.02.147.

[308] Benninghoven A. Chemical analysis of inorganic and organic surfaces and thin films by static time-of-flight secondary ion mass spectrometry (TOF-SIMS). Angew Chemie Int Ed English 1994;33:1023–43. doi:10.1002/anie.199410231.

[309] Hofmann JP, Rohnke M, Weckhuysen BM. Recent advances in secondary ion mass spectrometry of solid acid catalysts: Large zeolite crystals under bombardment. Phys Chem Chem Phys 2014;16:5465–74. doi:10.1039/c3cp54337d.

[310] Sodhi RNS. Time-of-flight secondary ion mass spectrometry (TOF-SIMS): Versatility in chemical and imaging surface analysis. Analyst 2004;129:483–7. doi:10.1039/B402607C.

[311] Holzlechner G, Kubicek M, Hutter H, Fleig J. A novel ToF-SIMS operation mode for improved accuracy and lateral resolution of oxygen isotope measurements on oxides. J Anal At Spectrom 2013;28:1080–9. doi:10.1039/c3ja50059d.

[312] Kubicek M, Holzlechner G, Opitz AK, Larisegger S, Hutter H, Fleig J. A novel ToF-SIMS operation mode for sub 100 nm lateral resolution: Application and performance. Appl Surf Sci 2014;289:407–16. doi:10.1016/j.apsusc.2013.10.177.

[313] Rafati A. The analysis of polymers for biomedical applications. University of Nottingham, 2011.

[314] Gilmore IS, Seah MP. Electron flood gun damage in the analysis of polymers and organics in time-of-flight SIMS. Appl Surf Sci 2002;187:89–100. doi:10.1016/S0169-4332(01)00787-5.

[315] Lee JLS, Gilmore IS, Seah MP, Fletcher IW. Topography and field effects in secondary ion mass spectrometry-Part I: Conducting samples. J Am Soc Mass Spectrom 2011;22:1718–28. doi:10.1007/s13361-011-0201-1.

[316] McDonnell LA, Mize TH, Luxembourg SL, Koster S, Eijkel GB, Verpoorte E, et al. Using matrix peaks to map topography: Increased mass resolution and enhanced sensitivity in chemical imaging. Anal Chem 2003;75:4373–81. doi:10.1021/ac034401j.

[317] Rangarajan S, Tyler BJ. Topography in secondary ion mass spectroscopy images. J Vac Sci Technol A 2006;24:1730–6. doi:10.1116/1.2217980.

[318] Vickerman JC, Briggs D. TOF-SIMS: Materials analysis by mass spectrometry. Second. IM Publications; 2013.

[319] Lee JLS, Gilmore IS, Fletcher IW, Seah MP. Topography and field effects in the quantitative analysis of conductive surfaces using ToF-SIMS. Appl Surf Sci 2008;255:1560–3. doi:10.1016/j.apsusc.2008.05.164.

[320] Binnig G, Quate CF. Atomic force microscope. Phys Rev Lett 1986;56:930–4. doi:10.1103/PhysRevLett.56.930.

[321] Jalili N, Laxminarayana K. A review of atomic force microscopy imaging systems: Application to molecular metrology and biological sciences. Mechatronics 2004;14:907–45. doi:10.1016/j.mechatronics.2004.04.005.

[322] Vansteenkiste SO, Davies MC, Roberts CJ, Tendler SJB, Williams PM. Scanning probe of biomedical microscopy interfaces. Prog Surf Sci 1998;57:95–136. doi:10.1016/S0079-6816(98)00014-8.

[323] Butt H-J, Cappella B, Kappl M. Force measurements with the atomic force microscope: Technique, interpretation and applications. Surf Sci Rep 2005;59:1–152. doi:10.1016/j.surfrep.2005.08.003.

[324] Hamers RJ. Scanned probe microscopies in chemistry. J Phys Chem 1996;100:13103–20. doi:10.1021/jp960054o.

[325] Bruker Corporation. PeakForce QNM-Quantitative nanomechanical property mapping. 2010.

[326] Corle TR, Kino GS. Confocal scanning optical microscopy and related imaging systems. Academic Press; 1996.

[327] Paddock SW. Principles and practices of laser scanning confocal microscopy. Mol Biotechnol 2000;16:127–49. doi:10.1385/MB:16:2:127.

APPENDIX A - DYNAMIC LIGHT SCATTERING

Dynamic light scattering (DLS), also known as photon correlation spectroscopy or quasi-elastic light scattering, is an established technique for determining average size and size distribution of particles typically in the submicron range [297,298]. In this technique, the Brownian motion, which is size dependent, is measured by focusing a laser onto a small volume containing particles. These particles scatter the light to the detector. The hydrodynamic particle diameter (d), which corresponds to a particle diffusivity within a fluid, is calculated by applying the Stokes-Einstein equation (Eq. A.1) [299]:

$$d = \frac{kT}{3\pi\eta D} \qquad \text{Eq. A.1}$$

where k is the Boltzmann's constant, T the temperature, η the viscosity and D the translational diffusion constant.

Light scattered by particles is usually categorised by two theories: Rayleigh scattering and Mie scattering [300]. Rayleigh scattering is applicable to particles that are much smaller than the wavelength of light used, typically $d < \lambda/10$ [297]. In this case, the light scattering is isotropic and the following approximation is valid (Eq. A.2) [300,301]:

$$I \propto d^6 \qquad \text{Eq. A.2}$$

where I is the intensity of scattered light and d the particle diameter. In contrast to Rayleigh scattering, the Mie theory describes most spherical particle scattering systems without a particular restriction on particle size and optical properties [300]. Particles with sizes in the same order as the wavelength of the illuminating light are effective Mie scatterers revealing complex functions of maxima and minima with respect to angles [301,302]. Larger particles scatter mainly in the forward direction.

APPENDIX B - TIME-OF-FLIGHT SECONDARY ION MASS SPECTROMERTY

Time-of-flight secondary ion mass spectrometry is a surface analysis technique which is capable of detecting elements in concentrations in the ppm to ppb range [303]. Therefore, ToF-SIMS must be performed under ultra high vacuum (UHV) for several reasons.

In this technique, ions from a pulsed primary ion beam impinge upon a target sample with high energy. This energy is transferred to target atoms which in turn generate collision cascades [304]. In these collision cascades, extensive fragmentation and bond breaking occur producing mostly neutral particles and a small proportion of positively and negatively charged ions [303]. Species fragmented in the uppermost one or two monolayers of the target sample have enough energy to overcome the surface binding energy and are ejected from the specimen. A collision cascade is represented in Figure B.1.

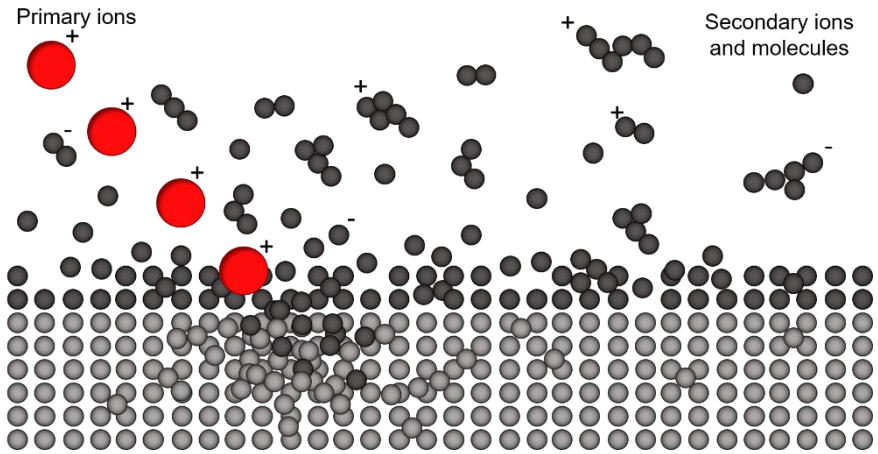


Figure B.1: A schematic drawing of a collision cascade initiated by the impact of primary ions (red).

The emitted secondary ions are extracted and accelerated in an extraction field to a common energy E by applying a potential between the sample surface and the time-of-fight (ToF) mass analyser [303,305]. By measuring the times, t, of the secondary ions to travel through the length L of the field-free flight tube until hitting the detector, the mass-to-charge ratio (m/z) is obtained from the formula Eq. B.1:

$$t = L\left(\frac{m}{2zE}\right)^{1/2} \qquad \text{Eq. B.1}$$

For instance, heavier ions will travel longer than lighter ions at the same kinetic energy, consequently a longer time will be measured. In other words, the mass-to-charge ratio (m/z) is analysed and presented in positive and negative secondary ion mass spectra

[303]. The ToF-SIMS analysis provides detailed information about the chemical structure, composition and orientation of species at the surface [306–308].

Modern SIMS instruments comprise the following major components: air lock, main analysis chamber, primary ion gun, mass spectrometer and the so-called transport optics as shown in Figure B.2. The air lock system facilitates to maintain the main chamber at a low pressure while loading the sample stage into the instrument. The transport optics extract ions of a given range of masses for transportation through the mass spectrometer to the detector where the mass-to-charge ratios are analysed.

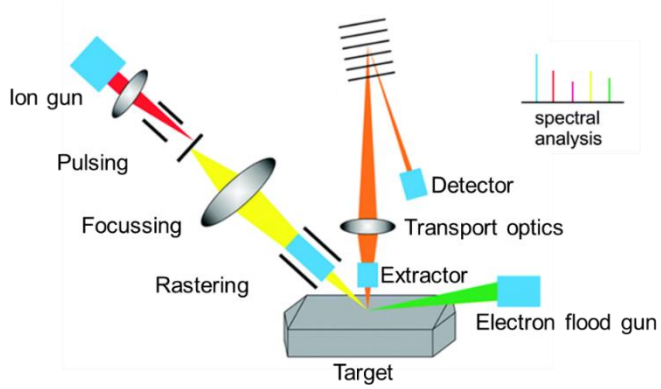


Figure B.2: Schematic illustration of the operating principle of a ToF-SIMS instrument with its main components. Image adapted from Hofmann et al. [309].

Modes of Operation

The ToF-SIMS technique can be applied in three different ways; surface spectrometry, surface imaging and depth profiling. For depth profiling, two ion beams are required which operate in a dual beam mode. In contrast to depth profiling, only one primary ion gun is applied in surface imaging and surface spectrometry. This primary ion gun can be operated in different modes that mainly differ in their mass resolution, primary ion intensity and achievable lateral resolution [310]. For surface spectrometry, a 'high current bunched' mode with a very intensive primary ion beam is applied. This mode allows for increased mass resolution ($m/\Delta m$ > 11000) at the expense of lateral resolution (2-10 µm). Additionally, this mode provides detailed elemental and molecular information from the outer monolayers [311,312]. A 'burst alignment' mode, however, is used for fast imaging with a high spatial resolution (250-300 nm) but a moderate mass resolution ($m/\Delta m$ > 200) [310,311]. A direct comparison of both modes is depicted in Figure B.3 showing the mass and spatial resolution obtained.

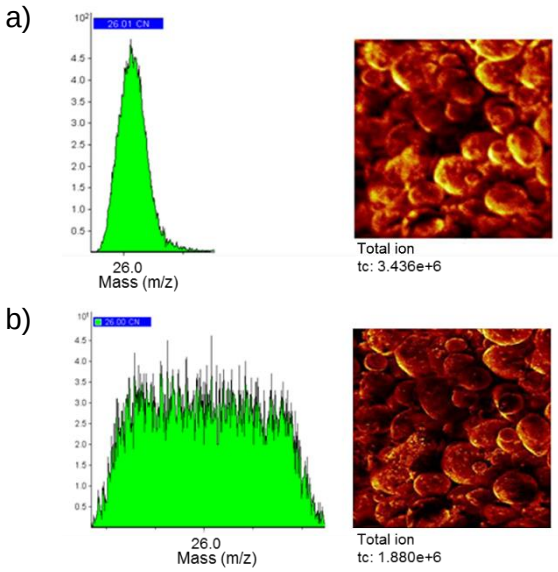


Figure B.3: Comparison of the CN^- peak derived from the negative ion spectrum and the corresponding total ion image. ToF-SIMS data was obtained from a microsphere system: a) in 'high current bunched' mode, b) in 'burst alignment' mode of operation. Images adapted from A. Rafati [313].

Charge Compensation

Charge compensation is a fundamental aspect of ToF-SIMS devices that needs to be considered when measuring electrically insulating materials. While measuring a substrate surface, primary ions are bombarded onto the surface resulting in emission of secondary ions and electrons [310]. The emission of electrons leads to a localised positive charge at the surface in the case of non-conductive samples [303]. As a result of this surface charge build-up, the secondary ion energy will change and therefore, the respective travel time until hitting the detector. In the worst case though, the trajectories of the secondary ions can be diverted, resulting in a loss of spectral data.

In order to compensate for this surface charging, pulses of low energy (20 eV) electrons are directed onto the surface between the pulses of the primary ion. The electron fluency must be kept low, otherwise delicate materials including some polymers degrade [314].

Topography Effects

Sample topography represents an issue when performing surface chemical analysis [315,316]. The interpretation of ToF-SIMS images obtained from samples such as particles, fibres and biological specimens can be difficult. The reason is that the variations in peak intensity are not only obtained from sample chemistry but also from topographical effects. Topographic effects consist of the influence of the height of topographic features, the inclination of the incident beam and variations in the electric field [317]. Topographical features can give rise to unwanted artefacts in ToF-SIMS images including distortion, shadowing and variations in ion yield [317,318]. Vickerman

et al. showed that the size and shape of a measured object is distorted in the direction in which the primary ion beam rasters across the surface [318]. Figure B.4 illustrates that the angle ρ between the surface normal and the incident beam changes across the substrate in case of a featured substrate. Moreover, some regions on the sphere, marked as 'a', cannot be analysed since the primary beam never impacts these areas.

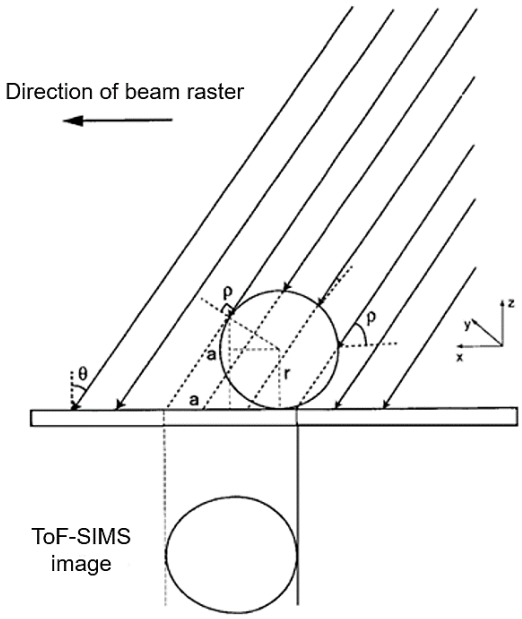


Figure B.4: Illustration of a microsphere that becomes distorted in the SIMS imaging process caused by the angle of incidence of the primary ion beam to the particle surface. The secondary ions are extracted in the z-direction. Image adapted from Rangarajan et al. [317].

Another artefact observed in ToF-SIMS images is a 'shadowed' region at the leading edge of particles. Such 'shadowed' regions, as depicted in Figure B.5, can occur around particles and fibres as a consequence of a lack in detecting of secondary ions below the equator [317,319].

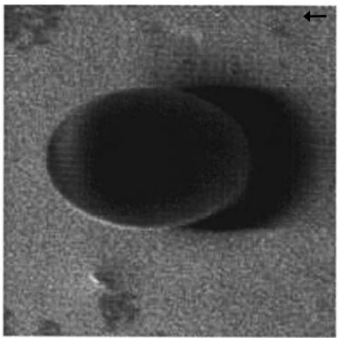


Figure B.5: Shadowed region formed around a pluronic-coated latex particle (25 µm in diameter) on a glass substrate. The direction of the primary ion beam is shown by an arrow in the top right corner. Image adapted from Vickerman et al. [318].

Probably the most confounding effect found is that both the absolute intensity of ion peaks and the peak ratios can be altered drastically as a result of topographical features [317].

The findings mentioned above indicate that the ion intensities obtained on complex topographies cannot be purely interpreted as a result of solely the chemical composition. Therefore, care was taken in the analysis step of preparing the ToF-SIMS data of microparticles in this thesis.

APPENDIX C - ATOMIC FORCE MICROSCOPY

Atomic force microscopy is a scanning probe technique that is capable of measuring surface topographies and intermolecular forces down to 2-3 Å [320,321]. A schematic of a typical AFM is presented in Figure C.1.

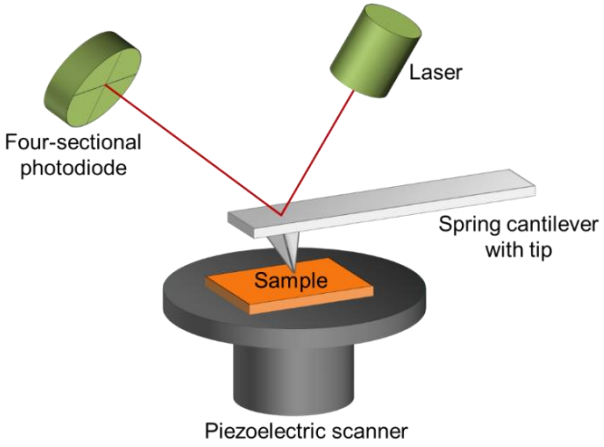


Figure C.1: Schematic representation of the main components of a typical AFM setup.

AFM operates by scanning a tip, which is mounted to a cantilever spring, over a sample surface with a feedback mechanism. This feedback mechanism allows the piezoelectric scanner to maintain the probe in proximity to the sample surface [321,322]. The force between the probe and the sample is measured by monitoring the deflection of the laser beam which is focused above the cantilever tip [323]. Therefore, any deflections of the cantilever result in alterations of the laser beam spot on the photo-detector. By measuring the changes in the movement of the laser spot, angular deflections of the cantilever are calculated. Consequently, accurate high resolution topographical images can be obtained through conversion of the signals recorded by the position-sensitive photo-detector [324].

Typically, AFM can be operated in three modes: non-contact, contact and tapping mode. Tapping mode combines the high resolution capability of the contact mode with the non-destructive nature of the non-contact mode by overcoming problems like friction and adhesion [321,322]. Therefore, tapping mode was the basic principle used for all AFM analysis in this thesis. In tapping mode, the cantilever is modulated at resonant frequency with a constant amplitude while the impact of the AFM tip on the sample is kept minimal.

For all surface topographical characterisation in this work, a mode called quantitative nanoscale mechanical (QNM) or PeakForce QNM mode was applied which operates in tapping mode [325]. This mode is able to directly acquire force-distance curves,

providing data of multiple mechanical properties such as adhesion, modulus, deformation while imaging the sample topography at high resolution [322,325].

APPENDIX D - CONFOCAL LASER SCANNING MICROSCOPY

Confocal laser scanning microscopy is an optical imaging technique that can be applied to obtain high-resolution images. CLSM has become widely used to study biofilm on various samples due to its non-destructive and non-invasive operation [242,243]. In addition, time-resolved 3D images can be reconstructed by stacking several 2D images acquired at different depths within a sample [240]. Unlike any conventional optical microscope, CLSM illuminates and images an object one point at the time through a pinhole [326]. Since the objective lens is used twice, for illuminating and imaging, the microscope is named 'confocal'. In this technique, a collimated beam from a laser is directly focused onto a pinhole as illustrated in Figure D.1. After passing through the pinhole, a diffraction-limited point is formed on the specimen that is raster scanned across the sample. In this way, the image is built up pixel by pixel [327]. The reflected light from the sample is deflected by a beam splitter to another pinhole, the detector pinhole. When the sample is moved away from the focal plane of the lens, the reflected light is defocused and cannot entirely pass through the pinhole anymore [326]. Consequently, the light intensity detected by the photomultiplier (PMT) gradually decreases until it eventually leads to a complete loss of the signal.

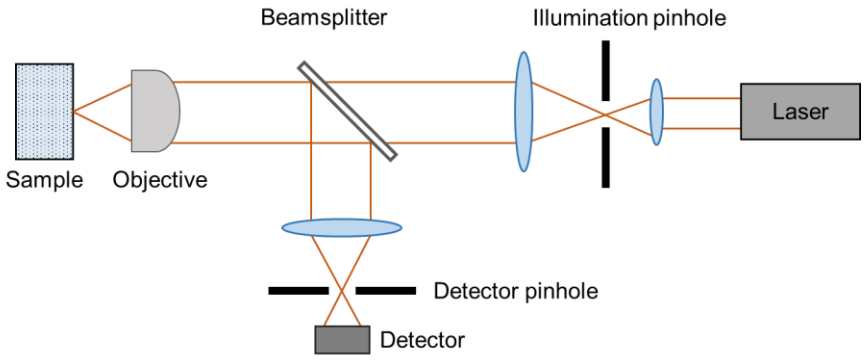


Figure D.1: Schematic representation of a confocal laser scanning microscopy.

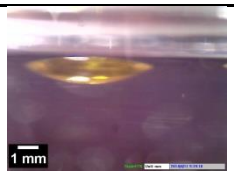
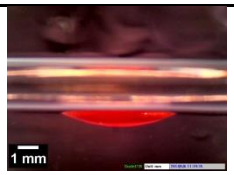
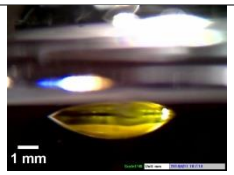
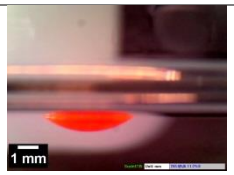
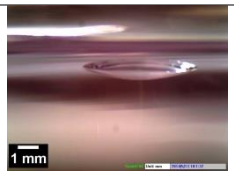
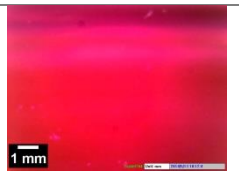
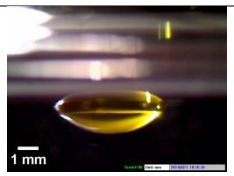
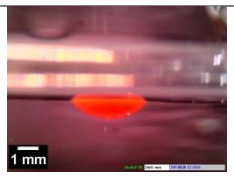
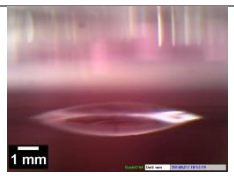
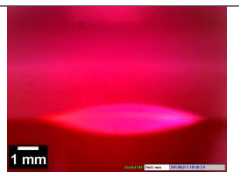
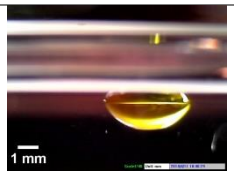
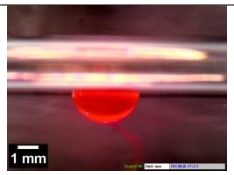
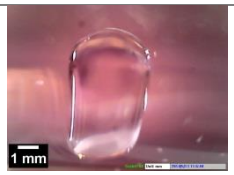
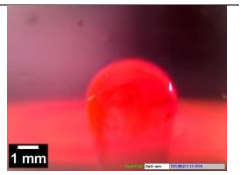
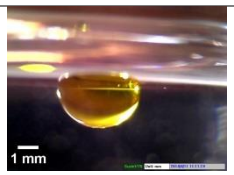
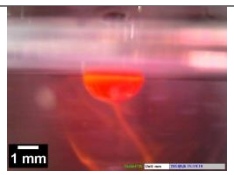
APPENDIX E - PRELIMINARY EXPERIMENTS

E.1. OPTIMAL SOLUTION RATIO OF ISOPROPANOL IN DEIONISED WATER

Breaking up a stream of fluid into spherical droplets is a phenomenon that behaves differently when surrounded by a gas or a liquid due to different driving forces present. In case of pipetting a monomer solution into a fluid, it can be assumed that a spherical drop is solely formed when floating in the surrounding fluid. If the drop has a higher density, it would sink. In contrast, if its density is less than the surrounding fluid, the drop would remain at the gas-liquid interface resulting in deformation of the drop shape assuming that the two fluids are not miscible. Therefore, it is crucial to understand the effect of changing the density and polarity of the collecting fluid on the droplet behaviour.

Two different inks, modified with and without rhodamine B, were pipetted into isopropanol in deionised water (IPA/DIW) with varied weight percentages. As shown in Table E.1, the MicroCapture images reveal differences in the transition range, where drops emerged between the two inks; droplets were generated in the range of 13-23 wt% and 15-20 wt% IPA/DIW in case of Solsys EMD6415 and PEGDA250-DMPA, respectively. Adding a dye to the inks resulted in minute changes compared to the undyed inks. This can be explained by the overall increase in drop density and the leakage of rhodamine B out of the droplet. Both inks share spreading of the ink at low IPA concentrations. Also, sinking followed immediately by dissolving of the drop, outlined in Table E.1 as empty boxes, has been observed at high IPA concentrations for both inks. The reason behind these observations is that increasing the IPA amount lowers the total density of the collecting fluid. Therefore, the ink drop becomes denser in comparison to the collecting fluid and sinks to the bottom. In addition, spreading of the ink droplet across the collecting fluid at low IPA concentrations indicates that both fluids have similar polarity and density. Finally, the drop-like shape of an ink depends on the surface tension and solubility of the ink in the collecting fluid.

Table E.1: Effect of changing the ratio of isopropanol in deionised water on droplet formation was analysed by pipetting two different inks (Solsys EMD6415, PEGDA250-DMPA) from 10 mm above the collecting fluid into a glass beaker. The inks were tested with and without rhodamine B (rho B). The images were acquired utilising an USB2-Micro-200x USB microscope.

Ratio of IPA in DIW [wt%]	Solsys EMD6415	Solsys EMD6415 + rho B	PEGDA250	PEGDA250 + rho B
13			Spreading of ink droplet	
15				
17				
20				
23			Sinking of the ink droplet followed by dissolution	
25	Sinking followed by dissolution			

E.2. High Speed Imaging of Pipetting

In order to determine which parameters affect the droplet generation and to analyse the behaviour of the droplet at the liquid-gas interphase, high speed footage of pipetting PEGDA250-DETX-EDB was recorded. Pipetting was performed from above and below deionised water, 17 wt% IPA/DIW, 1-octanol and air (reference) which is presented in Figure E.1. The images shown for pipetting in air are sharper and darker compared to the remainder due to differences in refractive indices.

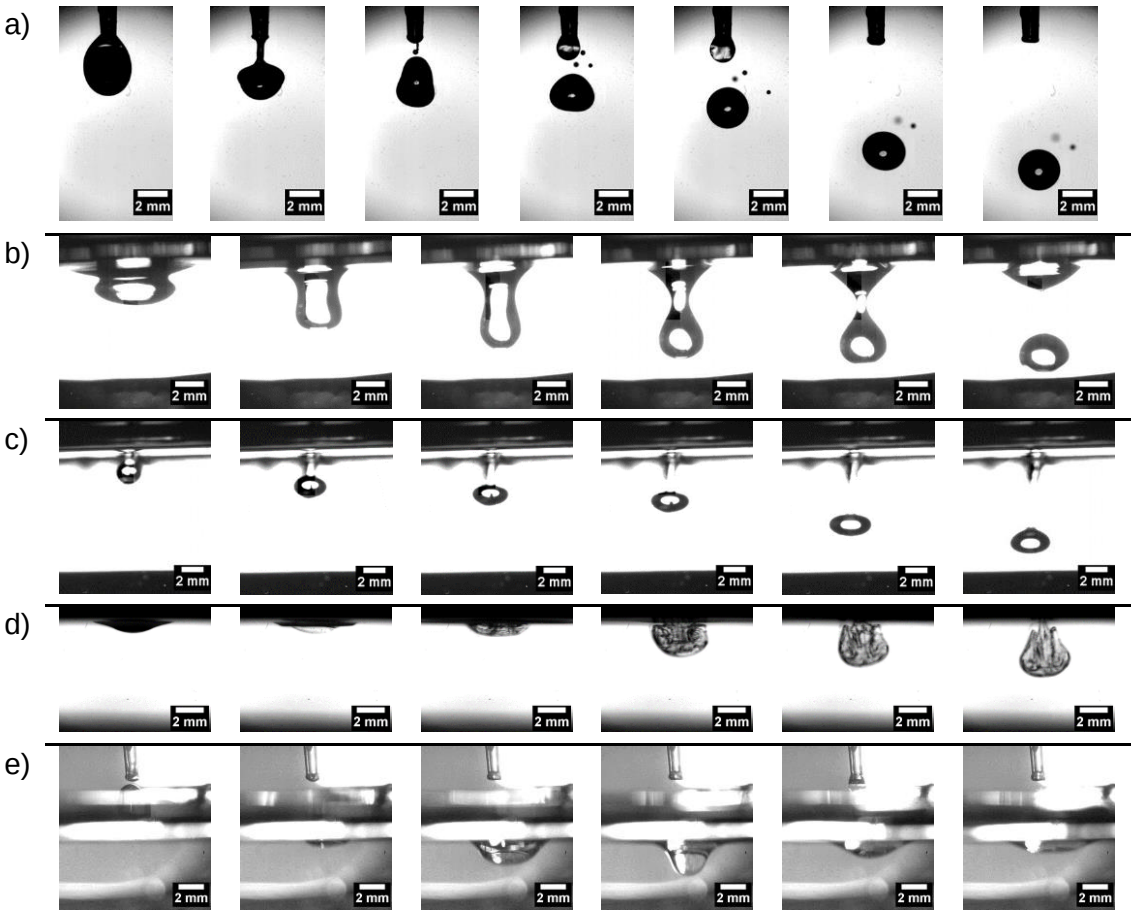


Figure E.1: Sequences of images are shown after pipetting 5 µl of PEGDA250-DETX-EDB: a) into air (reference), b) from above 17 wt% IPA/DIW, c) below 17 wt% IPA/DIW, d) from above 1-octanol, e) from above deionised water.

Droplets formed readily by dispensing into air (a) and into 17 wt% IPA/DIW both from above (b) and below the liquid-gas interface (c). In case of pipetting from above 17 wt% IPA/DIW, a stream of liquid was 'injected' into the bulk liquid, narrowed its cross-section and formed a drop below the surface, as shown in Figure E.1 b). In contrast, a drop ejected submerged sank without larger shape modifications (Figure E.1 c)). By employing deionised water and 1-octanol, spherical drops could not be produced irrespective of pipetting from above or below the collecting fluid. Sinking of the ink without retaining the shape was observed in 1-octanol. The data of pipetting from above into 1-octanol is shown in Figure E.1 d). In case of deionised water, spreading

of the ink occurred at the surface, presented for the above pipetting configuration in Figure E.1 e).

APPENDIX F - RESULTS OF MONOMERS PERFORMED IN MANUAL PIPETTING EXPERIMENTS

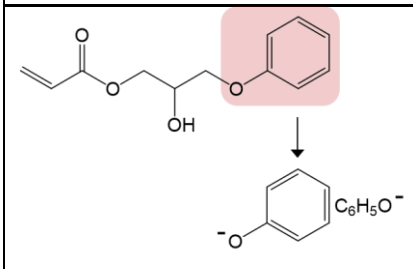
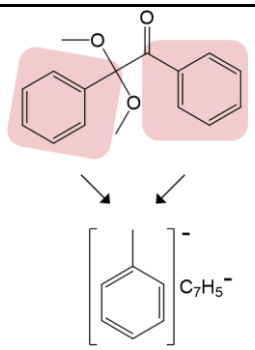
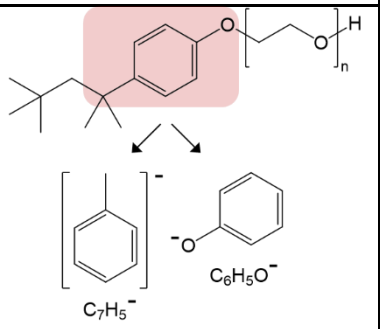
Abbr. old	Abbr. new	Monomer	Pipetting Air	Pipetting Argon	Printing Dimatix	Library
AD01	BDDA	1,3-Butanediol diacrylate				BDDA
AD04	HMDA	1,6-Hexanediol diacrylate				HMDA
AD10	TCDMDA	Tricyclo[5.2.1.$0^{2,6}$]decanedimethanol diacrylate				TCDMDA
AD15	DEGDA	Di(ethylene glycol) diacrylate				DEGDA
AD16	EGDA	Ethylene glycol diacrylate				EGDA
AD18	TEGDA	Tetra(ethylene glycol) diacrylate				TEGDA
AD22	TPGDA	Tri(propylene glycol) diacrylate, mixture of isomers				TPGDA
AD24	pPGDA	Poly(propylene glycol) diacrylate				pPGDA
AD25	HDMPDA	3-Hydroxy-2,2-dimethylpropyl 3-hydroxy-2,2-dimethylpropionate diacrylate				
AM06	HA	Hexyl acrylate				
AM08	iOA	Isooctyl acrylate				
AM17	TMSA	Trimethylsilyl acrylate				
AM19	tBCHA	4-tert-Butylcyclohexyl acrylate				
AM31	HPhOPA	2-Hydroxy-3-phenoxypropyl acrylate				HPhOPA
AM38	DMAPA	3-(Dimethylamino)propyl acrylate				
AM47	EGMEA	Ethylene glycol methyl ether acrylate				
AM48	EGdPEA	Ethylene glycol dicyclopentenyl ether acrylate				EGdPEA
AM51	EGPEA	Ethylene glycol phenyl ether acrylate				EGPEA
AM53	BACOEA	2-[[(Butylamino)carbonyl]oxy]ethyl acrylate				
AM54	pPGA	Poly(propylene glycol) acrylate				pPGA
AM55	pPGMEA	Poly(propylene glycol)methyl ether acrylate				
AM57	DFHA	2,2,3,3,4,4,5,5,6,6,7,7-Dodecafluoroheptyl acrylate				
AM68	PFPA	2,2,3,3,3-Pentafluoropropyl acrylate				
AM70	HFiPA	1,1,1,3,3,3-Hexafluoroisopropyl acrylate				
AM75	pEGPhEA	Poly(ethylene glycol) phenyl ether acrylate				pEGPhEA
AT02	TMPOTA	Trimethylolpropane propoxylate triacrylate				TMPOTA
AT03	TMPTA	Trimethylolpropane triacrylate				TMPTA
AT07	TMPETA	Trimethylolpropane ethoxylate triacrylate				
BD05	EG4DMA	Tetra(ethylene glycol) dimethacrylate				
BD06	EG3DMA	Tri(ethylene glycol) dimethacrylate				
BM06	MHMB	Methyl 3-hydroxy-2-methylene-butyrate				
BM08	BMA	Butyl methacrylate				
BM09	CMAOE	Caprolactone 2-(methacryloyloxy) ethyl ester				
BM15	iBuMA	Isobutyl methacrylate				
BM20	MMA	Methyl methacrylate				
BM22	SMA	Stearyl methacrylate				
BM25	MTEMA	2-(Methylthio)ethyl methacrylate				
BM31	TMCHMA	3,3,5-Trimethylcyclohexyl methacrylate, mixture of isomers				

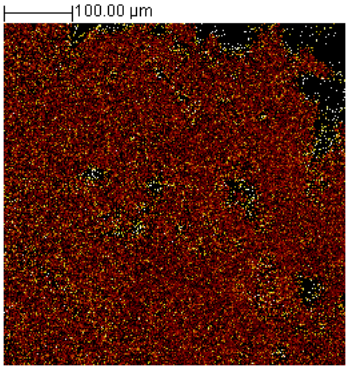
Abbr. old	Abbr. new	Monomer	Pipetting Air	Pipetting Argon	Printing Dimatix	Library
BM34	FuMA	Furfuryl methacrylate				
BM36	iBMA	Isobornyl methacrylate				
BM40	PhMA	Phenyl methacrylate				
BM53	DEGMA	Di(ethylene glycol) methyl ether methacrylate				
BM55	EGMMA	Ethylene glycol methyl ether methacrylate				
BM57	EGPhMA	Ethylene glycol phenyl ether methacrylate				EGPhMA
BM68	F6BMA	2,2,3,4,4,4-Hexafluorobutyl methacrylate				
BM81	pEGMA	Poly(ethylene glycol) methacrylate				
BM82	pEGMEMA	Poly(ethylene glycol) methyl ether methacrylate				
CD04	MBAm	N,N'-Methylenebisacrylamide, 96%				
CM07	MOPAm	N-(3-Methoxypropyl) acrylamide				
CM13	DMPAm	N-[3-(Dimethylamino)propyl] acrylamide				
DD01	MBMAm	N,N'-Methylenebismethacrylamide				
DEGDMA	DEGDMA	Di(ethylene glycol) dimethacrylate				
PEGDA250	PEGDA250	Poly(ethylene glycol) diacrylate (Mn-250)				PEGDA250
PEGDA575	PEGDA575	Poly(ethylene glycol) diacrylate (Mn-575)				PEGDA575
A4	A4	Ink2 - IIA4, 1,3-BDDA 35%, DMPA 2%				A4
C4-2	C4-2	Ink1 - IIpC4-2, TPGDA 20%, DMPA 2%				C4-2

Legend:

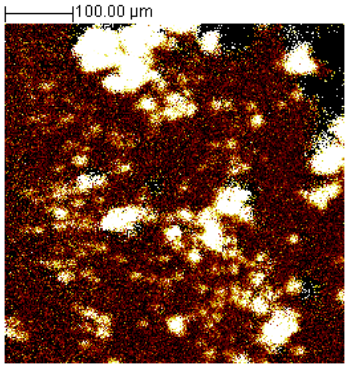
- Particle obtained
- Particle-like shape but not fully cured
- Particle but really sticky and rubbery
- Particle but only a few obtained
- No particles obtained
- Not tested

APPENDIX G - SURFACE CHEMICAL ANALYSIS OF INKJET PRINTED PARTICLES

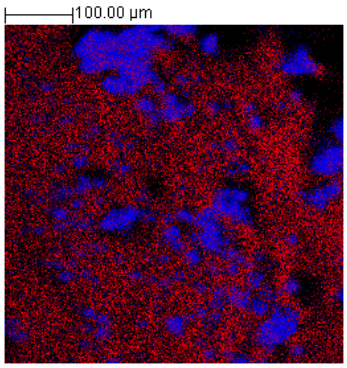
Monomer HPhOPA	Photoinitiator DMPA	Surfactant Triton X-100
		



$C_7H_5^-$ normalised to total



$C_6H_5O^-$ normalised to total



Overlay of $C_7H_5^-$ (red) and $C_6H_5O^-$ (blue)

APPENDIX H - ON-CHIP CO-POLYMERISED MICROSPHERES WITH APPLIED FLOW RATES AND MEASURED PARTICLE SIZES

On-chip monomers	Monomer 1 - Monomer 2 / PVA phase flow rate [ml/h]	Particle size [µm]
EGdPEA - HMDA	0.05 - 0.05 / 5.0	73.0 ± 2.9; 73.8 ± 0.8
EGPEA – EGdPEA	0.06 – 0.04 / 4.0	77.3 ± 1.4; 74.1 ± 2.2
EGPEA – TMPTA	0.05 – 0.03 / 4.0	72.5 ± 3.5; 77.9 ± 7.3
EGdPEA – HPhOPA	0.05 – 0.02 / 3.0	71.7 ± 4.2; 64.8 ± 2.2
TCDMDA – EGPEA	0.03 – 0.06 / 4.0	77.2 ± 1.2; 77.7 ± 1.1
HMDA – FuMA	0.10 – 0.10 / 4.0	75.7 ± 12.0; 73.4 ± 9.7
FuMA – TMPTA	0.05 – 0.05 / 4.0	70.3 ± 2.5; 69.7 ± 1.6
TMPTA – HMDA	0.03 – 0.07 / 4.5	67.1 ± 2.9; 58.7 ± 4.0
TMPTA – EGdPEA	0.05 – 0.05 / 4.0	83.9 ± 1.0; 73.1 ± 5.1

APPENDIX I - PHYSIOCHEMICAL PROPERTIES OF THE MONOMERS IN THE GENERATED LIBRARY

Abbr. old	Abbr. new	Monomer	Density* [g/ml]	Molecular weight	Viscosity* [cP]	Surface tension* [mN/m]	Glass transition [°C]	Partition coeff. ($clog\ P$)
AD01	BDDA	1,4-Butanediol diacrylate	1.05	198.2	4.5	35.2	45	2.20
AD04	HMDA	1,6-Hexandiol diacrylate	1.01	226.3	5.5	34.7	43	2.96
AD10	TCDMDA	Tricyclo[5.2.1.$0^{2,6}$]decanedimethanol diacrylate	1.10	304.4	138.6 12.9 at 70°C	38.4 31.0 at 70°C		4.36
AD15	DEGDA	Di(ethylene glycol) diacrylate	1.12	214.2	9.6	38.1		1.06
AD16	EGDA	Ethylene glycol diacrylate	1.09	170.2	2.8	34.6		1.68
AD18	TEGDA	Tetra(ethylene glycol) diacrylate	1.11	302.3	19.4	39.9		0.35
AD22	TPGDA	Tri(propylene glycol) diacrylate	1.03	300.4	12.1	32.4		2.35
AD24	pPGDA	Poly(propylene glycol) diacrylate	1.01	~800	67.9	32.1		4.39
AM31	HPhOPA	2-Hydroxy-3-phenoxypropyl acrylate	1.16	222.2	161.4 13.9 at 60°C	41.2 38.0 at 60°C	17	1.98
AM48	EGdPEA	Ethylene glycol dicyclopentenyl ether acrylate	1.09	248.3	17.5 9.4 at 40°C	33.2 35.0 at 40°C	19	2.96
AM51	EGPEA	Ethylene glycol phenyl ether acrylate	1.10	192.2	8.7	38.0	5	2.71
AM54	pPGA	Poly(propylene glycol) acrylate	1.02	~475	132.3	33.0		0.46
AM75	pEGPhEA	Poly(ethylene glycol) phenyl ether acrylate	1.13	324.0	32.3	42.2		1.65
AT02	TMPOTA	Trimethylolpropane propoxylate triacrylate	1.05	~644	108.5	32.8		4.38
AT03	TMPTA	Trimethylolpropane triacrylate	1.10	296.3	95.3	35.0 49.9 at 22°C		1.50

Abbr. old	Abbr. new	Monomer	Density* [g/ml]	Molecular weight	Viscosity* [cP]	Surface tension* [mN/m]	Glass transition [°C]	Partition coeff. ($clog\ P$)
BM57	EGPhMA	Ethylene glycol phenyl ether methacrylate	1.08	206.2	6.7	37.8		3.26
PEGDA (M_n-250)	PEGDA 250	Poly(ethylene glycol) diacrylate	1.11	250.0	12.0	38.4		
PEGDA (M_n-575)	PEGDA 575	Poly(ethylene glycol) diacrylate	1.12	575.0	59.5 15.0 at 60°C	42.0		
A4	A4	IIA4, 1,3-BDDA 35%, DMPA 2%			15.5 at 70°C			
C4-2	C4-2	IIpC4-2, TPGDA 20%, DMPA 2%		n=1-7 (n=2)	12.8 at 65°C			

*: measured at 25°C, otherwise mentioned

APPENDIX J - MOLECULAR PHYSIOCHEMICAL PROPERTIES OF SELECTED MONOMERS

Abbr. old	**Abbr. new**	**Monomer**	**Viscosity* [cP]**	**Partition coeff. ($c\log P$)****	**Number of rotatable bonds (nRoTB)**	**Molecular descriptor parameter α**
AD04	HMDA	1,6-Hexandiol diacrylate	5.5	2.96	7	0.12
AD10	TCDMDA	Tricyclo[5.2.1.$0^{2,6}$]decanedimethanol diacrylate	138.6	4.36	4	-2.60
AM31	HPhOPA	2-Hydroxy-3-phenoxypropyl acrylate	161.4	1.98	6	0.66
AM48	EGdPEA	Ethylene glycol dicyclopentenyl ether acrylate	17.5	2.96	4	-1.20
AM51	EGPEA	Ethylene glycol phenyl ether acrylate	8.7	2.71	4	-0.95
AT03	TMPTA	Trimethylolpropane triacrylate	95.3	1.50	22	8.18
BM34	FuMA	Furfuryl methacrylate	2.5	1.98	2	-1.10

*: measured at 25°C, **: $c\log P$ was calculated using ACD/ChemSketch V14.01 Software (ACD/Labs)